BEAM NORMAL SINGLE SPIN ASYMMETRY IN FORWARD ANGLE INELASTIC ELECTRON-PROTON SCATTERING USING THE Q-WEAK APPARATUS

A Dissertation

By

NURUZZAMAN

Submitted to the Graduate College of Hampton University in
partial fulfillment of the requirements for the degree of

DOCTOR OF PHILOSOPHY

December 2014

This dissertation submitted by Nuruzzaman in partial fulfillment of the requirements for the degree of Doctor of Philosophy at Hampton University, Hampton, Virginia is hereby approved by the committee under whom the work has been completed.

Liguang Tang, Ph.D.
Committee Chair

David J. Mack, Ph.D.

Eric Christy, Ph.D.

Alberto Accardi, Ph.D.

Patrena N. Benton, Ph.D.
Dean, The Graduate College

Date

ABSTRACT

Beam Normal Single Spin Asymmetry in Forward Angle Inelastic Electron-Proton Scattering
Using the Q-weak Apparatus. (December 2014)
Nuruzzaman, M. S., Mississippi State University;
M. Sc., Indian Institute of Technology Roorkee; B. Sc., University of Kalyani
Chair of Advisory Committee: Liguang Tang

The Q-weak experiment in Hall-C at the Thomas Jefferson National Accelerator Facility has made the first direct measurement of the weak charge of the proton through the precision measurement of the parity-violating asymmetry in elastic electron-proton scattering at low momentum transfer. There is also a parity conserving Beam Normal Single Spin Asymmetry or transverse asymmetry (B_n) on H_2 with a $\sin(\phi)$-like dependence due to two-photon exchange. If the size of elastic B_n is a few ppm, then a few percent residual transverse polarization in the beam, combined with small broken azimuthal symmetries in the detector, would require a few ppb correction to the Q-weak data. As part of a program of B_n background studies, we made the first measurement of B_n in the N-to-$\Delta(1232)$ transition using the Q-weak apparatus. The final transverse asymmetry, corrected for backgrounds and beam polarization, was found to be $B_n = 42.82 \pm 2.45$ (stat) $\pm$ 16.07 (sys) ppm at beam energy $E_{beam} = 1.155$ GeV, scattering angle $\theta = 8.3^\circ$, and missing mass $W = 1.2$ GeV. B_n from electron-nucleon scattering is a unique tool to study the $\gamma^*\Delta\Delta$ form factors, and this measurement will help to improve the theoretical models on beam normal single spin asymmetry and thereby our understanding of the doubly virtual Compton scattering process.

To help correct false asymmetries from beam noise, a beam modulation system was implemented to induce small position, angle, and energy changes at the target to characterize detector response to the beam jitter. Two air-core dipoles separated by $\sim$10 m were pulsed at a time to produce position and angle changes at the target, for virtually any tune of the beamline. The beam energy was modulated using an SRF cavity. The hardware and associated control instrumentation will be described in this dissertation. Preliminary detector sensitivities were extracted which helped to reduce the width of the measured asymmetry. The beam modulation system has also proven valuable for tracking changes in the beamline optics, such as dispersion at the target.

Dedicated to my parents Md. Shamsuzzoha, Nurun Nahar, my wife Shampa Samanta, my sister Arjun Nahar, my mentors Dave Mack, Liguang Tang, Dipangkar Dutta, Probodh Mondal, Biswanath Mondal, Malay Dutta, and Subrto Kundu.

ACKNOWLEDGEMENTS

This experiment was sponsored by the Department of Energy Office of Science (DOE), National Science Foundation (NSF), NSERC and the State of Virginia. I am very grateful for the support I received and the opportunities that were available during this time. I am indebted to a seemingly countless number of people for what I have accomplished. I would like to thank the individuals listed below.

My supervisor, Liguang Tang, provided me with many opportunities and I am very grateful for his support through the entire process. When I first joined Hampton University (HU) graduate program, Dr. Tang welcomed me to his research group and explained all the opportunities I can have. He provided many interesting projects to work on, including the weak charge measurement of proton at Jefferson Lab. He encouraged me to attend several conferences during my time at HU, including those in American Physical Society Atlanta, California and Washington conferences. I feel very proud and fortunate to work with my Jefferson Lab supervisor Dave Mack. It was delight working with him. He helped me to understand the lab environment and equipment in many ways. We discussed different topics of experimental nuclear physics field regularly, which helped me to build my knowledge about the field. He always encouraged me to think about great ideas. His deep knowledge and understanding of the field also helped me to solve problems very quickly. I can not thank Dr. Dipangkar Dutta enough for his encouragement and help in my professional and personal life. My research career started at Mississippi State University (MSU) with Dr. Dutta. He introduced me to the Jefferson Lab (JLab) and allowed me to work in different projects with him as my advisor, including the nuclear transparency of kaons and weak charge measurement of the proton at Jefferson Lab.

I am grateful to all of the friends and colleagues I have come to know at MSU, HU and at JLab. During the three years stay at MSU I had a wonderful experience with our medium energy physics group. Dr. James Dune along with Dr. Dipangkar Dutta helped me a lot. My colleagues at MSU, Amrendra Narayan, Luwani Ndukum, Adesh Subedi, Jed Leggett and Azmi al Masalha also frequently stretched out their helping hand. Special thanks are extended to Amrendra and Shloka Chandavar for their enormous help and support. They were with me always in my ups and downs. The graduate coordinator of the physics department, David Monts, was the nicest person that I can think of. He was always there with me whenever I needed help. I can't thank enough to my closest

friends in the department Saurabh Dayal, Nimisha Srivastava, Markandey Tripathi, Peeyush Sahay, Hazem Abusura, Chandrasiri Ihalawela and Ruiyuan Mu for their support throughout.

During my four years at HU I had a wonderful experience with our nuclear physics group. Michael Kohl, Cynthia Keppel and Dr. Liguang Tang helped me a lot. I would like to thank Monique Howard, Ebony Majeed, and Rashinda Davis for their help in administration . My colleagues in the group, Chunhua Chen, Anusha Liguang, Ozgur Ates, and Debaditya Biswas were with me frequently.

I spent a significant amount of time during my Ph.D career at Jefferson Lab. There were a number of people who were involved in my work and helped me. My experience with Paul King in the software work was great. He was very kind and helped whenever I needed him. Buddhini Waidyawansa and Rakitha Beminiwattha were very nice and helpful throughout the experiment. Wouter Deconinck and Jeong Han Lee were always helping me. Their hard work and dedication also inspired us. I would also like to thank my friends and colleagues, Don Jones, Manolis, Valery, Marty, Jim Dowd, Juan Cornejo, Wade, Josh Hoskins, John Leacock, John Leckey, Scott, Josh Magee, Jie, Peiqing, Siyuan, and Jean-Francois for their support.

A special thanks goes to my roommate Jonathan Miller who was been with me through my MS thesis. There aren't words to describe the importance of our friendship. John has been there with me in the best and worst of times.

I am thankful to the members of the Q^p_{weak} collaboration whose tireless efforts made the experiment a success. This includes the following spokespeople; Roger Carlini, Stanley Kowalsk and Shelley Page, and the other outstanding physicists involved in the core collaboration. I thank Dave Mack for his successful leadership of the testing, installation, commissioning and operation throughout. I wish to thank the entire Hall-C scientific and technical staff for their operational support of these experiments. I thank Steve Wood for his expertise with the Hall-C data acquisition system. I would like to thank Brad Sawatzky for his kind help to build several new online softwares. Special thanks to Mark Dalton for his helping hand in my analysis, when it needed most. I wish to recognize the efforts of the target group, and particularly Greg Smith, Silviu Covrig and Dave Meekins, for ensuring the successful operation of one of the most complex target used in Jefferson Lab. I want to thank Dave Gaskell for his outstanding contributions as a coordinator for running the experiment smoothly, including performing the Møller and arc energy measurements. I thank all the scientists and students who took shifts on the experiment so that it could run continuously.

I also wish to thank the accelerator staff and operators for their tireless and outstanding work delivering the high-energy, high-intensity, high-polarization, 100% duty-factor, stable CW electron beam to Hall-C. I want to thank accelerator operators I worked with, specially Sarin Philip for his

great help during the hardware assemble and testing. I want to thank Scott Higgins for his great work in the control system for beam modulation system. Special thanks to Mike Tiefenback for his brilliant ideas and Jay Benesch for his helping hand in my initial days at Jefferson Lab. Pitt Fransis, Simon Wood and Lee Broeker were very helpful in hardware installation and their valuable thoughts.

Also, I want to thank my committee members who read and provided useful feedback for this dissertation: Liguang Tang, Alberto Accardi, Eric Christy, and Dave Mack.

TABLE OF CONTENTS

LIST OF FIGURES

Figure Page

LIST OF TABLES

SECTION 1
INTRODUCTION

The Q-weak experiment at the Thomas Jefferson National Accelerator Facility, USA, (TJNAF or JLab) is aimed at determining the weak charge of the proton by measuring the parity-violating asymmetry of elastic electron-proton scattering at a low four-momentum-transfer squared (Q^2). The weak charge of the proton in the Standard Model (SM) is suppressed (very small in magnitude) and any significant deviation from the SM prediction found in this high precision measurement would suggest of new physics.

The Q-weak experiment is a rich program and consists of several auxiliary physics measurements. Measurement of parity-violating asymmetries in the N-to-Δ transition, which provides information about the axial transition form factor, is the topic of other theses. There is also a parity conserving beam normal single spin asymmetry or transverse asymmetry (B_n) generated in the scattering of transversely polarized electrons from unpolarized nucleons which is proportional to the imaginary part of the two-photon exchange amplitude. If the size of B_n is a few ppm, then a few percent residual transverse polarization in the beam, combined with small broken azimuthal symmetries in the detector, would require a few ppb correction to the Q-weak data. As part of a program of B_n background studies, we made the first measurement of B_n in the N-to-$\Delta(1232)$ transition.

1.1 Thesis Outline

This dissertation will present a preliminary analysis of the beam normal single spin asymmetry measured from the inelastic electron-proton scattering using the Q-weak apparatus. Another main focus of this thesis is the design, testing and operation of the beam modulation system designed to measure and correct for any false asymmetry. The outline of this dissertation is as follows:

- Chapter 1: INTRODUCTION - an introduction and motivation for the Q-weak experiment.
- Chapter 2: THEORY - a brief overview of the theory of beam normal single spin asymmetry measurements.
- Chapter 3: EXPERIMENTAL SETUP - a brief description of the experimental apparatus.

- Chapter 4: BEAM MODULATION - provides a detailed description of the beam modulation system emphasizing the work I have done on the design, hardware assembly, and operation.
- Chapter 5: BEAMLINE OPTICS AND FALSE ASYMMETRIES - application of beam modulation system, beamline characterization, and pedestal survey. This chapter present a summary of my other contributions to the Q-weak experiment to assist the main measurement of the weak charge of the proton.
- Chapter 6: BEAM NORMAL SINGLE SPIN ASYMMETRY - describes my work on the data analysis and treatment of systematic uncertainties of the beam normal single spin asymmetry in inelastic electron-proton scattering.
- Chapter 7: SUMMARY OF CONTRIBUTIONS AND CONCLUSIONS - a summary of this work and the analysis status.

1.2 The Standard Model and the Electroweak Interaction

The development of the SM in the twentieth century is one of the greatest achievements of particle physics, which is a theory concerning the electromagnetic, weak, and strong nuclear interactions [22]. The SM states that quarks and leptons are the fundamental particles which comprise all matter, and they interact through strong, weak, and electromagnetic fundamental interactions by exchanging force carrier particles. A summary of the SM particles with their mass, charge, and spin is shown in Figure 1.1. The weak interaction is unique among the four known forces since this is the only force known to violate parity. A parity transformation is defined as a discrete change of spatial coordinates from (x,y,z) to $(-x,-y,-z)$. The electromagnetic and weak interactions have been unified in an electroweak theory, which is one of the several successes of the SM. The Prescott experiment [23] at the Stanford Linear Accelerator Center (SLAC) helped confirm the SM predictions of the weak neutral current for the first time [24–26] by measuring the parity violating asymmetry in deep inelastic electron-deuteron scattering. This experimental verification of a prediction of the SM raised the acceptance of the SM over the other theories of particle physics at the time. Over the past half-a-century, the general structure of the SM has been confirmed by many experiments.

Despite many successes, there are many unresolved issues due to which the SM cannot be claimed as a complete theory. Some such drawbacks are that the SM does not account for dark matter, dark energy or gravity. The recently observed 3σ deviation of the anomalous magnetic moment of

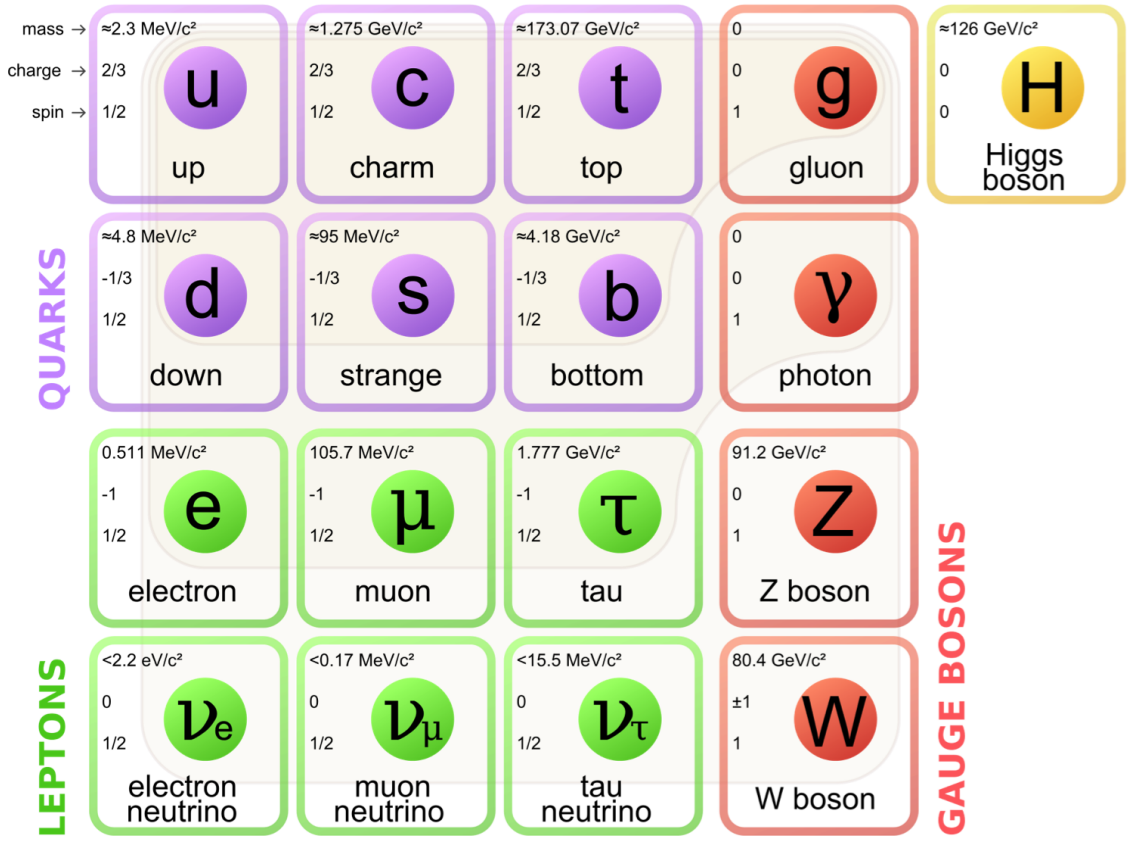

Figure 1.1 The Standard Model of elementary particles [1]. The three generations of matter, gauge bosons are shown in the fourth column, whereas the newly discovered Higgs boson in the fifth.

muon [27] at Brookhaven National Laboratory could also be related to particle physics beyond the SM.

The SM incorporates parity violation by expressing the weak interaction as a chiral gauge interaction. Over the last couple of decades, parity-violating electron scattering (PVES) has become an important experimental tool to investigate the contribution of the quark-antiquark sea[1] of the nucleon to its electromagnetic structure. Advancing technologies and improved experimental techniques have allowed us to do challenging experiments to measure parity-violating asymmetries at the parts-per-billion level. Figure 1.2 shows a brief history of the measured asymmetry in different PVES experiments. The difficulty level of an experiment increases with the decrease of the size and precision of the asymmetry. The Q-weak experiment is expected to measure the most precise value of the PV asymmetry in electron-proton scattering to date (see Figure 1.2).

[1] There is a quark-gluon sea within hadrons, where quarks and anti-quarks can fluctuate in and out of existence by pairproducing from the gluon fields.

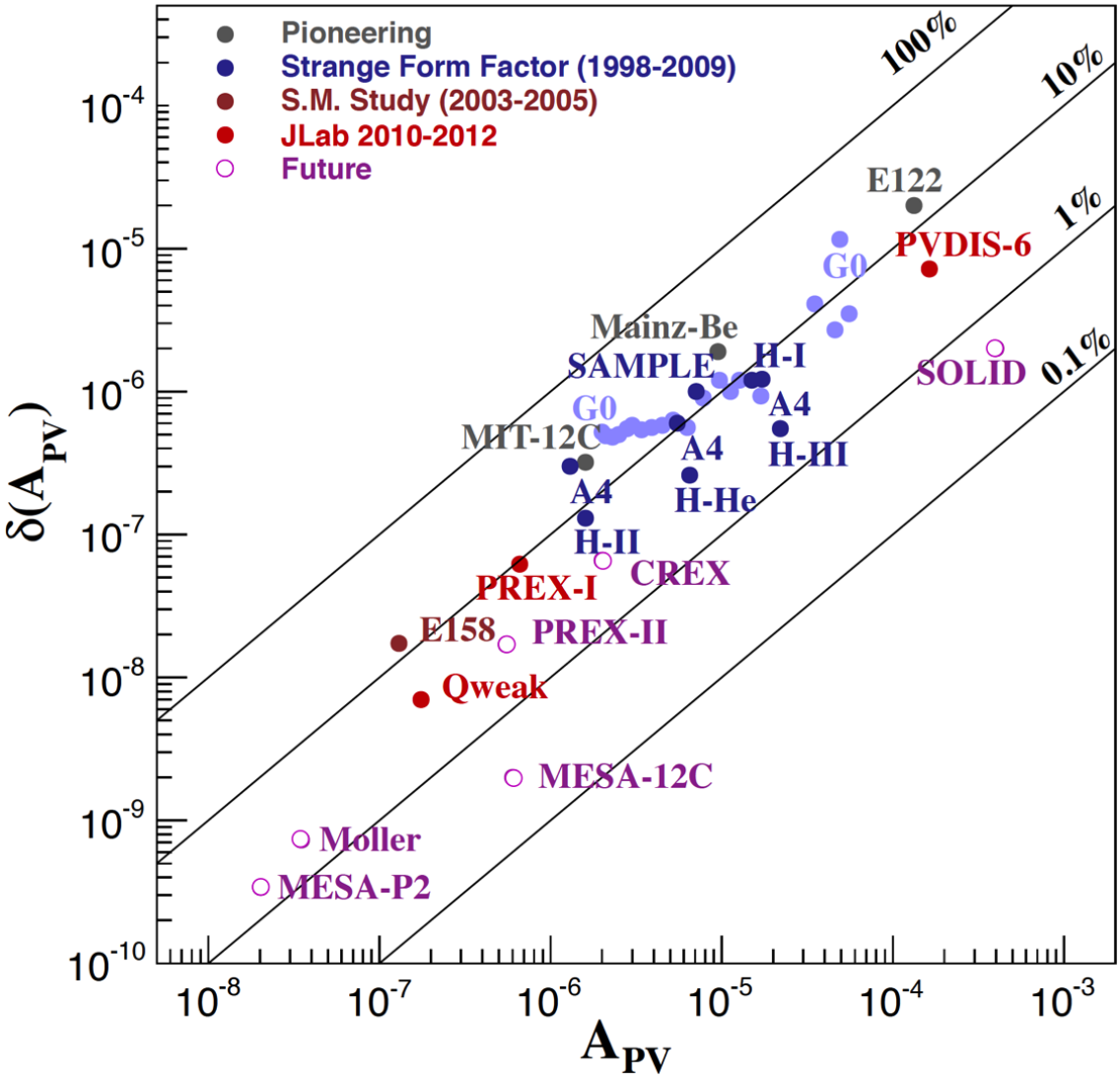

Figure 1.2 Q-weak will be the most precise (relative and absolute) PVES result to date. Technical progress over three decades since E122 has lead to smaller measured asymmetries and smaller absolute and fractional uncertainties on the asymmetries [2].

1.3 The Q-weak Experiment

The SM makes a firm prediction of the weak charge of the proton (Q_W^p) based on the running (Q^2 evolution) of the weak mixing angle $\sin^2\theta_W$ from the Z^0 pole mass down to low energies. Any significant deviation of $\sin^2\theta_W$ from the SM prediction at low Q^2 would be a signal of new physics, whereas agreement would place new and significant constraints on possible SM extensions. The weak charge of the proton is very small in magnitude in the SM (as shown in Table 1.1), and a precise measurement will challenge the SM predictions and search for new physics.

Table 1.1 The electromagnetic and weak charges of the up and down quarks, proton and neutron in the Standard Model. The third column gives the respective weak charges in terms of quark vector couplings C_{1u} and C_{1d}. At tree level, the weak charges can be written as a function of the weak mixing angle (θ_W).

Particle	EM Charge	Weak Charge		
u	2/3	-2C_{1u}	1 - (8/3)sin$^2\,\theta_W$	~1/3
d	1/3	-2C_{1d}	1 - (8/3)sin$^2\,\theta_W$	~1/3
p (uud)	1	-2(2C_{1u} + C_{1d})	1 - 4sin$^2\,\theta_W$	~0.07
n (udd)	0	-2(2C_{1u} + C_{1d})		~1

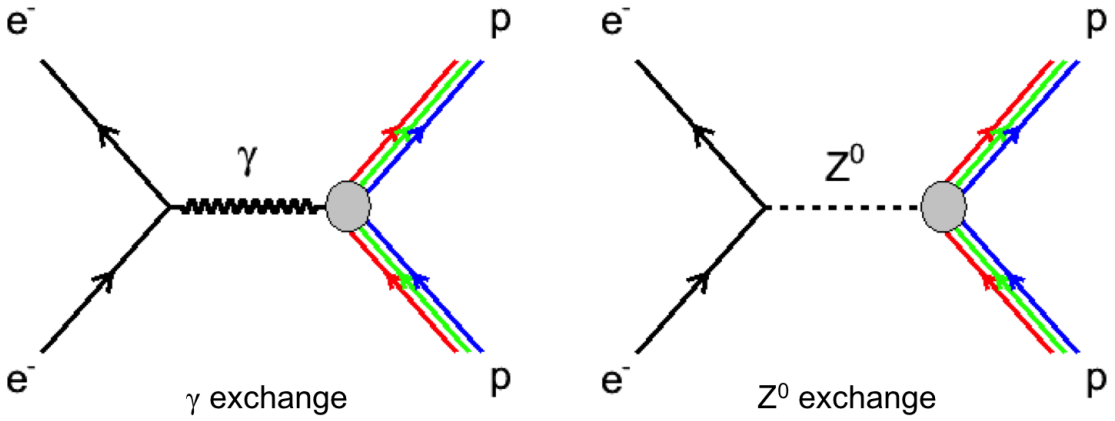

Figure 1.3 The Feynman diagrams for the parity conserving and parity violating semileptonic electroweak tree level interactions. The electromagnetic interaction (left) is mediated via the exchange of a virtual photon whereas a Z^0 boson is exchanged during neutral-weak interaction (right).

Neutral current electron-proton scattering can involve either an exchange of a photon or a Z^0 boson (Figure 1.3). The amplitude from the weak neutral-current exchange is highly suppressed, due to the large mass of the Z^0 boson. This interaction can be accessed through the violation of parity in the weak interaction and asymmetry is formed. The total cross section for neutral-current exchange is

$$\mathcal{M}_{total} \approx |\mathcal{M}_{EM} + \mathcal{M}_{weak}|^2 \approx |\mathcal{M}_{EM}|^2 + 2\Re\mathcal{M}^*_{EM}\mathcal{M}_{weak} + |\mathcal{M}_{weak}|^2, \tag{1.3.1}$$

where $\mathcal{M}_{EM}$ and $\mathcal{M}_{weak}$ are the amplitudes for the exchange of a photon and Z^0 boson, respectively. The sign of $\mathcal{M}_{weak}$ changes the sign of the interference term under a parity transformation. Experimentally, this is achieved by changing the helicity of a longitudinally polarized electron scattering from an unpolarized nucleon. The parity-violating asymmetry is then defined as

$$A_{PV} = \frac{\sigma^+ - \sigma^-}{\sigma^+ + \sigma^-}, \tag{1.3.2}$$

where σ^+ (σ^-) is the cross section for the electrons scattering with spin polarized parallel (anti-parallel) to their direction of motion. Given that $|\mathcal{M}_{weak}| \ll |\mathcal{M}_{EM}|$, this asymmetry reduces to being proportional to

$$A_{PV} \sim \frac{2\mathcal{M}_{weak}\mathcal{M}_{EM}}{|\mathcal{M}_{EM}|^2}. \tag{1.3.3}$$

At tree level[2] (lowest order diagrams), the full form of the asymmetry for electron-proton scattering can be written as [16]

$$A_{PV} = \left[\frac{-G_F Q^2}{4\sqrt{2}\pi\alpha}\right]\left[\frac{\varepsilon G_E^{p\gamma} G_E^{pZ} + \tau G_M^{p\gamma} G_M^{pZ} - (1 - 4\sin^2\theta_W)\varepsilon' G_M^{p\gamma} G_A^e}{\varepsilon (G_E^{p\gamma})^2 + \tau (G_M^{p\gamma})^2}\right], \tag{1.3.4}$$

where the Fermi constant is denoted by G_F. The kinematic factors in terms of proton mass M, scattering angle θ, and four-momentum transfer squared Q^2 are given by

$$\varepsilon = \frac{1}{1 + 2(1+\tau)\tan^2\frac{\theta}{2}},\ \varepsilon' = \sqrt{\tau(1+\tau)(1-\varepsilon^2)},\ \tau = \frac{Q^2}{4M}, \tag{1.3.5}$$

the neutral weak form factors for the proton can be expressed in terms of the electromagnetic form factors as

$$G_{E,M}^{pZ} = (1 - 4\sin^2\theta_W) G_{E,M}^{p\gamma} - G_{E,M}^{n\gamma} - G_{E,M}^{s}. \tag{1.3.6}$$

The weak charge of the proton in the SM is given by

$$Q_W^p = (1 - 4\sin^2\theta_W). \tag{1.3.7}$$

Defining

$$A_0 = \frac{-G_F Q^2}{4\sqrt{2}\pi\alpha}, \tag{1.3.8}$$

and using equations 1.3.4, 1.3.5, 1.3.6, 1.3.7, the reduced asymmetry, $\frac{A_{PV}}{A_0}$, can be written as

[2] In general tree diagrams are those without closed loops. The simplest "tree level" scattering diagram has two vertices.

$$\frac{A_{PV}}{A_0} = \left[\frac{\varepsilon G_E^{p\gamma}(Q_W^p G_E^{p\gamma} - G_E^{n\gamma} - G_E^s) + \tau G_M^{p\gamma}(Q_W^p G_M^{p\gamma} - G_M^{n\gamma} - G_M^s) - (1-4\sin^2\theta_W)\varepsilon' G_M^{p\gamma} G_A^e}{\varepsilon(G_E^{p\gamma})^2 + \tau(G_M^{p\gamma})^2}\right] \tag{1.3.9}$$

$$= Q_W^p + \left[(-1)\frac{\varepsilon G_E^{p\gamma} G_E^{n\gamma} + \tau G_M^{p\gamma} G_M^{n\gamma}}{\varepsilon(G_E^{p\gamma})^2 + \tau(G_M^{p\gamma})^2}\right] + \left[(-1)\frac{(1-4\sin^2\theta_W)\varepsilon' G_M^{p\gamma} G_A^e}{\varepsilon(G_E^{p\gamma})^2 + \tau(G_M^{p\gamma})^2}\right]. \tag{1.3.10}$$

The total reduced asymmetry then can be expressed as a combination of three reduced asymmetries as following

$$\frac{A_{PV}}{A_0} = A_{Q-weak} + A_{hadronic} + A_{axial}. \tag{1.3.11}$$

Here, the individual asymmetries are

$$A_{Q-weak} = Q_W^p, \tag{1.3.12}$$

$$A_{hadronic} = Q_W^n \left[\frac{\varepsilon G_E^{p\gamma} G_E^{n\gamma} + \tau G_M^{p\gamma} G_M^{n\gamma}}{\varepsilon(G_E^{p\gamma})^2 + \tau(G_M^{p\gamma})^2}\right], \tag{1.3.13}$$

$$A_{axial} = -G_A^e \left[\frac{(1-4\sin^2\theta_W)\varepsilon' G_M^{p\gamma}}{\varepsilon(G_E^{p\gamma})^2 + \tau(G_M^{p\gamma})^2}\right], \tag{1.3.14}$$

where the contribution from the strange form factors is ignored.

Under the kinematic condition of $\theta \to 0$, $\varepsilon \to 1$, and $\tau \ll 1$, the asymmetry simplifies as

$$\frac{A_{PV}}{A_0} = Q_W^p + Q^2 B(Q^2, \theta), \tag{1.3.15}$$

where the B(Q^2,θ) term contains the hadronic contribution to the asymmetry and is about 30%. Previous PVES experiments at higher Q^2 constrain this latter contribution.

The goal of the Q-weak experiment is to measure this parity violating asymmetry ($\sim$250 ppb) in elastic electron-proton scattering at $Q^2 = 0.025$ (GeV/c)^2 and forward angles to determine the proton's weak charge with 4% combined statistical and systematic uncertainties [16]. The experiment will also provide a $\sim$0.3% measurement of the weak mixing angle. A 2200 hours measurement using a 88% polarized electron beam of 180 μA on a 35 cm liquid Hydrogen target was performed during 2010 - 2012.

1.4 Inelastic Parity Violating Asymmetry

In addition to measuring the elastic PV asymmetry for Q-weak, dedicated data were taken to extract the inelastic PV asymmetry in electron-proton scattering. During normal production running, the detector signals were integrated. There is no way to separate the inelastic signal from the elastic signal. The inelastic asymmetry is expected to be a factor of 10 larger than the elastic asymmetry and the dilution was estimated to be as high as 0.2%. This meant a potential 2% inelastic contribution in the elastic asymmetry and hence, it was critical to measure and correct for it. The inelastic contribution in the Q-weak acceptance is mainly dominated by the production of the Δ resonance.

1.4.1 The Δ Resonance

The Δ is the first resonance of the nucleon with nucleon spin J=3/2 and mass 1232 MeV. In the ground state, the total spin of the proton is J=1/2, which is the sum of the spins of its constituent quarks (uud). The nucleon has two valence quark spins aligned parallel and one antiparallel. Therefore, only two possible flavor states (uud, udd) exist corresponding to isospin 1/2, protons and neutrons, whereas the Δ baryons have all three quark spins aligned parallel [28]. A list of allowed Δ resonance states and their properties is given in Table 1.2.

Table 1.2 Nucleons and Δ resonances and their associated properties. The Δ^{++} and Δ^{-} require the nucleon to undergo a spin flip and a quark flavor change given the initial state was a nucleon. Whereas, the Δ^{+} and the Δ^{0} can be created from the proton and nucleon, respectively, with solely a quark spin flip.

Particle	Quarks	EM Charge	Spin	Isospin	I_3
p	uud	+1	$\uparrow\uparrow\downarrow$	1/2	+1/2
n	udd	0	$\uparrow\downarrow\downarrow$	1/2	-1/2
Δ^{++}	uuu	+2	$\uparrow\uparrow\uparrow$	3/2	+3/2
Δ^{+}	uud	+1	$\uparrow\uparrow\uparrow$	3/2	+1/2
Δ^{0}	udd	0	$\uparrow\uparrow\uparrow$	3/2	-1/2
Δ^{-}	ddd	-1	$\uparrow\uparrow\uparrow$	3/2	-3/2

A photon or Z boson can interact with a nucleon and flip the spin of one of the quarks to make them all parallel to produce a Δ baryon. Only a Δ^{+} or Δ^{0} can be created by this kind of interaction if the target particle is a proton or neutron, respectively. On the other hand, in charged current scattering, a quark can change flavor and flip the spin to produce Δ^{++} and Δ^{-}. An electron-proton interaction that induces a quark spin flip can reveal information about how the

quark spin is redistributed during the transition. For the Q-weak experiment where the interactions were predominantly electron-proton, only the relevant resonance Δ^+ is considered.

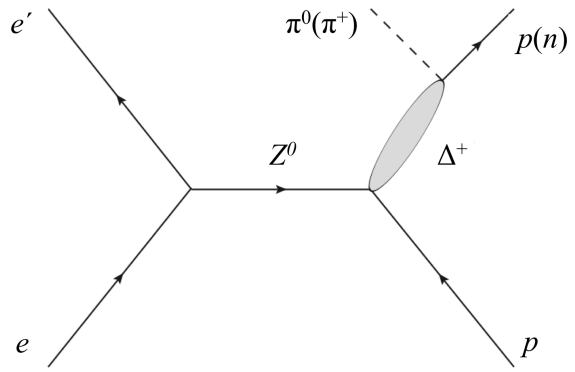

Figure 1.4 The schematic diagram for inelastic electron-proton scattering [3]. The incident electron (e) interacts with the proton (p) and loses energy (e′). The lost energy is transferred to the proton, which is excited to its first resonance (Δ^+) then decays to a pion and a nucleon.

In inelastic PV electron-proton scattering, the incident electron interacts with the proton and loses energy. The proton absorbs this energy and get excited to its first resonance (Δ^+), then decays to a pion (π) and a nucleon (as shown in Figure 1.4). The parity-violating asymmetry in the nucleon $\rightarrow \Delta$ transition can be expressed as [29, 30]

$$A_{PV}^{in} = \left[\frac{-G_F Q^2}{4\sqrt{2}\pi\alpha}\right]\left[\Delta_{(1)}^{\pi} + \Delta_{(2)}^{\pi} + \Delta_{(3)}^{\pi}\right], \tag{1.4.1}$$

where $\Delta_{(1)}^{\pi}$ contains the resonant terms, which are all isovector, $\Delta_{(2)}^{\pi}$ contains the nonresonant terms including both isovector and isoscalar, and $\Delta_{(3)}^{\pi}$ contains all axial-vector couplings at the hadron vertex. The asymmetry for the N $\rightarrow \Delta$ transition was measured as a part of the Q-weak background studies.

1.5 The Beam Normal Single Spin Asymmetry

The beam normal single spin asymmetry (BNSSA) is generated by polarized electrons when scattered from unpolarized protons and is a possible background asymmetry in parity violating electron scattering experiments (PVES). The BNSSA is a parity conserving asymmetry and can be expressed as

$$B_n = \frac{\sigma^{\uparrow} - \sigma^{\downarrow}}{\sigma^{\uparrow} + \sigma^{\downarrow}}, \tag{1.5.1}$$

where $\sigma^{\uparrow,\downarrow}$ are cross sections with incoming electrons polarized up or down, perpendicular to the scattering plane. Theoretical calculations [31] indicate that the size of this asymmetry can be several orders of magnitude larger than that of the parity violating asymmetry. For a precision experiment like Q-weak, it was important to estimate the background due to BNSSA and, therefore, a dedicated measurement was performed.

Elastic electron-nucleon scattering in the one-photon exchange approximation gives a direct access to the electromagnetic form factors of the nucleon which contain information about its structure. The ratio of the proton's electric to magnetic form factors (G_{Ep}/G_{Mp}) has been measured precisely up to large momentum transfer (Q^2) in precision experiments using two different methods, namely the polarization transfer [32, 33] and unpolarized measurements [34–36] using the Rosenbluth separation technique. These two different methods shows inconsistent results. This puzzle may be explained by a two-photon exchange amplitude as shown in Ref. [37]. A beam normal single spin asymmetry measurement provides direct access to the two-photon exchange process which is required to properly estimate the electron-nucleon scattering cross-sections beyond the Born approximation.

1.6 Inelastic Beam Normal Single Spin Asymmetry

The size of B_n is at least a few ppm, so a few percent residual transverse polarization in the beam, in addition to potentially small broken azimuthal asymmetries in the main detector, might lead to few ppb corrections to the Q-weak data. As part of a program of B_n background studies, we made the first measurement of B_n in the N$\rightarrow$ $\Delta(1232)$ transition using the Q-weak apparatus. In this dissertation, I will present the analysis of the transverse asymmetry in inelastic electron-proton scattering at beam energy E_{beam} = 1.155 GeV, scattering angle $\theta = 8.3^{\circ}$, and missing mass W = 1.2 GeV.

SECTION 2
THEORY

The electromagnetic form factors are the fundamental quantities of theoretical and experimental interest as they encode extensive information on the internal structure of the hadron [38]. These electromagnetic form factors express the non-local nature of the nucleon in its interactions with photons and have been studied extensively as the basic observables of the nucleon compositeness [39]. The increased precision of the electron-proton scattering experiments allowed the extraction of the form factors and using two methods: the Rosenbluth method - also known as the longitudinal-transverse separation technique [34, 40, 41], and the polarization-transfer technique [32, 33]. The two methods show incompatible results when considered in the one-photon exchange approximation, called the Born approximation, to extract the form factors. It is important to find an explanation of this discrepancy for the use of the electron-proton scattering as a precise and reliable tool in hadronic physics. Theoretical studies [42, 43] have indicated that the discrepancy could be partially resolved by including higher-order two-photon exchange corrections in the analysis in addition to the lowest-order one-photon exchange approximation. The calculation in Ref. [42] for the two-photon exchange diagrams considered only nucleons in the intermediate state. However, the Δ resonance has an important role in many hadronic reactions and it is essential to evaluate its contribution to the two-photon exchange in electron-proton scattering.

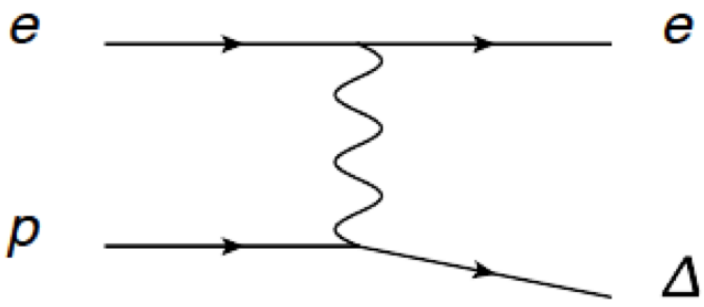

Figure 2.1 Electron-proton $\rightarrow$ electron-Δ transition in the one-photon exchange process.

2.1 Electron Scattering Beyond the Born Approximation

Beyond the Born approximation, the calculation of the amplitude of the scattering process becomes very complicated. Two or more photons are exchanged in the scattering process and one

needs to include all of the excited states of the proton. There are several existing models to calculate multi-photon processes [44], but they are incomplete.

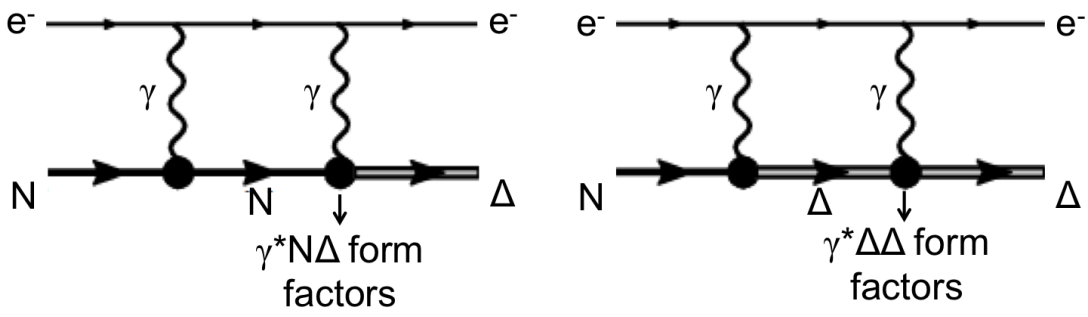

Figure 2.2 The beam normal single spin asymmetry in inelastic electron-nucleon scattering with Δ in the final state of the two-photon exchange process. The nucleon as the intermediate state is shown in the left, whereas Δ as intermediate state is shown in the right.

2.1.1 Two-photon Exchange

In elastic electron-proton scattering at leading order involves the exchange of a single photon (see Figure 2.1), followed by higher-order processes such as two-photon exchange (as shown in Figure 2.2). In the Born approximation this is usually approximated as a one-photon. This approximation is possible due to the small value of the electromagnetic coupling constant $\alpha \sim 1/137$. The higher order processes, such as two-photon exchange, are treated as radiative corrections. The two-photon exchange process involves the exchange of two virtual photons with an intermediate hadronic state that includes the ground state and all the excited states. In the analysis of the form-factor for electron-proton scattering, the contribution of the two-photon exchange amplitude is assumed to be very small [45]. The real (or dispersive) part of this amplitude is obtained by comparing electron-proton and positron-proton scattering cross sections. The calculations of the two-photon amplitude can be divided into two categories: unexcited intermediate proton states and excited intermediate proton states. The effect of the two-photon exchange contribution with an intermediate Δ resonance on the elastic electron-proton scattering cross section is smaller in magnitude than the nucleon contribution [39].

The first experimental evidence for the importance of the proper treatment of the two-photon exchange was seen with the measurement [32] of the protons electric (G_E) and magnetic form factor (G_M) ratio using the polarization transfer technique [46]. This is a complementary measurement to the Rosenbluth separation technique [47]. The discrepancy in the form factors extracted between

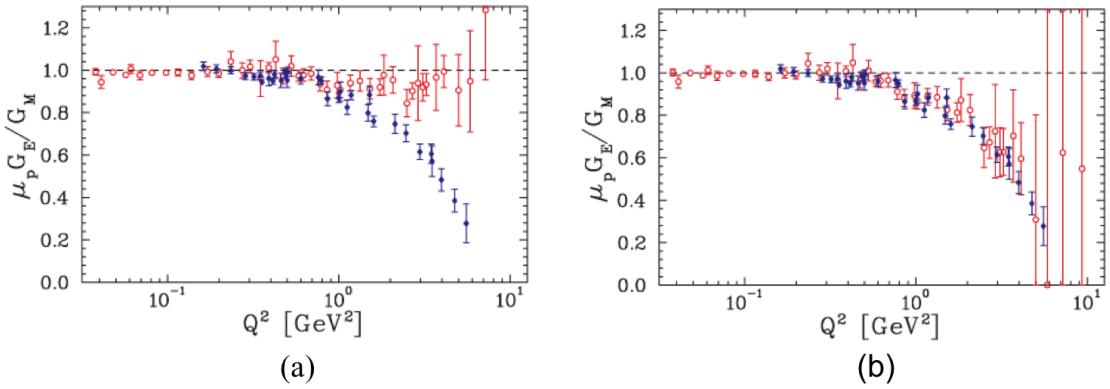

Figure 2.3 Ratio $\mu_p G_E/G_M$ extracted from the polarization transfer (filled diamonds) and LT measurements (open circles). The figure (a) and (b) shows LT separations without and with the two-photon exchange corrections applied to the cross sections, respectively. Figures are from Ref. [4].

the Rosenbluth separation and the polarization transfer techniques using the one-photon exchange approximation is shown in Figure 2.3 (a) [4]. The form factor results start to deviate above Q^2 of 1 (GeV/c)^2. After applying the two-photon exchange correction, the discrepancy seems to be resolved between the two methods, as shown in Figure 2.3 (b) [4]. The two-photon exchange calculations are not complete and have not been tested over a wider range of kinematics.

Another question naturally arises whether other higher-mass resonances could also have a non-negligible contribution to the two-photon exchange correction such as the $\Delta(1232)$ resonance [31]. The effects turn out to be not too important, as shown by Kondratyuk and Blunden [48] by generalizing the calculation to full spectrum of the most important hadron resonances as intermediate states involving spin 1/2 and 3/2 resonances.

2.2 Experimental Observation of Beam Spin Asymmetry

The beam spin asymmetries are time-reversal odd, parity conserving observables which vanish in the Born approximation. The beam spin asymmetry is an observable of the imaginary part of the two-photon exchange amplitude and can be extracted by observing only the electron (as shown in Figures 2.1 and 2.2). The asymmetry arises from the interference of the imaginary part of the two-photon exchange and one-photon exchange amplitude. Since the one-photon amplitude is real, only the imaginary part of the two-photon amplitude contributes to the beam spin asymmetry. The asymmetry is due to an electron helicity flip. The asymmetry can be obtained either by polarizing

the target perpendicular (transverse) to the incoming unpolarized electron beam, or by a transversely polarized beam on an unpolarized target. The asymmetry in the first case is known as target normal single spin asymmetry (A_n) while the latter case is called the beam normal single spin asymmetry (B_n). The measured asymmetry can be expressed as

$$\epsilon_M = \frac{\sigma^{\uparrow} - \sigma^{\downarrow}}{\sigma^{\uparrow} + \sigma^{\downarrow}} = \frac{\Im\left[\sum\limits_{spins} (\mathcal{M}^{\gamma})^* (Abs\mathcal{M}^{\gamma\gamma})\right]}{\sum\limits_{spins} |\mathcal{M}^{\gamma}|^2}, \tag{2.2.1}$$

where $\sigma^{\uparrow,\downarrow}$ are cross sections with incoming electrons polarized up or down, perpendicular to the scattering plane. Here, $\Im$ is the imaginary part and $Abs\mathcal{M}^{\gamma\gamma}$ is a sum over all the possible intermediate states in the two-photon exchange process. The cross section can be parameterized using six invariant amplitudes $\tilde{G}_E(\nu, Q^2)$, $\tilde{G}_M(\nu, Q^2)$, and $\tilde{F}_i(\nu, Q^2)$, which are complex functions of the Q^2 and ν. Here $\nu = K \cdot P$, where K and P are the average of the incoming electron and outgoing proton four-momenta, respectively [49,50]. In the Born approximation, the complex electromagnetic form factors become the usual Pauli and Sachs form factors of the nucleon, $\tilde{G}_E(\nu, Q^2) \to G_E(Q^2)$, $\tilde{G}_M(\nu, Q^2) \to G_M(Q^2)$, and $\tilde{F}_i(\nu, Q^2) \to 0$. Since $\tilde{F}_i$ and the phases of $\tilde{G}_E$ and $\tilde{G}_E$ vanish in the Born approximation, they must originate from processes involving at least the exchange of two photons. After Born approximation, using this parameterization, with the virtual photon polarization parameter,

$$\varepsilon = \frac{\nu^2 - M^4\tau(1+\tau)}{\nu^2 + M^4\tau(1+\tau)}, \tag{2.2.2}$$

the beam normal single spin asymmetry can be expressed as [51]

$$\begin{aligned} B_n = {} & \frac{2m_e}{Q}\sqrt{2\varepsilon(1-\varepsilon)}\sqrt{1+\frac{1}{\tau}}\left(G_M^2 + \frac{\varepsilon}{\tau}G_E^2\right)^{-1} \\ & \times \left[-\tau G_M \Im\left(\tilde{F}_3 + \frac{1}{1+\tau}\frac{\nu}{M^2}\tilde{F}_5\right) - G_E \Im\left(\tilde{F}_4 + \frac{1}{1+\tau}\frac{\nu}{M^2}\tilde{F}_5\right)\right] + \mathcal{O}(e^4), \end{aligned} \tag{2.2.3}$$

whereas the target normal spin asymmetry can be written as

$$\begin{aligned} A_n = {} & \sqrt{\frac{1\varepsilon(1+\varepsilon)}{\tau}}\left(G_M^2 + \frac{\varepsilon}{\tau}G_E^2\right)^{-1} \\ & \times \left[-G_M \Im\left(\delta\tilde{G}_E + \frac{\nu}{M^2}\tilde{F}_3\right) + G_E \Im\left(\delta\tilde{G}_M + \frac{2\varepsilon}{1+\varepsilon}\frac{\nu}{M^2}\tilde{F}_3\right)\right] + \mathcal{O}(e^4). \end{aligned} \tag{2.2.4}$$

An ultra-relativistic particle can be polarized in the direction normal to its momentum with a suppression factor m/E, where m is the mass and E is the energy of the particle [52]. The suppression

factor for the electron with beam energy in the 1 GeV range is of order 10^{-4} to 10^{-3}. The resulting beam normal single spin asymmetry is expected to be of order 10^{-6} to 10^{-5}, whereas the target-normal spin asymmetry is of order 10^{-2} [52].

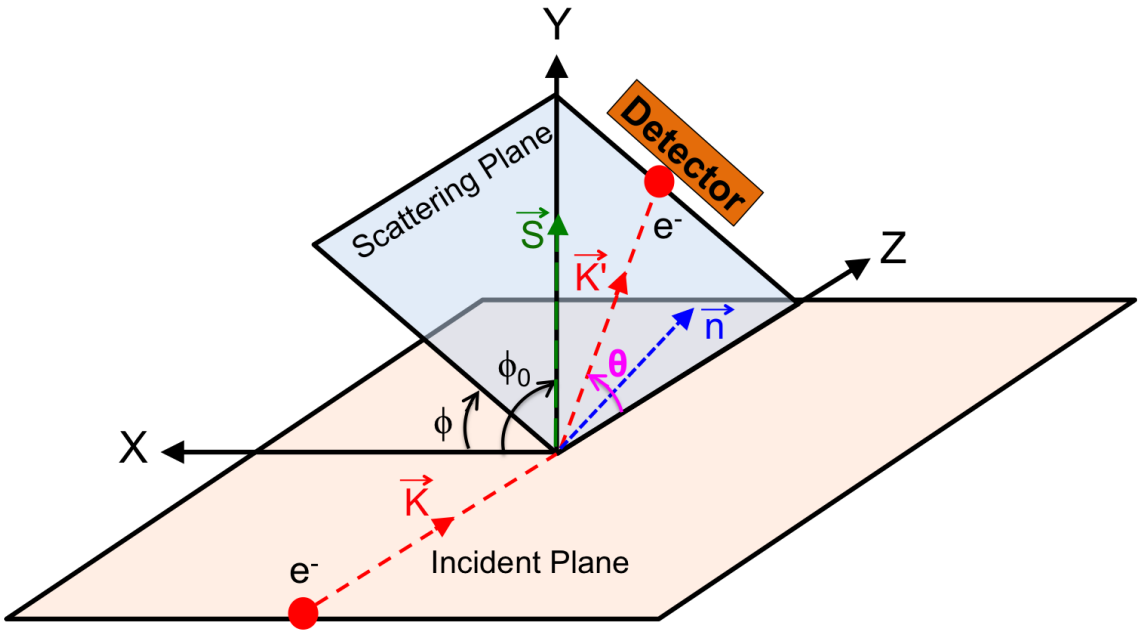

Figure 2.4 The schematic of transverse electron-nucleon scattering reaction. The electron spin is polarized in the vertical transverse direction. The initial (final) momentum of the electron is given by $\vec{K}$ ($\vec{K}'$).

2.2.1 Measurement of the Beam Normal Single Spin Asymmetry

The beam normal single spin asymmetry (BNSSA) is measured by scattering transversely polarized electrons from unpolarized nucleons. The measured asymmetry (ϵ_M) has a sinusoidal dependence about the beam axis

$$\epsilon_M(\phi) = -B_n \vec{S} \cdot \hat{n} = -B_n |\vec{S}| \sin(\phi - \phi_0), \tag{2.2.5}$$

where $\vec{S}$ is the electron spin in the transverse direction, and $\hat{n}$ is the unit vector normal to the scattering plane (see Figure 2.4). Here, ϕ_0 and ϕ are the azimuthal angles of $\vec{S}$ and the scattering plane, respectively with respect to incident plane. The beam normal single spin asymmetry can be measured and extracted from the asymmetry measured in the detectors placed at fixed scattering angle θ along the azimuthal angle ϕ.

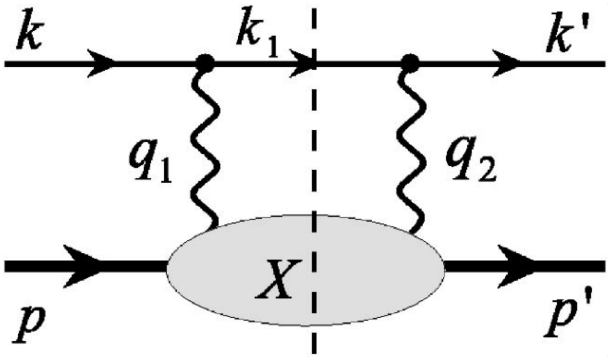

Figure 2.5 The two-photon exchange diagram. The filled blob represents the response of the nucleon to the scattering of the virtual photon [5, 6].

2.2.2 Imaginary Part of Two-photon Diagram

The imaginary part of the two-photon exchange amplitude is related to the absorptive part of the doubly virtual Compton scattering (DVCS) amplitude on the nucleon, as shown in Figure 2.5 and can be written as [53]

$$Abs\mathcal{M}^{\gamma\gamma} = e^4 \int \frac{|\vec{k}_1|^2 d|\vec{k}_1| d\Omega_{k_1}}{2E_{k_1}(2\pi)^3} \bar{u}(k')\gamma_\mu(\gamma k_1 + m_e)\gamma_\nu u(k) \frac{1}{Q_1^2 Q_2^2} W^{\mu\nu}(w, Q_1^2, Q_2^2) \tag{2.2.6}$$

The inelastic contribution to $W^{\mu\nu}$ corresponding with the πN intermediate states in the blob of Figure 2.5[1] [53] is given by

$$\begin{aligned} W^{\mu\nu}(p', \lambda'_N; p, \lambda_N) = & \frac{1}{4\pi^2} \frac{|\vec{p}_\pi|^2}{[|\vec{p}_\pi|(E_\pi + E_n) + E_\pi |\vec{k}_1| \hat{k}_1 \cdot \hat{p}_\pi]} \\ & \times \sum_{\lambda_n} \int d\Omega_\pi \bar{u}(p', \lambda'_N) J^{\dagger\mu}_{\pi N} u(p_n, \lambda_n) \times \bar{u}(p_n, \lambda_n) J^{\nu}_{\pi N} u(p, \lambda_N) \end{aligned} \tag{2.2.7}$$

where $p_\pi = (E_\pi, \vec{p}_\pi)$ and $p_n = (E_n, \vec{p}_n)$ are the four-momenta of the intermediate pion and nucleon states, respectively, and $k_1 = -\vec{p}_\pi - \vec{p}_n$. The integration runs over the polar and azimuthal angles of the intermediate pion, and $J^{\nu}_{\pi N}$ and $J^{\dagger\mu}_{\pi N}$ are the pion electro-production currents, describing the excitation and deexcitation of the πN intermediate state, respectively. u and $\bar{u}$ are matrix elements and can be parameterized. The inelastic contribution is dominated by the region of pion production threshold.

[1] can be calculated using the MAID model (resonance region)

2.3 The $\gamma^*\Delta\Delta$ Form Factors

The proton electromagnetic form factor is well known, experimentally. The proton $\rightarrow \Delta$ electromagnetic transition form factor is also fairly well known. For proton and Δ intermediate hadrons, vertices therefore are known except for the $\gamma^*\Delta\Delta$ electromagnetic vertex. The information about the $\gamma^*\Delta\Delta$ form factor has the potential to measure the charge radius of Δ and magnetic moment of Δ. Besides there have been many theoretical interest:

- Dyson-Schwinger approach [54]
- Covariant quark model [55]
- Lattice QCD [56]

This form factor has never been measured before. No dedicated calculations exist to relate $\gamma^*\Delta\Delta$ form factors to cross section or asymmetry data.

2.4 Model Calculations

The only model calculation of the beam normal single spin asymmetry in inelastic electron-nucleon scattering was performed (unpublished) by Pasquini & Vanderhaeghen for forward angles and low energies [7, 57]. The BNSSA as a function of the center-of-mass angle, θ_{cm}, for Δ (red) and nucleon (blue) intermediate states is shown in Figure 2.6. If the intermediate hadronic states are not included in the calculation, the prediction is nearly flat as a function of the θ_{cm}. This calculation was performed for lower energy than Q-weak, and an effort to extrapolate this result to the Q-weak kinematic settings is discussed in chapter 6. The beam normal single spin asymmetry is positive and of the order of 50 ppm. The large asymmetries in the forward region are dominated by quasi-virtual Compton scattering kinematics, where one exchanged photon becomes quasi-real. The asymmetry almost exponentially varies with scattering angle.

2.5 Goals of the Inelastic Transverse Physics Program

The objective of the Q-weak experiment is to challenge the predictions of the Standard Model in low Q^2 range and search for new physics at the TeV scale through a 4% measurement of the weak charge of the proton via the parity-violating asymmetry ($\sim$250 ppb) in elastic e+p scattering [16]. There is a parity conserving beam normal single spin asymmetry, or transverse asymmetry, B_n on H_2 with a $\sin(\phi)$-like dependence due to the two-photon exchange. The expected magnitude of B_n is few ppm which is an order of magnitude larger than PV asymmetry for the Q-weak and may

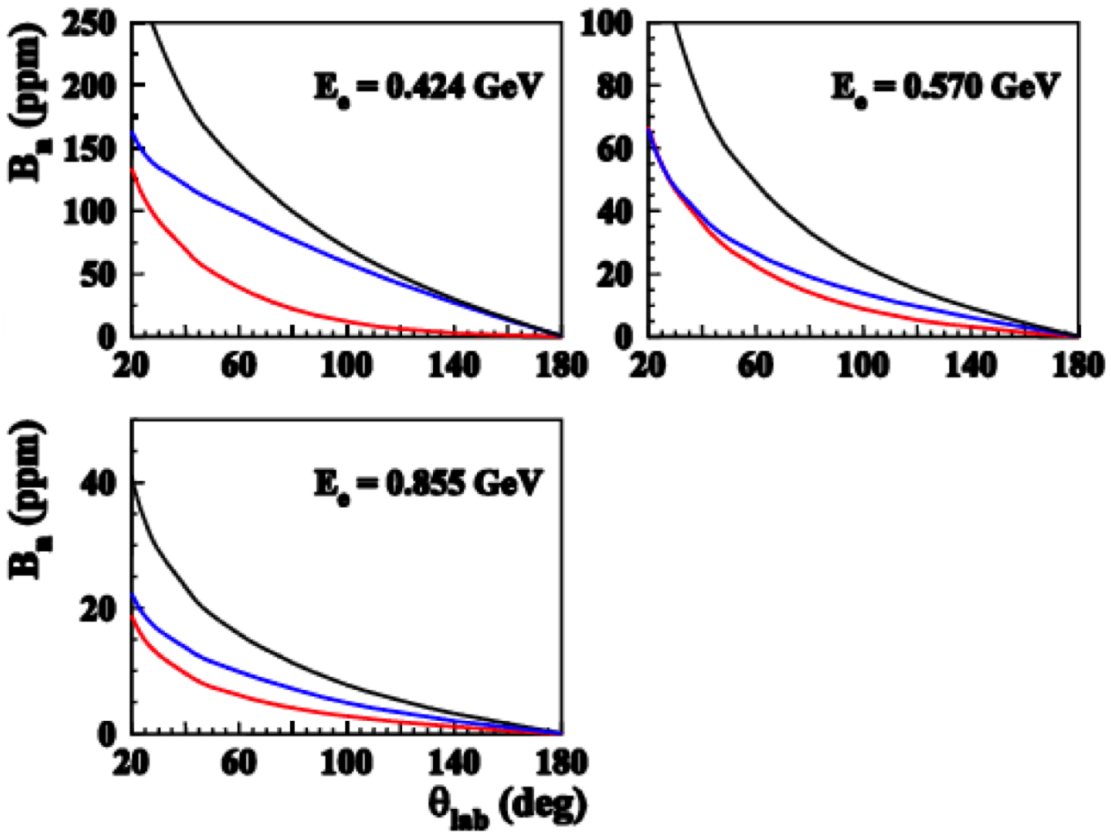

Figure 2.6 Inelastic transverse asymmetry model from Pasquini et al. [7]. Δ intermediate state is shown in red, N intermediate state is shown in blue, and total (Δ+N) contribution is shown in black.

produce a small background. Also B_n provides direct access to the imaginary part of the two-photon exchange amplitude. It will be interesting to see the magnitude of B_n in the N$\rightarrow \Delta$ region which has never been measured before. B_n from electron-nucleon scattering is also a unique tool to study the $\gamma^*\Delta\Delta$ form factors. This dissertation presents the analysis of the 9% measurement of the beam normal single spin asymmetry in inelastic electron-proton scattering at a Q^2 of 0.0209 (GeV/c)^2. This measurement will help to improve the theoretical models on the beam normal single spin asymmetry and thereby our understanding of the doubly virtual Compton scattering process.

SECTION 3

EXPERIMENTAL SETUP

The Q-weak experiment (E08-016) was performed at the Thomas Jefferson National Accelerator Facility (TJNAF/JLab) [58] in Newport News, Virginia from January 2011 to May 2012 [16,59,60]. The goal of the Q-weak experiment is to extract the weak charge of the proton by measuring parity violating (PV) asymmetry in elastic electron-proton scattering at low momentum transfer. The Standard Model (SM) predicts this asymmetry to be ~ -250 parts per billion (ppb) and the Q-weak collaboration proposed to measure this asymmetry with 2.1% statistical uncertainty. The Q-weak experiment has highly benefited from technologies developed by previous parity violating experiments such as SAMPLE [61] at the MIT/Bates Linear Accelerator Center, and G0 [62] and HAPPEX [63] at JLab. As the Q-weak PV asymmetry and its absolute uncertainty are an order of magnitude smaller than its predecessors, a dedicated design, significant improvement to hardware and software, and additional control of systematic uncertainties were needed to reach the proposed precision goals summarized in Table 3.1. A brief description of the experimental setup will be discussed in this chapter.

Table 3.1 Proposed error budget of the Q-weak experiment [16]. The second and third columns show the relative uncertainty of the parity violating asymmetry, and of the weak charge of proton, respectively. The total uncertainty is the quadrature sum of the statistical and systematic uncertainty.

Source of Error	$\frac{\Delta A_{PV}}{A_{PV}}$	$\frac{\Delta Q_W^p}{Q_W^p}$
Statistics	2.1%	3.2%
Hadronic structure	-	1.5%
Beam polarization	1.0%	1.5%
Absolute Q^2	0.5%	1.0%
Backgrounds	0.7%	0.7%
Helicity correlated beam properties	0.5%	0.8%
Total	2.6%	4.2%

3.1 Q-weak Kinematics

In two-body elastic electron-proton scattering, an incident electron with energy E and momentum p scatters from a stationary proton with mass M. The electron scatters with energy E' and momentum p_0 at an angle θ with respect to the incident electron as shown in Figure 3.1. The energy

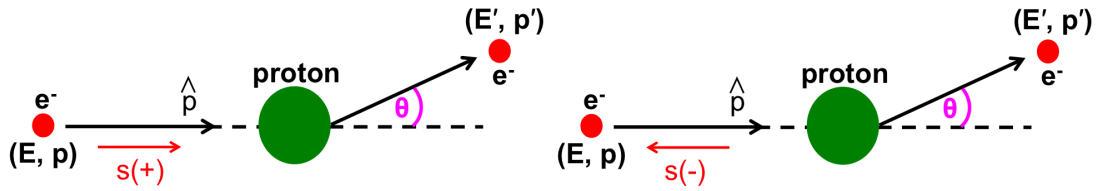

Figure 3.1 Sketch of the elastic electron-proton scattering process. An electron with energy (E) and momentum (p) scatters off a proton conserving the total energy of the system. E' and p' are the energy and momentum of the electron after scattering. The + helicity is denoted as the projection of the electron spin S along the direction of the momentum (shown in left), whereas the − helicity is the projection of the spin opposite to the direction of the momentum (shown in right).

transfer can be expressed as $\nu = E - E'$ and the 3-momentum transfer as $\mathbf{q} = \mathbf{p}$ - $\mathbf{p}'$. Then the four momentum transfer can be defined as

$$Q^2 = -q^2 = -(\nu^2 - \mathbf{q}^2) \geq 0 \tag{3.1.1}$$

Using energy and momentum conservation for two-body scattering, the scattered energy E' and Q^2 can be written as

$$E' = \frac{E}{1 + 2\frac{E}{M}\sin^2\frac{\theta}{2}} \tag{3.1.2}$$

$$Q^2 = \frac{4E^2\sin^2\frac{\theta}{2}}{1 + 2\frac{E}{M}\sin^2\frac{\theta}{2}}. \tag{3.1.3}$$

A dedicated tracking system was used to measure the scattering angle θ and Q^2 (more details in Section 3.12). Simulations were used to confirm the measurements. A longitudinally polarized electron beam with energy 1.155 GeV was incident on a 34.4 cm long liquid hydrogen target (LH_2). A magnetic spectrometer selected out the elastic electron-proton scattering at Q^2 ~0.025 $(GeV/c)^2$. A summary of the basic parameters and typical operating conditions for the experiment are shown in Table 3.2. The design parameters of the experiment were chosen to minimize the contributions from the anticipated systematic uncertainties shown in Table 3.1.

Table 3.2 Basic parameters and typical operating conditions of the Q-weak experiment [16–18].

Parameter	Value
Incident beam energy	1.155 GeV
Beam polarization	89%
Beam current	180 μA
LH_2 target thickness	34.4 cm
Cryopower	2.5 kW
Production running time	2544 hours
Nominal scattering angle	7.9°
Scattering angle acceptance	±3°
Acceptance	49% of 2π
Solid angle	$\Delta\Omega$ = 43 msr
Acceptance averaged Q^2	$\langle Q^2 \rangle$ = 0.025 (GeV/c)^2
Acceptance averaged physics asymmetry	$\langle A \rangle$ = -234 ppb
Acceptance averaged experimental asymmetry	$\langle A \rangle$ = -200 ppb
Luminosity	2×10^{39} s^{-1}cm^{-2}
Integrated cross section	4.0 μb
Integrated rate (all sectors)	6.5 GHz (0.81 GHz per sector)
Full Current Production Running	2544 hours

3.2 Experimental Techniques

The parity-violating asymmetry is defined as the difference over sum of the cross section for two different helicity states (+/-) as shown in Equation 3.2.1. The helicity state of the longitudinally polarized electron beam is flipped between "+" and "-" and scattered off of a fixed un-polarized proton target. The signal from elastically scattered electrons for each helicity state is integrated to measure the yield ($Y^{+/-}$). The difference in helicity correlated yield is sensitive to parity violating quantities. The raw asymmetry extracted from helicity correlated yields is defined as

$$A_{\text{raw}} = \frac{Y^+ - Y^-}{Y^+ + Y^-} \propto \frac{\left(\frac{d\sigma}{d\Omega}\right)^+ - \left(\frac{d\sigma}{d\Omega}\right)^-}{\left(\frac{d\sigma}{d\Omega}\right)^+ + \left(\frac{d\sigma}{d\Omega}\right)^-}. \tag{3.2.1}$$

The electron beam polarization was changed pseudo-randomly in a quartet (QRT) pattern of either "+ - - +" or"- + + -" with a helicity reversal rate of 960 Hz. The combination of fast helicity reversal and pseudo-random QRT patterns cancels slow drifts in yields, and minimizes target density fluctuations. Any common scale factors between the two helicity states cancel, but any difference does not. Hence Helicity Correlated Beam Asymmetries (HCBAs) in beam parameters like position, angle, energy, and charge can generate false asymmetries in measured asymmetry. Linear regression based on natural beam jitter or driven beam modulation is used to correct for such false asymmetries.

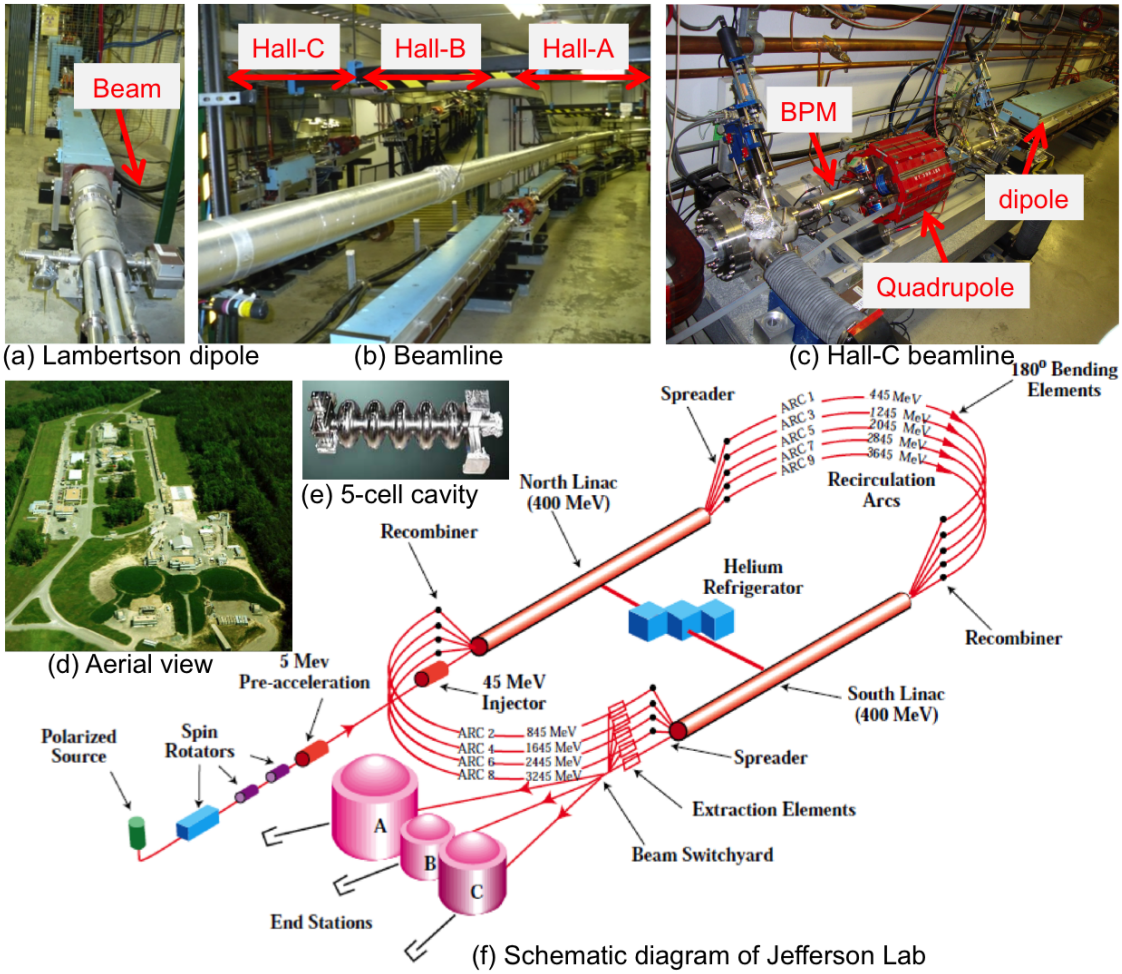

Figure 3.2 Schematic of Jefferson Lab and its beamline. (a) Dipole at Lambertson region where beam splits for three different experimental halls. (b) Three separate beamlines for three halls. (c) Hall-C beamline before entering in the hall. A typical quadrupole, dipole, and BPM are shown. (d) Aerial view of Jefferson Lab. (e) A JLab made 5-cell accelerating cavity. (f) Schematic diagram of Jefferson Lab. The elliptical region is the electron accelerator. Beam is accelerated by two linear accelerators, namely the North and South linacs, in the straight sections. Three existing Halls A, B, C are shown.

The asymmetry is then corrected for the beam polarization, several background contributions, and various experimental biases to obtain the final party violating asymmetry.

3.3 TJNAF Overview

The electron accelerator in TJNAF or Jefferson Lab (JLab) is known as the Continuous Electron Beam Accelerator Facility (CEBAF) [64], uses superconducting radio frequency (SRF) technology to accelerate electrons up to 6 GeV and is capable of simultaneous beam delivery to all three

experimental halls (A, B and C) at different energies, beam intensities, and orientations of beam polarization. The Q-weak experiment was carried out in experimental Hall-C during January 2011 to May 2012, although preparation began in 2001. In the future, JLab will upgrade its energy from 6 GeV to 12 GeV, and a new experimental hall (Hall-D) will be added [65]. A schematic of CEBAF is shown in Figure 3.2 (f). The JLab electron beam starts from a polarized source and ends in the beam dump at the end station. The longitudinally polarized beam starts from the source, travels through a series of spin rotators, is then accelerated by two linear accelerators and enters experimental Hall-C. Throughout the beamline, quadrupoles and dipoles are used to focus/defocus the beam and beam position monitors (BPMs), and beam current monitors (BCMs) are used to track the beam at any given point along the beamline. Polarimeters are used to measure the beam polarization before the hall entrance. Inside Hall-C there are various modules of the experimental apparatus like targets, collimators, toroidal magnet, and detectors. This chapter will discuss various key components of the experimental apparatus in following subsections.

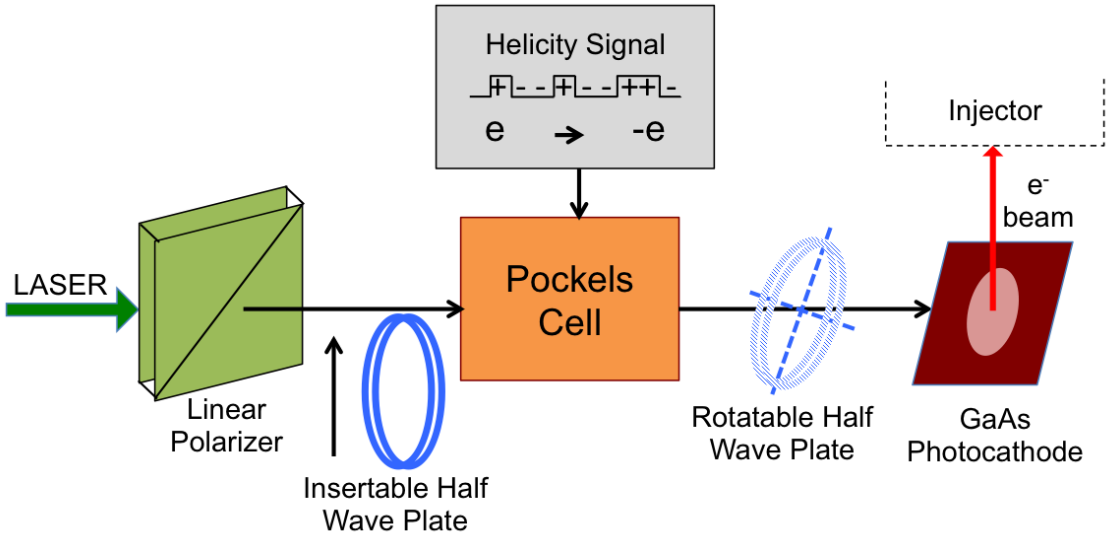

Figure 3.3 Schematic showing the process of producing circularly polarized light. The LASER is circularly polarized before GaAs photocathode using pockels cell.

3.3.1 Polarized Source and Helicity Reversal

The production of the electron beam starts with the polarized electron source. Circularly polarized light is used to produce polarized electrons from a strained super-lattice Gallium-Arsenide (GaAs) cathode via the photo-electric effect. This cathode is composed of several layers of material

containing GaAs with varying amounts of phosphorus doping, grown on a substrate. The supperlattice structure (alternating layers of GaAs and strained GaAs) increased the quantum efficiency (QE), which is the probability of electron emission per photon [66]. Each experimental hall has a dedicated laser that emits light at 1560 nm with pulses that are 120° out of phase in order to provide beam delivery in all halls simultaneously. To ensure total linear polarization, the light was passed through linear polarizers (shown in Figure 3.3). An insertable half wave plate (IHWP) was used to flip the relative direction of the linearly polarized light without changing the electronic helicity signal, helping to isolate false asymmetry effects. THe IHWP changes the spin of the electrons by 180°, this provided two independent data sets namely IHWP-IN and IHWP-OUT, that helped remove further helicity correlated beam asymmetries (HCBA). IHWP states were changed at a time interval of eight hours, called slugs. A Pockels Cell was used to convert linearly polarized light to circularly polarized electrons using induced birefringence. Just after the Pockels Cell, a rotatable half wave plate (RHWP) was used to rotate the residual linear polarization to circular polarization. This also helped to minimize the effect due to helicity-correlated beam parameters that arise from the residual linear polarization interacting with the photocathode. A more detailed overview of polarized electron beam technology with references to the scientific literature on the subject is available in [67].

A double Wien filter was used to rotate the polarization of the electron beam in order to fine tune and produce a fully longitudinally polarized beam during the experiment [68]. A single Wien system can flip the polarization of the beam by 90°. In a double Wien system both Wiens can rotate polarization by 90° which helps to cancel systematic false asymmetries. This method also helped to produce a fully transversely polarized beam for ancillary and background measurements. The transverse polarization measurement is discussed in a dedicated chapter.

3.4 Accelerator

The length of the accelerator is about 7/8 miles for one complete cycle. A thermionic electron gun is used as the source of electrons at the injector to extractan electron beam of energy 67 MeV with the standard setup. The electron beam is accelerated by two linear accelerators (linacs), the north and south linacs. A series of magnets bends the beam along the arcs which connects the two linacs. The beamlines, transporting the beam to the three halls are shown in the Figure 3.2 (f) by the red lines. Electrons from the injector are sent to the north linac at an energy of 67 MeV. Superconducting niobium RF resonant cavities, shown in Figure 3.2 (e) in the north linac section,

accelerate the electrons. In a standard tune, the maximum gain in energy per linac is 600 MeV. There are 20 cryomodules per linac, where each cryomodule consists of 8 cavities with an outer vacuum vessel, thermal radiation shield, magnetic shield, super insulation, and a welded helium vessel [8, 64]. The beam then goes through the east arc and into the south linac to accelerate for another 600 MeV energy gain. This beam can be sent directly to the Beam Switch Yard (BSY) for distribution to the experimental halls (Figure 3.2 (a)) or the beam can be steered along the west arc for another pass through the two linacs for another 1.2 GeV of energy gain. This process can be repeated up to four times. A maximum of five passes through both linacs provide energies from 445 MeV to 5945 MeV. As the beam energies are different in each pass, a different set of magnets are used to steer the beam around the arcs after each pass. A one pass beam was used for the Q-weak experiment as the required beam energy was 1.155 GeV.

3.5 Beamline

The beamlines that transport the beam from the accelerator to the experimental halls are shown in Figure 3.2. A two meter long dipole splits the beam for three different halls at the Lambertson (Figure 3.2 (a)). Beamlines for each hall (Figure 3.2 (b)) consists of a series of quadrupole and dipole magnets to transport the beam to the target in each hall (shown in Figure 3.2 (c) for Hall-C). The total length of Hall-C beamline from the Lambertson to the beam dump is 196.12 m. The beam position, profile and current were measured at various points along the beamline using BPMs (Figure 3.2 (c)) and BCMs, respectively. A part of Hall-C beamline also forms an arc, the bending magnets of which were used to measure the relative beam energy with a precision of $\Delta E/E \approx 10^{-4}$ (details in Section 3.6.4). A detailed sketch of Hall-C beamline elements is provided in APPENDIX A and discussed in technical document [69].

3.6 Beam Monitoring

3.6.1 Beam Position Monitor

The beam position was continuously monitored at many places along the Hall-C beamline and throughout the accelerator by SEE beam position monitors (BPM) during data collection to ensure that the beam was centered on the target. Each beam position monitor consists of a resonant cavity of a fundamental frequency equal to that of the accelerator and the Hall-C beam. The position of the beam is measured using four antennae rotated by 45^o in the plane (y axis is in direction opposite

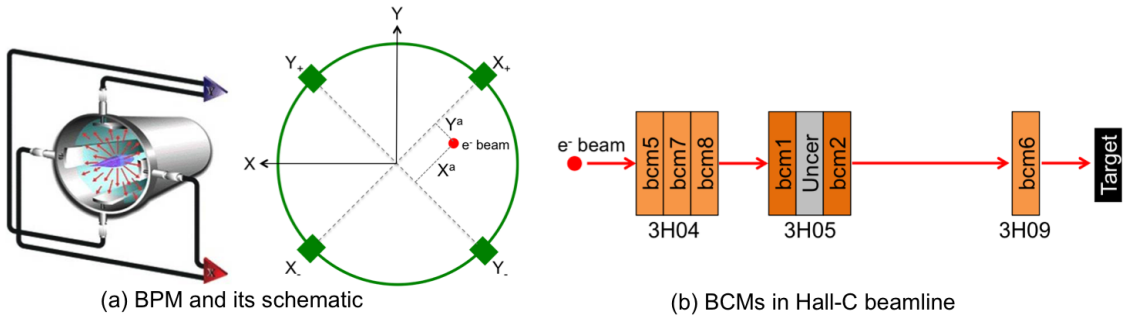

Figure 3.4 Beam position and current monitors. (a) Beam Position Monitors with four antennae rotated by 45^o in the plane. Z axis is perpendicular to the plane. (b) Beam Current Monitors and their locations at Hall-C.

to gravity, x is horizontal) perpendicular to beam direction (z-axis) shown in Figure 3.4 (a). Four antennae inductively pick up the fundamental frequency of the beam as it passes through the BPM. Then the radio frequency (RF) signal from each antena (wire) is processed electronically which yields a DC signal proportional to the beam current times the distance between the wire and the beam. The DC signals were sent through voltage-to-frequency converters and recorded with scalers that are read out by the Experimental Physics Industrial Control System (EPICS), the system used by the accelerator and end stations for slow control and monitoring of accelerator and experiment parameters with the rest of the data from the experiment. The beam position X^a and Y^a along the axis of the wires are calculated by a difference over sum of each opposite wire as:

$$X^a = k\frac{(X_+ - X_{\text{offset}+}) - \alpha_X\,(X_- - X_{\text{offset-}})}{(X_+ - X_{\text{offset}+}) + \alpha_X\,(X_- - X_{\text{offset-}})} \tag{3.6.1}$$

Where $X_{\text{offset}+(-)}$ is the offset for the $X_{+(-)}$ wire, k is the sensitivity of the BPM at 1497 MHz and α_X is a measure of the possibly different gains between the X_+ and X_- antennae [70, 71]. The gain difference α_X is defined as

$$\alpha_X = \frac{X_+ - X_{\text{offset}+}}{X_- - X_{\text{offset-}}} \tag{3.6.2}$$

The center of gravity of the four antenna signals measures relative changes in the offset of the beam from its ideal trajectory. The same approach is used to compute the relative beam position Y^a. Then the position of the beam in hall co-ordinate system can be written as:

$$\begin{pmatrix} X \\ Y \end{pmatrix} = \frac{1}{\sqrt{2}} \begin{pmatrix} 1 & -1 \\ 1 & 1 \end{pmatrix} \left[\begin{pmatrix} X^a \\ Y^a \end{pmatrix} - \begin{pmatrix} X^a_{\text{offset}} \\ Y^a_{\text{offset}} \end{pmatrix} \right] \tag{3.6.3}$$

The information from a BPM for an event can not be understood as the exact beam position on target for that event, as the signals are not synchronized with the event data itself and also because the actual position on target is constantly changing due to the fast raster system. Practically, an average beam position is calculated using a rolling average of BPM data information over a specified number of previous events depending on the experiment data rate. This average beam position is then corrected for each event using the fast raster signals [72]. Normally, the average beam position on target is very stable over the period of a single CODA run, it is more practical to simply ignore the event-by-event BPM information and fix the average beam position as a parameter of the analysis, and to use the raster signals to measure the change in beam position relative to the fixed average position. BPMs were calibrated using the super harps in Hall-C beamline [73]. Typically, calibrated BPMs have a resolution of 1 μm. Basic details about the BPMs can be found in [74].

Six BPMs in the Hall-C beamline over a span of 10 m upstream of the target were used to project the beam path at the target continuously during the experiment. Error averaged postion changes over six BPMs were used to measure the position and angle changes at the target, where BPMs in front of the target were used for the same to verify the result. A Detailed description about the target BPM can be found in [75, 76] and B. Waidyawansa's thesis [19].

3.6.2 Superharp

A more precise and accurate determination of the beam position and profile is obtained using the superharp system. Each superharp consists of a set of two vertical wires and one horizontal wire strung on a moveable frame. These wires can be scanned across a low current beam to measure its profile and absolute position. The signals induced on the wires as they are scanned across the beam are digitized by an analog to digital converter (ADC) and correlated with the wire positions as recorded by an encoder equipped with absolute position readout electronics. Since a harp scan interferes destructively with the electron beam, data taking must be interrupted to perform the measurement. In addition to measuring the beam profile, the superharp system provides a reference coordinate against which the BPMs were calibrated.

3.6.3 Beam Current Monitor

Čerenkov detector yields were normalized with beam current monitors to remove charge fluctuation . A series of six beam current monitors (BCMs) were used continuously for relative measurement of the beam current in the Hall-C beamline (as shown in Figure 3.4 (b)). The BCMs were coupled cylindrical stainless steel resonant cavities [77, 78] which were used to measure the beam current by measuring the resonance of the TM_{010} mode at 1497 MHz. This signal was then converted to a voltage in an RMS-DC voltage converter and read by TRIUMF made ADCs. This voltage signal was also sent to a 1 MHz voltage to frequency (V-F) converter and scalers for event-mode normalization. In the beginning, the only available BCMs were 1 and 2 and latter BCMs 5, 6, 7, 8 with low noise digital receivers were added. The BCMs were calibrated using a parametric current transformer device called an Unser monitor for the high beam current (1-180 μA) whereas for low current (10 nA to 1 μA) a Faraday cup was used for calibration. The detector yields were normalized with BCM1 and 2 during Run-I and BCM8 during Run-II. The nominal current measured by these BCMs during production running was 180 μA. More details about the BCMs used during the Q-weak experiment is discussed in a technical report by Ramesh Subedi [79].

3.6.4 Beam Energy

The four momentum transfer squared, Q^2, is approximately proportional to square of the absolute beam energy, E^2 (see Equation 3.1.3), and measured precisely. The helicity correlated energy asymmetry was also measured to remove false asymmetry.

3.6.4.1 Absolute Beam Energy

The Hall-C beamline arc was used as a spectrometer to measure the absolute beam energy [80]. The initial beam energy before scattering was defined as the absolute beam energy. An electron passing through magnetic fields, such as the beamline arc, changes its direction. That change can be related to the momentum as

$$p = \frac{e}{\Delta\theta} \int Bdl \tag{3.6.4}$$

where $\Delta\theta$ is the change in direction and $\int Bdl$ is the magnetic field integral over the electron path. Three sets of superharp scanners [81] were used to determine the position and the angle by scanning

the beam at the beginning, end, and middle of the Hall-C (or 3C[1]) arc. All the active elements (quadrupole, corrector magnets) of the beamline were turned off to avoid any distortion. This procedure is an invasive process and needs dedicated measurements. A typical energy measurement using this method yielded the energy as 1160.39 ± 1.74 MeV [8].

3.6.4.2 Energy Asymmetry

One of the helicity correlated beam parameters is beam energy asymmetry. Small deviations of the energy asymmetry from zero could result in false experimental asymmetries, hence precise measurement of the energy asymmetry is important for Q-weak. The middle of the 3C arc has the highest dispersion and is represented as 3C12 in JLab accelerator coordinate system. Any change in beam energy could result a big horizontal position change in the 3C12. A relative energy change at the target can be expressed as

$$\Delta\left(\frac{dE}{E}\right)_{\text{target}} = \frac{1}{M_{15}}\Delta X_{\text{3C12}} - \frac{M_{11}}{M_{15}}\Delta X_{\text{target}} - \frac{M_{12}}{M_{15}}\Delta X'_{\text{target}} \tag{3.6.5}$$

where ΔX_{3C12}, ΔX_{target}, $\Delta X'_{\text{target}}$ are position change at 3C12, position change at target, and angle change at the target, respectively. The first order beam transport matrices between 3C12 and target, M_{11}, M_{12}, and M_{15}, were determined using OptiM [82]. This calculation works for linear models and any residual dispersion at the target or X-Y coupling are not considered in this first order calculation. More details about this model will be discussed in the following chapter. The typical energy asymmetry at the target during the experiment was $\mathcal{O}(1)$ ppb.

3.6.5 Beam Modulation

To first order, the e-p scattering rate depends on five beam parameters: horizontal position (X), angle (X'), vertical position (Y), angle (Y'), and beam energy (E). Changes in these beam parameters when the beam polarization is reversed can create false asymmetries. Although different techniques were used to keep helicity-correlated parameter changes as small as possible, one must still correct for such false asymmetries. To do this, X, X', Y, Y' were modulated using four air-core dipoles in the Hall C beamline and the beam energy was modulated using a superconducting RF cavity. The goal of the beam modulation system was to occasionally induce controlled beam parameter changes ΔX_i, measure the resulting detector false asymmetry A_{false}, and determine the detector sensitivities $\partial A/\partial X_i$. This will allow later correction of beam false asymmetries via

[1] According to JLab accelerator division coordinate system, 3C symbolize for Hall-C beamline. Similarly 1C and 2C represents Hall-A and Hall-B beamlines, respectively.

$$A_{\text{false}} = \sum_{i=1}^{5} \frac{\partial A}{\partial X_i} \Delta X_i. \tag{3.6.6}$$

Even if these corrections prove to be small under ideal running conditions, the modulation system will allow the determination of any undesirable changes [83]. A dedicated chapter on beam modulation system will be discussed in following chapter.

3.6.6 Halo Monitors

Another important property of the beam is the beam halo which consists of stray electrons that move along with the primary beam but are far from the beam center and can contribute to the background. Beam halo can be generated via space-charge effects of electrons during bunching, scraping in the beam pipe, or poor vacuum. Halo can be measured using plastic Lucite detectors and scintillation counters. An 8 mm square opening and 13 mm diameter hole were used as halo targets. The halo monitors were located immediately downstream of the halo targets and upstream of the LH_2 target. The beam halo can also be estimated using the main detectors and luminosity monitors which can be normalized using the hole targets.

3.6.7 Fast Feed Back

The electron beam at JLab has fluctuations in beam position and energy. These fluctuations mostly occur at the power line frequencies of 60, 120, 180 etc. Hz and are rooted in the electromagnetic fields generated by the accelerator electronic equipment [84]. These deviations were largely nullified by using the Fast Feed Back (FFB) system which applies real time corrections, targeted at the power line harmonics [85], to the RF verniers along the beamline. The FFB system was implemented by modifying the existing BPM system and integrating it to the algorithm for correction signals. The control system for the FFB is EPICS based which provides a graphical interface on Unix workstations connected via Local Area Network (LAN) to a Input/Output Controller (IOC[2]). The FFB system was able to correct the energy fluctuation to better than 10^{-4} at power line harmonics up to 720 Hz using a frame rate of 3 kHz [84].

3.7 Polarimetry

One of the dominant systematic experimental uncertainty for the Q-weak experiment is expected to come from a 1% absolute uncertainty on beam polarization as shown in Table 3.1. In order

[2]VME bus embedded processor

to achieve this goal two polarimeters, a well tested invasive low current Møller polarimeter and noninvasive relatively new Compton polarimeter, were used to measure the beam polarization.

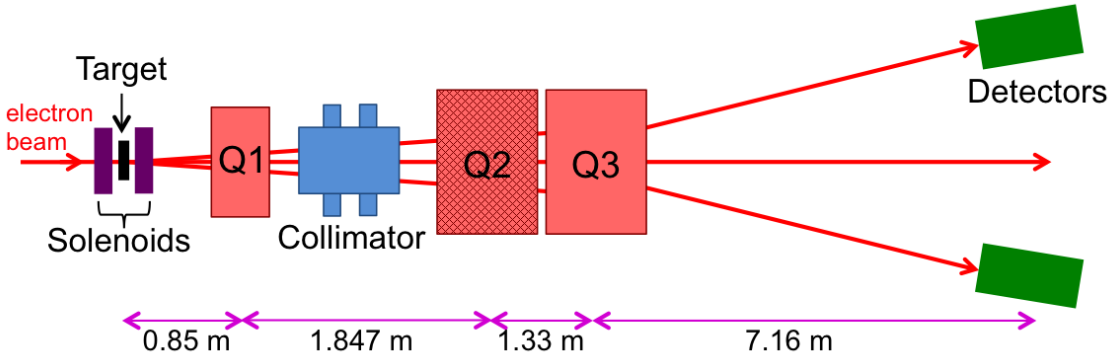

Figure 3.5 Layout of the Hall C Møller polarimeter showing tin foil target, set of superconducting solenoids, quadrupoles (Q2 was off during Q-weak), collimator box, and symmetric detectors.

3.7.1 Møller Polarimetry

The Møller polarimeter is used to measure the polarization of the longitudinally polarized electron beam entering Hall-C [86]. To accomplish this goal, the polarimeter measures the spin-dependent asymmetry in the elastic scattering of polarized electrons from polarized electrons i.e. $e^- + e^- \rightarrow e^- + e^-$(Møller scattering). This is a pure Quantum Electrodynamics (QED) process and its cross section can be calculated accurately. The target used for the scattering is a thin foil of iron magnetized by superconducting solenoids with field of ∼4 T. A pair of quadrupole magnets, Q1 and Q3, was used (Q2 was off during the experiment) to focus the scattered and recoil electrons into the symmetric detectors in coincidence. Then detectors measure the asymmetry and then the polarization is computed after correcting for the backgrounds. Figure 3.5 shows the layout of the Hall-C Basel Møller polarimeter. It was designed to operate with currents lower than 8 μA whereas the Q-weak production current was 180 μA. During the experiment, Møller measurements were performed invasively at low currents (1 μA) three times a week. The typical measured longitudinal polarization using the Møller polarimeter was about 88%. A sample of the Møller result will be shown in later chapters. A more elaborate description of the Møller polarimeter can be found in M. Loppacher's thesis [87] and the polarization technique used during Q-weak can be found in R. Beminiwattha's [88] thesis.

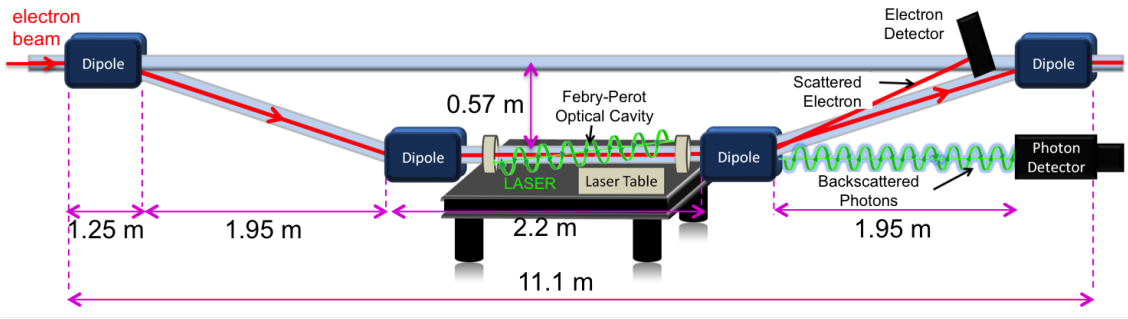

Figure 3.6 Schematic of the Hall-C Compton polarimeter. The incoming electron beam interacts with the green LASER at the straight section of the chicane. The scattered electrons and back-scattered photons are detected by electron detector and photon detector, respectively for each helicity (MPS) state.

3.7.2 Compton Polarimetry

A new Hall-C Compton polarimeter was installed and used for the Q-weak experiment [89]. This was a noninvasive high current polarimeter which continuously took data during production data taking (with $\sim$180 μA). The apparatus for the Compton polarimeter includes four dipoles in a chicane, a green laser, an electron detector, and a photon detector as shown in Figure 3.6. The Compton polarimeter use the Compton scattering ($e^- + \gamma \rightarrow e^- + \gamma$) of the incident electron beam with photons from a green laser. The scattered electrons and back-scattered photons provides two independent measurements of the polarization using both electron and photon detector, respectively. The dipole chicane was used to move the interaction point away from primary beam in order to detect back-scattered photons in the photon detector. A CsI crystal with photo multiplier tube was used as a photon detector. Later in the experiment, germanium silicon oxide (GSO) and lead-tungstate ($PbWO_4$) were used instead of CsI in the photon detector. The electron detector consists of radiation hard diamond micro-strips which were used for the first time as a tracking device in an experiment. The scattered electrons were detected in a array of 96 diamond strips after third dipole. There were four detector planes, each with 200 μm thick 96 strips and readout by four VME 1495 boards. The measured beam polarization using Compton polarimeter was about 87-89%. A sample of the Compton results will be shown in later chapters. More detailed descriptions of the Compton polarimeter and its electron and photon detector measurements will be discussed by A. Narayan [90] and J. Cornejo [91], respectively in their future theses.

3.8 Targets

The Q-weak target system has two main components: a main liquid hydrogen (LH_2) cell for production data taking and a matrix of solid targets used for background measurements and ancillary tests. The solid target ladder was thermally coupled to the bottom of the LH_2 cell. A schematic of the target system is shown in Figure 3.7.

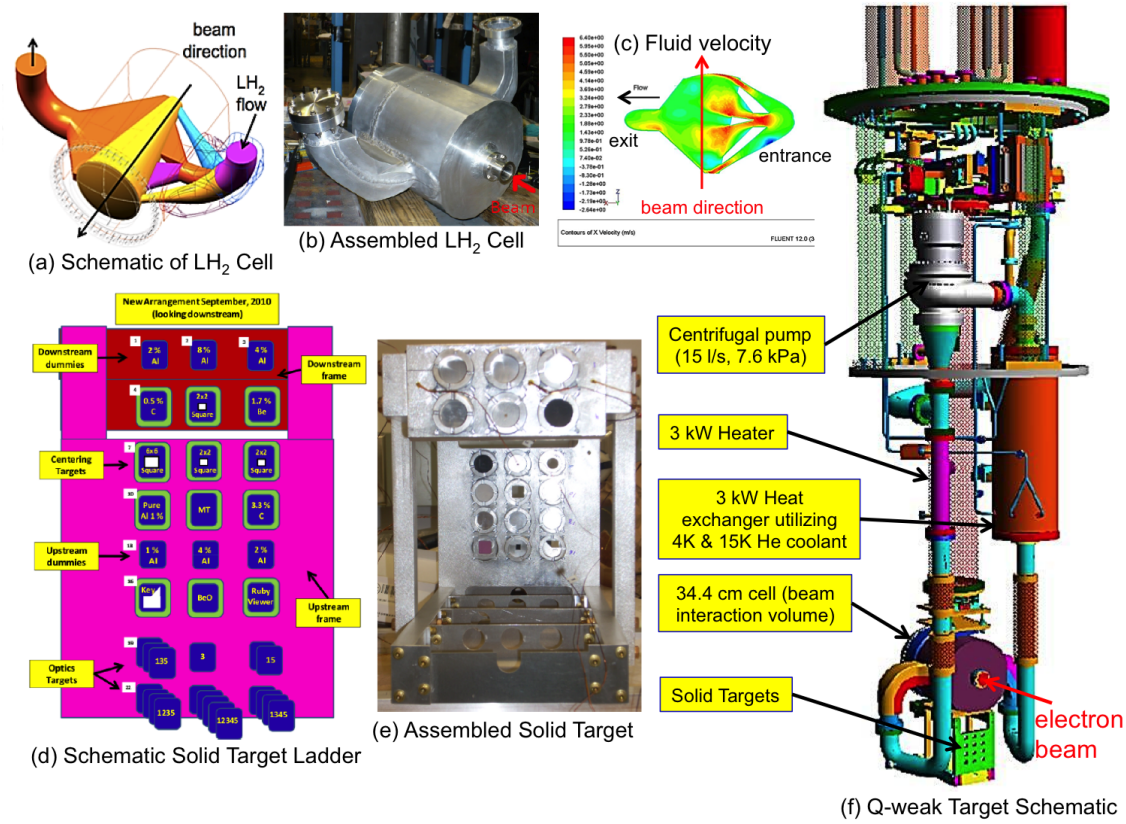

Figure 3.7 Q-weak target system. (a) Conical shaped Computer Aided Drawing (CAD) model of target cell design. (b) Assembled LH_2 target cell. (c) Simulation of LH_2 velocity contours inside target cell using CFD. (d) Schematic of solid target ladder. (e) Assembled solid target. (f) Full schematic of the target system with key components such as main LH_2 target cell, pump, heater, heat exchanger, solid targets are shown.

3.8.1 Liquid Hydrogen Target

A 34.4 cm long liquid hydrogen (LH_2) cell was used as the primary target for the Q-weak experiment [92]. This target can dissipate 2.5 kW of power deposited by the 1.155 GeV, 180 μA, 4 mm $\times$ 4 mm rastered electron beam and is the highest powered cryogenic target in the world to date. A unique hybrid cooling system used. 15 K coolant from the End Station Refrigerator

(ESR) and 4K coolant from the Central Helium Liquefier (CHL) were mixed in the heat exchanger (Figure 3.7 (f)). A high power heater was used to replace the heat deposited by the electron beam in case of beam trips. It also helped to stabilize the LH_2 target temperature in conjunction with the coolants in a proportional integral derivative (PID) feedback system. The 55 liters of LH_2 was contained within a target cell with thin aluminum (Al) alloy windows operated under 35 psi pressure at 20 K temperature and with a transverse flow of 1.2 kg/s maintained by a modified automobile centrifugal turbo pump with a rotational frequency of 30 Hz.

The long canonical shaped (see Figure 3.7 (a,b)) cell accommodated the 7.9° scattering angle and helped to achieve the high luminosity and statistical goal. The current mode production data taking was very sensitive to target density fluctuations. Therefore, the target was designed using Computational Fluid Dynamics (CFD) and simulated using ANSYS [93] (a fluid dynamics simulation code) to minimize noise from density fluctuations and maintain nominal fluid density. The simulation shows that the main hot spots were the entrance and exit windows of the cell as shown in Figure 3.7 (c). The exit window was 0.02 inch thick aluminum alloy with a 10 inch radius of curvature and a 0.005 inch nipple to minimize backgrounds.

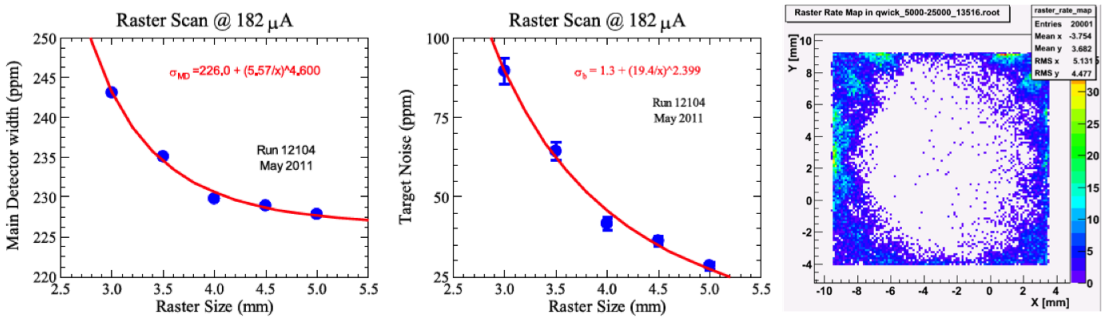

(a) Main detector vs raster size (b) Target boiling noise vs raster size (c) Raster rate with hole target

Figure 3.8 Raster studies. (a) Main detector width dependence on raster size. (b) Target boiling noise studies at 180 μA [8]. (c) 2d raster rate map with a hole target.

3.8.1.1 Raster

The intrinsic size of the electron beam (perpendicular to beam direction) at JLab is ~2 μm and creates localized high power density on the LH_2 target. This could result in boiling the target. Hence the beam was rastered on the target over an area of 4 mm × 4 mm by the fast raster system. The raster was designed to have a matching beat frequency with fast helicity flip of 960 Hz. This method assures each integration period has the same complete raster pattern on the target and prevents

systematic differences in the beam position between Macro Pulse Signal (MPS). The contribution of target density fluctuation and raster size dependence to the statistical width was measured by using known detector asymmetry widths from statistics and other sources (shown in Figure 3.8 (a)). In typical production running with 180 μA, 4 mm $\times$ 4 mm rastered beam the contribution from target boiling noise was 46 ppm (shown in Figure 3.8 (b)), which is relatively small contribution to the statistical width of $\sim$200 ppm.

3.8.2 Solid Target

Along with LH_2 target an array of solid targets [94] consist of aluminum (Al) dummy targets, optics targets, and centering targets were used for background and ancillary measurements. The solid target ladder was thermally coupled to the bottom of the LH_2 cell as shown in Figure 3.7 (f). A detailed schematic of solid target matrix looking upstream is shown in Figure 3.7 (d,e). Horizontal and vertical motion controller were used to insert different targets into the beam. Three different Al dummy target thicknesses for both upstream and downstream locations were used to measure the effect of radiative corrections in the measured asymmetry. The optics targets were primarily used for particle origin reconstruction in the tracking measurements. Optics target helped to locate the position of the target ladder in raster rate scan as shown in Figure 3.8 (c).

3.9 Collimators and Shielding

A set of three lead collimators were used to define the experiment's angular acceptance and minimize the inelastic and neutral background contribution to the detector. The collimator system is shown in Figures 3.9 and 3.10 (c). The first collimator, a water cooled tungsten plug of inner radius $\sim$7 mm, was placed just downstream of the target and was used to reduce the electron scattering from the beamline. The second (or primary) collimator defined the acceptance as 4% of π in θ and 49% of 2π in ϕ. The angular acceptance of the primary collimator from the upstream end of the target window is θ = 5.8° - 10.2° and θ = 6.6° - 11.5° from the downstream end. The third collimator was before the Q-weak Toroidal Magnetic Spectrometer (QTor) and further cleaned the electron flux before it reached to QTor magnetic field. Besides these three collimators a 80 cm thick shielding wall of barite-loaded (Ba_2SO_4) high-density (2.7 g/cm^3) concrete was used after QTor for addition shielding. A details description of shield wall and collimator system can be found in J. Mammei [50], and K. Myers's [8] theses.

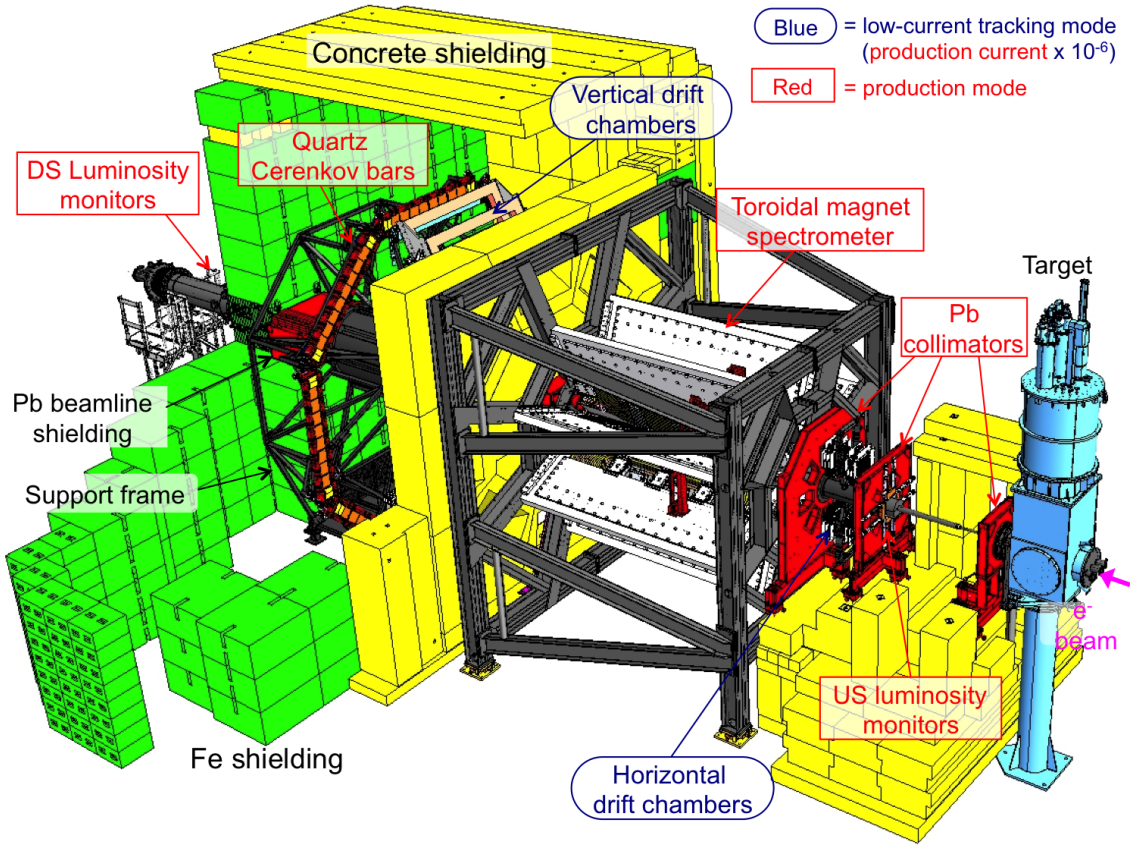

Figure 3.9 Schematic diagram of the Q-weak apparatus. The basic experimental design showing the target, collimators, toroidal magnet coils, and detectors. Elastically scattered electrons focus at the Čerenkov detectors. High current production mode apparatus components are shown in red rectangular boxes and low current tracking mode components are shown in blue elliptical boxes. Beam direction is from right to left.

3.10 Q-weak Toroidal Magnetic Spectrometer: QTor

The eight fold symmetric torodial magnetic spectrometer used for the Q-weak experiment is known as QTor (shown in Figure 3.10 (a,d)). It has race track shaped water cooled copper (iron free) magnetic coils (shown in Figure 3.10 (e)). The dimensions of the each magnet coil are 2.2 m long along the straight sections with an inner radius of 0.235 m and outer radius of 0.75 m. Eight such identical coil packages with $\Delta\phi \sim 45^\circ$ gaps between them made the QTor structure (relevant coordinate system is shown in Figure 3.10 (b)). The primary objective of the QTor magnet was to focus the elastically scattered electrons to the main Čerenkov detector at the focal plane of apparatus (shown in Figure 3.10 (c)). Neutral particles (neutrons, photons, etc.) remain undeflected. Also the QTor did not affect the unscattered beam as there was no field along the geometric center of

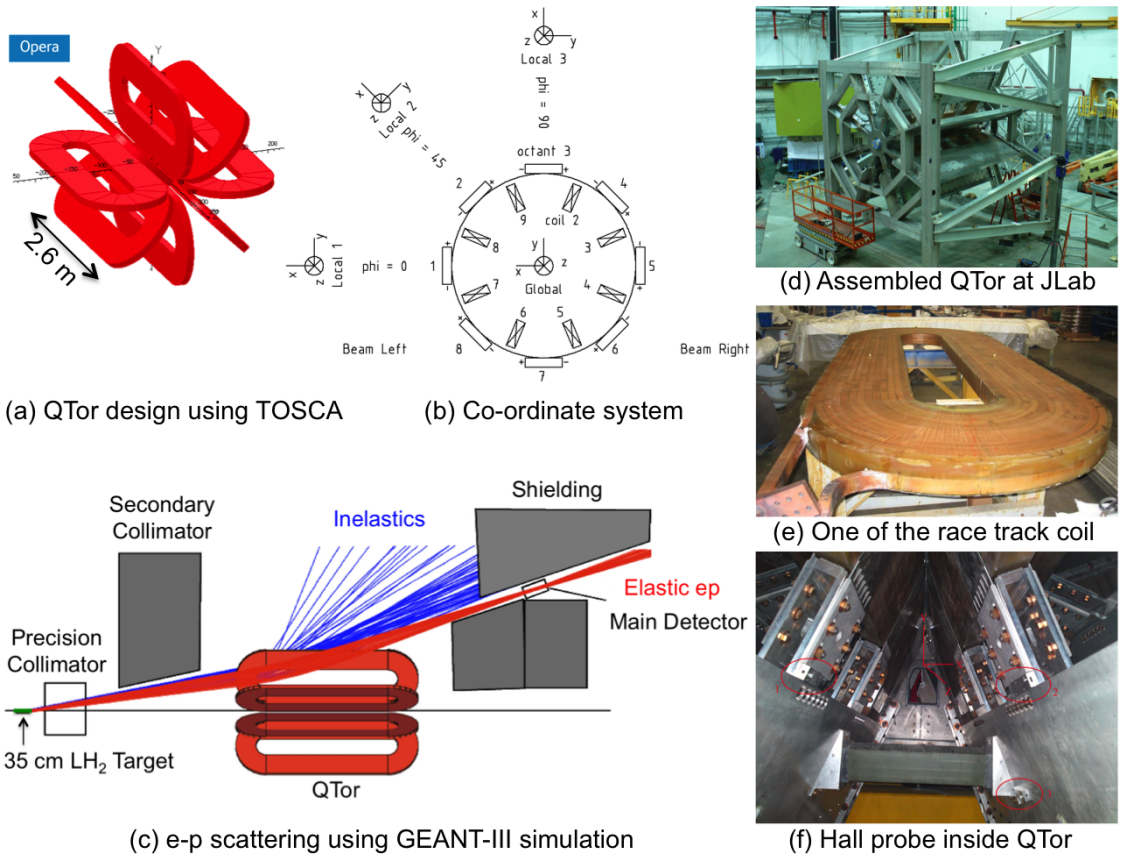

Figure 3.10 Q-weak torodial magnetic spectrometer (QTor). (a) QTor design using TOSCA. (b) Co-ordinate system. (c) e-p scattering using GEANT-III simulation. (d) Assembled QTor at JLab. (e) One of the race track coil. (f) Hall probe inside QTor.

the magnet. During the elastic asymmetry measurement, QTor was operated at 8921 A, whereas during the inelastic ($N \rightarrow \Delta$) asymmetry measurement, the operational current was 6700 A. The magnet required a 10 kA power supply operated at 130 V and produced a field integral of $\int \vec{B} \cdot \vec{dl}$ = 0.67 T.m along the central trajectory. P. Wang has more details about the QTor design structure and field map in his master's thesis [95].

3.10.1 Hall Probe

A transverse (Lake Shore MNT-4E02-VH) hall probe was used to measure the QTor magnetic field in real time. Three hall probe mount panels were designed and attached to the inside wall of QTor as shown in Figure 3.10(f). The probe was inserted inside the mount and attached with a Lake Shore 460 3-channel Gaussmeter controller [96] via a 30 m long special magnetically shielded

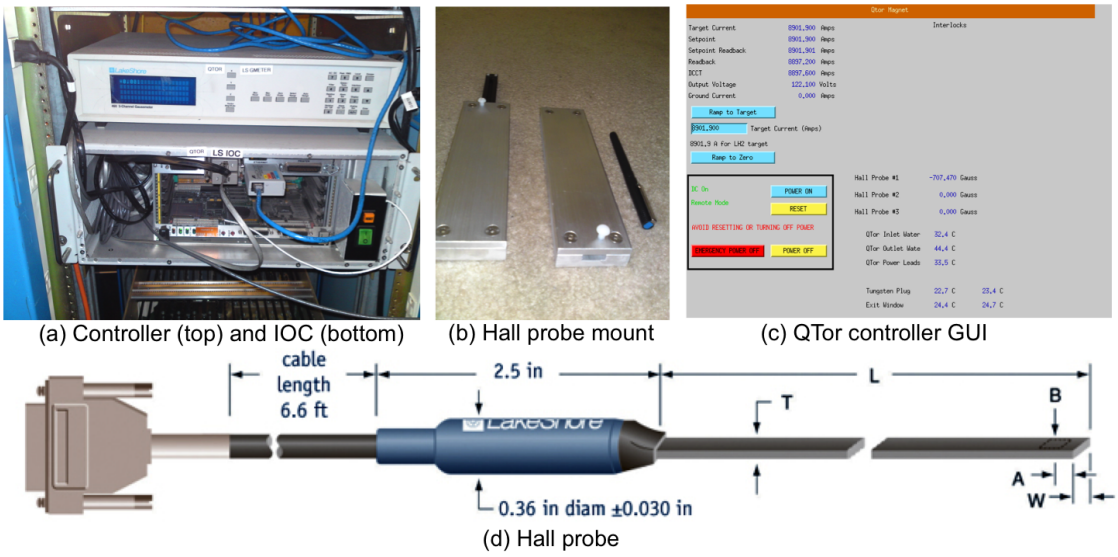

Figure 3.11 QTor controls and hall probe. (a) Lake Shore controller and IOC. (b) Hall probe mount. (c) QTor controller GUI. (d) Hall probe.

cable (MPEC-100). A VME IOC (vmec18) was then connected to the controller in order to read the system remotely. EPICS controls were used as a live read back system via the active EPICS channel (Q1HallP). More details about design and functionality of the QTor hall probe can be found in [97].

3.11 Detector System

The Q-weak detector system consists of the main Čerenkov detectors and two sets of luminosity monitors.

3.11.1 Main Čerenkov Detectors

The Q-weak main detectors are 200 cm × 18 cm × 1.25 cm fused silica Čerenkov quartz bars. The QTor magnetic spectrometer focuses elastically scattered electrons onto the eight main detector bars azimuthally oriented around the beamline (Figure 3.12 (b,c)). Each detector consists of two 100 cm long quartz bars optically coupled together. A 5 cm diameter photo-multiplier tube (PMT) is optically glued at end of the coupled bars. The PMTs are located outside of electron flux (shown in Figure 3.12 (a)). Electrons entering the quartz produce a cone of Čerenkov light that undergoes total internal reflection. Light that reaches the ends of the bars enters the PMTs. The silica was chosen for its radiation hardness and low scintillation. A lead (Pb) pre-radiator was installed in front

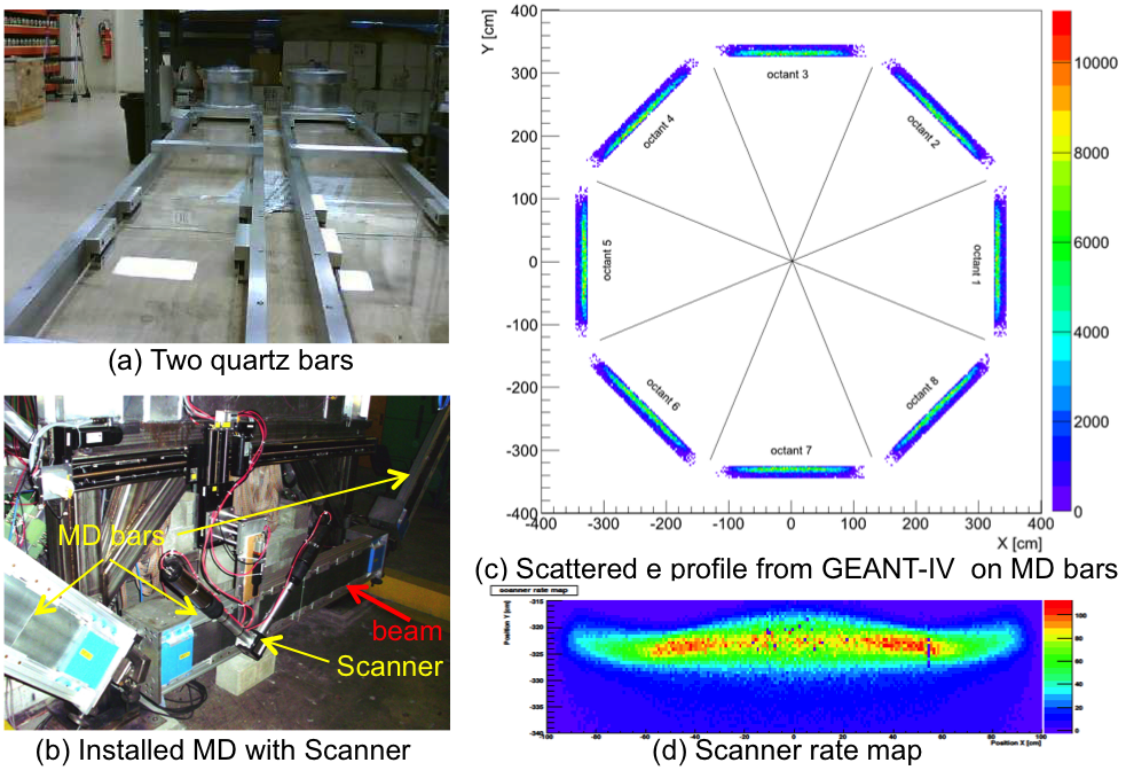

Figure 3.12 Q-weak main Čerenkov detector system. (a) Two quartz bars. (b) Installed main detectors in Hall-C with scanner system. (c) A GEANT-IV simulation showing the elastic scattered electron profile on the quartz bars [9]. (d) The measured rate distribution in the main detector at 50 μA beam current with LH_2 target using the scanner [10].

of the main detectors to improve elastic electron light yield and reduce neutral backgrounds. The pre-radiator improved the signal to noise ratio by absorbing soft photon backgrounds from primary electron bremsstrahlung and by producing low energy electron shower from the primary electrons. A more detailed description of the Čerenkov detector development, construction, and installation can be found in P. Wang's thesis [98].

3.11.1.1 Low Noise Electronics

Low noise current-voltage preamplifiers and digitizing integrators were designed and built by TRIUMF [99] to minimize the contribution of electronic noise to the statistical uncertainty. The preamplifiers convert the DC anode current coming from the PMTs to a voltage, ∼6 V signal for nominal production running. This signal is then digitized by 18-bit analog to digital converters (ADCs) at a sampling rate of 500 kHz to integrate at 1 kHz [100]. Each ADC module has eight

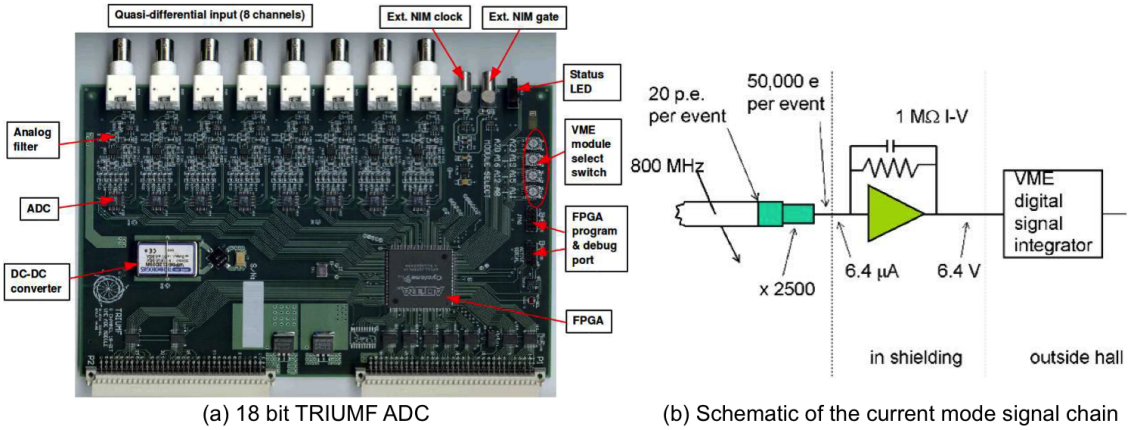

Figure 3.13 Schematic of a TRIUMF made ADC and current mode signal chain.

ADC channels which were synchronized and triggered by the MPS signal from helicity board. A signal with 960 Hz event rate was integrated by summing the samples within the event window. The samples were stored in the channel's memory on a First-In-First-Out (FIFO) basis to avoid data loss due to delayed read-cycles. Another feature of this module was to produce the sum of the samples over four equal sub-blocks within an event. This sub-block feature of the ADCs was very useful to observe signal variations within an event for diagnostics.

3.11.1.2 Focal Plane Scanner

A focal plane scanner was used to measure the beam profile in both high current production running and low current tracking mode in order to test systematic effects like target density change. Two 1 cm×1 cm×1 cm fused silica quartz radiators overlapped in a "V" shape and signals were read by individual PMTs in the scanner. This scanner system was mounted on MD octant 7 (as shown in Figure 3.12 (b)) for beam profile scans. One example of such a scan at 50 μA beam current with the LH_2 target is shown in Figure 3.12 (d). J. Pan has described in detail the construction, schematic and analysis of focal plane scanner in her thesis [10].

3.11.2 Luminosity Monitors

The luminosity monitors (lumis), like the main detectors, were based on fused silica Čerenkov radiators with a light guide flushed with nitrogen gas to minimize corrosion. Two types of azimuthally symmetric luminosity monitors were used as beam diagnostic tools for the Q-weak experiment. The upstream luminosity monitors were located on the front face of the primary collimator 5 m from

the target (shown in Figure 3.14 (a)) and the downstream luminosity monitors were located 17 m downstream of the target, very close to the beam dump area (shown in Figure 3.14 (b)). Both lumis were expected to detect electrons from small angle electron-proton and electron-electron scattering with an anticipated null asymmetry (ppb-level asymmetry). The upstream lumis were extremely useful for estimating beamline backgrounds. In some cases the asymmetries measured by the lumis were not as small as expected and and were also time dependent. Examples will be discussed in a later chapter. A more detailed description of luminosity monitors and analysis can be found in J. Leacock's thesis [3].

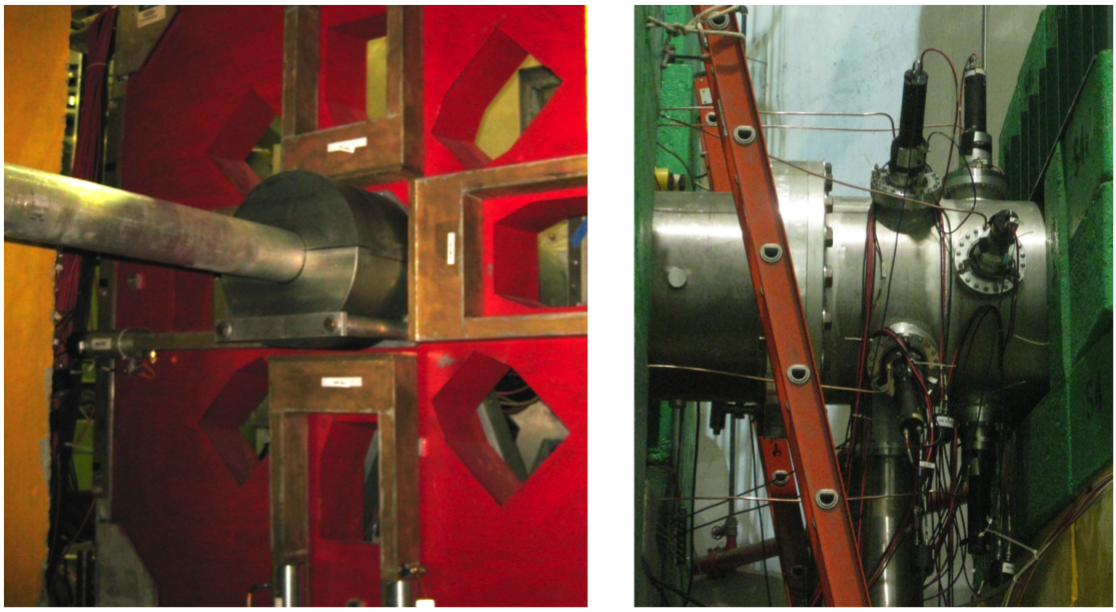

Figure 3.14 Luminosity monitors. (a) Four upstream luminosity monitors installed on the face of the primary collimator. (b) Eight downstream luminosity monitors near beam dump.

3.12 Tracking Detector System

The asymmetry of elastically scattered electrons is approximately proportional to the four momentum transfer squared, Q^2 (details in Equation 3.1.3). A tracking system was necessary to measure Q^2 with a 0.5% relative uncertainty as proposed by the experiment (shown in Table 3.1). A pair of horizontal drift chambers (HDCs) in region 2 (R2) was used to determine the scattering angle θ with an angular resolution of $\sim$0.6 μrad and a particle trajectory with a position resolution of $\sim$200 μm (as shown in Figure 3.9). Four vertical drift chambers (VDCs) and two trigger scintillators were

used downstream of the target (shown in Figure 3.9) in region 3 (R3) to measure Q^2 (more details in J. Lackey's thesis [101]). The detector packages in R2 and R3 can be rotated into each MD octant pair using a mechanical rotor to measure any octant dependence. The relationship between Q^2 and θ is shown in Equation 3.1.3. The tracking system operated at ∼6 order of magnitude smaller beam current than the current for parity production data taking. A detailed description of the tracking system can be found in J. Pan's thesis [10].

3.13 Data Acquisition

The Q-weak data acquisition (DAQ) system was based on the CEBAF Online Data Acquisition (CODA) [102, 103] framework designed for experiments at Jefferson Lab. Two independent DAQ configurations were used for the experiment: integration mode for high current production data taking and counting mode for low current tracking measurements. The data taking during integration mode was triggered by the MPS signal from the accelerator at a frequency of 960 Hz while the trigger scintillators were used as the trigger for the event mode running. A software prescale factor was used to control how often the DAQ was triggered by the specific trigger for each hardware trigger. Several read out controllers (ROCs) were used to read different subsystem electronics. The CODA system used ethernet to communicate with all the ROCs. The Event Builder (EB) system was used to generate complete events from data fragments read from the ROCs and the Event Transfer (ET) system provided central access to data events for multiple clients in real-time. The data rate during integration mode was approximately 5.6 MB/s. An hour of data was defined as run and each run was segmented into 1.9 - 2.0 GB data files called runlets. One run has about 9 - 12 runlets. During the entire experiment, ∼120 TB of raw data were collected. The averaged data such as yields, asymmetries, differences, HWP state, target, regression slopes, flags for data quality were saved to a MySQL database. B. Waidyawansa [19] and R. Beminiwattha [88] provided more technical details on data acquisition in their theses.

3.14 Online Displays and Data Monitoring

The collected raw data files were processed to produce CERN ROOT and MySQL structured files for real time data quality monitoring and to store for future analysis. The real time analyzer produced a ROOT file for the first 100,000 events for each one hour production run. This ROOT file was used to generate all the necessary figures and summary tables to monitor the data quality and key physics parameters. Then the C++, ROOT, and HTML based analysis structure `qwanalysis`

with a Hall-C wrapper script `hclog_post` [104] was used to produce HTML files and upload them automatically to the Hall-C electronic log book (HCLOG) for each run. A CODA trigger was used to initiate the analysis process when ROOT file generation for the first 100,000 events was completed. Necessary precautions and changes were made for the next run based on careful screening of standard acceptable set of parameters for the ongoing run.

One of the key components of the experiment was the target and it was necessary to monitor it constinuously. A C++ and Virtual Network Computing (VNC) based software setup was used to monitor the target, and related parameters and to publish the status on the web. A snapshot of the target controls, all the key parameters, temperature from different sensors, cryogenic liquid flow, alarm handler, and cameras that monitor the target were taken every few minutes by the software and uploaded to the website [105]. This system was also used as a backup control system for the target in the case of a failure of the computer that controlled the target. The same software and technique was also used to monitor the beamline optics [106] for each production run by monitoring the BPM responses to the beam modulation signals and will be discussed in a later chapter.

3.15 Parity Analysis

To extract the main detector normalized yields for asymmetry calculations, several corrections were applied on raw yields as described below.

$$Y^{+/-} = \frac{(Y_{\rm raw}^{+/-} - Y_{\rm ped}) \times g}{\frac{N_s}{I^{+/-}}} \tag{3.15.1}$$

where $Y_{\rm raw}^{+/-}$ is the raw ADC signal in the "+/-" helicity state, $Y_{\rm ped}$ is the measured beam off signal or pedestal (a details pedestal analysis of the entire experiment is discussed in a latter chapter), g is the calibration factor to convert ADC counts per sample to volts, N_s is the number of 2 μs read-out samples per MPS state, and $I^{+/-}$ is the beam current for the "+/-" helicity state. The pedestals were subtracted from the raw signals to remove the effect of the DC offsets in the electronics chain, dark current due to thermal noise and cosmic rays. In order to sum the two PMT signals for one detector to obtain the detectors yield, or to sum the total 16 PMT signals to obtain the yield for all detectors, the gains of those PMT channels were matched to each other. The main detector yields are normalized to beam current to reduce the dependence on beam intensity fluctuations. A beam stability cut was applied to the raw detector yield to eliminate data taken

during a beam trip or unstable beam excursion [88]. Further cuts to the data were made on a runlet-by-runlet basis during the data quality checks.

The parity analysis engine processes raw data to extract event and pattern based quantities. Events which pass the event and pattern number checks are grouped into patterns of four events, known as quartets and the pattern based differences, yields, and asymmetries are computed as shown in Table 3.3. In the final step of the data analysis process, event and pattern based processed data were saved into a set of pre-defined histograms and ROOT trees. Event based yields were saved in the Mps_Tree and pattern based differences, yields, and asymmetries were saved in the Hel_Tree. Additionally, event based EPICs values for key components (QTOR current, target position, etc.) were stored in a Slow_Tree. The running averages, running sums, uncertainties on the running averages and the slow control values were written into the MySQL databases.

Table 3.3 Definition of different variables used in the experiment [19]. The subscripts indicate the event sequence in a quartet pattern defined as 1, 2, 3, 4 with helicity "+−−+". The definition of differences, yields, and asymmetries are shown here. Two different ways of combining yields and asymmetries were used in the experiment. The barsum yields are extracted using yields of the left/right PMTs ($Y_{L/R}$) with proper weights ($W_{L/R}$). The yields and asymmetries for each detector bar or for the whole detector were computed using the barsum yields and asymmetries. Another way to combine yields and asymmetries was pmtavg. The yield and asymmetry for each PMT were calculated first and then averaged to get yields and asymmetries for each detector or whole detector.

Quantity	Definition	Comments
differences	$D = \frac{(Y_1^+ + Y_4^+) - (Y_2^- + Y_3^-)}{2}$	BPMs, Combined BPMs, Energy calculator
yields	$Y = \frac{(Y_1^+ + Y_4^+) + (Y_2^- + Y_3^-)}{2}$	All detectors
asymmetry	$A = \frac{(Y_1^+ + Y_4^+) - (Y_2^- + Y_3^-)}{(Y_1^+ + Y_4^+) + (Y_2^- + Y_3^-)}$	PMTs, Lumis, BCMs,BPM effective charge
barsum	$Y_{\text{barsum}} = \frac{W_L Y_L + W_R Y_R}{W_L + W_R}$	A_{barsum} calculated using yields
pmtavg	$A_{\text{pmtavg}} = \frac{1}{2}(A_L + A_R)$	$A_{L/R}$ is calculated from PMT yields
mdallbars	$Y_{\text{allbars}} = \frac{1}{8}\sum_{i=1} Y^i_{\text{barsum}}$	A_{allbars} calculated using yields
mdallpmtavg	$Y_{\text{pmtavg}} = \frac{1}{16}\sum_{i=1}(Y^i_L + Y^i_R)$	A_{pmtavg} calculated using yields

SECTION 4
BEAM MODULATION

4.1 Introduction

The electron-proton scattering rate largely depends on the five beam parameters: horizontal position (X), horizontal angle (X'), vertical position (Y), vertical angle (Y'), and energy (E). Changes in these beam parameters when the beam polarization is reversed create false asymmetries. Although attempt has been made to keep changes in beam parameters during reversal as small as possible, it is necessary to correct for such false asymmetries. A challenge for the Q-weak experiment was to keep these helicity-correlated parameter differences as small as possible and measure the detector sensitivities. The goal of the beam modulation system was to occasionally induce controlled beam parameter changes ΔT_i, measure the resulting detector false asymmetry A_{false}, and determine the detector sensitivities $\dfrac{\partial A}{\partial T_i}$. This technique allows estimation and correction for the beam false asymmetries as shown in Equation 5.1.1. Even if these corrections were small under ideal running conditions, the modulation system described in this chapter will allow to quickly determine if undesirable changes have occurred. The following sections will discuss the basis of the beam modulation system design. More detailed application of modulation to removing false asymmetries will be discussed by J. Hoskins [107] and D. Jones [108] in their future theses.

$$A_{\text{false}} = \sum_{i=1}^{5} \left(\frac{\partial A}{\partial T_i} \right) \Delta T_i \tag{4.1.1}$$

4.2 Design Measurement Time vs Modulation Asymmetry

It was assumed that it would be helpful to measure the whole-detector sensitivities to 10% accuracy every few days [109]. Stable sensitivities would yield uncertainties of a few percent by the end of the experiment, which is much better than one would need to regress out the helicity-correlated differences seen in the previous parity violating experiment HAPPEX [110]. However, frequent whole-detector sensitivity measurements might reveal important changes in the beam, etc. Furthermore, accurate single octant sensitivities (which would be obtained as a by-product) are an essential prerequisite to extract the $\sin\phi$ and $\cos\phi$ dependence which are characteristic of residual transverse beam polarization.

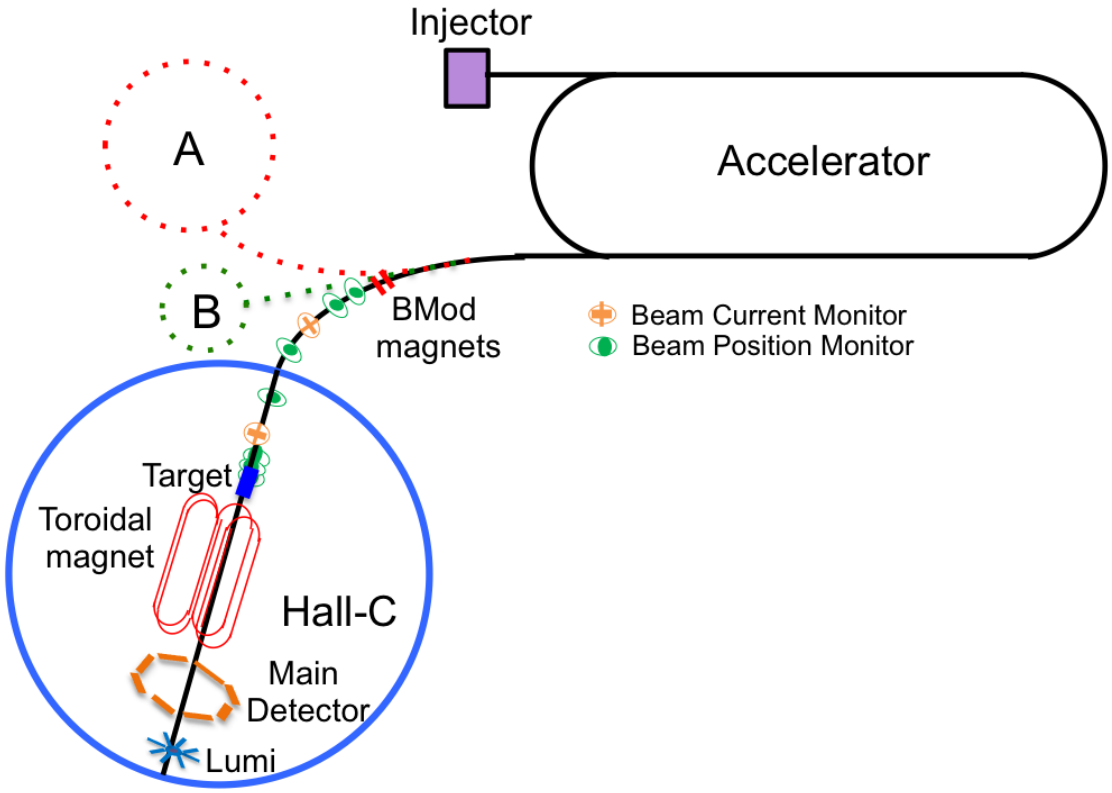

Figure 4.1 Simple cartoon of the accelerator. The beam modulation magnets are shown in Hall-C beamline. The BPMs, BCMs, and other key components of the experiment are shown in the Hall-C beamline.

For the size and duration of the modulations discussed here, the natural beam jitter and the SEE BPM (section 3.6.1) electronic noise of roughly 5 $\mu m/\sqrt{Hz}$ will be negligible [109]. If this was not the case, measurement times would become much longer. This means that the uncertainty on the detector sensitivities is dominated by the statistical uncertainty on the detector false asymmetry. At nominal luminosity, the Q-weak experiment has a rate of 800 MHz/octant, hence the whole-detector statistical sensitivity, dA, is 12.5 ppm/$\sqrt{t}$(sec) or 1 ppm in 156.25 seconds. The clock times needed to measure a single beam sensitivity to 10% are therefore given by

$$t(s) = \frac{1}{\mathrm{DF}} \frac{\left(\frac{12.5\ \mathrm{ppm}}{A_{\mathrm{false}}(\mathrm{ppm})}\right)^2}{\left(\frac{dA}{A}\right)^2} = \frac{1}{\mathrm{DF}} \left(\frac{12.5\ \mathrm{ppm}}{A_{\mathrm{false}}(\mathrm{ppm})}\right)^2 100 \tag{4.2.1}$$

Table 4.1 estimates required clock time for a 10% measurement of a single beam sensitivity with different assumptions about the modulation asymmetry and the modulation duty factor. A

Table 4.1 Dead time calculation for beam modulation. The clock time needed to measure detector sensitivity for a single parameter and how it varies with asymmetries are shown here. The clock times given below are calculated assuming a square wave modulation.

Modulation asymmetry [ppm]	Clock time required		
	10% DF [Hours]	1% DF [Hours]	0.1% DF [Hours]
1	43	430	4300
10	0.43	4.3	43

modulation of 10 ppm would permit a measurement of all 5 sensitivities to 10%, require about 1-10 calendar days, and have minimal negative impact on production duty cycle. For fixed uncertainty, smaller amplitudes would require at least quadratic increases in measurement time or duty factor (DF). For fixed measurement time and duty factor, smaller amplitudes would cause at least linear increases in the uncertainties.

4.3 Design Modulation Amplitude

The next important step was to estimate the modulation amplitudes for beam position and angle necessary to achieve $A_{\text{false}} = 10$ ppm. Detailed simulations on sensitivities have been performed using Geant 3 and discussed in [111]. The simulated single octant detector sensitivities are dominated by the interaction of e+p elastic scattering with the defining collimator, and are shown in the second column of Table 4.2. Except for energy, the whole detector sensitivities were much smaller. They were much more complicated since they were determined by imperfect cancellation of the linear sensitivities due to broken symmetries (coil misalignment, radiator radial positions), plus quadratic sensitivities which depend on beam offsets. It was not clear what expected suppression factor to use in going from single octant sensitivities to whole detector sensitivities. Therefore, the relatively conservative cancellation factor was assumed to be 50, which leads to the required modulation amplitudes for position, angle, and energy to generate 10 ppm whole detector asymmetry (see Table 4.2.

The estimated whole detector sensitivities were small. Compared to the Q-weak statistical uncertainty of ∼5 ppb, the beam parameter corrections resulting from the helicity-correlated differences seen in the previous parity violating experiments [110] $\mathcal{O}$(1 nm, 0.1 nrad, 0.1 ppm in energy) were negligible.

Table 4.2 A crude estimate of the modulation amplitudes to generate 10 ppm whole detector asymmetries.

Beam Parameter	Single Octant Sensitivity	Assumed Cancellation	Whole Detector Sensitivity	Modulation Amplitude for 10 ppm
Position	10 ppb/nm	50	0.2 ppb/nm	50 μm
Angle	30 ppb/nrad	50	0.6 ppb/nrad	20 μrad
Energy	1 ppb/ppb	1	1 ppb/ppb	10 ppm ($\sim$10 keV)

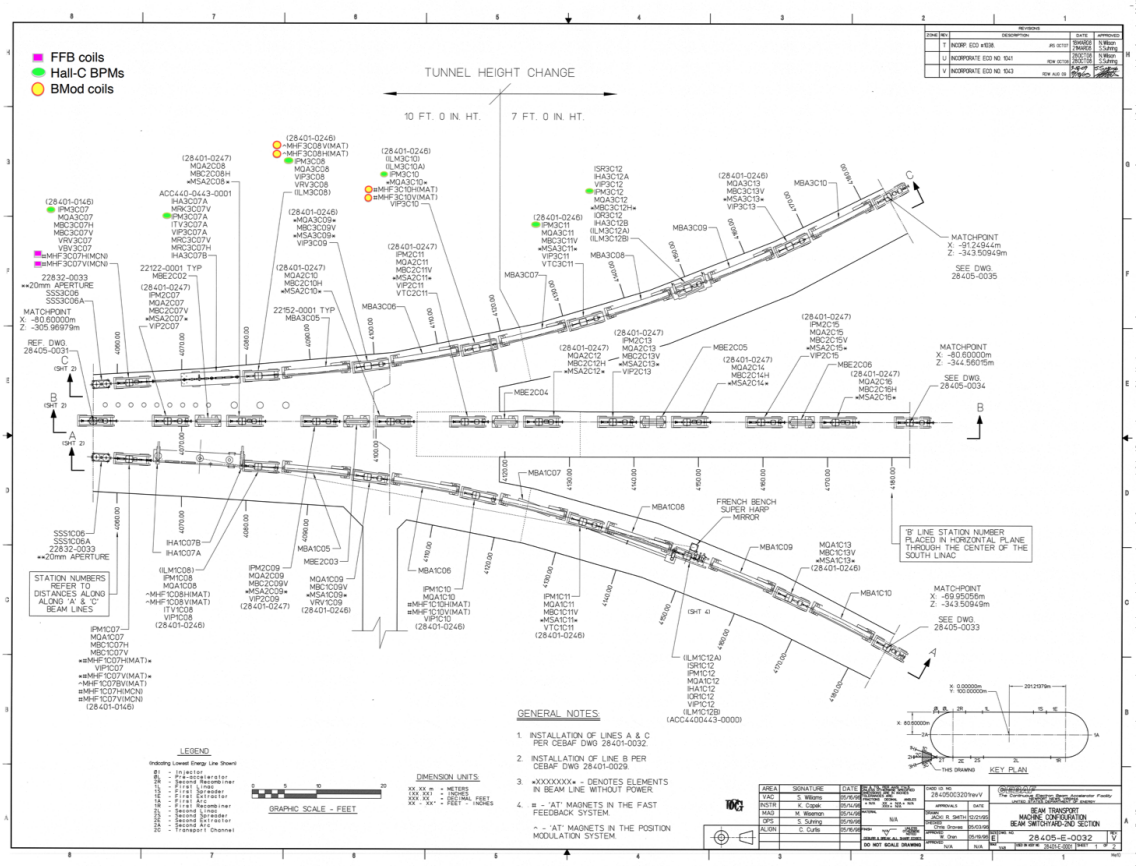

Figure 4.2 Jefferson Lab and its beamline schematic for all three experimental halls using Computer Aided Design (CAD) drawings (informally referred as songsheets at Jefferson Lab) are shown. Beam modulation magnets, fast feed back coils, and BPMs in the Hall-C beamline are labeled separately.

4.4 Optics Calculation

A program written by Valery Lebedev for linear and non-linear optics calculations, OptiM [82], and an input deck prepared by Jay Benesch [112] (JLab) were used to simulate the Hall-C beamline (3C). The 3C beamline was substantially modified before Q-weak to accommodate the Compton

polarimeter. A schematic view of the Hall-C beamline (songsheet[1]) along with the other halls are shown in Figure 4.2. The goal for the beam modulation system was to achieve robust modulation in X, $X^{'}$, Y, $Y^{'}$, and E at the target. These modulations do not have to be strictly pure, but they have to be linearly independent to yield solutions for the individual sensitivities. The asymmetries from position modulations were an order of magnitude larger than the asymmetries from angle modulations for similar sized magnet kicks in the Q-weak and will be discussed in later sections of this chapter. This fact, plus the relatively large statistical noise in the detector asymmetries, plus the certainty of small drifts in the optics, suggested that mixed mode modulation is unlikely to be robust. Running times and uncertainties were also quite difficult to estimate for the mixed mode modulation. Therefore, we attempted to produce relatively pure modulations in which $\sim$90% of the asymmetry arises from the variable of interest.

4.4.1 Simulation using OptiM

The main OptiM deck [113] contains the information about the location, field strength, size, orientation, etc., for each component of the Hall-C beamline. The OptiM deck was used to obtain transfer matrices, orbit excursions, beta functions, and simulated trajectories between any two beamlime elements in the forward or inverse direction.

4.4.2 Inverse Beamline

An insightful exercise was to start with a pure position or angle deviation at the target and use OptiM to send tracks in the upstream direction. This was called the inverse beamline or orbit. Figure 4.3 shows the orbit from the target to the Lambertson (beginning of the 3C line). All 4 panels have the same qualitative features: the beam moves to the right with piece-wise continuous motion, there is a discontinuity at each quadrupole location, and there is at least one zero crossing. The reason this inverse trajectory is so interesting is that, due to time-reversal invariance of electromagnetic interactions, it provides the information about how to perturb a forward beam to obtain a pure position or angle change at the target. As long as the inverse orbit stays inside the beampipe, such a figure is an existence proof that pure modulation at the target is possible with a forward beam.

[1]The CAD drawings were informally referred as songsheets at Jefferson Lab. The CAD annotation is static. Only element names are shown in the drawings.

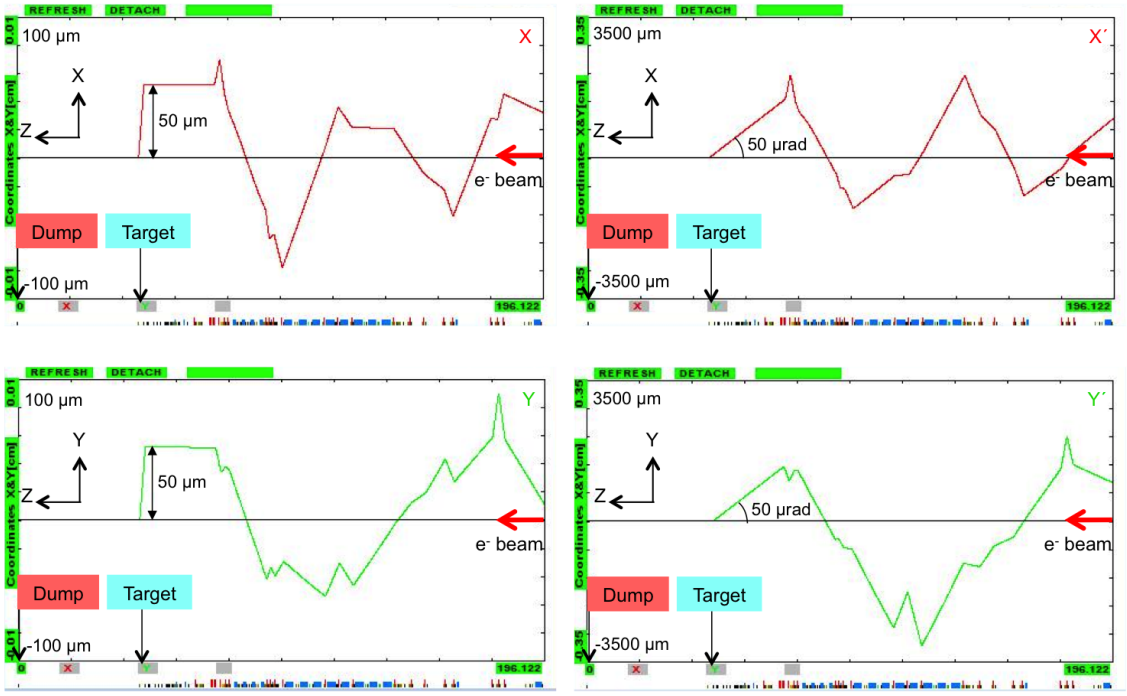

Figure 4.3 Inverse orbit excursions simulation from OptiM. The direction of the beam is from right to left. The tiny blue and red boxes on the horizontal axis at the bottom of the figures are dipoles and quadrupoles, respectively. The location of the target and beam dump are also marked. The orbit excursion for the relatively pure X, X', Y' and Y displacement at the target are shown in the four panels (from top left in clock wise direction). The electron beam direction is from right to left, whereas for this exercise the beam tracks were created at the target and sent in the upstream direction.

4.4.3 Forward Beamline with Position or Angle Kicks

The simplest way to perturb an arbitrary forward beam onto the magic trajectory suggested by the inverse beamline is to kick the beam with a *single* dipole at one of the zero crossings. However, if driving coils were restricted to the first half of the 3C arc, this strategy would not be feasible because there was only one zero crossing in that region (corresponding to pure X' modulation), with no zeros corresponding to X, Y, or Y' modulation. A better approach was then suggested by Mike Tiefenback [114], similar to that used in the JLab Fast Feedback System (FFB) [84, 85]. As schematically shown in Figure 4.4, pairs of separated coils could be used to take an arbitrary forward ray, offset its position and angle, and re-inject it along the appropriate trajectory to produce a pure position or angle change at the target. Detailed OptiM solutions for forward rays are shown in Figure 4.5 for a pair of coils separated by 9.5 m. Note that position modulation of $\pm$ 250 μm at the target yields orbit deviations of similar magnitude in the beamline, while angle modulation of

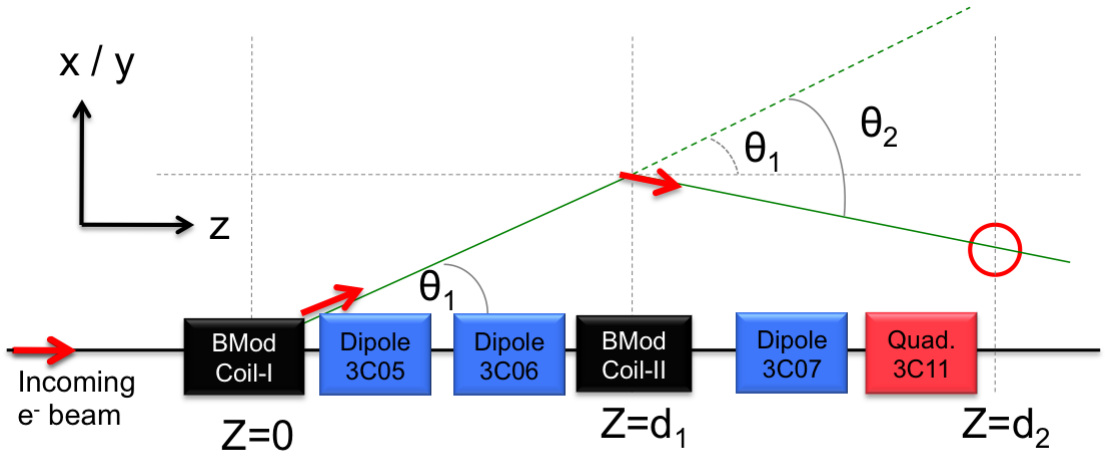

Figure 4.4 A sketch of beam modulation concept. A pair of magnets (at Z=0 and Z=d_1) with opposite kick were used to match a trajectory at a point (Z=d_2) in the beamline. There were two big dipoles between the modulation magnets. Using simple algebra θ_1 and θ_2 can be expressed in terms of position and angle at the match point. Hence required field integral in the beam modulation magnets can be calculated to generate a particular trajectory (details of the calculation in APPENDIX A).

$\pm$ 50 μrad at the target yields orbit deviations of up to 3 mm. The size of the latter orbit deviations is large enough to cause some concern about scraping of the beam or halo. Hence the angle kick was reduced by an order of magnitude to match the size of the orbit deviations. This might be a better match to the size of natural beam jitter, but the time required in Table 4.2 for a single 10% measurement would increase by at least a factor of 100. The field integrals for that yielded pure modulations at the Q-weak target were calculated using most updated available OptiM deck [113] and are shown in Table 4.3. These field integrals were converted to currents using the measured MAT coil field constant of 330 G-cm/A. This two-coil scheme was very convenient, as any changes in the 3C line was easily simulated for the modulation system by re-tuning the ratio of coil currents without having to move coils.

4.4.4 Forward Rays with Energy Kick

The beam energy was modulated using a superconducting RF cavity in the South Linac of the accelerator. The effect of a simulated 10 ppm energy kick from OptiM is shown in Figure 4.6. At 3C12, the point of highest dispersion (the middle of the 3C arc), the induced motion is shown by a 41 μm red spike. From a comparison of Figures 4.5 and 4.6, it is clear that energy changes could

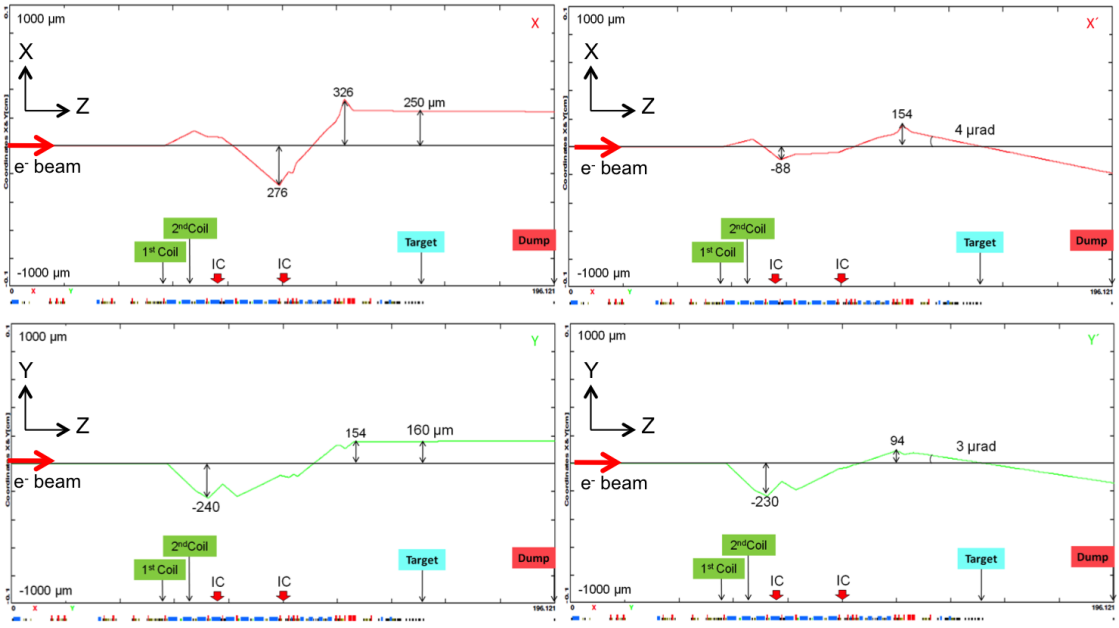

Figure 4.5 Forward orbit excursions simulation from OptiM. Beam moves from left to right. The ting blue and red boxes on the horizontal axis at the bottom of the figures are dipoles and quadrupoles, respectively. Simulated location of the modulation magnets and recommended location for ion chambers are shown in the figures. The forward orbit excursion for the relatively pure X, X', Y' and Y motion at the target are shown in the four panels (from top left in clock wise direction).

Table 4.3 Required field integrals for the modulation dipole pair to generate relatively pure position and angle at the target from OptiM are shown here. Coil currents to produce such field integrals are calculated. The ratio between coil current in 2nd and 1st coil is defined as the "tune". A negative tune signifies opposite current in the two coils.

Beam Parameter	Amplitude for 10 ppm	I_1 [A]	$\int \vec{B} \bullet d\vec{l}_1$ [G-cm]	I_2 [A]	$\int \vec{B} \bullet d\vec{l}_2$ [G-cm]	"Tune"
X	250 μm	0.159	52.4	-0.372	-122.9	-1.875
X'	4 μrad	0.554	183.0	-1.872	-618.0	-3.864
Y	160 μm	-0.242	-80.0	0.060	20.0	-0.367
Y'	3 μrad	-1.606	-530.0	0.771	254.0	-0.489

not possibly be confused with position or angle changes. Further downstream in the beamline, the small green bump represents the dispersion inside the vertically bending Compton chicane. Because of the lower dispersion, the induced motion in the Compton was only about 5 μm, much smaller than the nominal JLab electron beam rms width. The energy change at the target was identified in terms of change in beam position at 3C12 and at any arbitrary non-dispersive location. A pair of BPMs at the beginning or the end of the 3C arc would seem to be the most natural choice

for energy change measurement. Any two X BPMs on the beamline could be used as long as the magnifications were favorable. But there were advantages to work in terms of target position (X_T) and angle (X'_T) because: 1) these were the coordinates that were used in the simulations to estimate the beam sensitivities, and 2) there were seven BPMs in the drift region upstream of the target which provided flexibility to determine X_T and X'_T with relatively high accuracy [75]. The position or angle at 3C12 in terms of target parameters can be expressed as

$$\overleftrightarrow{X}_{3\text{C12}} = \underline{M}\,\overleftrightarrow{X}_{T} \tag{4.4.1}$$

Expanding the Eq. 4.4.1

$$\begin{bmatrix} X \\ X' \\ Y \\ Y' \\ \frac{dE}{E} \end{bmatrix}_{3\text{C12}} = \begin{bmatrix} M_{11} & M_{12} & M_{13} & M_{14} & M_{15} \\ M_{21} & M_{22} & M_{23} & M_{24} & M_{25} \\ M_{31} & M_{32} & M_{33} & M_{34} & M_{35} \\ M_{41} & M_{42} & M_{43} & M_{44} & M_{45} \\ M_{51} & M_{52} & M_{53} & M_{54} & M_{55} \end{bmatrix} \begin{bmatrix} X \\ X' \\ Y \\ Y' \\ \frac{dE}{E} \end{bmatrix}_{T} \tag{4.4.2}$$

where the matrix elements were obtained from [113] and can be written as

$$M = \begin{bmatrix} 0.69 & -928 & 0 & 0 & 411 \\ -5\times10^{-4} & 2.1 & 0 & 0 & -0.5 \\ 0 & 0 & -0.60 & -3.5\times10^{4} & -1 \\ 0 & 0 & -6\times10^{-4} & -5 & -1\times10^{-3} \\ 0 & 0 & 0 & 0 & 1 \end{bmatrix} \tag{4.4.3}$$

Using Equation 4.4.2 and 4.4.3, the energy change at the target can be written in terms of horizontal position change at 3C12, and horizontal position and angle changes at the target as

$$\Delta\left(\frac{dE}{E}\right)_{T} = \frac{1}{M_{15}}\Delta X_{3\text{C12}} - \frac{M_{11}}{M_{15}}\Delta X_T - \frac{M_{12}}{M_{15}}\Delta X'_T \tag{4.4.4}$$

In practice, large residual dispersion in X_T and/or Y_T made Equation 4.4.4 only approximate. More detailed calculation about the energy modulation can be found in [115].

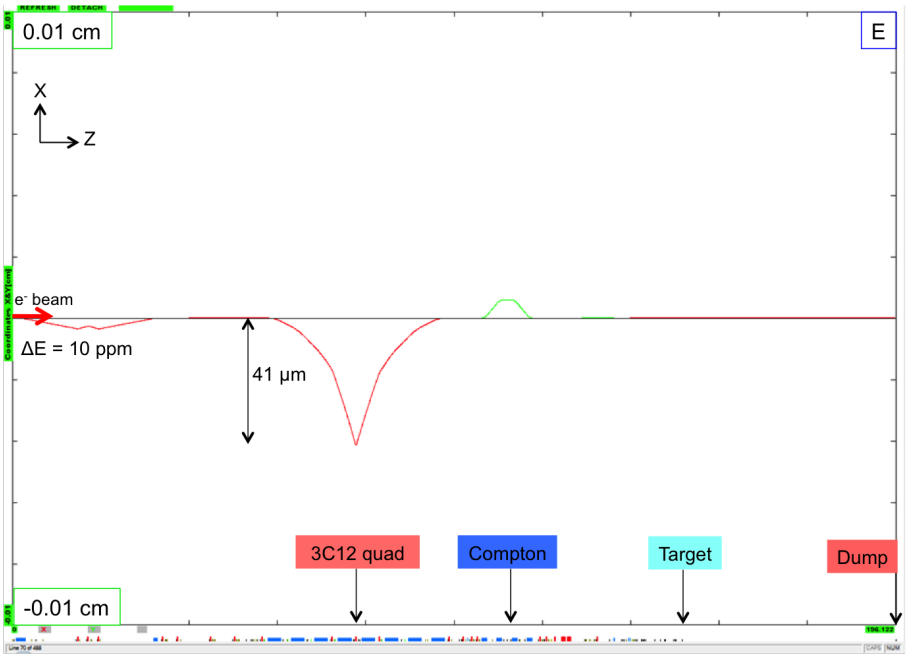

Figure 4.6 Forward orbit excursions simulation for energy modulation from OptiM. Beam moves from left to right. The energy was changed by 10 ppm using a horizontal corrector in the simulation. The pronounced horizontal position (red) change of 41 μm at the middle of the arc is due to the energy change of 10 ppm. A small vertical position (green) bump can be identified at the Compton region.

4.5 Beam Modulation Hardware

The hardware of the beam modulation system spans three different regions: the BSY service building, accelerator beamline, and Hall-C. In the BSY service building, there were two signal generators controlled by an IOC. The sinusoidal signals from signal generator were sent to power amplifier, and the amplified signals were sent to two pairs of air core coils and one SRF cavity in the beamline. The read-backs from signal generators, power amplifiers, current transducers to measure the coil current, and BPM responses were sent to two sets of ADCs at the Q-weak cage at Hall-C counting house and at BSY service building to monitor the system and to perform further analysis. A trigger from the parity violating DAQ in the Hall-C counting house was sent to the IOC at the BSY service building to start the process. The schematic diagram of the beam modulation hardware is shown in Figure 4.7.

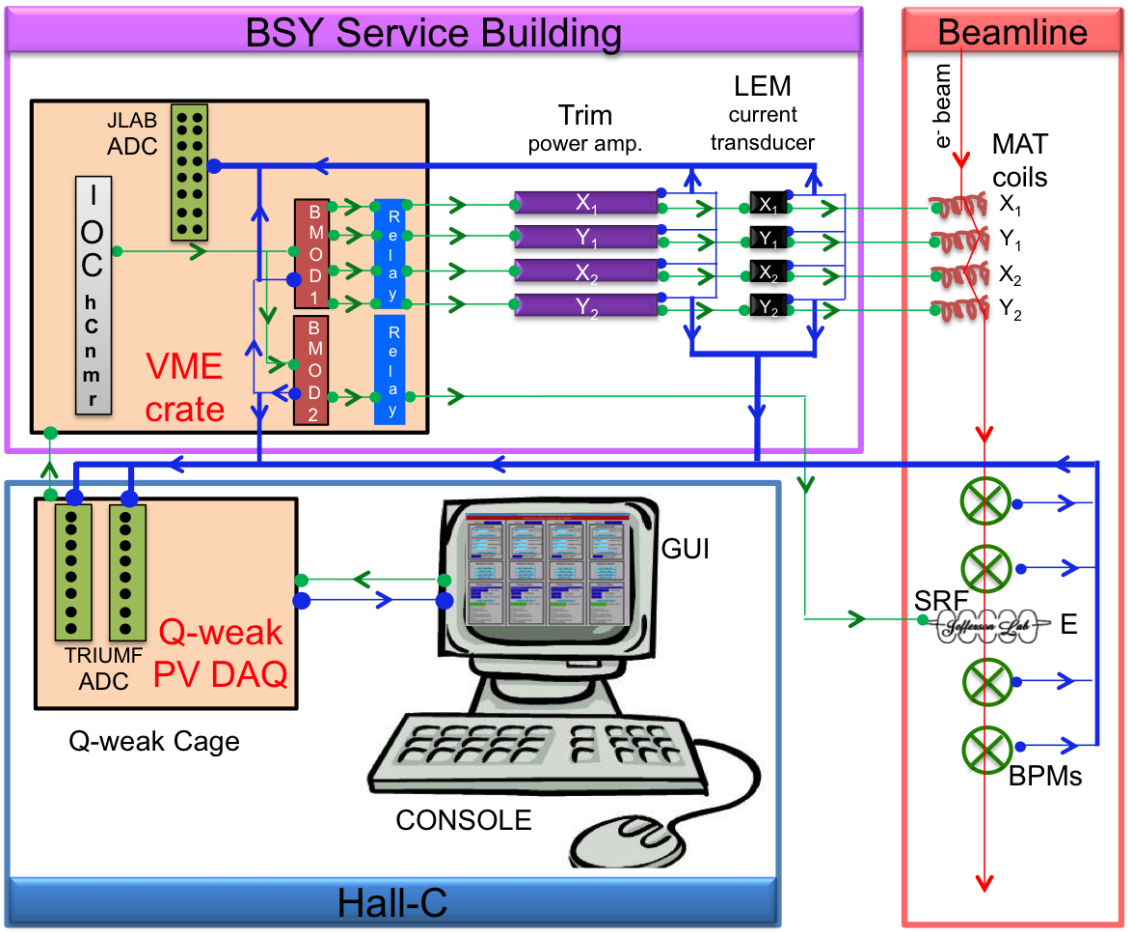

Figure 4.7 Beam modulation hardware sketch. BMod hardware spans three different regions: BSY service building, accelerator beamline, and Hall-C. In BSY service building there were two VME-4145 signal generators controlled by an IOC (iochcnmr). The sinusoidal signals from signal generator were sent to Trim power amplifier, and amplified signals were sent to two pairs of MAT coils and one SRF cavity (SL20 vernier) in the beamline. The read-backs from signal generators, power amplifiers, current transducers, BPMs, and cavity were sent to two ADCs at Q-weak cage and one ADC at BSY service building. The drive or input signals are shown by green and read-backs by blue lines, respectively. In order to trigger the process, a signal from parity violating DAQ in the Hall-C counting house were sent to the IOC.

4.5.1 Air-Core Coils

Two pairs of JLab MAT(HF) air-core coils were used to perturb the electron beam for the modulation system as they produced sufficient field integral, were readily available, and were compact enough (each 10 cm long) to be inserted easily almost anywhere in the beamline. Their properties have been measured and summarized by Sarin Philips in [116]. The MAT coils were calibrated in bench test and the most critical parameters are summarized in Table 4.4. The total impedance of the

coil was related to the frequency (f) as $X_{\text{total}} = 1.6\ \Omega + 2\pi f(0.0038\ \text{H})$. The reduction in field due to the skin effect in a standard stainless steel beampipe was estimated to be roughly 10% at 1 KHz, and less than a few percent at 125 Hz. The skin effect was ignored as the used frequency of the sinusoidal modulation was 125 Hz, which was constrained by the power amplifier (see section 4.5.5).

Table 4.4 Basic properties of the air core MAT coils used for the beam modulation system.

Magnet Parameter	Value
Magnet Constant (B/I)	33 G/A
$\int \vec{B} \bullet \vec{dl}$ = (B/I) × Length	(330 G-cm/A)×I
Length	10 cm
Inductance	3.8 mH
Resistance	1.6 Ω

4.5.2 IOC

A VME based Input Output Controller (IOC) *hcnmr* at the BSY service building was used to operate the beam modulation system. The crate contained a processor, various input/output (I/O) modules, and VME modules that provide access to other I/O buses [117]. The IOC was used to establish communication with two VME 4145 Signal Generator boards through two patch panels and controlled the drive signal of the VME 4145 board via a database access library that works on Unix, VxWorks[2], and EPICS databases.

4.5.3 VME 4145 Signal Generator

Two GE Fanuc Intelligent Platforms' VME-4145 programmable function generator boards [118] were used to drive the two pairs of MAT coils (shown in Figure 4.7). The VME-4145 has an analog output board that provides four high-quality analog output channels with 16-bit resolution. Each output has a dedicated Digital-to-Analog Converter (DAC), and can source or sink ±10 V. Each channel has a dedicated 64 Kword[3] waveform buffer. Each buffer may be segmented to provide independent subwaveforms. The unit was capable of downloading an arbitrary bipolar waveform and then replay it. Two pairs of MAT coils were driven using sine waveform from the four channels of the first VME-4145 board. Only two channels of the second board were used. One channel was used to drive the superconducting RF cavity for energy modulation with a sine waveform and the other channel was used to produce a ramp (sawtooth) wave to monitor the phase of the all five

[2]VxWorks is a real-time operating system developed as proprietary software by Wind River Systems of Alameda, California, USA. First released in 1987, VxWorks is designed for use in embedded systems.

[3]KWord is a deprecated word processor and a desktop publishing application, part of the KOffice suite [119].

drive signals. Each waveform was generated start to finish and then the next was seamlessly started. All of the waveforms were preloaded before waveform generation began to program the sequencing of segments in real time by the host processor (a link list software approach) [118]. An external trigger input from Q-weak main DAQ was used to start playback of the waveform. This feature allowed to trigger the drive signal and ramp wave channels to synchronize in phase. The boards were programmed to run in the continuous mode (Type II) which scanned the waveform table, ran for 510 cycles and then halted. The next cycle started again when the boards were triggered from the Q-weak DAQ.

4.5.4 Relay Board

Two sets of JLab-made 16-channel relay output register modules [120] were used for machine protection. The board consists of four 16-bit registers used to control 16 relays and read-back status information. The front panel contains indicator LED's for power, heartbeat and relay on/off status. Relay contacts are brought out on a 50-pin D connector. A DC shift of $\sim$0.015 V was observed on the sinusoidal drive signal due to the relay boards which seem to have no effect on the driven coils (more details in [121]).

4.5.5 Trim Power Amplifier

Four 1-12 A series pass regulator power supplies, known as Trim Card I, were used as power amplifiers to control two pairs of the MAT dipoles for the beam modulation system. The Trim-I was programmable, 200 W, bipolar, power supply and was realized as a single plugin circuit board, approximately with dimensions $9'' \times 20''$. Our bench tests were done with Trim Card II [122] but they were deemed unsafe to use. Thirty two Trim cards were housed in card-cages within a single rack (BS04B14) at BSY service building. But only four of those cards were used for the modulation system and the rest were used to power other components in the beamline. The Trim cards consisted of a Motherboard which helped to interconnect all the daughter cards, distribute power to the daughter cards, and house the power amplifier section (shown in Figure 4.10). A 48-pin connector, mounted on the rear apron, was used to engage a mating connector in the card cage where $\pm$ 27 V bulk power, 5 V power, and RS-485 communication were derived. External programming commands and data read-backs were exchanged with the EPICS via a RS-485 data link. The cards had a display module in the front connected to a digital temperature sensor which was used to set warning flags or shutdown the trim card in case of overheating. The Trim cards setup suffers from a discontinuity

when conduction changes from the positive to negative pass bank transistor arm as the output passes though the zero point. This effect was suppressed by the feedback loops, and was problematic for fast ramps or step changes. The drive signal for the modulation was constrained by this phenomena, so instead of square wave, sinusoidal wave was chosen. Originally, the Trim cards were designed to operate in the DC regime, but managed to amplify a 250 Hz sine wave linearly. The used frequency of the sinusoidal modulation was 125 Hz. A higher frequency such as 500 Hz was not possible.

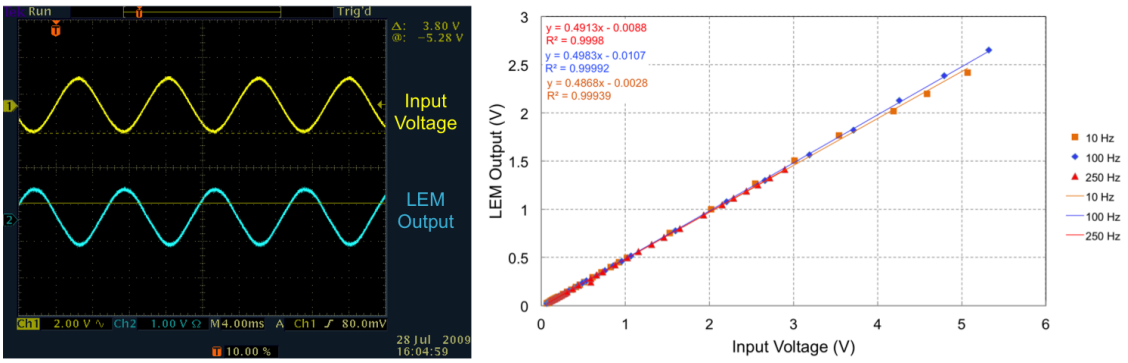

(a) Drive signal and LEM output from oscilloscope

(b) LEM output vs drive signal for different frequency

Figure 4.8 LEM current transducer output response (blue) to input sine drive signal (yellow) seen by oscilloscope (left). The output from the LEM was out of phase with the input signal. The figure on the right shows LEM calibration up to 5 V of input signal. The frequency dependence of the input signals were studied up to 250 Hz.

4.5.6 LEM Current Transducer

Four LEM CT-10T [123] were used to monitor the current through the two pairs of the MAT dipoles. The LEM has two pins for the input current in one side and two power supply pins (±15 V) on the other side along with two pins for output voltages. The LEMs were calibrated up to 5.5 V of input voltage, whereas nominal input operating voltage during the experiment was ∼1 V. The calibration was performed using a bench top and VME-4145 signal generators. A typical drive signal and its readback signal by a LEM are shown in Figure 4.8 (a) and the variation of LEM output with input drive voltage has been shown in Figure 4.8 (b). There was a 180° phase shift between the input (or Trim) signal and the LEM output signal. The measured gain was ∼0.5 for all the LEMs. There was no frequency dependence of the gain for the LEMs in the voltage domain 0-5 V as shown in Figure 4.8 (b). The LEMs were assembled in an insulated box and installed in the Hall-C patch panel VME crate in the BSY service building [124] and were connected in series with the MAT dipoles.

During the experiment, the LEMs were usually disconnected since they induced a small position motion in the beam at 240 Hz. During bench tests, LEM LA 50-P current transducer [125] was used to monitor the current. LEM LA 50-P used the induction method to measure the current; hence there was no series connection with the coils for the measurements. Use of the induction current transducer has a lesser chance of injecting noise in the system. For future work, one might consider LEM LA 50-P or similar current transducer for precision parity measurements. The LEM current transducers have also helped to calibrate the strength of the magnets during the commissioning tests. More details about LEMs and its calibration are described in Ref. [126].

4.5.7 Energy Modulation Hardware

A 125 Hz sinusoidal signal was sent to an energy vernier SL-20 of a cryo-module in South linac of the accelerator to modulate the energy. One of the standard features of the accelerator is the use of Fast Feed Back (FFB) system (Section 3.6.7) to maintain a steady beam position. Unfortunately, the energy FFB system did a perfect job of countering the 125 Hz energy modulation signal. The energy monitor BPM 3C12X saw no response in Figure 4.9 (bottom) for the energy modulation signal (top) when the FFB was on. So, the FFB system had to be paused during the energy modulation to avoid any suppression from the FFB system.

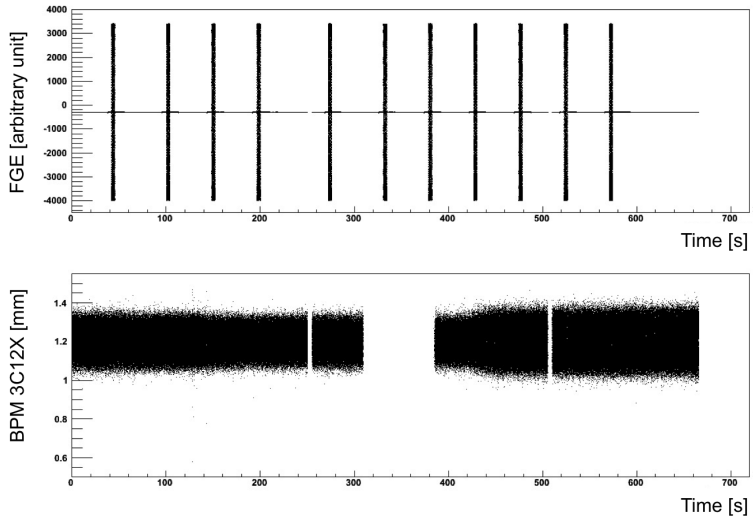

Figure 4.9 The effect of Fast Feed Back (FFB) system on energy modulation [11]. Top panel shows function generator drive signal vs time. Bottom panel shows the response of the BPM 3C12X (which is located in the middle of the arc and supposed to see maximum response for energy modulation) for the same drive signals. No response was observed in the BPM when FFB was on. The missing portions of the BPM response are beam trips removed by the software stability cut.

4.5.8 ADCs

Two sets of TRIUMF-built 18-bit analog to digital converters (ADCs) were used to study the readback signals from different components of the beam modulation system. Each module had eight ADC channels which were synchronized and triggered by the MPS signal sent by the helicity board. The ramp wave and 5 drive signals (X, X', Y, Y', E) from VME function generator, 4 readback signals from LEM current transducer, 4 readback signals from Trim-II power amplifiers were read by the TRIUMF ADCs (more details in section 3.11.1.1 and [99, 100]).

All the readback channels (the above mentioned 14 channels and a readback from SL-20 vernier for energy modulation) were also sent to a VME 32-channel ADC module [127] which was used to monitor the peaks of the signals. The ADC had 16-bit resolution and supported up to a 100 kHz sample rate. The ADC was configured by 36 16-bit registers and read the analog input data. The data format was configured depending on the selected bipolar or unipolar input range. The analog inputs were fully differential and configured to detect the peak of the input signals. The input connectors for the analog inputs were 50-pin D style connectors. The front panel had indicator LED's for power and heartbeat. The JLab-made peak detection ADC was used as a standalone (independent of Q-weak parity violating data acquisition system) modulation readback system and was installed in the BSY service building.

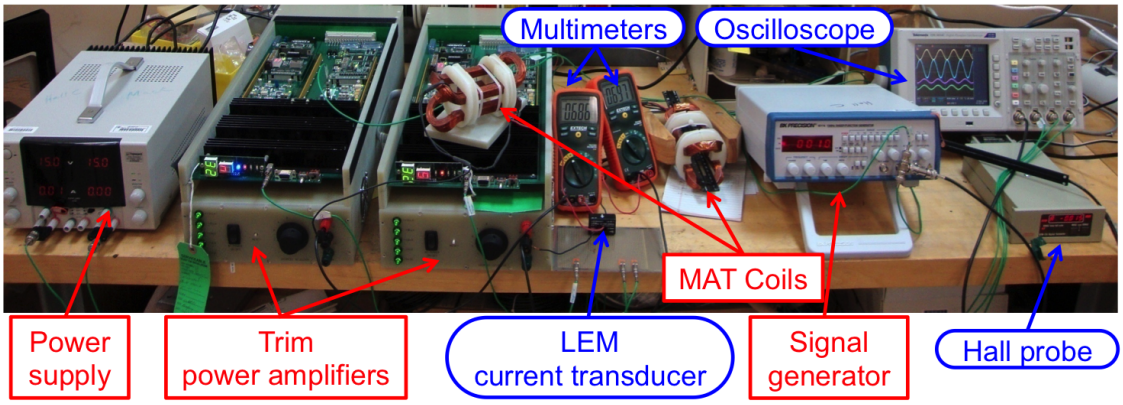

Figure 4.10 Beam modulation hardware bench test setup. It consists of one ±15 V power supply, two Trim power amplifiers, a pair of assembled MAT coils, and one signal generator. A VME signal generator was also used during the latter part. To see the responses, two multimeters, a LEM current transducer, a Hall probe, and an oscilloscope were used.

4.6 Hardware Components Calibration and Important Constraints

Extensive bench tests were performed with the beam modulation system so that (except for the absence of long drive cables) it would be possible to predict how the installed system would work. The Trim amplifier was controlled via an analog input from a simple bench-top function generator at the beginning and latter with VME 4145 board. The signal generator produces sine waves of different amplitudes and frequencies as the input voltage to the Trim power amplifier. The amplified signal goes to ∼10 cm long MAT coil through a single LEM current transducer. The rms currents through the coils were measured by ammeter. The rms magnetic fields of the coils were measured by the Hall probe. All the individual components were tested and calibrated in the bench test. The bench test setup is shown in Figure 4.10.

4.6.1 Coil Positioning

There were significant constraints on where perturbing coils could be located. One absolute requirement was that coils be located upstream of the high dispersion point at 3C12 (the center of the 3C arc) so that modulations in X, X', and E could be disentangled. Another highly desirable constraint was that the coils be located downstream of any expected deviations from design optics. Accelerator operations agreed to complete matching in 3C beamline by quadrupole MQA3C08, the beginning of the 3C arc dipole string. Considerations of stability therefore excluded regions upstream of this point, leaving only the first half of the 3C arc as a potential site for coils. The coil positioning and orbit excursions were simulated using OptiM. Initially, it was attempted to insert both coils into a single ∼1 m drift, but the angle kicks of interest required excessively high field integrals and the approach did not work. Separating the coils by more than 1 meter required straddling other beamline elements. The coils were mounted between two dipoles with no intervening quadrupoles or active elements. The 1st pair of MAT coils, MHF3C08H (X_1) and MHF3C08V (Y_1), were installed in the drift oD7028, which was located just after quadruple 3C08 and before the dipole 3C05. The 2nd pair MAT coils, MHF3C10H (X_2) and MHF3C10V (Y_2), were installed in the drift 0D7034, which was located between dipoles 3C06 and 3C07. The separation between these two pairs of coils was about ∼9.5 m. The first coil X_1 was located ∼92.7 m upstream of the Q-weak target. The X_1 and X_2 coils were driven simultaneously and in opposite phase in an attempt to produce relatively pure horizontal position or angle changes at the target (see Figure 4.4).

4.6.2 Waveform

The preferred waveform was to generate at least square-ish modulation (similar to the square helicity reversal). The Trim power amplifier was unable to drive square waveforms in the frequency range of interest. Satisfactory results were obtained only with sinusoidal waveform, which was hence was used to drive the magnets. Due to schedule pressure, existing Trim amplifiers were used.

4.6.3 Waveform Phase

A 1 V of sawtooth wave with the same frequency of 125 Hz as sinusoidal drive signal from VME 4145 was used to monitor the phase of the drive signals. The sawtooth ramp wave goes from 0 to 1 V as the phase of the sinusoidal drive signal goes from 0 to 360^o (Figure 4.11). The drive signal and ramp wave were triggered. The edges of the ramp wave were not very sharp hence were removed during the analysis to avoid any edge effect. The edges were recreated using a ramp fill method in the software as described in Ref. [128].

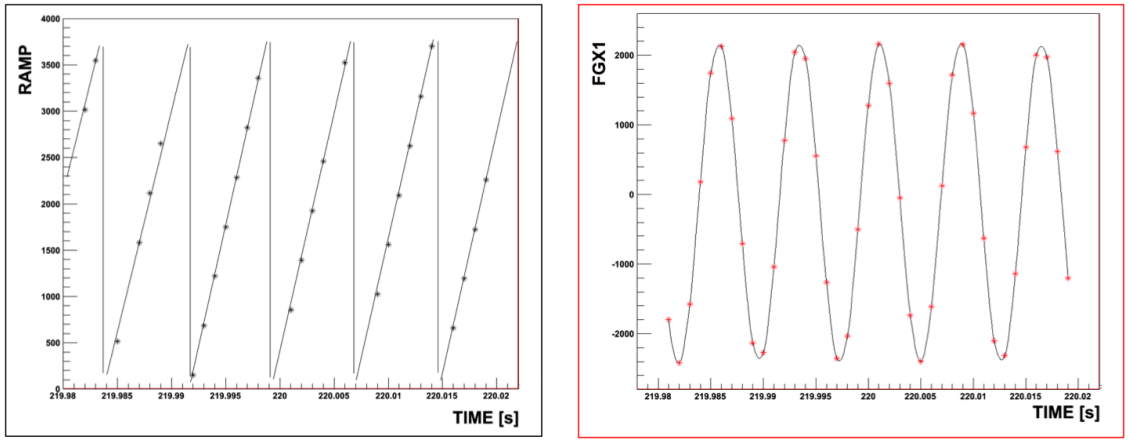

(a) Ramp signal vs Time (b) Drive signal vs Time

Figure 4.11 Zoomed ramp and drive signal from a beam modulation cycle during a typical production run. (a) Ramp signal vs time. The ramp signal is a sawtooth wave used to track the phase of the sinusoidal drive signals. (b) Drive signal vs time. The drive signal is a sinusoidal wave.

4.6.4 Frequency Range

The frequency of the waveform was tested for the range of 10-500 Hz at 3 A (peak) output. The Trim cards reliably drove sinusoidal waveforms up to 250 Hz. At that frequency, the coil impedance becomes approximately $X_{\text{total}} = 1.6\ \Omega + 2\pi f\ (0.0038\ \text{H}) = 7.6\ \Omega$, so the amplifier has to provide

22.8 V (peak). The maximum output voltage of the Trim-II amplifier appeared to be approximately ± 27 V, but it was not strictly bipolar due to the use of NPN diodes for one polarity and PNP diodes for the other. So while one could go a bit higher in frequency than 250 Hz, there would be a rapidly increasing risk of generating asymmetrical sine-like waves (and hence a small DC beam position offset). During production data collection, the nominal drive signal frequency was 125 Hz which allowed the parity DAQ to take 7-8 samples. Another criteria for choosing the frequency was to avoid the power line frequencies (60, 120, 180, etc. Hz) suppressed by FFB system.

4.6.5 Maximum Current

With sustained operation, the coils became quite hot to the touch at $I_{\text{peak}} = 7.07$ A ($I_{\text{rms}} = 5$ A). This was significantly above Q-weak's nominal maximum current $I_{\text{peak}} = 3$ A, but it is worth discussing since future experiments at higher beam energy might try to push the envelope. Although measurements at 1% duty factor would take only 36 seconds per hour, one must assume that a parity violation experiment will eventually take long, dedicated beam modulation runs. Unless cooling fans installed, damage to the enamel-insulated wires or any plastic components could result if $I_{\text{peak}} = 7.07$ A is significantly exceeded. The "smoke point" of the magnets was not determined, but bear in mind that $P = I^2R$, so the temperature would increase rapidly with current above $I_{\text{peak}} = 7.07$ A. It should be emphasized that $I_{\text{peak}} = 7.07$ A refers to the peak current of a sinusoidal waveform, and not to a maximum DC current which would have twice the average power dissipation. Constraint on maximum current based on machine protection simulation is discussed in the Section 4.9.

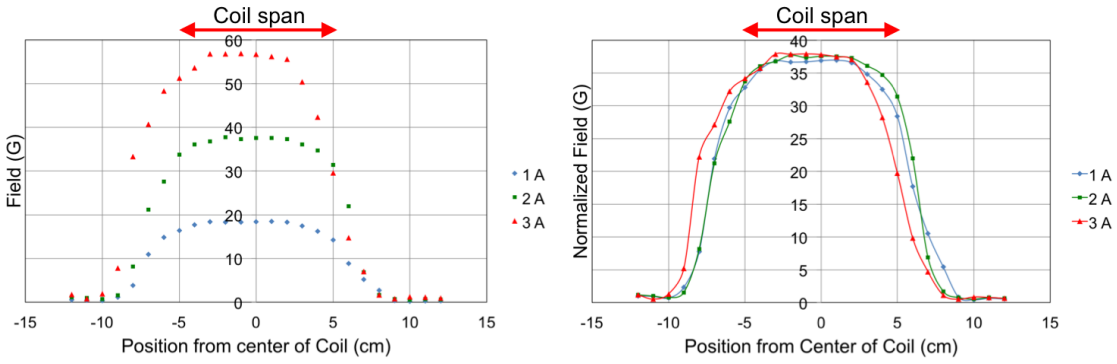

(a) Field map of MAT coil for different current

(b) Normalized field map of MAT coil

Figure 4.12 Field map of MAT coil for different input coil currents (left). The field was linear in the region of the coil span of 10 cm. The field profile did not change with coil current up to 3 A. The field was normalized with respect to 1 A (right).

4.6.6 Magnetic Field Calibration of the MAT Coils

The MAT coils were calibrated using a bench test setup, as shown in Figure 4.10. The magnetic field was measured using a GMW Hall Probe. The measured field integral for a 10 cm long MAT coil was ∼330 G-cm/A. The field was reasonably uniform over the span of the coil (Figure 4.12 (a)). There was no current dependence of the field as shown in Figure 4.12 (b). The magnetic field for the MAT coils falls quite sharply with distance beyond the coil span, hence reduces the possibility of interaction with other elements in the beamline.

4.7 Controls and Software Sketch

A standalone control system for the beam modulation system was designed by Scott Higgins [129–131]. The drive signals of two VME-4145 signal generator boards were controlled via an EPICS database access library that works on Unix and vxWorks. In the control system, the first VME-4145 card was referred as `BMOD1` and the second card as `BMOD2`. Each function generator card has 4 channels and they are named as `CHAN0`, `CHAN1`, `CHAN2`, and `CHAN3`. All four channels of `BMOD1` and `CHAN0` and `CHAN3` of `BMOD2` were used for the modulation system. The EPICS variable for the master switch was `BEAMMODSWITCH`. A value for `BEAMMODSWITCH` of 0 was considered as `OFF` and 1 was `ON`. This switch allowed operations to control whether or not to allow any beam modulation requests. The off state was entered when the master switch was set to `OFF`. In the `OFF` state the Relays to the Trim cards were set to ground. The `OFF` state was the default state for the system after an IOC reboot. The `CONFIG` state was entered when the operations toggles the master switch from `OFF` to `ON`. Once the board was in the `CONFIG` state all, the channels in `BMOD1` and one channel `BMOD2` loaded a sine wave, whereas `CHAN0` of `BMOD2` loaded ramp wave. The adjustable inputs controlling the sine wave were frequency and amplitude. The allowed frequency range was set to be 10-250 Hz, and amplitude was limited to ± 0.3 A, as discussed in previous sections. A negative amplitude would shift the phase of the sine wave by $180°/\pi$. The output for ramp wave was 0-1 V.

Before the transitions to the trigger state, it was necessary to enter the number of periods for the sinewave or rampwave to run the system. This setting ranged from 1 to 511. A value of 511 would cause the hardware to run the sinewave or rampwave continuously which was a feature of the hardware. Nominal cycle for the system was set to 510.

The sine waves could be initiated by both a hardware and software trigger. The software trigger was a button that is activated by writing a value of "1" to the EPICS `TRIGGER` variable. This feature was primarily used in testing the system. The hardware trigger was initiated from the Hall-C DAQ.

All of the 8 channels shared the same hardware trigger so any of the channels that were in the `TRIGGER` state would initiate sine wave outputs. It should be noted that if another trigger comes in while the VME-4145 is outputing a sine wave, the output will be interrupted and the card will restart the sine wave from the beginning. There were 2 things that could cause a channel to leave the trigger state: if operations selects Beam Modulation Off with the master switch or the user selects to leave the trigger state. The EPICS variables to leave the trigger state is activated by writing a value of "1".

If the user entered the trigger state after having previously run a sinewave, the last loaded sine wave would be executed. There was no need to reload the sine wave in the `CONFIG` state if amplitude and frequency were to stay the same. If, however, the user desired to change either the frequency or amplitude, a new sinewave must be loaded. There was a time delay in the reporting of the running of a sinewave from the VME-4145. A sine wave could be triggered and finished before the card reported that it was actively running a sinewave. Therefore there was no deterministic way to see the status of the card generating a wave for a particular channel in real time, at least not by monitoring the VME-4145. An external method was needed. A JLab-made ADC was used to monitor those channels in real time. There was a signal that went back to the hall which showed the output of the VME-4145 function generator. The goal of this signal was to show real time values written to the trim card. In order for the output of the function generator to reach the trim card, a relay needed to be set. The signal going back to the Hall-C of the function generator was between the relay board and the trim card. A value of "1" meant the relay was enabled and the function generator was connected to the trim card. A value of "0" meant the relay was off and the trim card was tied to ground. More details about the modulation control system can be found in technical documents [129, 131].

4.8 Modulation Modes

Two possible modulation modes were exercised during the experiment. One mode was with single coil modulation, where all four coils X_1, X_2, Y_1, and Y_2 were pulsed *individually*; this mode was mainly used to calibrate and test the system during commissioning period. The other mode was, in which one pair of coils was pulsed together to achieve a relatively pure position or angle at the target, the nominal mode of operation. A pulse with a combination of X_1, and X_2 was used for horizontal position and angle, and one with a combination of Y_1, and Y_2 was used for vertical position and angle motion. The energy modulation was the same for both the single and coil pair

modes. The nominal current through the MAT dipole for the pair mode is shown in Table 4.3. A unique pattern number was assigned in the software to identify the different modulation modes, and parameters as listed in Table 4.5.

Table 4.5 Different beam modulation modes and related pattern numbers. In single coil mode, just one coil was pulsed and the response was a linear combination of position and angle. In pair of coils, two coils were pulsed at a time to produce relatively pure position or angle.

Mode	Parameter	Coils Pulsed	Pattern Number
Single coil	X and X'	X_1	1
	X and X'	X_2	2
	Y and Y'	Y_1	3
	Y and Y'	Y_2	4
	E	E	5
Pair of coils	X	X_1 and X_2	11
	Y	Y_1 and Y_2	12
	E	E	13
	X'	X_1 and X_2	14
	Y'	Y_1 and Y_2	15

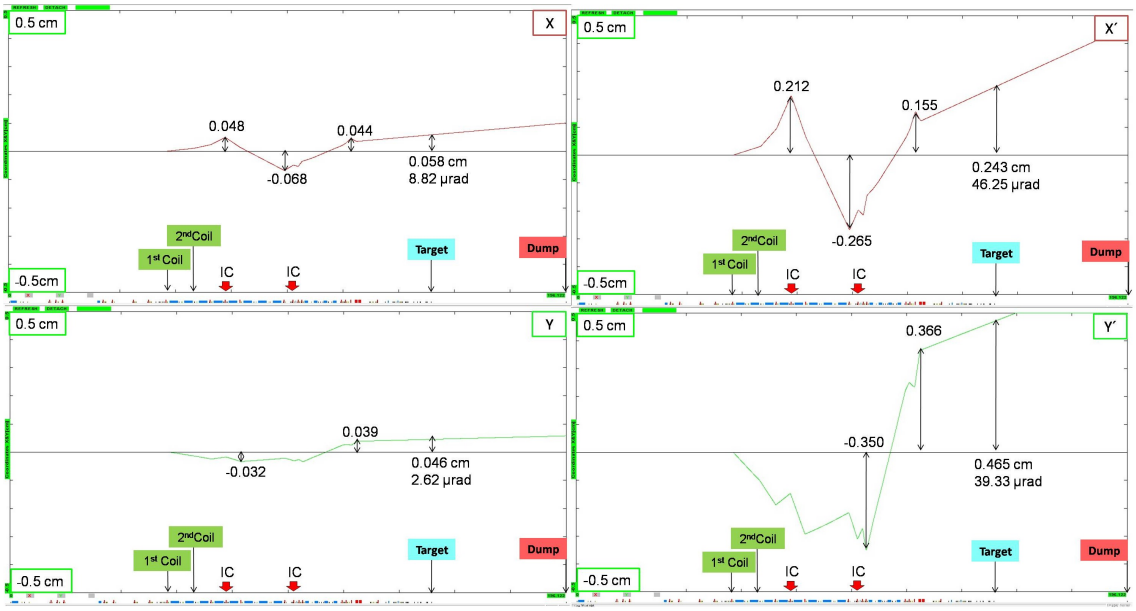

Figure 4.13 Orbit excursions using a pair of coils with incorrect polarity on one of the coils. Beam moves from left to right. Large excursions would be observed for angle modulation. The used field strength was 5 times higher than nominal. The recommended locations for ion chambers (IC) based on this study are shown by the thick arrows at the bottom of each panel.

4.9 Machine Protection Analysis

OptiM simulations were performed to check the maximum possible excursion in the beamline. The nominal field integrals for the modulation MAT coils are given in Table 4.3 and the corresponding excursions are shown in Figure 4.5. Increasing the fields by 5 times would move the beam only 1.3 mm upstream of the target and 1.0 mm at the dump. To check the worst possible scenario, the polarity of the magnets was reversed, hence coherently kicking (using the same 5 times of nominal field); the simulated orbits are shown in Figure 4.13. The reversed polarity deviations upstream of the target were 3.6 mm and 6.6 mm at the beam dump. The same simulation with only one coil energized deviations was 2.4 mm upstream of the target and 3.8 mm at the beam dump for $I_{\max} = 0.6$ A. Considering all of these cases, the maximum obtained excursion was about 4.6 mm at the target for a maximum current of 0.6 A. For angles, the excursions were much larger than position excursion mainly in the regions middle of the arc (around quadrupole 3C12) and end of the arc (around quadrupole 3C17). The deviation at the beam dump was 6.6 mm for $I_{\max} = 0.6$ A. The orbit excursions for all the cases are summerized in Table 4.6. For protection of the machine, considering all the above cases, the recommended place to install ion chambers (IC) was at the highest beam excursion region of the beamline around 3C12 and 3C17 (as shown in Figure 4.13). The worst case scenario was found to be the case of incorrect polarity. In order to avoid any mishap, when system was commissioned, a hard coded software limit of $I_{\max} = 0.3$ A was implemented. More details about the machine protection analysis can be found in Q-weak internal technical document [132].

Table 4.6 Summary of orbit excursions from the machine protection simulation.

Modulation Type	Orbit excursion at target		Position excursion at dump [cm]
	Position [cm]	Angle [μrad]	
Pair of coils mode			
X	0.058	8.82	0.100
X'	0.243	46.25	0.470
Y	0.046	2.62	0.048
Y'	0.465	39.33	0.660
Single coil mode			
X_1	0.106	11.4	0.380
X_2	-0.127	-34.8	-0.180
Y_1	0.062	2.2	0.120
Y_2	-0.129	-16.9	-0.370

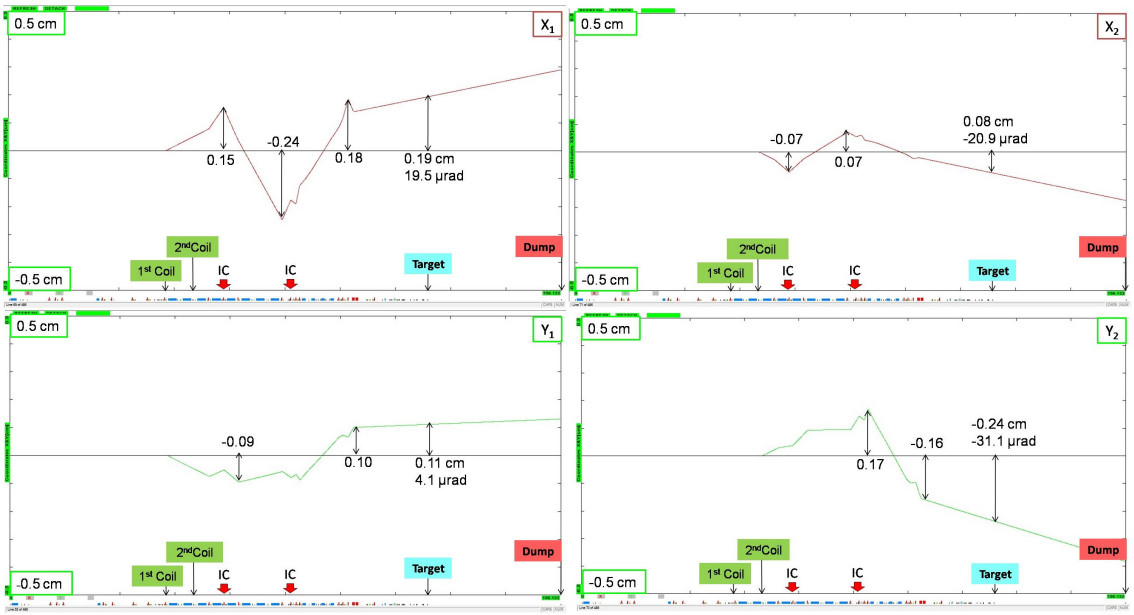

Figure 4.14 Orbit excursions with only one coil energized. Beam moves from left to right. Large excursions were observed for X_1 and Y_2 coils. The maximum current used for all the coils was $I_{\max} = 0.6$ A. A hard coded restriction of $I_{\max} = 0.3$ A in the software was set for the safety of the accelerator based on this analysis.

4.10 Beam Modulation Cycle

A typical beam modulation cycle vs time during production run is shown in Figure 4.15. A micro cycle ran for 510 cycles with a nominal frequency of 125 Hz for each beam parameter, hence lasted 510 (cycles)$\times \dfrac{1}{125\ Hz} \simeq 4.08$ s. One macro cycle consisted of the X, X', E, Y, Y' cycles and ran for 320 s. Each macro cycle was then continuously repeated. The dead time between each active micro cycle was ∼75 s. This dead time was set high to collect modulation data noninvasively with production running, which yielded a duty factor of ∼6%. A zoomed version of the ramp and sinusoidal drive signal from the Figure 4.15 is shown in Figure 4.11.

4.11 Response to Modulation Signal and Applications

The main detector response to horizontal position (X) modulation is shown in Figure 4.16. The detector coordinate is shown in the center of the figure. Detectors 1 and 5 show the maximum response for the X modulation and are anti-correlated. Negligible response is been seen in octants 3 and 7. Detector responses correlated with modulation were used to extract sensitivities for the main detector and are discussed in the next chapter.

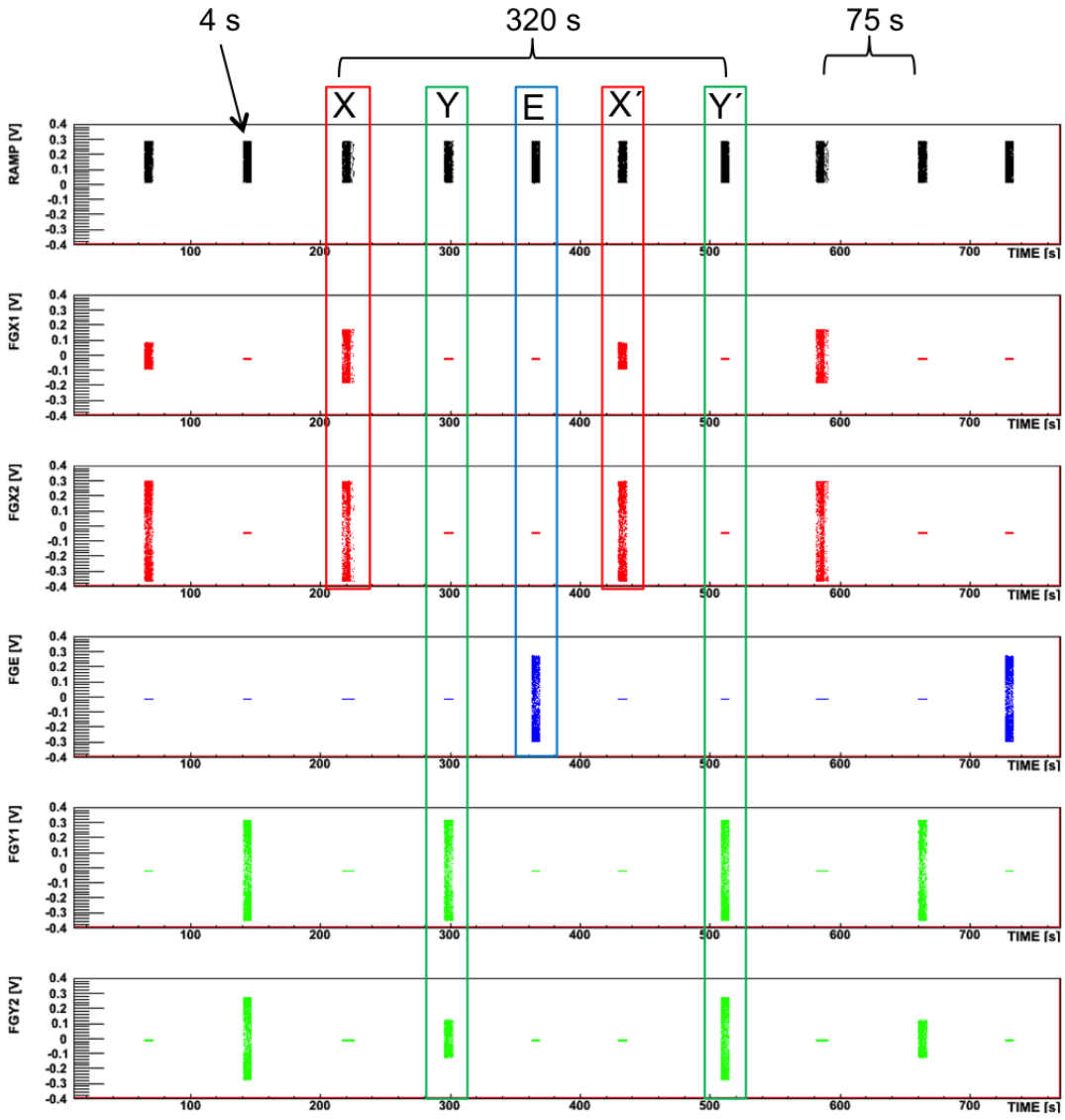

Figure 4.15 Beam modulation cycle during a typical production run. 1st panel shows ramp wave to calibrate sinusoidal signals vs time. 2nd and 3rd panels show sinusoidal drive signals for horizontal position (X) and angle (X') modulation vs time. 4th panel shows sinusoidal drive signals for energy (E) modulation vs time. 5th and 6th panels show sinusoidal drive signals for vertical position (Y) and angle (Y') modulation vs time. The cycle for each parameter is ∼4 s. One macro cycle consists of the X, X', E, Y, Y' cycles and ran for 320 s.

A typical BPM response to nominal modulation drive signal is a sinusoidal of amplitude ∼200 μm, as shown in Figure 4.17. Compared with natural beam jitter, this is an order of magnitude larger and has fewer correlations among the parameters, providing an independent way of measuring sensitivities. Figure 4.17 shows a pair of drive signals for X modulation in top two panels, whereas

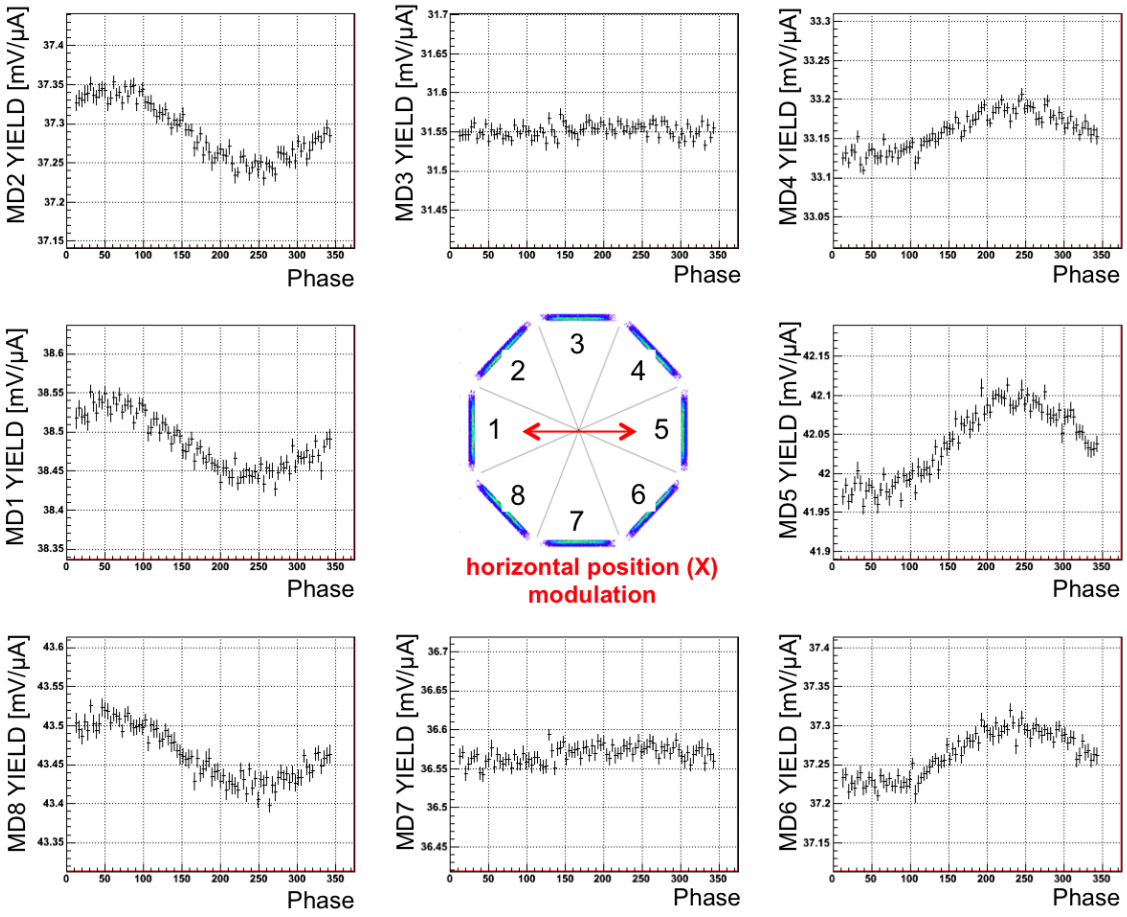

Figure 4.16 Main detector response to X position modulation. Main detector yields vs modulation phase (ramp wave) plotted for each detector.

the target BPM X and Y responses are shown in the bottom two panels. As expected, the BPM X shows a significant sinusoidal response to the horizontal drive signal but no response in Y. A small phase shift was observed between the drive signals and BPM responses (more details in next chapter). Besides measuring sensitivities, the BPM response to the modulation signal helped to track any optics change in the Hall-C beamline. The following chapter will discuss the application and products of the beam modulation system.

4.12 Extension to Other JLab Parity Violation Experiments

The beam modulation system described in this chapter should be useful for other parity violation experiments such as the Moeller experiment at 11 GeV in Hall-A, JLab [133]. Some basic limitations should be kept in mind. First of all, the modulation amplitude of the system described here will scale

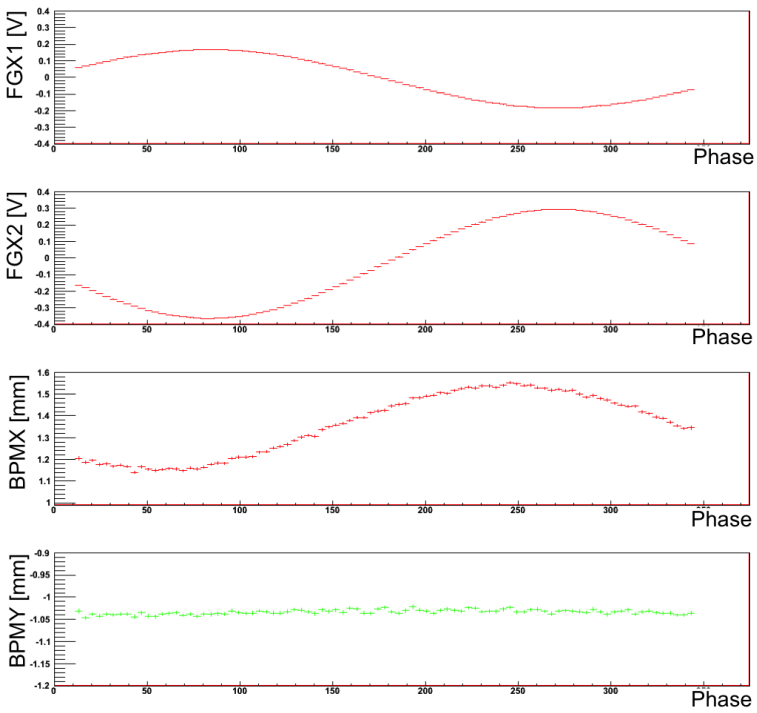

Figure 4.17 Target BPM response to X position modulation. The signals were plotted vs modulation phase. The drive signals in coils X_1, and X_2 are shown in top two panels and the corresponding BPM response in X, and Y are shown in bottom two panels. There is a small phase shift between the drive signals and BPM responses.

like $E_{\rm beam}$ (GeV)/1.165, hence the amplitudes at 11 GeV will be smaller by an order of magnitude. If the amplitude becomes smaller than the random beam jitter, convergence will be greatly slowed. The air-core coils can be driven harder if the duty factor is limited or if fans are used to cool the coils, but at about 5 A (rms) they become hot enough to risk damaging the enamel coatings on the wires under continuous duty. Secondly, at the frequencies of interest, the coil is an almost purely inductive load, so the voltage needed to drive a given current is nearly proportional to frequency. If one wishes to modulate the beam faster than the 250 Hz system described here, faster, higher voltage power amplifiers than the Trim-II would be needed. Alternatively, larger field integrals could be obtained for a given current by replacing air-core coils with ferrite magnets. Finally, because the final quadrupole is closer to the target in the Hall-A beamline (1C) line [134], it should be somewhat easier to generate a given angle kick for the same beam energy as compared to the 3C line.

4.13 Summary

The beam modulation system presented here was designed for sinusoidal modulation up to 250 Hz which was robust and well-suited for experiments measuring small parity violating asymmetries like the Q-weak experiment. At the cost of 1% of beam time for one parameter, the system was able to measure all sensitivities to 10% accuracy each day. The pairs of coils were tuned to deliver relatively pure positions or angle modulations, making it much less likely that singular matrices are encountered when solving for the sensitivities. The ratio of coil currents was adjusted to incorporate any optics change in the beamline compare to move the coils physically, which made the system independent of the design optic. For 1.165 GeV electron beam, using 125 Hz sinusoidal drive signal, the Trim power amplifier was able to provide the desired beam modulation amplitudes with existing air-core HF (MAT) coils. The modulation system worked quite well for the span of two years during the Q-weak experiment and collected data noninvasively with production running. However, to providing similar amplitudes for the Møller PV experiment at 12 GeV in Hall-A may require an upgrade of the amplifier or magnets.

SECTION 5
BEAMLINE OPTICS AND FALSE ASYMMETRIES

5.1 Detector Sensitivities

As described in the previous chapter, unwanted helicity correlated changes in the transverse beam positions X (horizontal) and Y (vertical), beam angles X′ and Y′, and incident energy E on the target give rise to false asymmetries. These helicity correlated beam asymmetries A_{false}(X, Y, X′, Y′, E) can be heavily suppressed with careful tuning at the polarized source and a symmetric detector array. However, the residual effects must be measured and controlled. The regressed asymmetry can be expressed using the following expression:

$$\begin{aligned} A_{reg} &= A_{msr} - A_{false}, \\ A_{false} &= \sum_{i=1}^{5} \left(\frac{\partial A}{\partial T_i} \right) \Delta T_i \end{aligned} \tag{5.1.1}$$

Here, the slopes $\partial A/\partial T_i$ are the measured main detector sensitivities of the asymmetry A_{raw} defined in Equation 5.1.1 to changes in the beam parameters ΔT_i at the helicity quartet level, and ΔT_i is the helicity correlated (HC) difference of each beam parameter ΔT_i measured at the quartet level. The virtual target BPM, described in section 3.6.1, was used to continuously measure the HC beam position and angle differences at the target. The measurement of the HC energy difference relied on BPM3C12, as described in Equation 4.4.4 of section 3.6.4.2. The natural jitter of the beam was used to determine the detector sensitivities, $\partial A/\partial T_i$. However, a better decoupling of the 5 sensitivities was achieved by varying the beam parameters in a controlled manner using a beam modulation system built specifically for this purpose. Relatively decoupled position and angle motions were separately produced by varying the current in pairs of air-core magnets placed along the beamline; two pairs in X and two pairs in Y, approximately 82 and 93 m upstream of the target.

A typical detector sensitivity for X modulation during an hour long run is shown in Figure 5.1. The detector sensitivities for all beam parameters for a few days during Run 1 are shown in Figure 5.2. Beam modulation amplitudes at the target, as well as typical monthly results measured for the HC beam properties ΔT_i and detector sensitivities $\partial A/\partial T_i$ during Run 2 can be found in Table 5.1. The HC beam asymmetries for X, X′ are anti-correlated and largely cancel. The same is true for Y and

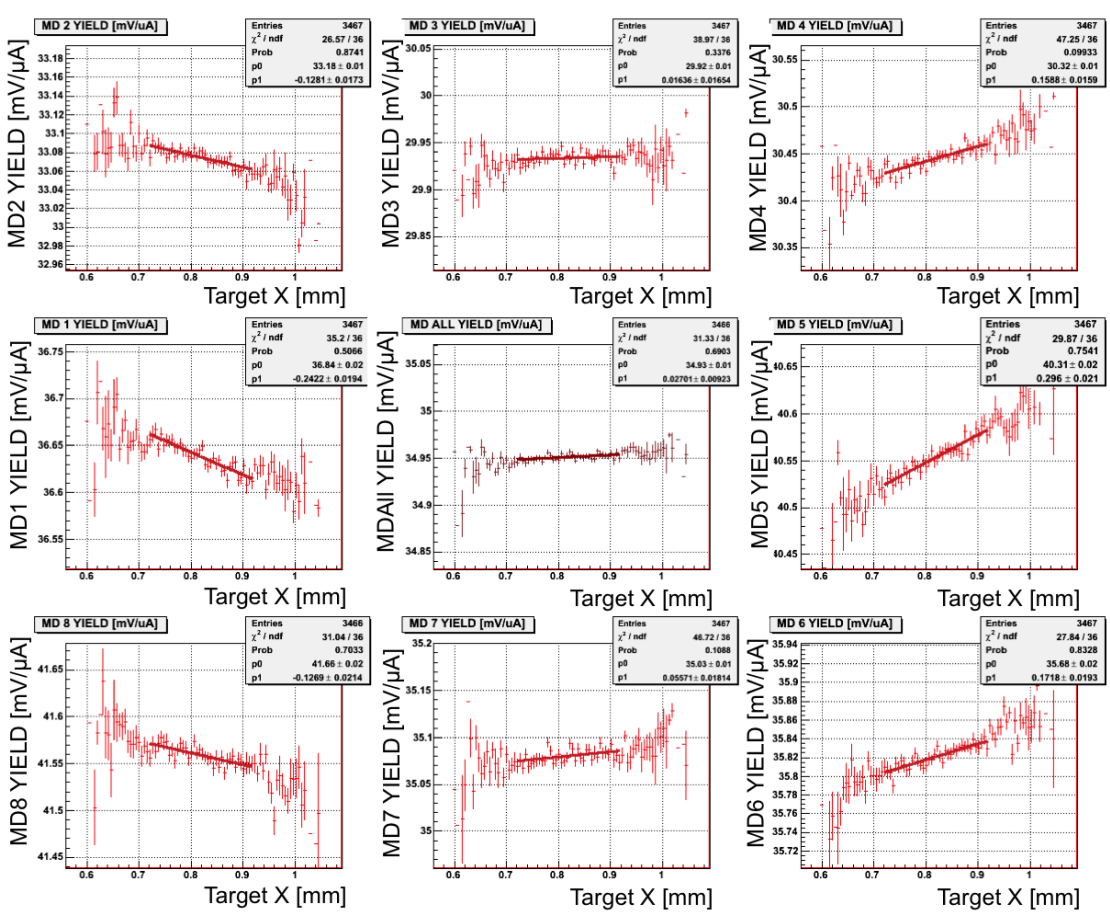

Figure 5.1 Main detector sensitivities with respect to target BPM X position for X Position Modulation.

Y′. The uncertainties associated with the monthly HC position (angle) differences ΔT_i are 0.07 nm (0.01 nrad) based on the quartet level BPM resolution (discussed in section 5.4), shown in Table 5.1.

A subset of the Run 2 parity violating electron-proton scattering production data showing the blinded asymmetry grouped by (monthly) Wien state is shown in Figure 5.3 [12]. Two different approaches to determine the sensitivities of the apparatus to HC beam properties were used to correct for the false asymmetry. The measured asymmetries without any correction (solid squares) are compared to the asymmetries after correction using the intrinsic random variations in beam properties (natural motion: triangles) and to the asymmetries using the beam modulation (beam modulation: inverted triangles). The asymmetries derived using each techniques are consistent with each other, and the overall correction for HC beam asymmetries is small. The data shown here

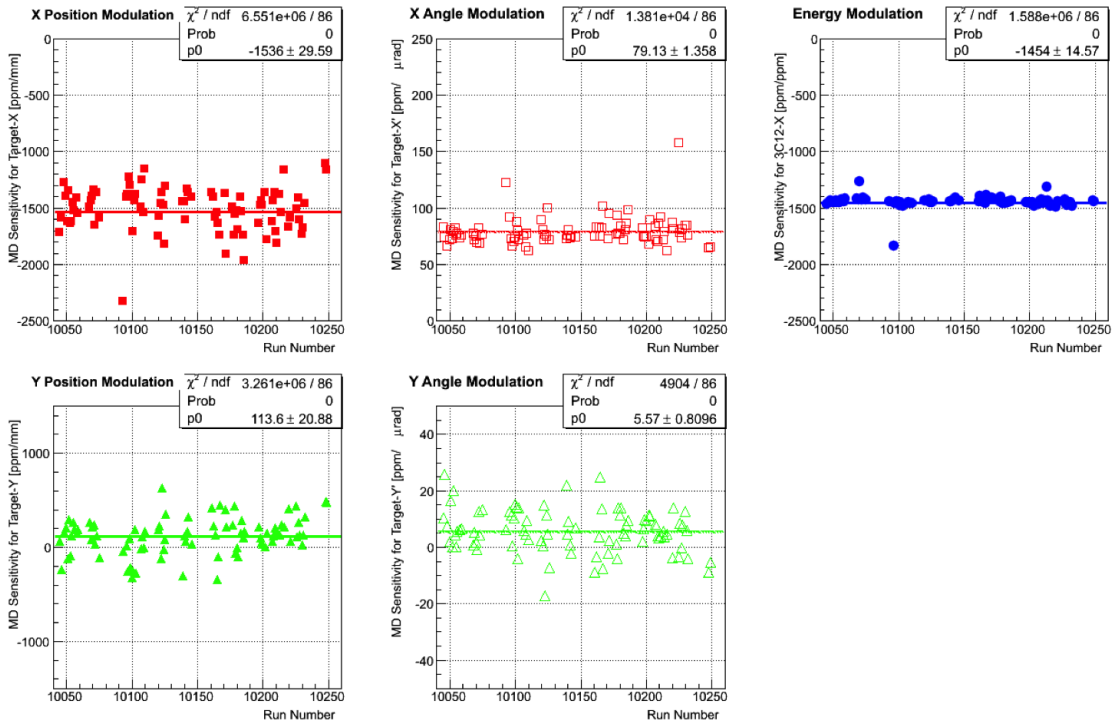

Figure 5.2 Main detector sensitivities for X (solid red square), X′ (empty red square), E (solid blue square), Y (solid green triangle), and Y′ (empty green triangle) are shown.

Table 5.1 A typical amplitudes used for driven beam modulation (column 2). Columns 3 and 4 provide typical average monthly results measured during Run 2 for the helicity correlated beam parameter differences ΔT_i and detector sensitivities $\partial A/\partial T_i$ for the beam parameters i listed in the first column. The total HCBA for this example is only 0.4 ppb. The uncertainties associated with ΔT_i and $\partial A/\partial T_i$ are discussed in the text [12].

Beam Parameter	Modulation Amplitude	Differences [monthly]	Sensitivities [monthly]
X	±125 μm	-3.3 nm	-2.11 ppm/μm
Y	±125 μm	2.5 nm	0.24 ppm/μm
X′	±5 μrad	-0.7 nrad	100.2 ppm/μrad
Y′	±5 μrad	0.002 nrad	-0.0 ppm/μrad
E	±61 ppm (70 keV)	0.1 nm	-1.56 ppm/μm

represent 80% of the Run 2 data for which modulation was available. An additional 1/3 of the total data acquired in the experiment was provided by Run 1 dataset. More detailed description of modulation sensitivity analysis and recent results will be discussed by J. Hoskins [107] and D. Jones [108] in their future theses.

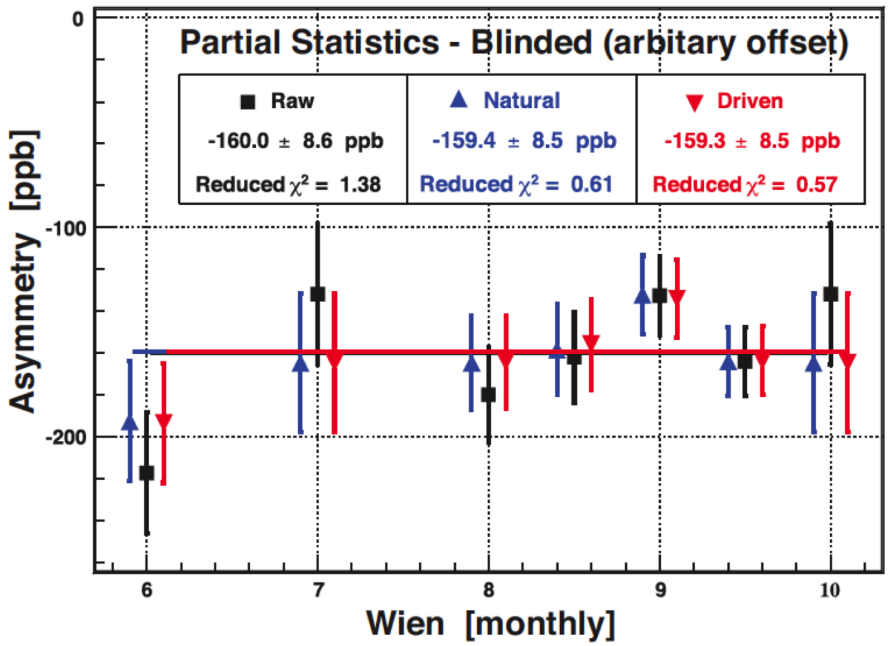

Figure 5.3 Subset of the Run 2 production data showing the blinded asymmetry (in ppb) grouped by (monthly) Wien state, and corrected using two different approaches to determine the sensitivities of the apparatus to HC beam properties that can give rise to false asymmetries. Other needed corrections are not applied to the data in this figure. The results without any correction (solid squares) are compared to the results after correction using the intrinsic random variations in beam properties (Natural motion: upward pointing triangles) and to the results using the driven beam motion (Beam modulation: downward pointing triangles) where the sensitivities are derived by actively modulating each property of the beam with a magnitude significantly larger than that intrinsically carried by the beam. The asymmetries derived using each technique are consistent with each other, and the overall correction for HCBAs is small. The data shown here represent the 80% of the Run 2 data for which driven motion was available. Run 1 provides an additional ∼1/3 of the total data acquired in the experiment [12].

5.2 Beamline Optics

A typical BPM response to modulation drive signal is sinusoidal and is shown in Figure 4.17 in the previous chapter. The responses from all 23[1] BPMs in the Hall-C beamline to modulation signal were observed throughout the production data collection. The BPM responses in X due to X modulation are shown in Figure 5.4. The vertical axis is the BPM X-signal for X kick and the horizontal axis is the phase (the ramp-wave was used to monitor the phase of the drive signals). The data are shown in red and fits are in dark red. The BPM responses are arranged according to the distance from the target. Beam position response amplitudes of all the BPMs to X modulation (from

[1]There were 24 BPMs in the Hall-C beamline. BPM 3H09B died after Run 1, hence excluded from the analysis.

Figure 5.4) with respect to Z locations from the target are shown in Figure 5.5. The location of all the BPMs are shown at the top of the plot by short vertical lines. All the quadrupoles, dipoles, Compton dipoles, Møller magnets, target, and beam modulation magnets are shown by short vertical lines at the bottom. Data are shown in solid circles, and simulated points from OptiM are shown in empty squares. This figure represents the evolution of the position response amplitude to modulation drive signal along the Hall-C beamline. The data matches quite well with the simulation. This method of tracking BPM response also helped to find any optics change or hardware failure in the beamline.

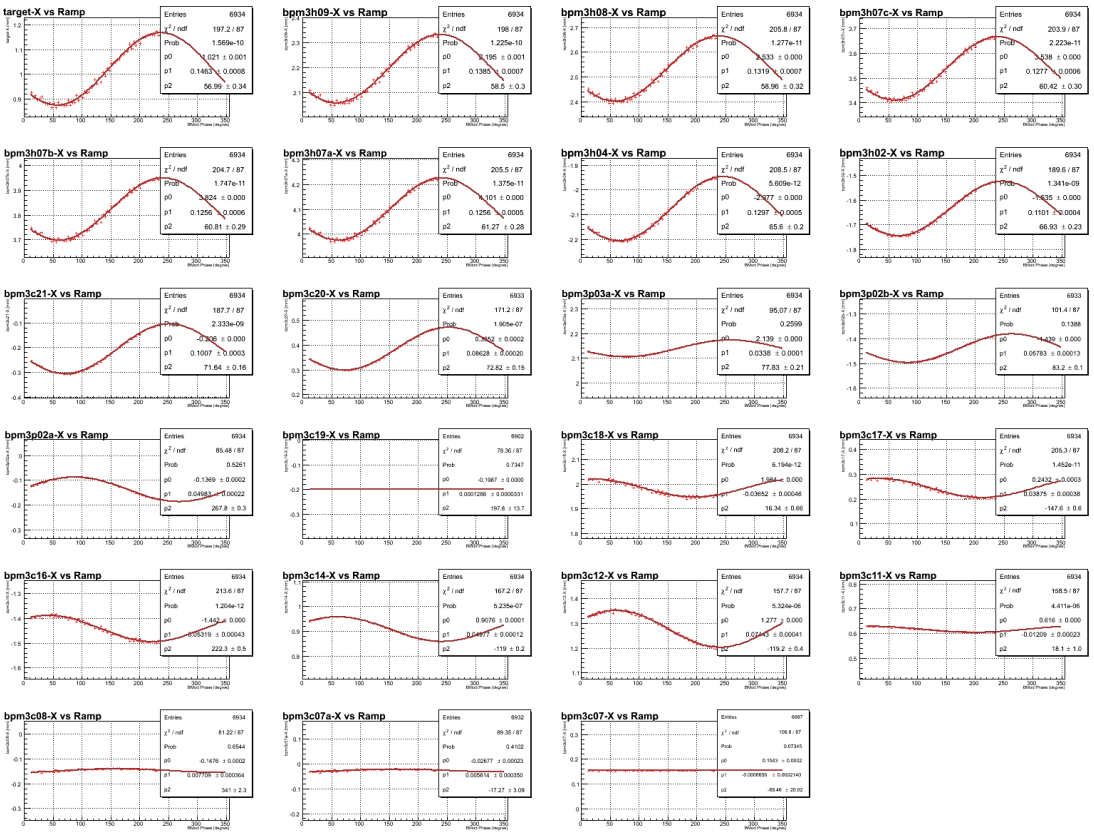

Figure 5.4 All Hall-C BPM responses in X due to X modulation using a pair of coils. The vertical axis is BPM X-response and horizontal axis is ramp-wave (the ramp-wave was used to monitor the phase of the drive signals). The data are shown in red and fits are shown in dark red. Starting at the target BPM in the top left, upstream BPMs are shown along the left to right and top to bottom directions, BPM 3C07 being the first BPM in the Hall-C beamline.

The BPM responses in X due to X' modulation, responses in Y due to Y modulation, responses in Y due to E modulation, and responses in X due to E modulation are shown in Figure 5.6 (from top left along the clockwise direction). The Fast Feed Back (FFB) system was fighting with the

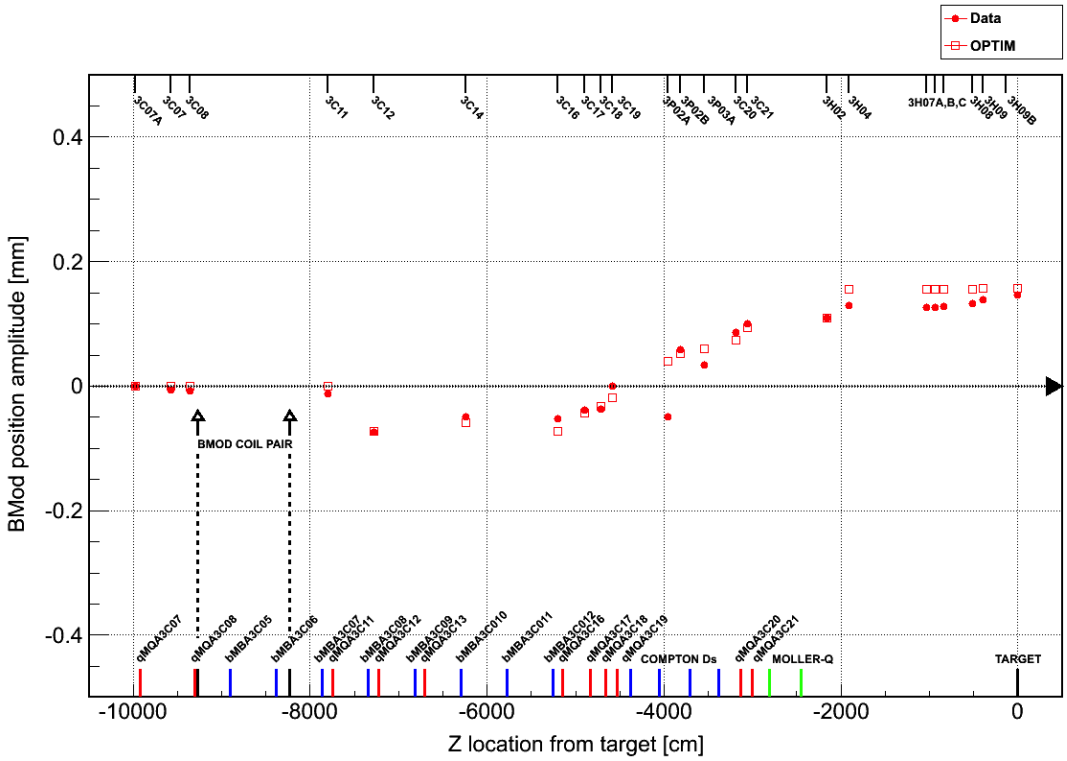

Figure 5.5 Beam position response of all the BPMs in the Hall-C beamline to X modulation. The locations of all the BPMs are shown at the top of the plot by vertical line. All the quadrupoles, dipoles, Compton dipoles, Møller magnets, target, and BMod magnets are shown at the bottom of the plot by vertical lines. Data are shown in solid circles, and simulated points from OptiM are shown in empty squares.

modulation system which is more evident in the X' modulation response (see section 5.2.3 for more details). There was a defocus in Y modulation and the system was not able to achieve a relatively pure Y position at the target. The residual dispersion at the target X was evident from the E modulation and was as high as $\sim$1/7th of the dispersion of the middle of the arc. The residual dispersion in Y was also non-negligible. These responses were recorded for all the production runs. The target BPM and BPM 3C12 position responses to X modulation vs. time for Run 1 and Run 2 are shown in Figure 5.7. The target X position was unstable at the beginning of the experiment. The big dip in the amplitude around run number 10900 was due to change in "tune" (BMod magnet current ratio) in order to achieve a better decoupling in the beam parameters. The optics was very stable from run number 11900 onward. There was a constant residual dispersion at the target throughout the experiment.

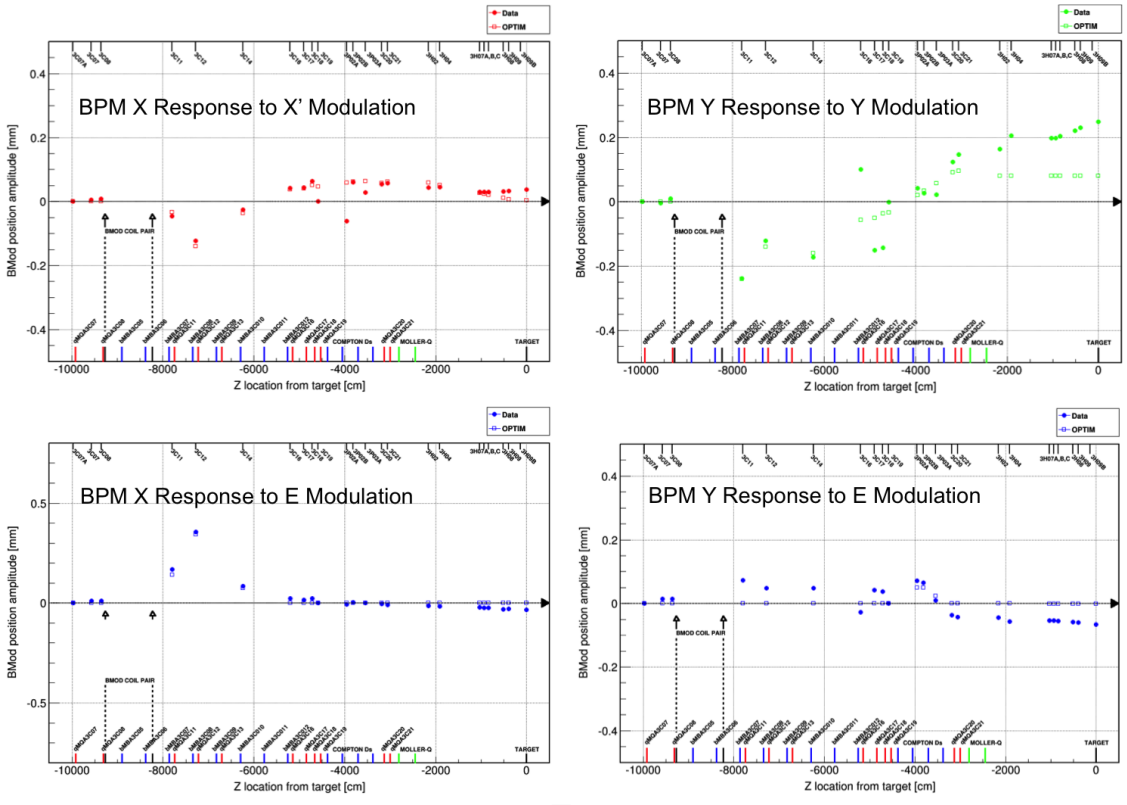

Figure 5.6 Beam position response of all the BPMs in the Hall-C beamline to X modulation. The locations of all the BPMs are shown at the top of the plot by vertical line. All the quadrupoles, dipoles, Compton dipoles, Møller magnets, target, and BMod magnets are shown at the bottom of the plot by vertical lines. Data are shown in solid circles, and simulated points from OptiM are shown in empty squares.

5.2.1 BPM Sign Corrections

The beam modulation system also helped to track some of the problems in the BPMs in the Hall-C beamline. During Run 1, BPM 3C19X (as shown in Figure 5.8) and Y showed no response to any modulation drive signals, whereas BPM 3C16Y showed an inverted response (more details in APPENDIX A.1). After investigation, misconnected cables were found for those BPMs and repaired before Run 2. Another problem was found with the BPMs 3P02A and 3P02B in the Compton region. These Compton BPMs had a different rotation in the beamline compared to the all other BPMs, hence they responded differently to the modulation signal. This problem was fixed in the software by giving an offset angle for these BPMs. The BPMs discussed above did not affect any physics results for Run 1, as they were not used in any asymmetry or regression calculation.

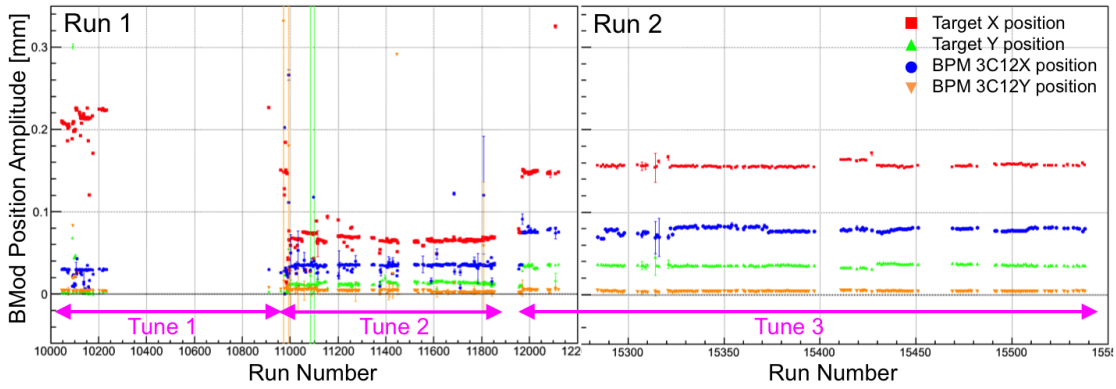

Figure 5.7 Hall-C target BPM responses due to modulation kick using a pair of coils in X. The sinusoidal response of the target BPM of a modulation signal for relatively pure X is fitted and the amplitude of the sinusoidal signal is plotted in vertical axis. The vertical axis is BMod BPM position in mm. The X target position is shown with solid red diamond, Y target position is shown with solid green triangle, BPM 3C12 X position is shown with solid blue square, BPM 3C12 Y position is shown with solid orange circle. For a relatively pure X position motion, we expect largely X target response and very small X angle response. We do not expect any Y position or Y angle response in this case. BPM 3C12X position response is relatively constant and 3C12Y is consistent with zero.

5.2.2 Beam Modulation Tune Parameter Scan

The idea of this analysis was to find a relatively pure angle and position "tune" at the target for the modulation system. In order to achieve a pure X and Y position and angle at the target, scan of the "tune" parameters was performed by varying the ratio of the drive signals in small steps. The maximum amplitudes of the function generator drive signals for this test were set to 0.444 times of the nominal amplitudes (shown in Table 4.3, chapter 4) for caution. The tune parameters were changed by changing the current in one coil (I_1) in steps of 50%, 25%, 0%, -25%, and -50%, respectively keeping the other coil (I_2) fixed to achieve a "tune" that generates a relatively pure angle at the target. A relatively pure X-angle tune was found to be in between the tune parameters -5.882 (nominal) and -9.009 (53.2%), and Y-angle to be in between -0.500 (nominal) and -0.675 (35%). The "tunes" for X and Y positions were already good to produce relatively pure position at the target. Based on this analysis, the modulation "tunes" were changed during Run 1 and are shown in Figure 5.7.

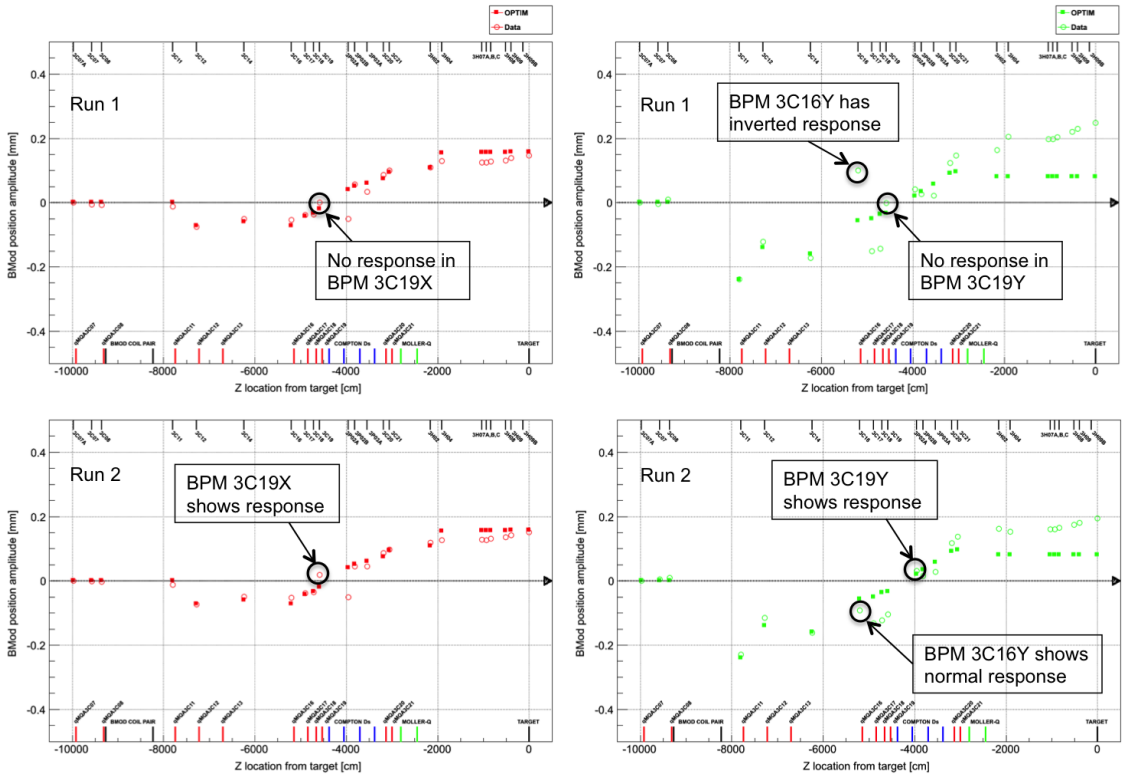

Figure 5.8 The beam position response of all the BPMs in the Hall-C beamline to X modulation. The locations of all the BPMs are shown at the top of the plot by vertical line. All the quadrupoles, dipoles, Compton dipoles, Møller magnets, target, and BMod magnets are shown at the bottom of the plot by vertical lines. Data are shown in solid circles, and simulated points from OptiM are shown in empty squares.

5.2.3 Effect of Fast Feed Back on Beam Modulation

The Fast Feed Back (FFB) system was designed to suppress any position and energy fluctuation in the beam position monitors. So it was important to inspect the effect of FFB system on the modulation system. The beam position responses of all the BPMs in the Hall-C beamline to X' modulation for FFB ON (by red empty circles) and OFF (by black empty triangles) are shown in Figure 5.9, respectively. The simulated position responses from OptiM are also shown in the figure (by solid red squares). The driven signals were 0.444 times of the nominal amplitudes for this test (shown in Table 4.3, chapter 4) for caution. There were minimal effects of FFB on BPM responses amplitude for X, Y and Y′ modulation (see APPENDIX A), but noticeable suppression was observed for X′ modulation (see Figure 5.9). This preliminary study exhibited no big position suppression of the BPM responses amplitude due to FFB system, as shown in Figure 5.9, although the effect on the phase of the BPM response along the beamline was not insignificant [135]. The FFB was

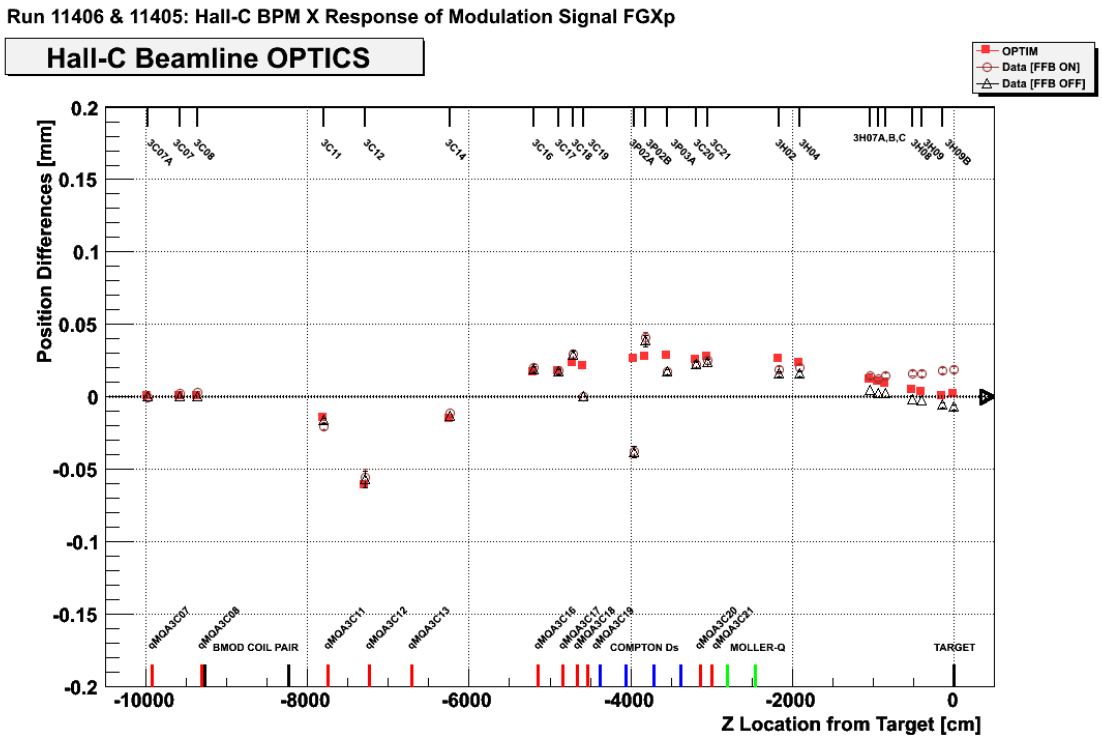

Figure 5.9 Hall-C BPM responses in X due to X angle modulation using a pair of coils. The vertical axis is BPM X-signal amplitude and horizontal axis is beamline elements. The simulated points from OptiM are shown in solid red squares, data with FFB ON are shown in empty red circles and data with FFB OFF are shown in empty black triangles. There is almost no effect of FFB on data for X motion. The locations of all the BPMs are shown at the top of the plot by vertical lines. All the quadrupoles, dipoles, Compton dipoles, Møller magnets, target, and BMod magnets are shown at the bottom of the plot by vertical lines.

not paused during position modulation and might have been responsible for the phase slip in BPM responses. Originally FFB was paused during Run 1 during position modulation, and the energy was also locked during energy modulation. In an effort to be less invasive during production running, the FFB was always kept on for position and angle modulations, and number of energy modulation cycles was reduced to half during Run 2. A new analysis approach was used to counter the phase slip problem [136]. The position-dependent phase slip was assumed to be a sum of modulation from two different locations, and two independent transfer functions from each of the driving locations can be used to decompose the response. The FFB response can be decomposed into a combination of two harmonic functions, one sine and one cosine, that match phases with the modulation drive signals. The FFB sine response combined with modulation drive sine function become the effective

driving signal and FFB cosine response averages to zero amplitude for the sine fit. More details on the analysis will be discussed by D. Jones [108] in his future thesis.

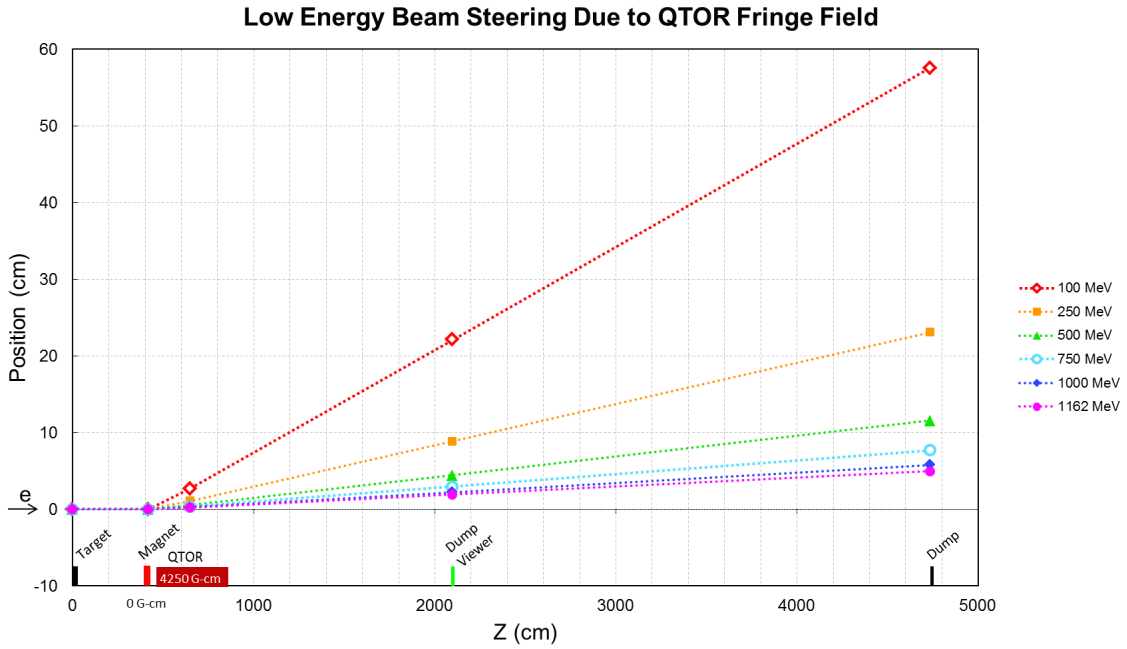

Figure 5.10 A simulation of the beam steering due to QTor fringe field (4250 Gauss-cm) for the primary electron beam (1.2 GeV) is shown in purple. The simulated tracks of the low energy electrons are also shown here. The primary beam spot moved ∼2 cm on the dump viewer between QTor OFF and ON.

5.3 QTOR Fringe Field and Optics Change

There was a vacuum leak activated by heating due to low energy electrons near the beam dump during Run 1. This unplanned event forced a delay in the experiment for months. Smaller bellows diameter with two stainless steel flanges might have been activated due to low energy electrons coming from upstream which might have caused the vacuum leak. It was found that the QTor has a non-zero field integral along the beam axis and might have deflected the low energy electrons in the dump viewer flanges. So, the plan of the collaboration was to improve the hardware assembly near the beam dump with a larger bellows diameter (see Figure 5.11 top panel) before Run 2. The new structure was built to minimize the stainless exposure, and low energy electrons coming from radiative tail stripe landed on aluminum, which helped to reduce the activation (see Figure 5.11 bottom panel). Another strategy was to design and build a corrector magnet to counter steer the fringe filed of the QTor.

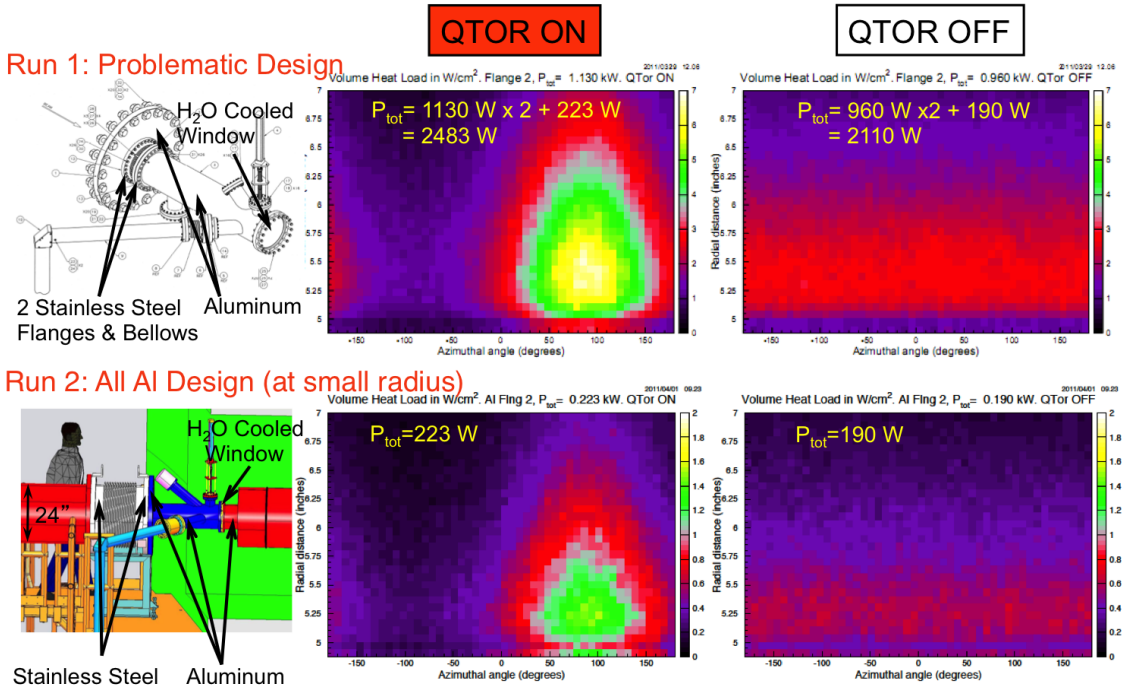

Figure 5.11 Bellows hardware and vacuum heat load before and after the activation. The top panel shows the Run 1 hardware of the bellows in the left and volume heat loads in the flange during QTor ON and OFF, respectively. Run2 bellows hardware and volume heat loads are shown in the bottom panel.

At the beginning of the experiment, it was observed that QTor steers the forward beam and one important question was to examine whether the steering could be caused by the expected QTor fringe field along the beam axis, or whether the steering indicates misalignment or motion of any coils. The primary beam (1.2 GeV) spot moved ∼2 cm on the dump viewer between QTor OFF and ON. The magnet steered the beam up and right towards the observed hot spot in the dump viewer (see Figure 5.11 top panel). The steering implies a residual field integral of 4250 Gauss-cm in QTor. The natural fringe field near the axis of an ideal eight-fold toroid scales like r^7 [137], and was not strong enough to cause the observed steering unless the beam was many centimeters away from the axis for most of the length of the toroid. However, a radial shift of one coil by 3 mm generates a large enough residual field on the axis to steer the beam as observed. The effect of the QTor fringe field (4250 Gauss-cm) along the beam axis was simulated using OptiM [138]. The simulation conditions were as follows:

- QTor and dump viewer in the OptiM model were added to the Q-weak main input deck [112] for this analysis.

- No microscopic model of the QTor field symmetry breaking was used. The QTor region was treated as a 4 m long dipole with a 4250 Gauss-cm field integral.
- Earth's magnetic field was ignored in the simulation.

A beam steering of ∼2 cm at the beam dump viewer due to QTor fringe field (4250 Gauss-cm) was observed in the simulation for the primary electron beam (1.2 GeV) and confirmed the earlier observation. The effect of the fringe field on lower energy electrons was much higher, and the simulated tracks are shown in Figure 5.10 [139].

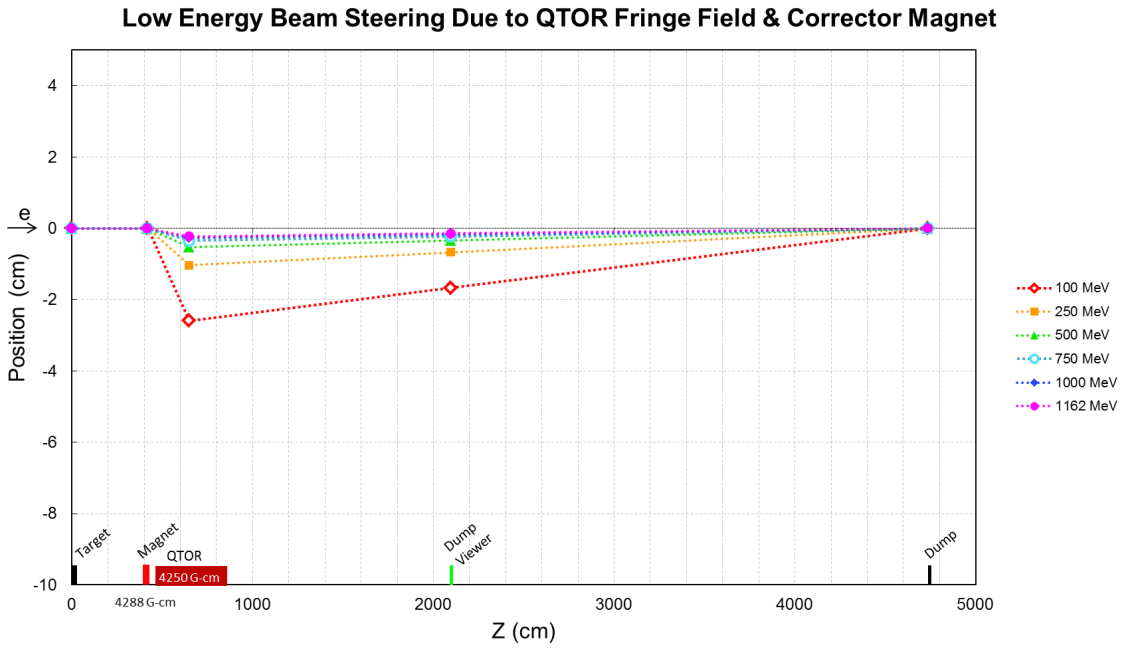

Figure 5.12 The simulated tracks of the primary and low energy electrons, after inserting a corrector magnet in front of the QTor with a magnetic field of 4000 Gauss-cm in the simulation, are also shown here. The corrector magnet focuses electron tracks on the dump by correcting the fringe field (4250 Gauss-cm) in QTor.

5.3.1 QTOR Corrector Magnet

The next step was to design a corrector magnet that could suppress the fringe field in the QTor and fit into existing beamline structure. The ideal location for the corrector magnet was simulated to be in front of the QTor [140]. The estimated magnet field strength for the corrector magnet, placed before QTor, to compensate beam steering due to the QTor fringe field was ∼4000 Gauss-cm. The effect of the corrector magnet on the QTor fringe field is shown in Figure 5.12. Besides containing the

primary electrons, the corrector magnet also helped in suppressing the lower energy electrons [141]. The corrector magnet had a bedstead structure and was designed using TOSCA [142, 143] (see Figure 5.13).

Table 5.2 The design parameters for the QTor corrector magnet.

Parameters	Inner	Outer
X-radius [cm]	14.0	28.0
Y-radius [cm]	20.0	32.0
Z-length [cm]	8.0	10.0
Cross section [cm^2]	2.5×4.0	2.5×2.5
Current [A]	2600	-1000
No. of turns	240	150
Length per turn [cm]	132.48	240.96
Current per turn [A]	10.84	6.67
Resistance [Ω]	1.15	1.30
Total length [cm]	34947	39727
Mass [kg]	11.87	13.49
Power [W]	149.56	64.38
Voltage drop [V]	13.79	9.65
Temperature rise [K/s]	3.23×10^{-2}	1.22×10^{-2}

The design parameters for the QTor corrector magnet are summarized in Table 5.2. There were some constraints designing the corrector magnet as follows:

- The space available for the corrector magnet was 25.4 cm along Z-direction.
- The lower edge of the collimator opening was ∼40 cm from the center of the beam pipe.
- The beam pipe diameter inside QTor was 27.4 cm.
- The corrector magnet had to be non-magnetic material to reduce EM interference.

The corrector magnet was designed to fit in the available space in front of the QTor and was capable of producing the desired field to counter steer the QTor fringe field. The power dissipation, voltage drop, temperature rise, and other important parameters associated to the coils were calculated and showed promising behavior (more details in [144]). The corrector magnet sensitivity to position and angle changes in space was simulated using TOSCA by moving each coil individually in all possible orientations. The simulation yields the magnet to be mostly insensitive to the position and angle changes (more details in [145]).

The field integral produced by the corrector magnet is shown in Figure 5.14. The Figure 5.14 also shows the field along X and Y direction at the collimator opening. The variation of magnetic field along the different octants has also been studied [146] (see Figure B.6, APPENDIX B). The

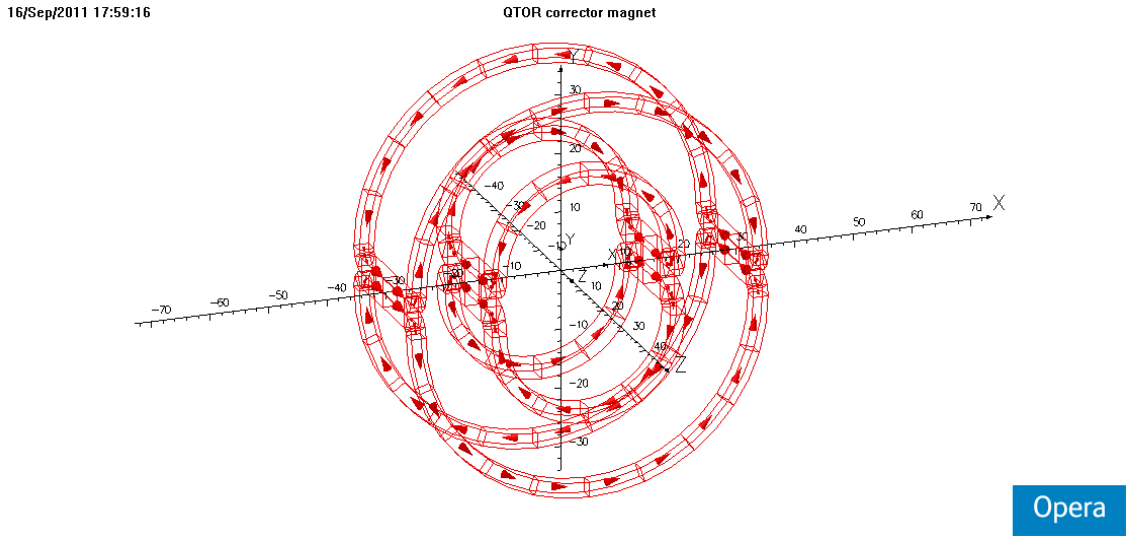

Figure 5.13 A 3-dimensional view of the QTOR corrector magnet design is shown here. The radius of the inner coil is half of the outer coil radius. The two coils carry currents in opposite direction (the direction of the current is shown by the arrows).

field seems to decay very fast along the radial direction. The summary of the magnet design can be found in [147]. As the hardware in the beam dump region was improved, it was decided not to build the corrector magnet in order to adhere to the schedule.

5.4 BPM Resolution

The BPMs in front of the target e.g; 3H09B, 3H09, 3H07C, 3H07B, and 3H07A were used for the linear regression as well as for the calculation of the virtual target BPM. Hence, it was important to know their position and angle resolutions. The BPM position resolution was extracted from the collected production data and the angle resolution was simulated using the relation between the position and the angle resolution at a fixed beam current.

5.4.1 Position Resolution

The target BPM is a virtual BPM calculated using five BPMs in the drift region (more details on virtual target BPM in section 3.6.1 and [19]). The position resolution of the BPM in front of the target was extracted by observing the residual of beam position differences (between two helicity states) on any BPM and the orbit projected from the target. This is expressed in Equation 5.4.1 (see cartoon diagram in Figure 5.16).

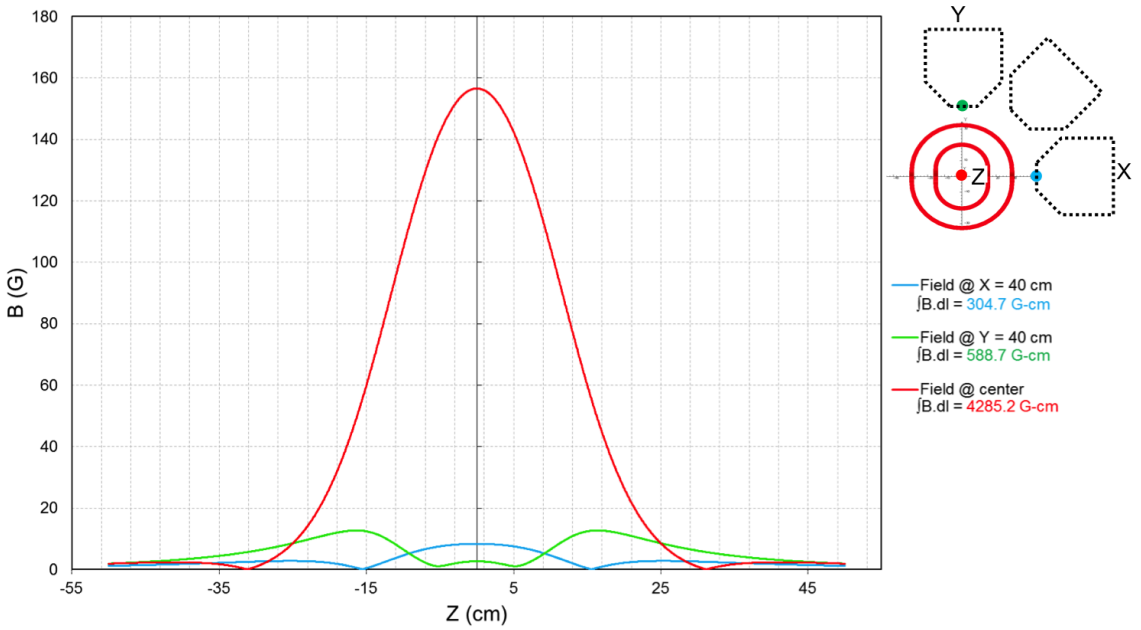

Figure 5.14 The field integral of the QTOR corrector magnet along the X, Y, and Z axes are shown in blue, green, and red, respectively. The filed along the Z axis was measured along the center of the magnet, whereas the filed along X and Y axes were measured at collimator openings (40 cm away from the center).

$$\begin{aligned} \text{BPM resolution} \approx \sigma_{Residual} &= diff_{BPM} - \text{Orbit Position Differences} \\ \text{Orbit Position Differences} &= (Z_{BPM} - Z_{Tgt}) diff_{TgtSlope} + diff_{Tgt} \end{aligned} \tag{5.4.1}$$

Here $diff_{BPM}$ represents the beam position differences between two helicity states, $diff_{Tgt}$ represents the target position differences, $diff_{TgtSlope}$ represents the target slope differences, Z_{BPM} is the location of the BPM in the beamline, and Z_{Tgt} is the location of the target.

The average BPM resolution using selective data samples from the commissioning phase of the experiment (Wien 0) is found to be 0.70 and 0.77 μm for X and Y, respectively at a fixed beam current of 145 μA. The position resolutions for all the BPMs in front of the target were stable during Wien 0 at fixed current and are summarized in Table 5.3. Y resolutions were quite similar to the X resolutions. An independent study of BPM 3H07B resolution by B. Waidyawansa [148] has shown that the resolutions of 0.945 $\pm$ 0.003, and 1.060 $\pm$ 0.003 for X and Y, respectively at beam current 150 μA and roughly agrees with this result. The BPM 3H09B had relatively good resolution but was not available during Run 2. The resolution for BPM 3H04 was poor, as shown in Figure 5.15

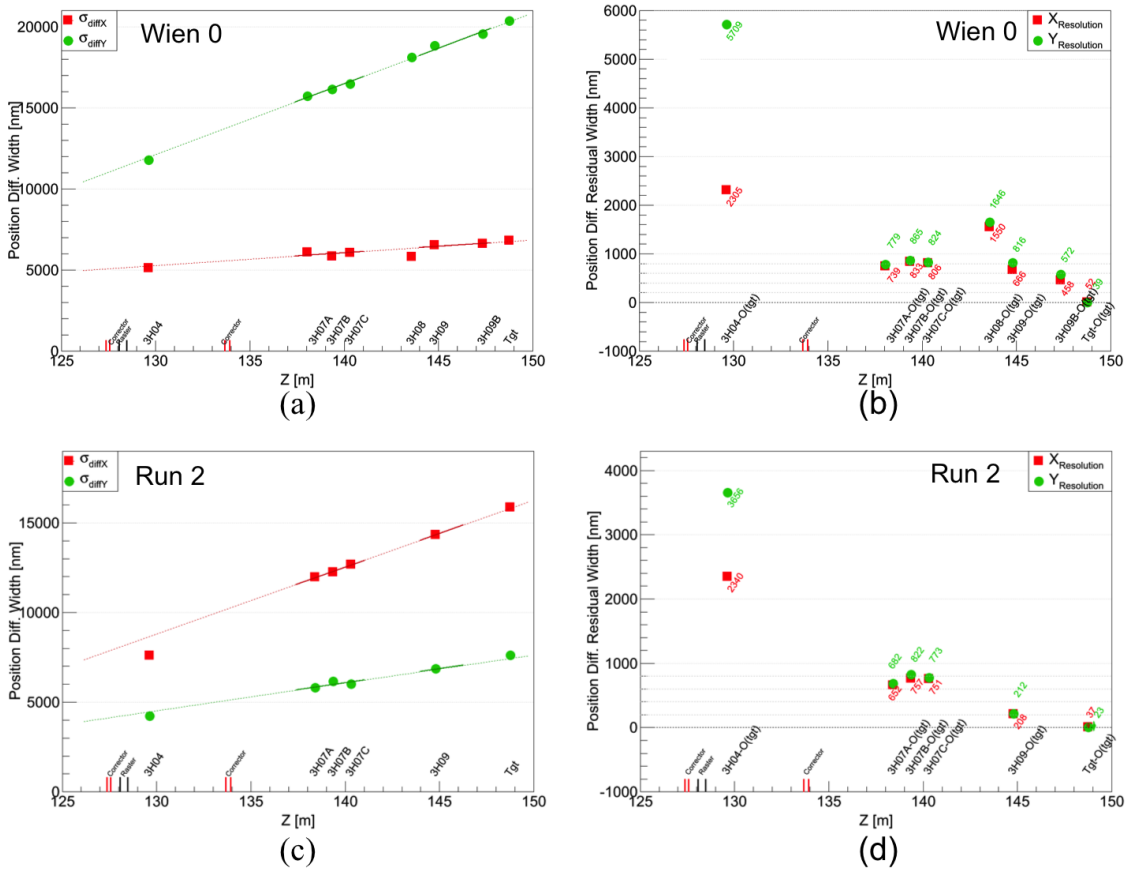

Figure 5.15 BPM position resolution. (a) Beam position differences for a typical one hour production run during Wien 0 at beam current of 145 μA. Error weighted pol1 fits are shown by solid lines. BPM 3H04, 08 and, Tgt are not included in the fit. Fit is extrapolated using dashed line to guide the view. (b) Extracted BPM resolutions using (a) are shown for Wien 0 at beam current of 145 μA. (c) and (d) show beam position differences and BPM resolution, respectively for Run 2 at beam current of 180 μA.

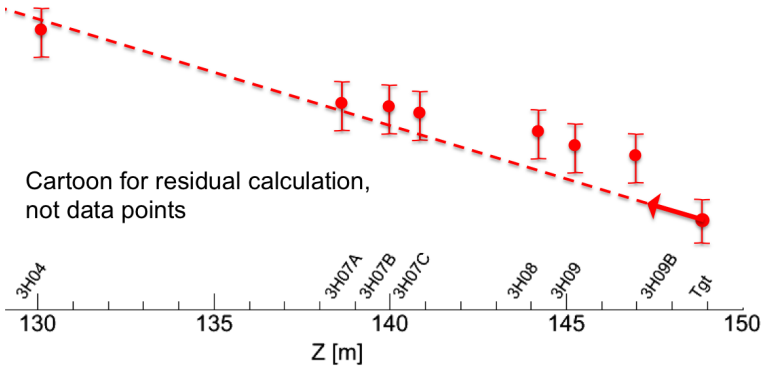

Figure 5.16 BPM resolution cartoon.

(b). This inconsistency might be due to the noise injected by the existing corrector magnets between the BPM 3H04 and 3H07A. The BPM 3H08 had a different hardware compared to the other BPMs. Hence, the BPM 3H04 and 3H08 were not included for the construction of the virtual target BPM. The same analysis was repeated for Run 2 with a beam current of 180 μA, as shown in Figure 5.15 (c) and (d). The BPM resolution improves with the increase in beam current. A study of the BPM resolution variation with beam current can be found in [148].

Table 5.3 BPM position resolution at beam current of 145 μA.

BPM	X Resolution [μm]	Y Resolution [μm]
3H09B	0.46	0.57
3H09	0.67	0.81
3H07C	0.81	0.83
3H07B	0.83	0.87
3H07A	0.74	0.78
3H04	1.70	3.55
Average (3H04 excluded)	0.70	0.77

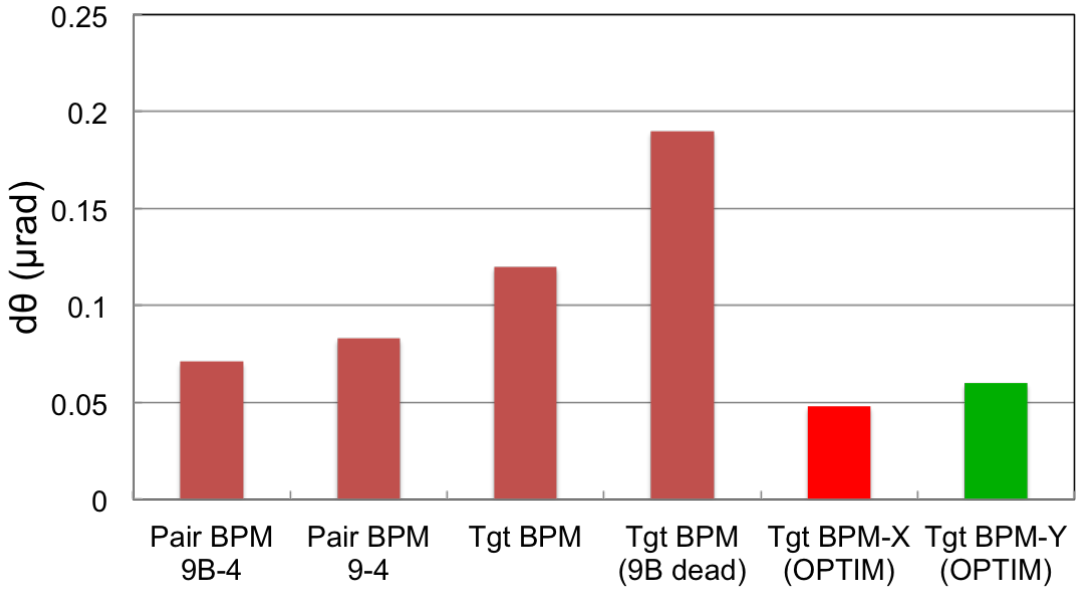

Figure 5.17 Target BPM angle resolution at beam current of 180 μA.

5.4.2 Target BPM Angle Resolution

The target BPM angle resolution was simulated using OptiM [82]. In order to estimate the target BPM angle resolution, a relatively pure position measurement which corresponds to a pure angle

measurement at the target was needed. A study of the strength sharing between angle and position in the various BPMs along the beamline for Wien 0 shows that the Compton BPMs (3P02A and B) were insensitive to the position at the target [149]. Then the known BPM position resolution and the transport matrices between the Compton BPMs and the target BPMs were used to estimate effective angle resolution. Assuming the X(Y) position resolution to be 0.90 (0.96) μm, the estimated target BPM X (Y) angle resolution at a fixed beam current of 180 μA is 0.048 (0.060) μrad. A simple model calculation, where the angle jitter at the target corresponds to a pure position at BPM 3P02A (without using the transport matrix), agrees with this simulation. The simulated target BPM resolution in this analysis is better than the existing calculation with other BPMs [150]. A comparison of the resolution using different BPM pairs is shown in Figure 5.17.

5.4.3 Consistency Check of the Target Variable

The most commonly used independent variables for the linear regression were target positions and angles. So it was important to check the consistency of the target variable since it was created using 5 BPMs in the drift region in the beamline over a span of 10 m upstream of the target (more details about target variable can be found in section 3.6.1 and in [19, 75]). In order to check the consistency of the variable, the BPM differences used for the calculation were projected back to the target. A schematic diagram is shown in Figure 5.16. The beam position differences and the BPM residuals from the projected orbit are shown in the Figure 5.18. The target BPM was consistent, but the target intercept in the Q-weak database sometimes was significantly inconsistent and made χ^2/DOF of the fit worse. As in the regression or any of the Q-weak calculations, the intercept was not used, hence this inconsistency in the intercept did not make any impact on the physics result. A linear fit of the BPMs in front goes through the target BPM within 0.03 nm. The X position differences uncertainties are usually underestimated; this is necessary to assign the uncertainties in the regression. The BPM 3H04 effectively has the wrong units in the analysis software and a scale factor of 0.75 can eliminate this inconsistency. It is not very clear yet how big a problem this is for regression, since 3H04 was used in few regression schemes. The beam jitter was stable and Y jitter was larger than X jitter during Wien 0, but X jitter became larger than Y during Run 2.

5.5 Helicity Correlated Pedestal Analysis

The Q-weak collaboration proposed to measure the small parity violating asymmetry ($\sim$250 ppb) in elastic electron-proton scattering precisely [16]. The goal of the collaboration is to reduce any false

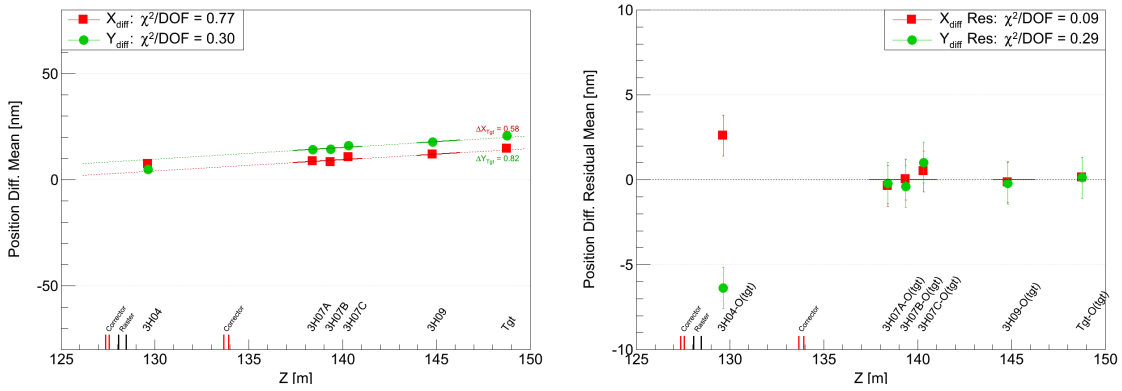

Figure 5.18 Target BPM consistency check. Beam position differences for a typical one hour production run during Run 2 at beam current of 180 μA are shown in (a). Error weighted pol1 fits are shown by solid lines. BPM 3H04, 3H08 and, Tgt are not in the fit. Fit is extrapolated using dashed line to guide the view. The residual of the BPM position differences and extrapolated orbit from target are shown in (b).

asymmetry from various sources. One such potential source is helicity correlated pedestal differences for different detectors. The beam off detector yields at nominal operation and settings are known as pedestals of that detector. Pedestal can be determined by the preamplifier offset and backgrounds with beam off data.

5.5.1 Motivation

A helicity correlated pedestal difference is a detector pedestal that is consistently different between the two helicity states. Any non-zero helicity correlated pedestal differences can cause false asymmetries in the measured parity violating asymmetry. The stability of the detector pedestal in the current mode (Y_{ped}) is directly related to the detector yield determination and can affect the detector linearity and asymmetry calculation. Helicity correlated pedestal differences could occur in many possible ways. One such process can be leakage from the Pockels cell's high voltage which can change the polarization of the laser light that produces electrons from the photocathode. Main detectors, luminosity monitors and beam charge monitors need to be isolated from this Pockels cell voltage flip in order to suppress helicity correlated pedestals. A small mV level leakage can create a huge false asymmetry (as shown in Equation 5.5.2), making this the primary motivation to monitor helicity correlated pedestal differences throughout the experiment.

5.5.2 Analysis Procedure and Goal

Typically, 5 minutes of dedicated beam off pedestal runs were taken during production running once a day during Run 1 and once every eight hours during Run 2. There were also ∼1 hour long beam off pedestal runs taken throughout, whenever there was an opportunity (for details see section D.1, APPENDIX C). The purpose of these pedestal runs was to minimize nonlinear distortions of asymmetries due to incorrect pedestals in the main detectors in the DC regime and estimate false asymmetry due to leakage current [3, 151]. The goal of this analysis is to survey the helicity correlated pedestal differences and raw pedestal signal for the entire experiment. The mean of the helicity correlated pedestal differences distribution gives an idea about the scale of false asymmetries and its width conveys a sense about the electronic chain noise level. Studying raw pedestal signals also helps to estimate the detector non-linearity due to wrong pedestals and the rms width of the raw signal provides an impression about the detector resolution.

5.5.3 Experimental Method

For a quartet of "+ - - +", measured asymmetry can be expressed as

$$A_M(+--+) = \frac{S_1^+ - S_2^- - S_3^- + S_4^+}{(S_1^+ - P) + (S_2^- - P) + (S_3^- - P) + (S_4^+ - P)}, \tag{5.5.1}$$

where S's are the detector signals and P is the detector pedestal. A typical beam ON detector signal size was ∼6 V. In order to estimate false asymmetry due to helicity correlated differences, consider a 0.01 μV voltage difference between + and - helicity states for the nominal detector signal. Then a false asymmetry due to this voltage difference can be calculated as

$$\frac{0.01 \times 10^{-6}\ V}{6\ V} = 1.7 \times 10^{-9} = 1.7 \text{ ppb}. \tag{5.5.2}$$

The magnitude of the expected measured asymmetry for the Q-weak experiment is ∼250 ppb. From the example in Equation 5.5.2, the false asymmetry can be 0.7%. To sense the effect of a wrong raw pedestal signal, consider a typical 120 mV pedestal error in a 6 V signal as an example. Then the potential non-linearity due to this error in the detector can be written as

$$\frac{120 \times 10^{-3}\ V}{6\ V} = 2\%. \tag{5.5.3}$$

As shown in the above examples, a small leakage in the Pockels cell's high voltage and wrong pedestal measurement can create significant false asymmetries in the measured asymmetry and non-

linearity in the detector signals. So it was important to survey helicity correlated pedestal difference for the important detectors that can impact the Q-weak measured asymmetry.

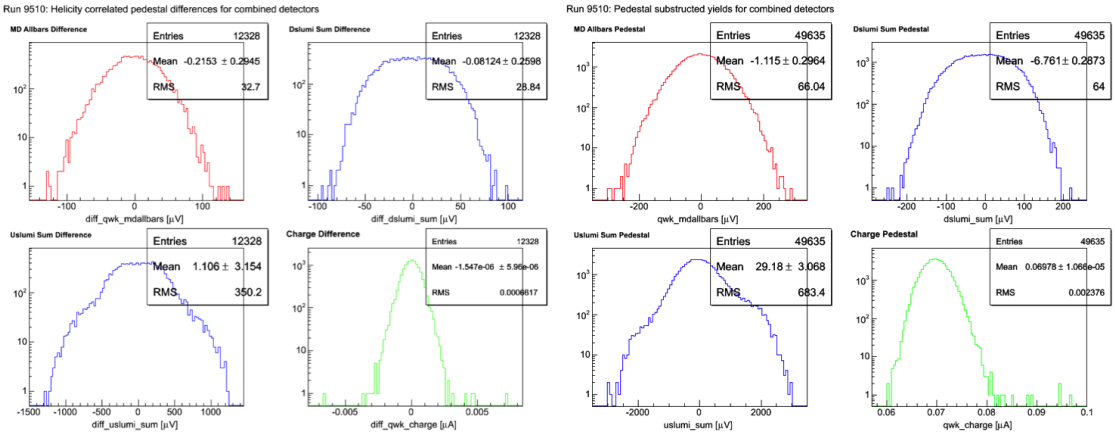

Figure 5.19 A typical beam off pedestal run (run# 9510). Helicity correlated differences for MDAllbars, DSLumiSum, USLumiSum, Charge (clockwise from top left corner) from Hel_Tree are shown in the left panel. Pedestal subtracted signal for MDAllbars, DSLumiSum, USLumiSum, Charge (clockwise from top left corner) from Mps_Tree are shown in the right panel.

5.5.4 Results

The main detectors and luminosity monitors are normalized to the charge monitors so it is important that neither have any evidence of helicity correlated pedestal differences. Helicity correlated differences from Hel_Tree of a typical 5 minutes pedestal run are shown in Figure 5.19. Even with only 5 minutes of data, no evidence of any helicity correlated pick ups for combined Čerenkov main detector (MDAllbars), downstream luminosity monitor (DSLumiSum), upstream luminosity monitor (USLumiSum), and beam charge monitor (Charge) were seen. The channels surveyed during this analysis are 17 MDs, 9 DSLumis, 9 USLumis, and 9 BCMs (details of the variables are described in APPENDIX C, section C.1.4). The individual channels of the MDs, DSLumis, USLumis, and BCMs showed no significant pickup. All these channels were investigated individually for each run and then averaged (error weighted) over a Wien[2]. The Wien averaged helicity correlated differences for most important channels for the experiment MDAllbars, DSLumiSum, USLumiSum, and Charge[3] are shown in Figure 5.20.

[2]Experiment has total 11 Wien period. Double Wien filters were rotated to change the electron beam polarization. This help reducing the false asymmetry.

[3]Charge = bcm1 + bcm2 for Run 1 and = bcm8 for Run 2.

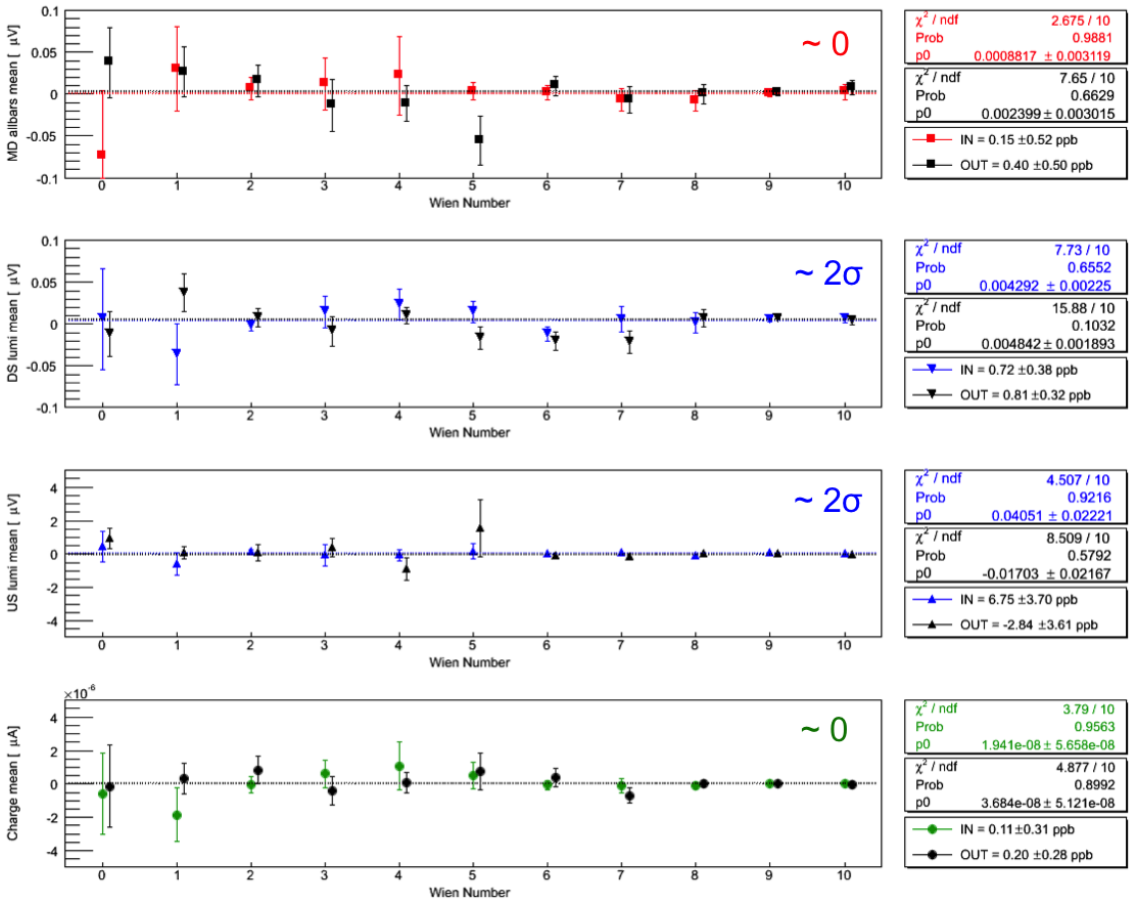

Figure 5.20 The mean of the pedestal differences from Hel_Tree for MD allbars, DS lumi, US lumi and Charge are shown. Each data point is averaged over a Wien. Two half wave plate states are shown separately.

5.5.4.1 Helicity Correlated Pedestal Signal Pickup

The mean of the pedestal differences from Hel_Tree in Figure 5.19 represent the helicity correlated pickup by a device. The surveyed result shows that the average pickup for MD is 0.15 ± 0.52 ppb for insertable half wave plate (IHWP) IN, and 0.40 ± 0.50 ppb for IHWP OUT (shown in Figure 5.20 by colored and black data points, respectively). So helicity correlated pedestal differences have negligible contribution (∼0.2%) to any false asymmetries in the measured asymmetry. DS Lumi has a similar level of pickup as the MD. US Lumi shows ∼7 ppb pickup in worst case scenario which can be improved by using a better pedestal subtraction. BCMs have no pickups for the whole experiment. Overall pickup was much smaller during Run 2 (Wien 6 - 10) compared to Run 1 (Wien 0 - 5), and Run-0 (Wien 0).

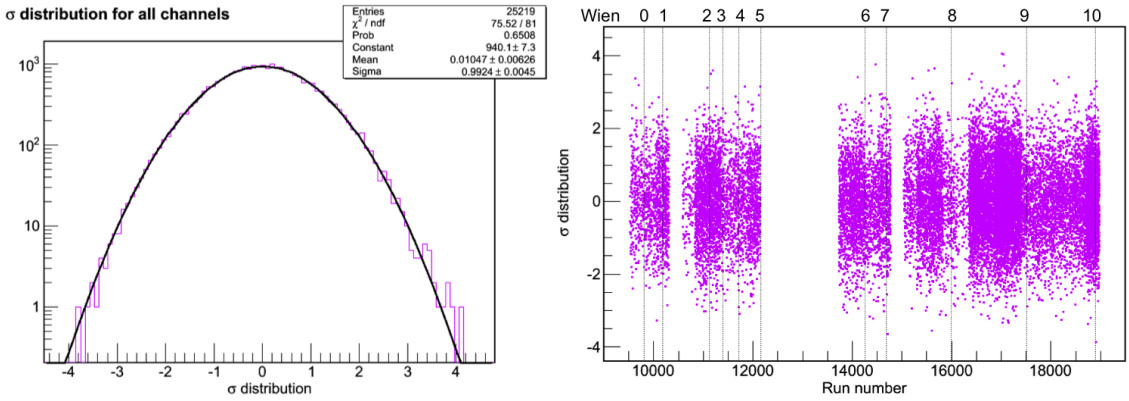

Figure 5.21 The pull distribution of helicity correlated pedestal differences for all channels and Wien (left). The data are from the pedestal runs taken during the Q-weak experiment. The black curve in the pull distribution plot is the Gaussian fit. The ostensibly non-zero mean is probably statistical and corresponds to roughly 0.1 ± 0.06 ppb. The pull of helicity correlated pedestal differences vs run number for all the channels are shown (right). The vertical dotted lines represent the Wien periods.

A pull variable helps to evaluate data points that pull the mean of the distribution and can be defined as

$$\sigma(ped)_{i,j,k} = \frac{< P >_{i,j,k}}{error_{i,j,k}} \tag{5.5.4}$$

where $< P >$ is the mean helicity correlated pedestal difference and the indices i,j,k denote channel number, run number and IHWP state, respectively. The distribution of $\sigma(ped)_{i,j,k}$ for each channel and run is shown in Figure 5.21. The distribution of $\sigma(ped)_{i,j,k}$ is Gaussian and the mean is zero for each channel and run. The few σ from zero pickup for different detectors are within the statistical fluctuation. Mean of the helicity correlated differences for important background detectors (MD9, PMT only, PMT lightguide) were zero within $\sim 1\sigma$ for each Wien whereas for other background detectors pickups were zero within $\sim 3\sigma$. Several channels were examined in many pedestal runs, hence it was not unexpected to find a few channels that were non-zero by 3-4σ off the mean.

5.5.4.2 Helicity Correlated Pedestal Sensitivities

The helicity correlated pedestal difference width from Hel_Tree represents the sensitivity of a device to the helicity. It also depicts the measure of the electronic noise level for the detectors with low frequency rejection. The Wien averaged helicity correlated differences width for MDAll-bars, DSLumiSum, USLumiSum, and Charge are shown in Figure 5.22. The average noise level of

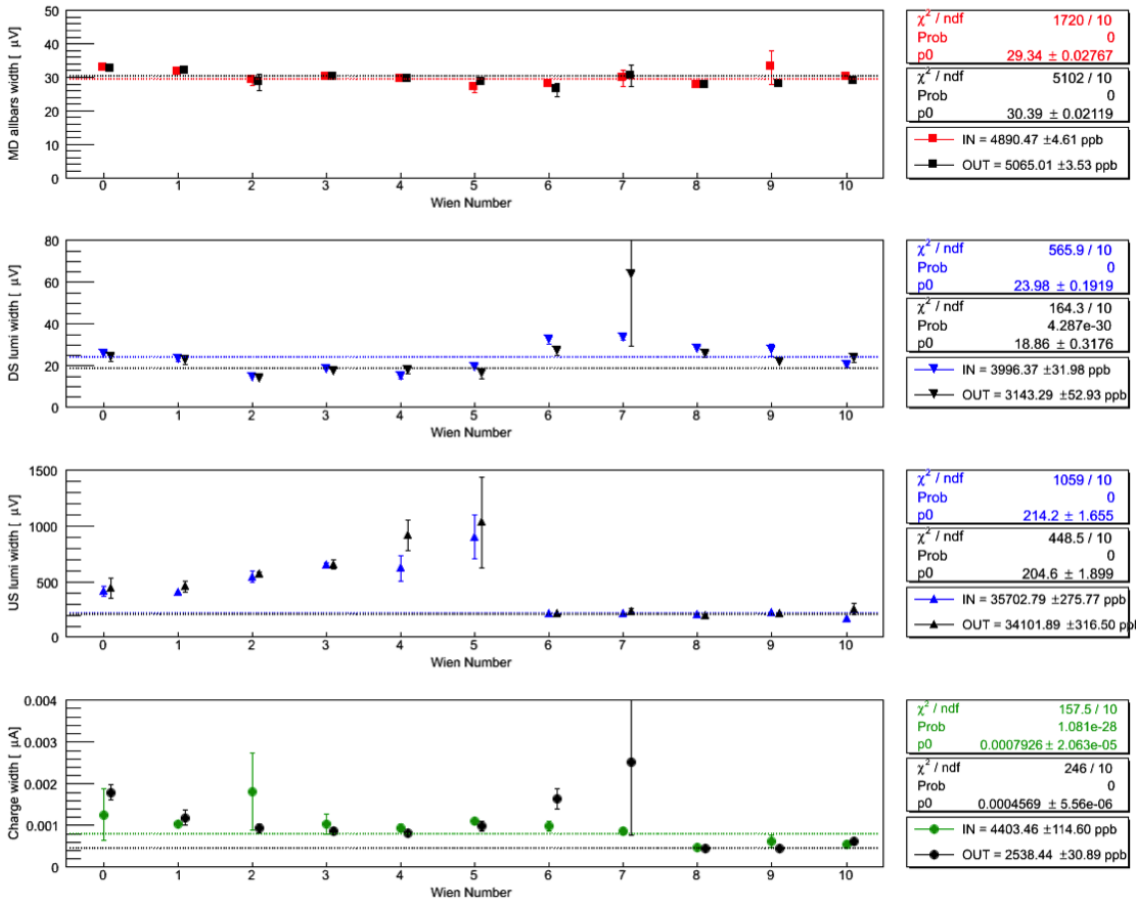

Figure 5.22 The width of the pedestal differences from Hel_Tree for MDAllbars, DSLumiSum, USLumiSum and Charge are shown.

MDAllbars was 25 μV. The MDs and the DSLumis noise levels were acceptable and well behaved throughout the experiment. USLumi electronic noise could have limited the detector's resolution near the end of Run 1, but improved in Run 2 after hardware repairs. Background detectors noise levels were reasonably stable during the experiment.

5.5.4.3 Stability of Pedestal Subtracted Signal

The mean of pedestal subtracted signal from Mps_Tree represent the relative change in pedestal signal compared to last pedestal. A wrong pedestal for a detector can cause nonlinearity in the detector system. MD pedestal was good to less than a mV (Figure 5.23). This results a nonlinearity of $\ll 0.1\%$ for 6 V signals. The detector yields are smaller for Aluminum and N$\rightarrow \Delta$ running compared to normal production running. The signal sizes are $\sim$30-40% of 6 V. So the nonlinearity for these cases are higher but still $< 1\%$, allowing for smaller yields. DSLumi pedestal was off by at

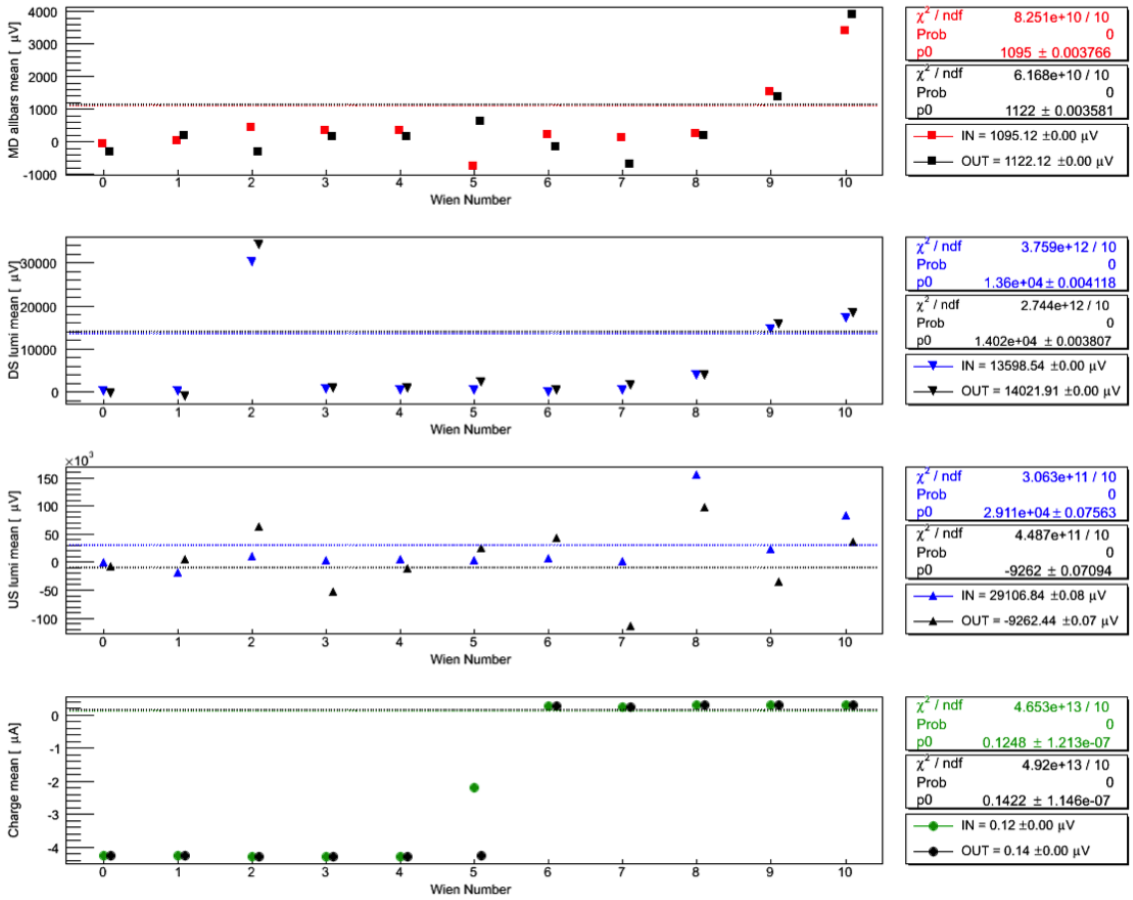

Figure 5.23 The mean of pedestal subtracted signal from Mps_Tree for MDAllbars, DSLumiSum, USLumiSum and Charge are shown.

most 34 mV. The resulting nonlinearity would be $< 1\%$ assuming 6 V signals. To support Aluminum and N$\rightarrow \Delta$ running, pedestal subtraction should be improved in Wiens 2, 9, 10. USLumi pedestal was off by 100-150 mV in Wiens 7, 8 and could result a nonlinearity of several percent.

5.5.4.4 Detector Resolution

The width of pedestal subtracted signal from Mps_Tree describes the measure of detector resolution. Resolutions for MDs and DSLumis were very good ($\sim$70 μV) and reasonably stable during the experiment (see Figure 5.24). USLumis resolutions were $\sim$15 times worse than MDs and DSLumis but were very stable. The resolutions for charge monitors and background detectors (except PMT LED) were steady throughout the experiment.

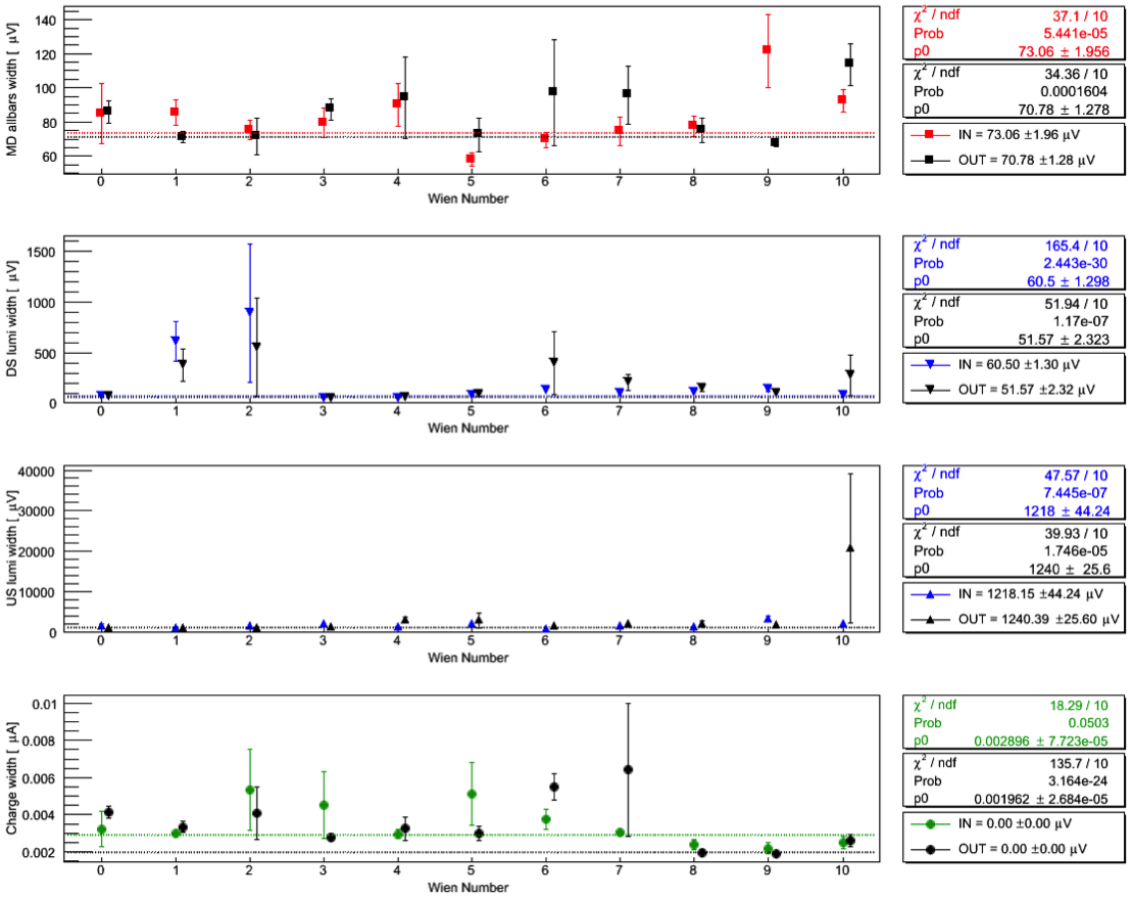

Figure 5.24 The widths of pedestal subtracted signal from Mps_Tree for MDAllbars, DSLumiSum, USLumiSum and Charge are shown.

5.5.5 Summary of Helicity Correlated Pedestal Survey

No helicity correlated pickups were seen for most of the detector channels for the entire experiment and were at $\mathcal{O}(1)$ ppb. Electronic noise levels were generally acceptable, though potentially marginal, for the USLumi channels near the end of Run 1 but improved during Run 2. The nonlinearities due to pedestal errors for MDs were extremely small. USLumi also had a nonlinearity of few percent. There is a scope for improvement in USLumi pedestal. The nonlinearity could be very large for low-yield production running on Aluminum and N$\rightarrow \Delta$ but still be under 1%. Resolutions for all the detectors were reasonably stable. The helicity correlated pedestal survey results are summarized in Table 5.4.

Table 5.4 Summary of helicity correlated pedestal survey.

Channels	False Asymmetry [ppb]	Sensitivity	Nonlinearity [%]	Electronic Noise
MDAllbars	0.4	30 μV	$\ll$0.1	73 μV
DSLumiSum	0.8	24 μV	$<$1.0	61 μV
USLumiSum	6.8	214 μV	$\sim$1.0	1240 μV
Charge	0.2	0.0079 μA	$<$0.1	0.0029 μA

SECTION 6

BEAM NORMAL SINGLE SPIN ASYMMETRY

6.1 Introduction

Dedicated measurements of the beam normal single spin asymmetry in inelastic electron-proton, and electron-nucleus scattering near missing mass, W, ∼1.2 GeV were performed during 18 - 20 February 2012 at Hall-C of Jefferson Lab using Q-weak apparatus. The Q-weak longitudinal measurement setup [16] was used for an inelastic transverse measurement. The electron beam polarization was changed from the nominal longitudinal setup to produce fully horizontal/ vertical polarization using the double Wien filter at the injector (section 3.3.1). The torodial magnet setting was lowered to 6700 A to focus inelastically scattered electrons onto the main Čerenkov detectors.

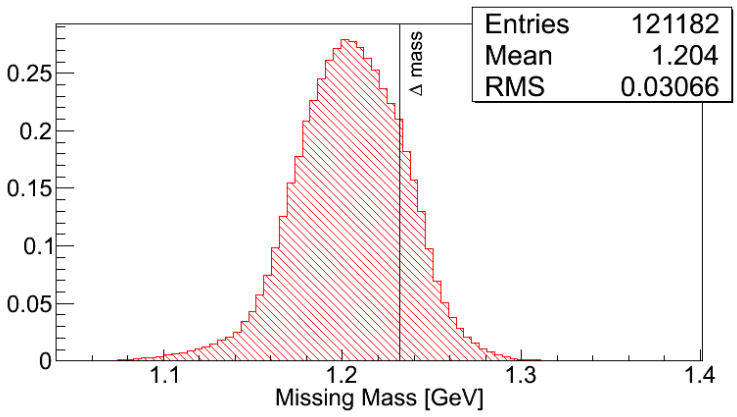

Figure 6.1 Simulated missing mass, W, distribution at the inelastic QTor setting.

6.2 Available Data Set and Conditions of Experimental Data Taking

The total collected data after hardware and software quality cuts is shown in Table 6.1. The QTor current of 6700 A selects the inelastic events near W ∼1.2 GeV (Figure 6.1). Data on both sides of the inelastic peak (6000 A and 7300 A) were taken to better constrain the elastic dilution. Two transverse spin orientations, horizontal and vertical, were used. Data were collected on a liquid hydrogen (LH_2) cell, 4% thick downstream aluminum alloy (Al), and a 1.6% thick downstream carbon foil (^{12}C) with 1.155 GeV beam for both spin orientations. Different beam currents were used on different targets (see Table 6.1). The beam was rastered on the target over an area of

4 mm×4 mm by the fast raster system to minimize the target boiling or damage. The Insertable Half Wave Plate (IHWP) was used to help suppress helicity correlated beam asymmetries and was reversed at intervals of about 2 hours. More information about the conditions of data taking is given in APPENDIX-D section D.1.

Table 6.1 The transverse N→ Δ data set. The runs with vertical transverse polarization are in parentheses, the rest are from horizontal transverse polarization. Data collected in an hour was defined as run. The beam currents are shown in second to last row. Total charge on target in Coulombs is shown in the bottom row.

IHWP	QTor current					
	6000 A	6700 A			7300 A	
	$LH_2^{\dagger}$	$LH_2^{\dagger}$	$Al^{\dagger\dagger}$	^{12}C	$LH_2^{\dagger}$	$Al^{\dagger\dagger}$
IN	16152 16153	(16066) 16131 16132	(16067) 16115 16116	16150 16151	16133 16134 16135	16122 16123 16124 16160
OUT	16154 16156 16157 16158	(16065) 16129 16130	(16068) (16069) 16117 16118 16119	16148 16149	16136 16137	16120 16121 16161
Beam current I [μA]	180	180	60	75	180	60
Collected Data [C]	1.5	1.8 (1.9)	0.8 (0.4)	0.6	2.0	0.9

In this dissertation, a full analysis of the beam normal single spin asymmetry from inelastic electron-proton scattering on LH_2 target, indicated by † in Table 6.1, will be discussed. The transverse asymmetry on Al target, indicated by †† in the table, was also analyzed as a background correction for the LH_2 target. The analysis of the remaining data are ongoing and will not be covered in this dissertation.

6.3 Extraction of Raw Asymmetries

A single detector asymmetry was obtained by averaging the two PMT asymmetries from each Čerenkov detector. The error weighted average of the asymmetries from runlets, ∼5 minute long data samples, was extracted for a given data set. To extract the raw asymmetry $A_{\rm raw}$ from the detectors, the average asymmetry for the two different Insertable Half Wave Plate (IHWP) settings, IN and OUT, were determined separately for each main detector bar. The asymmetries measured in the IHWP configurations were sign corrected for the extra spin flip and averaged together after checking for the IHWP cancellation of the false asymmetries. The error weighted value of <IN,-OUT>

determined the measured raw asymmetry for each bar. These raw asymmetries were then plotted against the detector octant number, which represents the location of the detector in the azimuthal plane (ϕ = (octant - 1)×45°), and they were fitted using a function of the form in Equation 6.3.1. This analysis will focus on the azimuthal dependence of the detector asymmetries representing the transverse asymmetries.

$$f(\phi) = \begin{cases} \text{Horizontal transverse: } \epsilon_M^H \sin(\phi + \phi_0^H) + C^H \\ \text{Vertical transverse: } \epsilon_M^V \cos(\phi + \phi_0^V) + C^V. \end{cases} \tag{6.3.1}$$

Here, ϕ is the azimuthal angle in the transverse plane to the beam direction. $\phi = 0$ indicates beam left, ϕ_0 is a possible phase offset expected to be consistent with zero. ϵ_M is the measured asymmetry (amplitude) of the azimuthal modulation generated by BNSSA, and C is a constant appearing for monopole asymmetries such as the parity violating asymmetry generated by residual longitudinal polarization in the beam. The measured un-regressed raw asymmetries for the horizontal and vertical transverse polarization on LH_2 target are $\epsilon_{\text{raw}}^H = 5.34 \pm 0.53$ ppm and $\epsilon_{\text{raw}}^V = 4.60 \pm 0.81$ ppm, respectively.

6.4 Asymmetry Correction using Linear Regression

The helicity correlated changes in the electron beam position, angle, and energy change the yield of the electrons in the detector acceptance. This can create false asymmetries in the detector and needs to be corrected before the extraction of the physics asymmetry. A multi-variable linear regression [152] is used to remove the beam asymmetries from the raw Čerenkov detector asymmetries as shown in Equation 6.4.1.

$$\epsilon_M = \epsilon_{\text{raw}} - \sum_{i=1}^{6} \left(\frac{\partial \epsilon_{\text{raw}}}{\partial T_i} \right) \Delta T_i \tag{6.4.1}$$

Here ϵ_M is the measured asymmetry after regression, and $(\partial \epsilon_{\text{raw}}/\partial T_i)$ is the detector sensitivity to a helicity-correlated beam parameter T_i with helicity-correlated differences ΔT_i. During this measurement period, the helicity-correlated differences were fairly stable except for charge (shown in Figures D.10, and D.11, APPENDIX D) and are summarized in Figure 6.3 and Table 6.2. The detector sensitivity slopes are calculated with linear regression, which uses natural beam motion during a runlet and considers correlations between different beam parameters. The asymmetries presented in this dissertation are regressed against six "5+1" beam parameters (T_i): horizontal position (X),

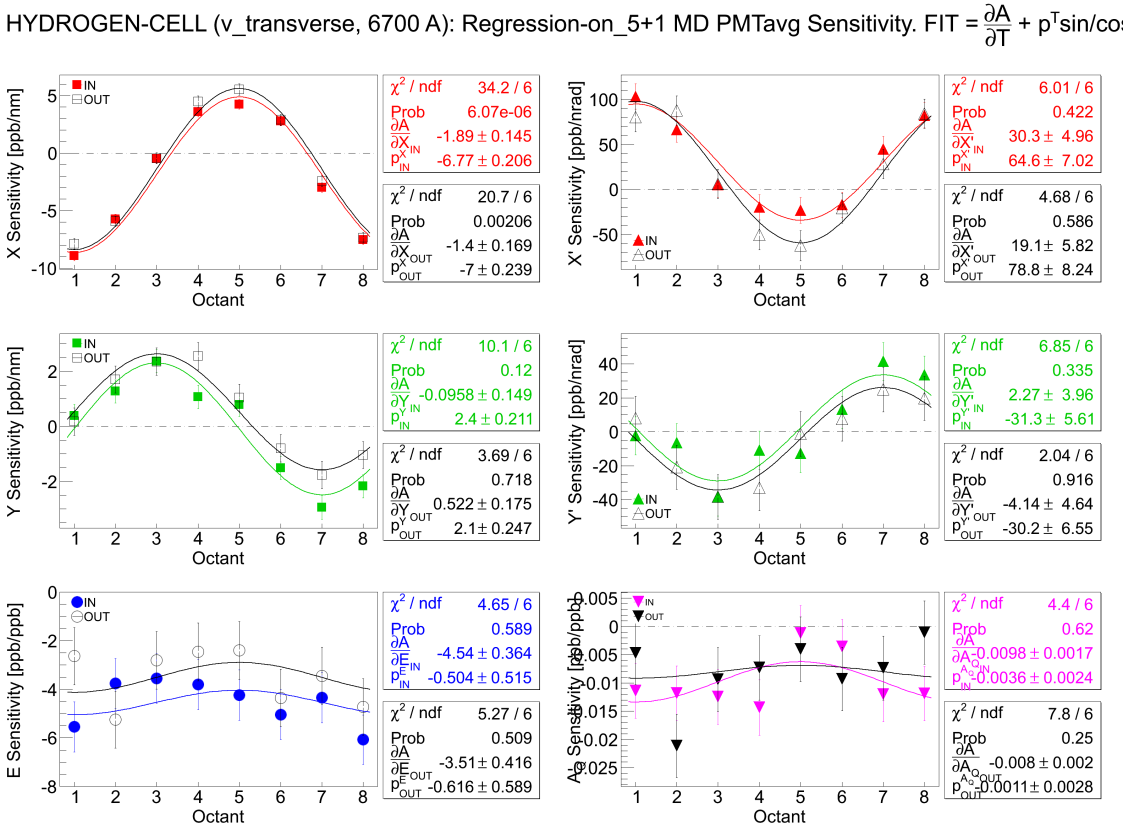

Figure 6.2 Azimuthal dependence of the main detector sensitivities to HCBA for the "5+1" regression scheme in the vertical LH_2 transverse data set are shown here. Sensitivities for beam positions and angles have sinusoidal dependence with octant. No such strong dependence is seen for energy and charge. Two IHWP states are shown separately for each beam parameter. Fit functions used to fit the parameters are shown on the plot. The constant in the fit gives the error weighted average of the sensitivities. See APPENDIX-D, section D.4 for the sensitivities and corrections from full data sets.

horizontal angle (X'), vertical position (Y), vertical angle (Y'), the energy asymmetry (A_E), and the charge asymmetry (A_Q). The sensitivities of the Čerenkov detectors to different helicity correlated beam parameters have azimuthal dependence, as shown in Figure 6.2 (shown for vertical transverse data only, horizontal transverse can be found in Figure D.7). This azimuthal dependence of the position and angle sensitivities are a result of the movement of the scattered electron profile across the octants which changes the effective scattering angle of the detected electrons not specific to the transverse asymmetry measurement. The position and angle sensitivities are anti-correlated. The energy and charge sensitivities are not expected to have a strong azimuthal dependence since they do not change the acceptance. The size of the applied correction to the raw asymmetries depends on the size of the helicity-correlated beam parameter differences ΔT_i and the sensitivities ($\partial\epsilon_{\rm raw}/\partial T_i$).

The size of the corrections were ∼2-3 orders of magnitude smaller than the size of the measured asymmetry and are shown in Figure 6.4 (shown for vertical transverse data only, horizontal transverse can be found in Figure D.8). The total applied regression correction (Figure 6.5) is dominated by the X correction (Figure 6.4 top left). The corrections are summarized in Figure 6.6.

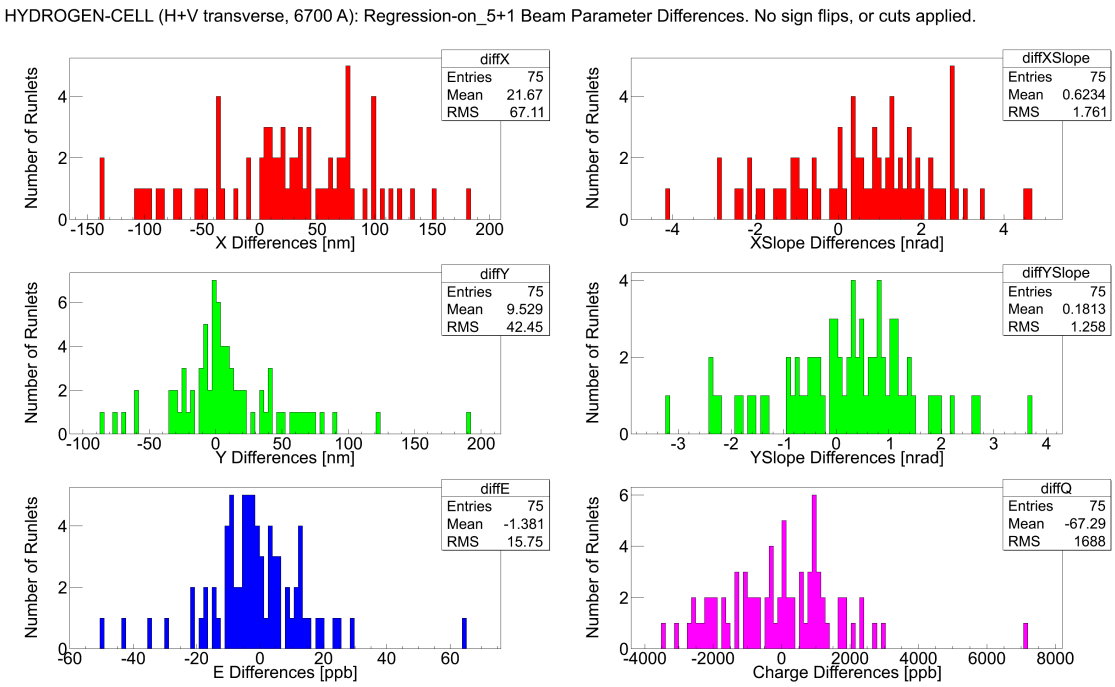

Figure 6.3 Beam parameter differences for the Hydrogen transverse data set.

Table 6.2 Beam parameter differences for the Hydrogen horizontal and vertical transverse data sets. The X differences are higher compared to Y differences.

Beam parameter differences	IHWP IN	IHWP OUT	(<IN>+<OUT>)/2	(<IN>,-<OUT>)
Horizontal Transverse				
ΔX [nm]	23.8 ± 2.1	20.6 ± 2.3	22.2 ± 1.6	3.6 ± 1.6
ΔY [nm]	6.9 ± 2.1	5.6 ± 2.3	6.2 ± 1.6	1.2 ± 1.6
ΔX′ [nrad]	0.7 ± 0.1	0.7 ± 0.1	0.7 ± 0.1	0.1 ± 0.1
ΔY′ [nrad]	0.2 ± 0.1	-0.3 ± 0.1	-0.0 ± 0.1	0.3 ± 0.1
ΔE [ppb]	-2.3 ± 2.1	-1.5 ± 2.3	-1.9 ± 1.6	-0.6 ± 1.6
ΔA_Q [ppb]	8.2 ± 0.5	-237.3 ± 55.6	-114.6 ± 27.8	8.2 ± 0.5
Vertical Transverse				
ΔX [nm]	15.4 ± 3.1	58.0 ± 3.7	36.7 ± 2.4	-15.2 ± 2.4
ΔY [nm]	20.2 ± 3.1	15.4 ± 3.6	17.8 ± 2.4	5.3 ± 2.4
ΔX′ [nrad]	0.6 ± 0.2	1.3 ± 0.2	1.0 ± 0.1	-0.2 ± 0.1
ΔY′ [nrad]	0.6 ± 0.2	0.9 ± 0.2	0.7 ± 0.1	-0.0 ± 0.1
ΔE [ppb]	0.5 ± 3.1	-5.4 ± 3.6	-2.4 ± 2.4	2.6 ± 2.4
ΔA_Q [ppb]	60.1 ± 0.7	158.1 ± 88.1	109.1 ± 44.1	60.1 ± 0.7

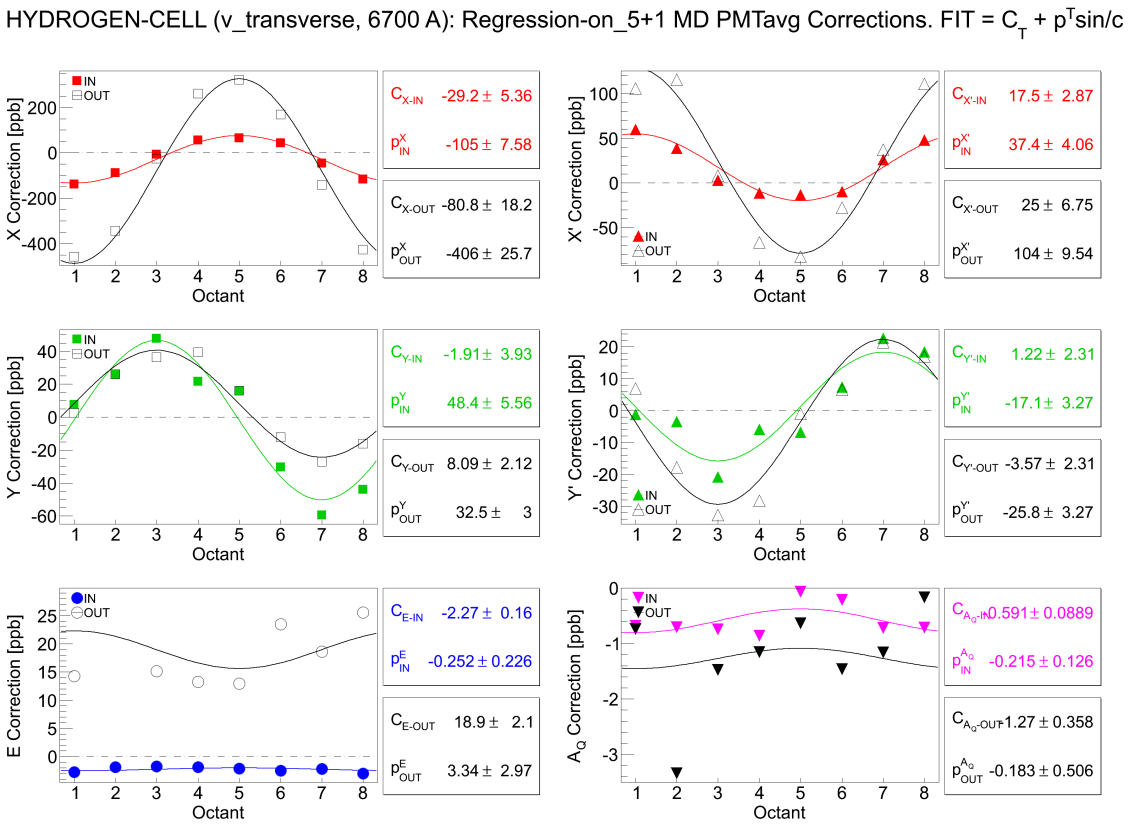

Figure 6.4 Main detector corrections (using sensitivities from "5+1" regression scheme) vs octant for vertical LH_2 transverse data set are shown here. Beam positions and angles have sinusoidal dependence with octant inherited from the sensitivities. No such dependence is seen for energy and charge. Both IHWP states are shown separately for each beam parameter.

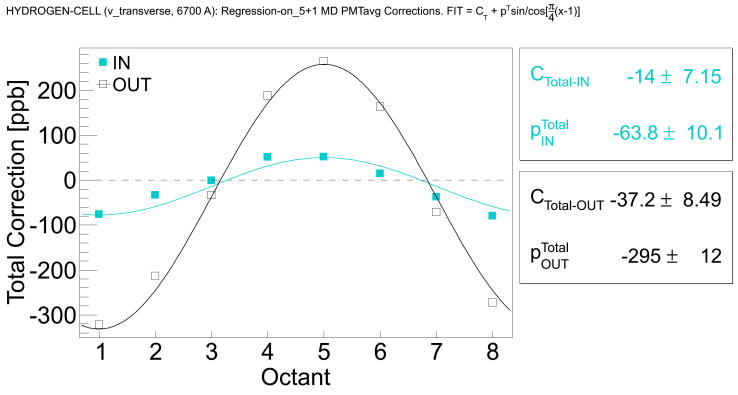

Figure 6.5 Total corrections in "5+1" regression scheme vs octant for vertical LH_2 transverse data set are shown here. The total correction is the sum of all the corrections (with sign) shown in Figure 6.4.

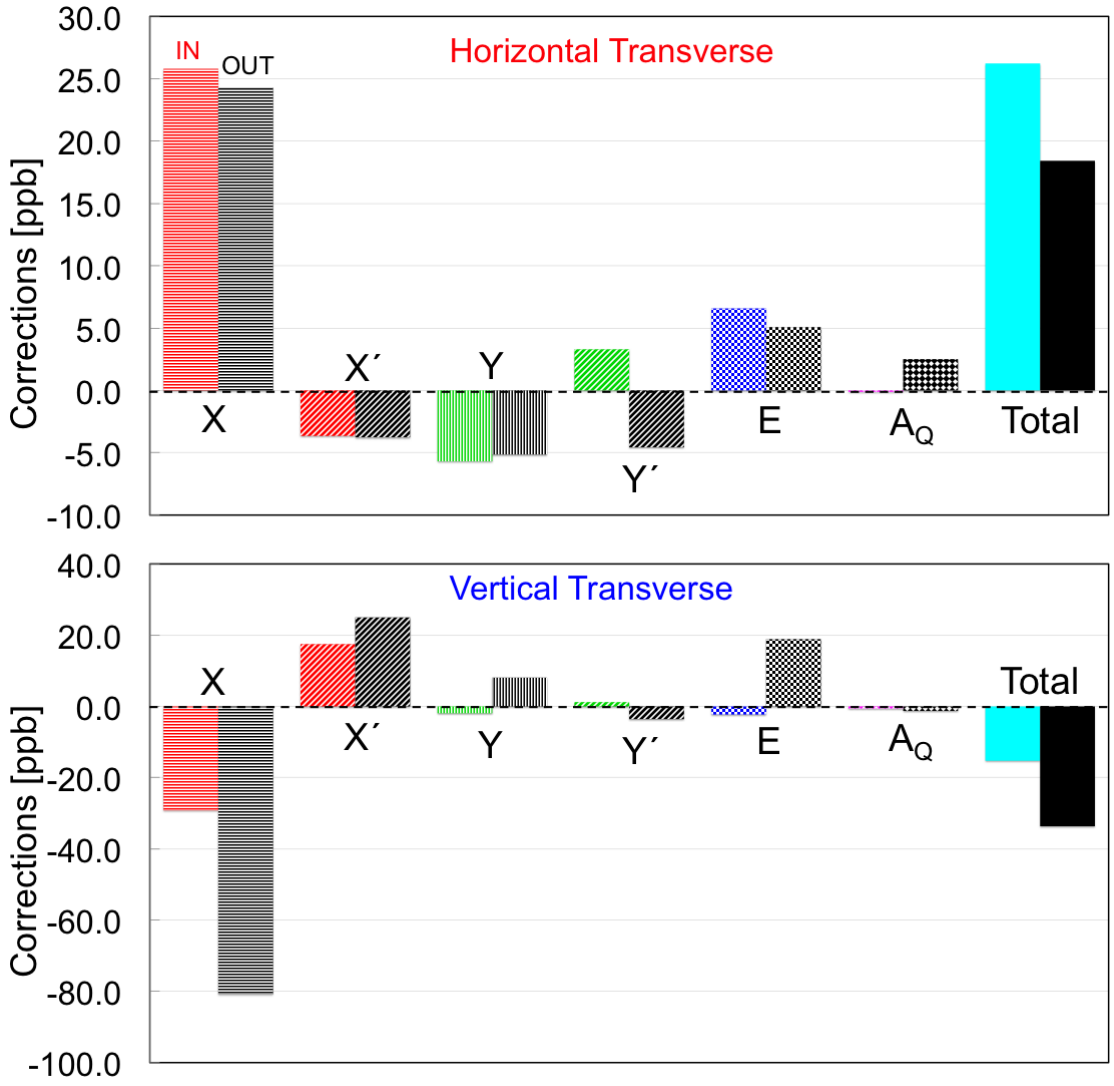

Figure 6.6 Main detector corrections (using sensitivities from "5+1" regression scheme) for horizontal (top) and vertical (bottom) LH_2 transverse data sets are shown here. Both IHWP states are shown separately for each beam parameter. The total correction is the sum of all the corrections (with sign).

The regressed "5+1" asymmetries measured using horizontal and vertical transverse polarization beam on LH_2 target are shown in Figure 6.7. The azimuthal modulating asymmetry flips sign with the insertion of the IHWP as expected. The vertical asymmetry fits may show sign of phase shift between IHWP IN and IHWP OUT settings, but may be explained due to statistical fluctuation. Transverse polarization angle was ∼2-3° off from ideal settings during the measurement [153, 154], which can not be confirmed with the statistics in hand. The null asymmetry (<IN>+<OUT>)/2

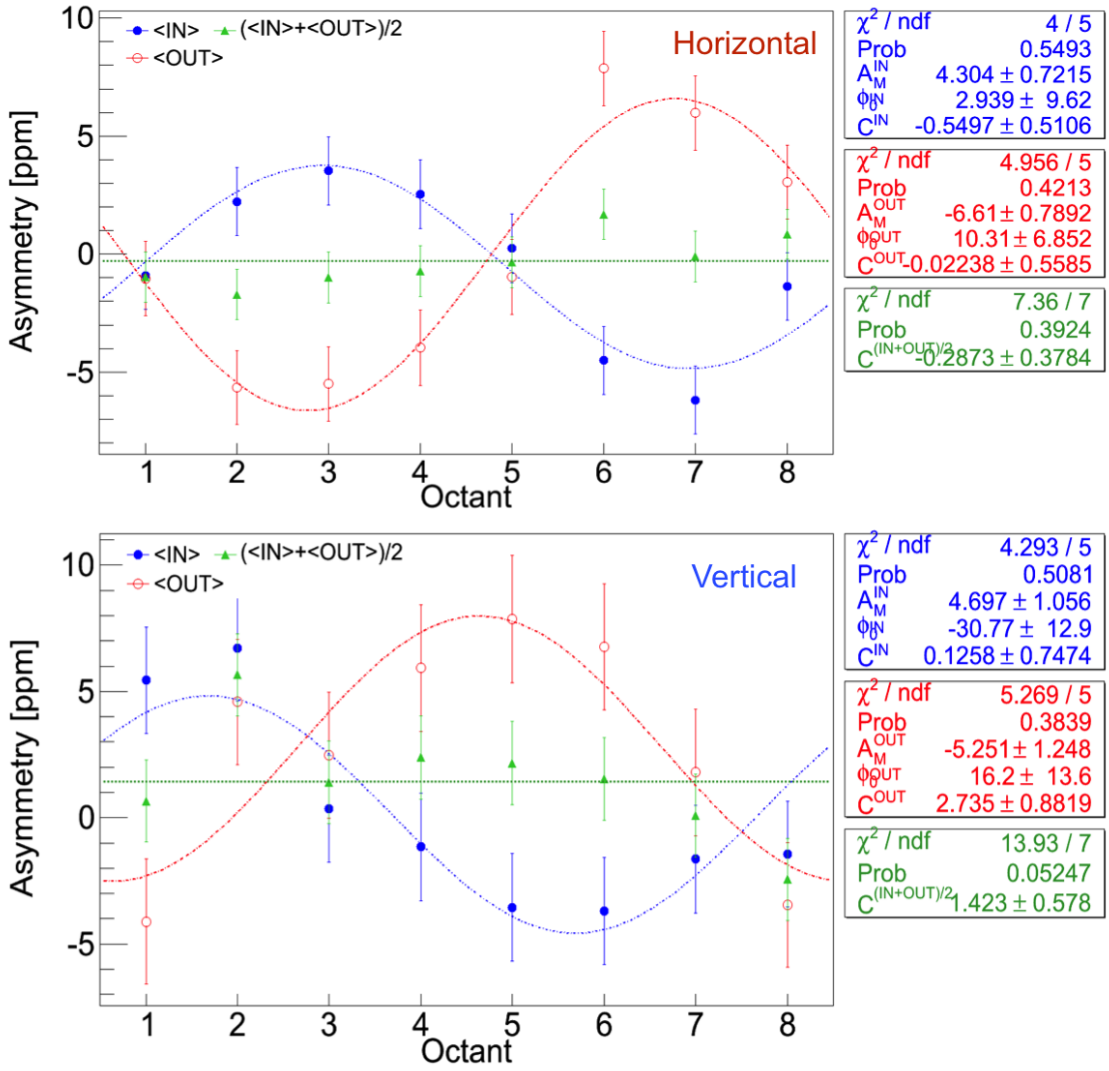

Figure 6.7 Main detector asymmetry for horizontal (top), vertical (bottom) data set. For comparison, asymmetries for IN and OUT data are also shown separately. The regressed asymmetries change sign with the insertion of the IHWP with comparable amplitudes. The (<IN>+<OUT>)/2 asymmetries of the eight Čerenkov detectors, given by $C^{(\mathrm{IN+OUT})/2}$ is compatible with zero except in the vertical data set. The extraction of BNSSA depends on the amplitudes in the fits and by comparison of IN and OUT, not the constant term.

given by the $C^{(\mathrm{IN+OUT})/2}$ are compatible with zero within the measurement uncertainties. This indicates the azimuthal modulating signal in both IHWP IN and OUT are the same, and the non-polarization dependent false beam asymmetries were successfully removed by the regression.

The error weighted value of IN-OUT yields the measured regressed asymmetry for each bar. As expected from the azimuthal dependence of the BNSSA, there is a 90° phase offset between horizontal

and vertical, as shown in Figure 6.8. The measured five-parameter[1] regressed asymmetries using horizontal and vertical transverse polarization are extracted as $\epsilon_M^H = 5.343 \pm 0.532$ ppm and $\epsilon_M^V = 4.525 \pm 0.806$ ppm, respectively. The combined (error weighted average) regressed asymmetry from horizontal and vertical transverse polarization is given by

$$\epsilon_M = 5.047 \ \pm \ 0.444 \text{ ppm (stat)}. \tag{6.4.2}$$

This measurement provides a ∼9% statistical measurement of the BNSSA in inelastic e+p scattering (not corrected for backgrounds, polarization or other experimental related systematic uncertainties). Regression has small effect on the extracted measured asymmetries ($\lesssim$4%).

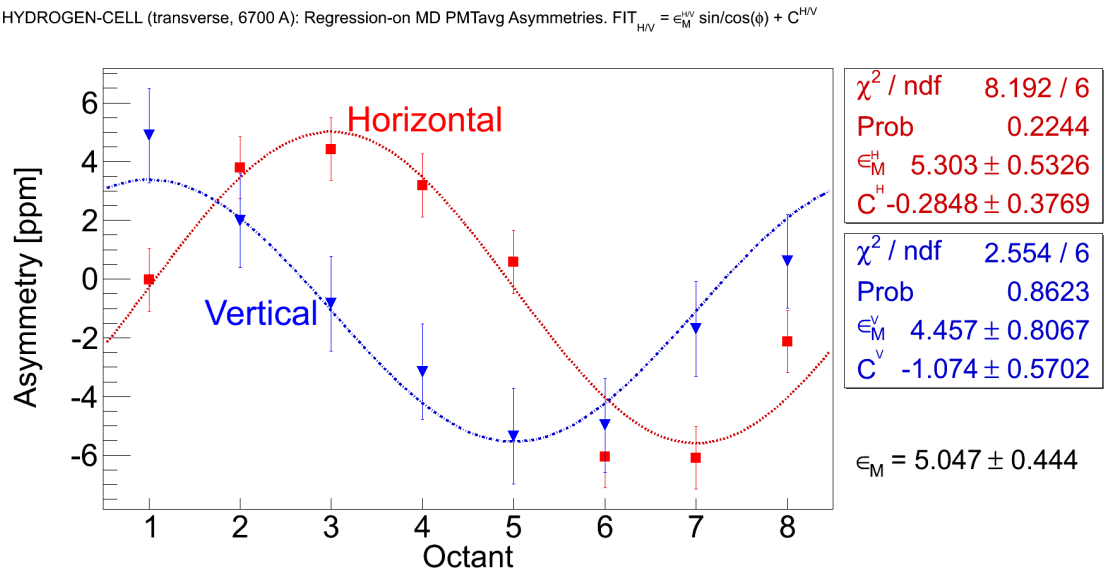

Figure 6.8 Regressed main detector asymmetry for horizontal, vertical transverse polarization are shown with red circle and blue square, respectively. Data points for horizontal transverse are ∼4 hour long measurement, whereas vertical transverse data points are ∼2 hour long. The fit functions used are $\epsilon_M^H \sin(\phi + \phi_0^H) + C^H$ for horizontal transverse and $\epsilon_M^V \cos(\phi + \phi_0^V) + C^V$ for vertical transverse, respectively. Asymmetries in each case shows ∼90° phase offset, as expected between horizontal and vertical configurations.

[1]The charge asymmetry was not included as regression parameter in the final asymmetry calculation, as it is not an helicity correlated beam property (more details in section 6.5.1).

6.5 Systematic Uncertainties

The dominant uncertainty in the measured asymmetry for this measurement is statistical (9%). A preliminary treatment of the systematic uncertainty performed on the data set is presented in this section.

Table 6.3 Asymmetries from different regression schemes, along with the raw asymmetry, are shown for horizontal and vertical transverse data sets from Run 2 Pass 5 database. Corrections are small ($\lesssim$4%) compared to the amplitude of the measured asymmetry. The schemes without and with charge as regression variable are shown separately. Set 5 and 6 were not available due to failure of BPM 9b during Run 2. Set 9 was ignored for this analysis as it used the upstream luminosity monitor as an independent variable (more details about regression variables are in APPENDIX G).

Regression scheme	Horizontal		Vertical	
	Asymmetry [ppm]	Correction [ppm]	Asymmetry [ppm]	Correction [ppm]
UnReg	5.339	0.000	4.602	0.000
std	5.343	0.004	4.524	-0.078
set7	5.347	0.007	4.529	-0.073
set11	5.343	0.004	4.524	-0.078
5+1	5.343	0.004	4.525	-0.077
set3	5.343	0.004	4.525	-0.077
set4	5.343	0.004	4.527	-0.076
set8	5.346	0.007	4.531	-0.072
~~set9~~	~~5.343~~	~~0.003~~	~~4.534~~	~~-0.069~~
set10	5.343	0.003	4.526	-0.077
Max - Min	set8 - set10	0.004	set8 - set11	0.006

6.5.1 Regression Scheme Dependence

Since the five-parameter ("std") linear regression scheme used for this analysis is only one of the many different schemes available, it was worth investigating the scheme dependence. A list of all the independent variables for different regression sets are shown in APPENDIX G. Ideally, the regression corrections from all the schemes should agree if all equipment is functioning properly and the regression is being done properly. Small differences in the corrections can arise from differences in the noise, resolution, and non-linear response of the monitors. To compare for the systematic studies, a common set of event cuts [88] are applied to all regression schemes to match the quartets used by each scheme. The results are summarized in Table 6.3. The regression scheme dependence uncertainty is defined as the largest difference between all of the schemes and estimated to be 0.004 ppm for horizontal transverse and 0.006 ppm for vertical transverse data set.

6.5.2 Regression Time Dependence

The standard regression algorithm works with 5 minute runlet averaged quantities. The detector sensitivities are averaged over each runlet and corresponding differences are used to correct for the false asymmetry for each quartet in the runlet. There is another systematic uncertainty associated with regression time period that is considered. The effect of using slug, few hours (∼2), as time period for the regression instead of runlets was determined. The MD error weighted average sensitivities for a slug were calculated and average beam parameter differences for that slug were used to get the corrections, as shown in Equation 6.5.2. These slug averaged corrections were then used to regress asymmetries (Equation 6.5.1).

$$\langle \epsilon_{\text{reg}} \rangle_{\text{slug}} = \langle \epsilon_{\text{UnReg}} \rangle_{\text{slug}} - \langle C \rangle_{\text{slug}} \tag{6.5.1}$$

$$\langle C \rangle_{\text{slug}} = \sum_{i=1}^{6} \left\langle \frac{\partial \epsilon}{\partial T_i} \right\rangle_{\text{slug}} \langle \Delta T_i \rangle_{\text{slug}} \tag{6.5.2}$$

where T_i's are X, X', Y, X', A_E, and A_Q. The slug averaged sensitivities and beam parameter differences for the data set are shown in Figure 6.2 (also Figure D.7 for horizontal transverse) and Table 6.2, respectively. The impact on regressed asymmetries due to change in the regression averaging time period for horizontal and vertical transverse data set are 0.006 ppm and 0.008 ppm, respectively and are assigned as regression time dependence systematic uncertainties. More details in APPENDIX-D section D.8.1.

6.5.3 Nonlinearity

The Čerenkov detector signals are normalized to the charge and the charge asymmetry is actively suppressed using a charge feedback system. The nonlinearity of the BCM electronics, the main detector electronics, and target density changes can induce nonlinear distortions in the charge asymmetry and hence in the measured asymmetry [155]. This nonlinearity of the system is seen to be non-zero from the non-zero charge sensitivity constant term in the "5+1" regressed detector asymmetries, as shown in Figure 6.9. For both horizontal and vertical polarization data sets, the nonlinearity is found to be -1%. At present, no proper method of handling the measured asymmetry distortion due to nonlinearity is available. The nonlinearity term is multiplied with the measured asymmetry to calculate the false asymmetry [156]. The systematic uncertainties due to nonlinearity for horizontal and vertical transverse measurements are given by 0.053 ppm and 0.045 ppm, respectively.

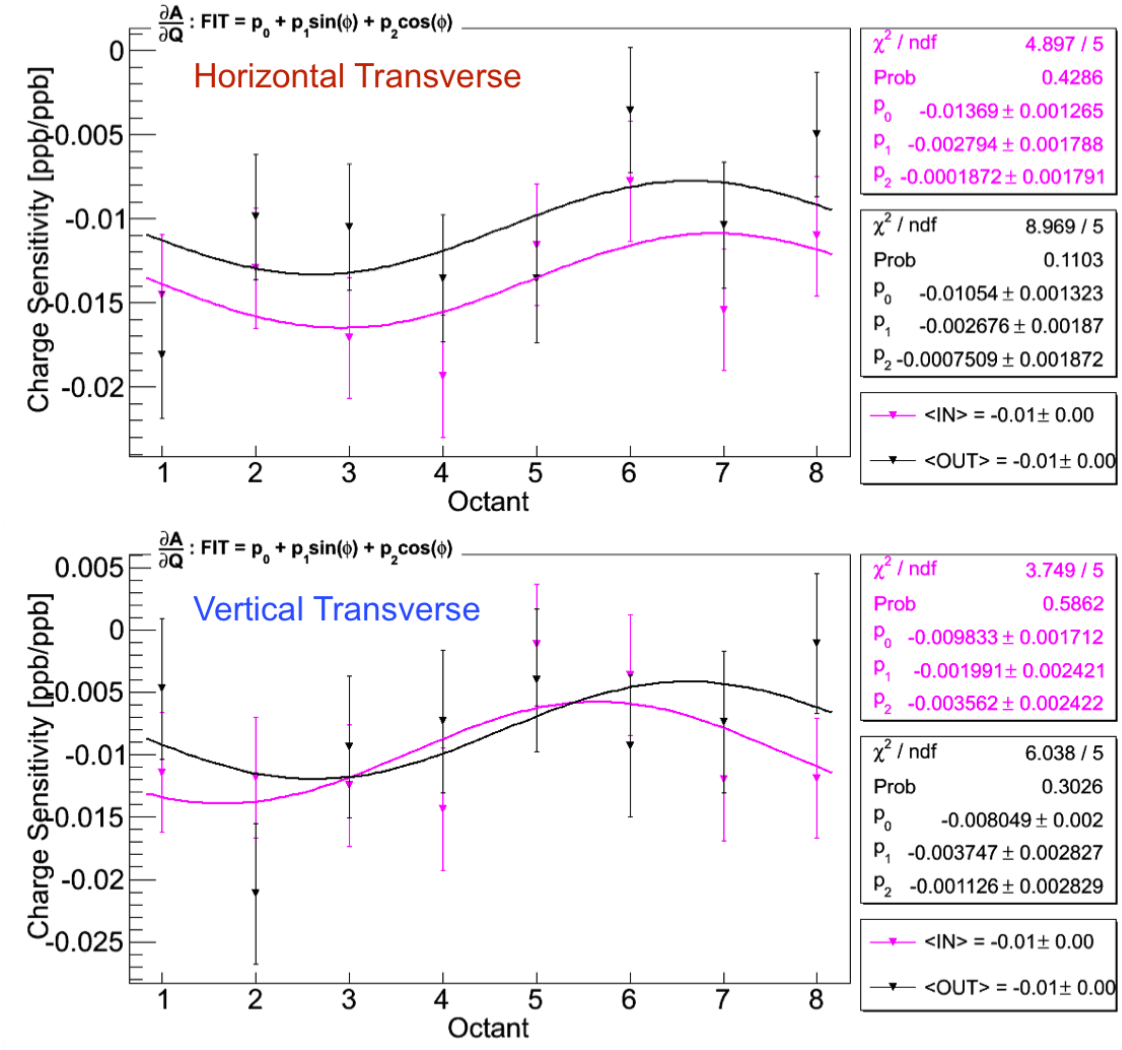

Figure 6.9 Charge sensitivity for horizontal (top) and vertical (bottom) transverse polarization data set. Average charge sensitivities of the measured detector asymmetries extracted from the six parameter (five parameter + charge) regression at beam current 180 μA. Purple (Black) represents the charge sensitivity of the IHWP IN (OUT) data which are consistent with each other. The sensitivities of the eight Čerenkov detectors vary from -0.5% to - 2.0% and are stable within the running period. Average non linearity is -1% for both the cases.

6.5.4 Cut Dependence

The goal of the cut dependence analysis was to assign a systematic uncertainty that comes from shifts in the mean value of the regressed asymmetry beyond statistical fluctuations after applied cuts. If linear regression is working properly, large false asymmetries in runlets with large HCBAs should be removed from the measured asymmetry after linear regression is applied and there should

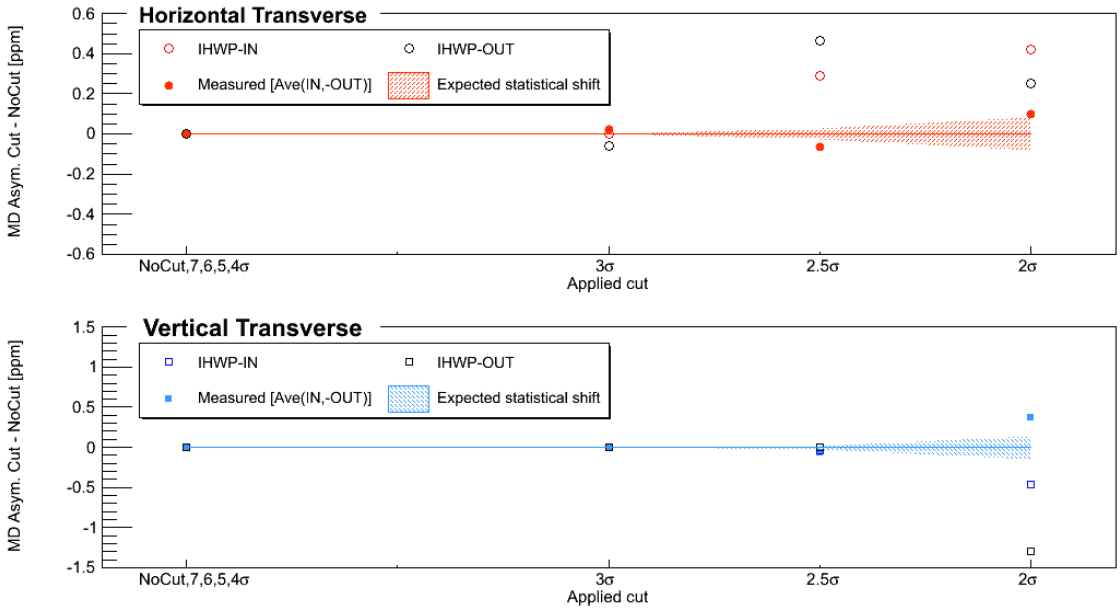

Figure 6.10 Cut dependence study. Shift in the central value of the regressed asymmetry for different cut widths for LH_2. The expected statistical shift is shown by the shaded region using the total number of quartets lost when a cut is applied to all parameters.

not be any shift in the mean value of the regressed asymmetry beyond statistical shifts (as shown in Figure 6.10). The point-to-point uncertainty in going from cut i to cut j is estimated to be

$$\Delta_{i\to j}^{\mathrm{pt-to-pt}} = \left(\frac{\sigma_j}{\sqrt{N_j}} - \frac{\sigma_i}{\sqrt{N_i}} \right) \tag{6.5.3}$$

Here the σ is the root mean square (RMS) of each HCBA. Inclusive cuts of 7, 6, 5, 4, 3, 2.5 and 2σ are applied to all HCBAs and difference between regressed asymmetry with cut and without cuts are shown in Figure 6.10. The observed shift in the measured asymmetry from these cuts are larger than the expected statistical shift and 2.5σ cuts on the HCBAs were used to assign a systematic uncertainty. The total percentage of quartets lost for cuts with respect to no cut are used to estimate the expected statistical shift, shown as the shaded region in Figure 6.10. Beyond a cut of 2.5σ, most of the data were removed to extract a meaningful asymmetry. This analysis was performed to assign systematic uncertainty only, no data was removed from main data set. Cut dependence for horizontal and vertical transverse data set are found to be $\sim$0.064 ppm and $\sim$0.068 ppm, respectively.

6.5.5 Fit Scheme Dependence

A sinusoidal fit to main detector octant asymmetries is used to extract measured transverse asymmetry. So it was important to find the impact of the function on fitted asymmetry. The measured asymmetry was fitted using four different functions, and the solutions are summarized in Table 6.4. The difference in measured asymmetry obtained using standard function $\epsilon_M \sin(\phi + \phi_0) + C$ and rest gives an idea about the fit function dependence of the measured asymmetry. More insightfully, the constant term in the fit function can be thought of as the apparent parity violating asymmetry contamination to the parity conserving transverse asymmetry. The size of $P_T B_n$ is much larger than $P_L A_{\rm PV}$ so the latter has significant effect on the transverse measurement. So this PV asymmetry is buried under the fit scheme dependence and give rise to the systematic uncertainties of 0.040 ppm for horizontal and 0.083 ppm for vertical transverse data sets.

Table 6.4 Fit scheme dependence of the measured asymmetry. The fit function was varied to observe the effect on measured regressed asymmetry. The difference in asymmetry between case 1 and rest are shown. Biggest offset comes from the possible phase shift.

	Fit Function	Asymmetry [ppm]	Difference (1-i) [ppm]
	Horizontal Transverse		
1	$\epsilon_M^H \sin(\phi + \phi_0^H) + C^H$	5.343 ± 0.532	0.000
2	$\epsilon_M^H \sin(\phi + \phi_0^H)$	5.344 ± 0.532	0.001
3	$\epsilon_M^H \sin(\phi) + C^H$	5.303 ± 0.533	0.040
4	$\epsilon_M^H \sin(\phi)$	5.304 ± 0.533	0.039
	Vertical Transverse		
1	$\epsilon_M^V \cos(\phi + \phi_0^V) + C^V$	4.525 ± 0.806	0.000
2	$\epsilon_M^V \cos(\phi + \phi_0^V)$	4.510 ± 0.806	0.015
3	$\epsilon_M^V \cos(\phi) + C^V$	4.458 ± 0.807	0.067
4	$\epsilon_M^V \cos(\phi)$	4.442 ± 0.807	0.083

6.5.6 Summary of Systematic Uncertainties

Summary of systematic uncertainties of the measured inelastic beam normal single spin asymmetry is given in Table 6.5. The systematic studies contain uncertainties related to the extraction of the measured asymmetry such as regression, nonlinearity, cut dependence, and detector acceptance correction. The systematic studies for horizontal and vertical transverse polarization data set were performed separately; these are summarized in Figure 6.11. The statistical uncertainty weighted average of the systematic uncertainties from horizontal and vertical transverse data sets is used for the total systematic uncertainty. The total uncertainty is the quadrature sum of the statistical and

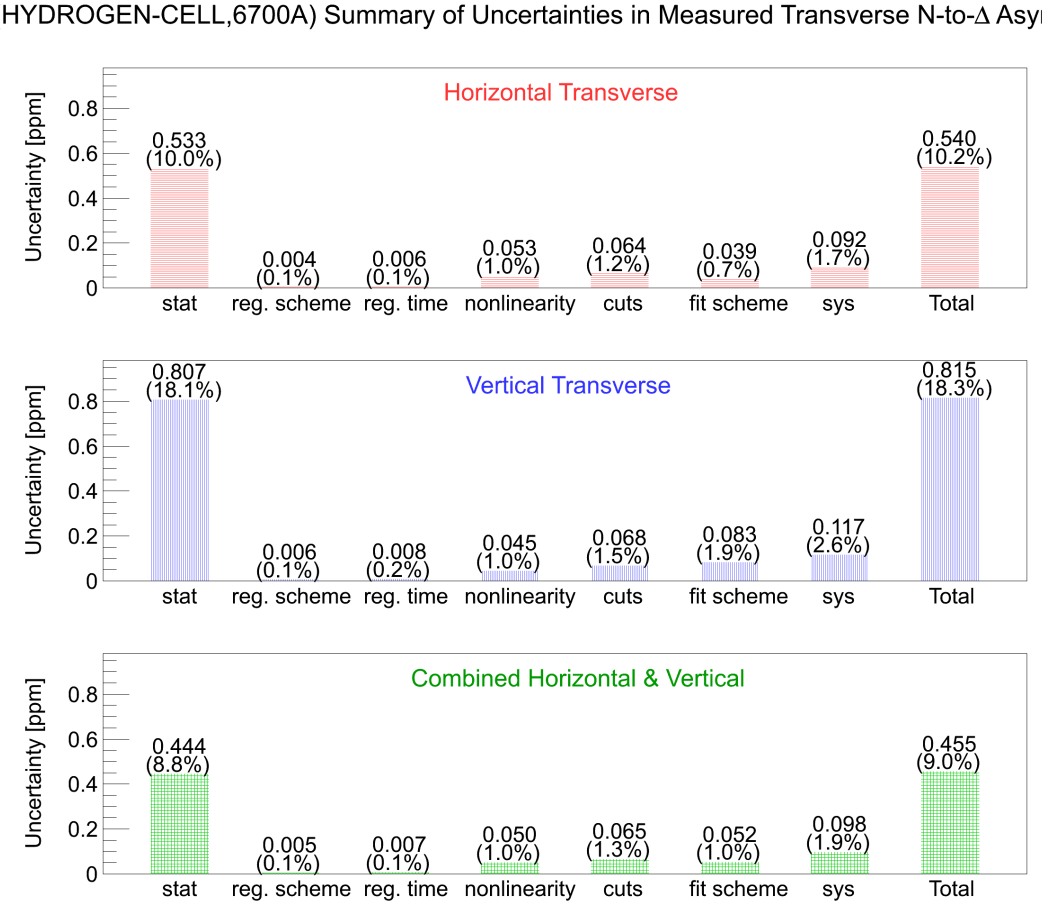

Figure 6.11 Summary of uncertainties on measured asymmetry for horizontal and vertical data set. The relative total uncertainty is dominated by statistical uncertainty compared to systematic uncertainties.

systematic uncertainties. The total uncertainty is dominated by 9% statistical uncertainty compared to 1% systematic uncertainty.

6.6 Extraction of Physics Asymmetry

The beam normal single spin asymmetry from inelastic e+p scattering is obtained from measured asymmetry using Equation 6.6.1 by accounting for EM radiative corrections, kinematics normalization, polarization, and backgrounds.

$$B_n = M_{total}\left[\frac{\left(\frac{\epsilon_{reg}}{P}\right) - \sum_{i=1}^{4} B_{bi} f_{bi}}{1 - \sum_{i=1}^{4} f_{bi}}\right] \tag{6.6.1}$$

Table 6.5 Summary of uncertainties on measured asymmetry for combined horizontal and vertical data sets. The relative uncertainties are also shown in the table.

Uncertainty from	Contribution to ϵ_M [ppm]	Relative Contribution [%]
Statistics	0.444	8.8
Regression scheme	0.005	0.1
Regression time binning	0.007	0.1
Non-linearity	0.050	1.0
Cuts	0.065	1.3
Fit scheme	0.052	1.0
Systematic only	0.098	1.9
Total	0.455	9.0

Here M_{total} is a correction factor for the experimental bias and radiative effects, P is the beam polarization, and B_{bi} is i^{th} background asymmetry with fraction of backgrounds in the total detector acceptance (dilution) f_{bi}. The corrections to the physics asymmetry and the associated uncertainties are discussed in the following sections.

6.6.1 Beam Polarization

The Hall-C Møller polarimeter and the Compton polarimeter were used to measure the beam polarization for the experiment. The photocathode Quantum Efficiency was stable and hence the beam polarization was stable for the period [157]. The Møller polarimeter is only sensitive to longitudinally polarized beam, so measurements performed with the longitudinally polarized beam right after the transverse data taking was used to determine the beam polarization. The Møller runs used for this analysis are 1593 - 1599, carried out on 20th February 2012. Each run is ∼10 min long. Slug averaged polarizations from this Møller measurement are shown in Table 6.6. The measured beam polarization is $P = 87.50 \pm 0.28$ (stat) $\pm$ 0.74 (sys)% [158]. Details of systematic studies for the Møller polarization measurement can be found in the Q-weak internal technical document [20].

Table 6.6 Beam polarization using Møller polarimeter for Run 2 transverse data set [20].

IHWP	Polarization [%]	Statistical Uncertainty [%]
Out	87.029	0.398
In	- 87.939	0.387
Total	87.497	0.277

6.6.2 Background Corrections

The largest background source in beam normal single spin asymmetry arises from the elastic radiative tail. Small background contributions also come from electrons scattering from aluminum target windows, beamline scattering, and other soft neutral scattering. The analysis of the background asymmetries and their contributions to the BNSSA is described in the following sections.

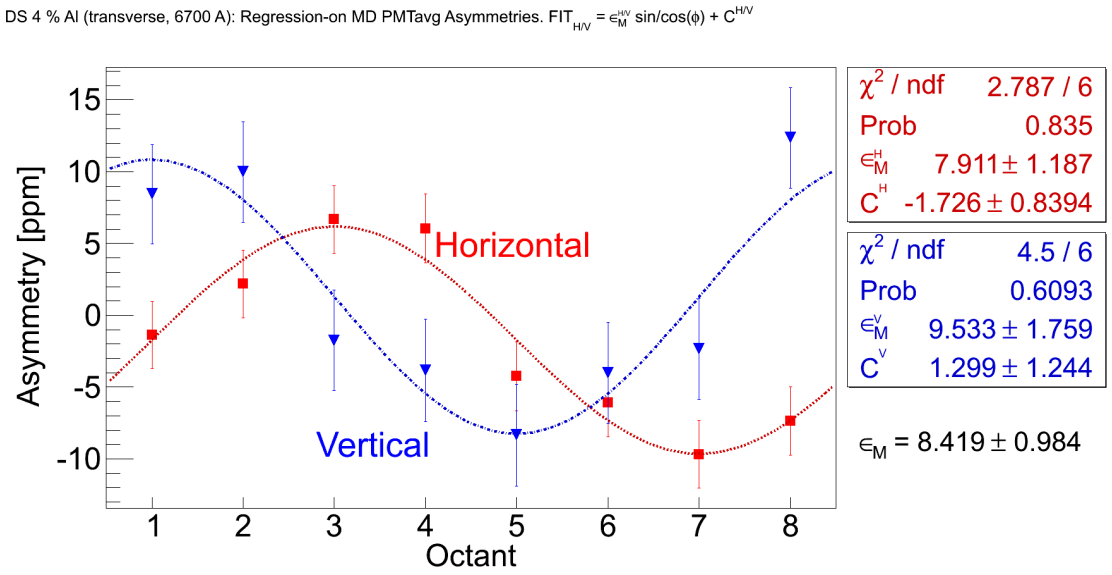

Figure 6.12 Azimuthal dependence of asymmetry from the 4% downstream aluminum target. The uncertainties are statistical only. The octant dependence in either polarization orientation are similar to what was observed for the LH_2-cell. The asymmetry is larger than the LH_2-cell asymmetry. The fit functions used for horizontal and vertical transverse data points are $\epsilon_M^H \sin(\phi + \phi_0^H) + C^H$ and $\epsilon_M^V \cos(\phi + \phi_0^V) + C^V$, respectively.

6.6.2.1 Target Aluminum Windows

One of the important background contributions to the measured asymmetry comes from electrons scattering from the aluminum alloy target windows. Data were taken on the 4% downstream aluminum alloy target to determine the asymmetry and dilution. The measured regressed asymmetry for horizontal and vertical transverse are $\epsilon_M^{H-DSAl} = 7.911 \pm 1.187$ (stat) $\pm$ 0.482 (sys) ppm and $\epsilon_M^{V-DSAl} = 9.533 \pm 1.759$ (stat) $\pm$ 0.870 (sys) ppm [159], as shown in Figure 6.12. Combined (error weighted) regressed aluminum alloy asymmetry is $\epsilon_M^{DSAl} = 8.419 \pm 0.984$ (stat) $\pm$ 0.603 (sys) ppm. The systematic studies for 4% downstream aluminum alloy target contain uncertainties related to the extraction of the measured asymmetry such as regression, nonlinearity, cut dependence, and detector acceptance correction, as described in section 6.5 (see APPENDIX D for more details on

Al analysis). The acceptance difference between the upstream and downstream target windows need to correct before the background correction. This acceptance difference causes a 20% relative difference between the mean Q^2 of the electrons coming from the upstream window compared to the downstream window, as shown in GEANT4 simulations [8] (Q^2_{USAl}=0.8×Q^2_{DSAl}). The beam normal single spin asymmetry from nuclei at forward angle scattering asymmetry is proportional to $\sqrt{Q^2}$ as described in theoretical models [160, 161]. So, asymmetry for upstream aluminum target can be calculated as $\epsilon_M^{USAl} = \sqrt{0.8}\epsilon_M^{DSAl} = 7.530$ ppm. Downstream and upstream aluminum target windows are expected to contribute equally [8] to the aluminum dilution in the main detector asymmetries resulting in an effective aluminum asymmetry of $\epsilon_M^{Al} = (\epsilon_M^{DSAl} + \epsilon_M^{DSAl})/2 = 7.974$ ppm. The polarization corrected asymmetry for background windows correction is $B_{Al} = \epsilon_M^{Al}/P = 9.061 \pm 1.405$ ppm.

Table 6.7 Measured asymmetry on aluminum target.

Target	Asymmetry [ppm]
DSAl	8.419
USAl	7.530
<DS+US>	7.974

The measured aluminum windows dilution is $f_{Al} = 0.033 \pm 0.002$ [162]. Dedicated measurements were performed with different pressures of hydrogen gas in the target cell. Using the known pressure of hydrogen gas at different points, the pressure was extrapolated to zero.

The correction to the physics asymmetry from aluminum alloy windows is $c_{Al} = M_{total}B_{Al}f_{Al}/(1-f_{total}) = 1.416 \pm 0.246$ ppm.

6.6.2.2 Beamline Background

The beamline background correction is a polarization-independent mechanical asymmetry which should be lumped with linear regression corrections [163]. The beamline scattering produces light in the detectors and there is a contribution to the dilution. The beamline background dilution factor for inelastic running is an order of magnitude larger than in the elastic kinematic setting. The total rate at the inelastic peak drops to 10% of the total rate at the elastic peak, whereas the number of events originating in the beamline remains similar. The measured dilution for inelastic beamline scattering is 0.018 ± 0.001 [3, 164]. A 50% uncertainty on the dilution was assigned to allow the sinusoidal modulation specific to the BNSSA. The beamline scattering dilution used for the background correction is $f_{BB} = 0.018 \pm 0.009$.

6.6.2.3 Other Neutral Background

An additional correction was applied to include soft neutral backgrounds arising from secondary interactions of scattered electrons in the scattered electron transport line, and was not accounted in the blocked octant studies [165]. This can arise from Møller scattering, electron-proton elastic scattering, etc. Simulations are in progress [166]. The other neutral background asymmetry could be as large as 5 ppm (size of the transverse asymmetry). To make the sign of the asymmetry uncertain, the asymmetry for other neutral background was assumed to be $B_{QTor} = 0.000 \pm 10.000$ ppm. Here, uncertainty of 100% of the measured transverse asymmetry was assigned to give an upper bound on the neutral background asymmetry.

The neutral background dilution for the inelastic scattering has been measured as $f_{\text{neutral}} = 0.0520 \pm 0.0040$ (stat) $\pm$ 0.0014 (sys) [167]. The dilution for the other neutral background was obtained by subtracting the blocked octant background from the total neutral background measured by the main detector and is given by $f_{QTor} = f_{\text{neutral}} - f_{BB} = 0.034 \pm 0.010$.

The correction to the physics asymmetry due to other neutral background is $c_{QTor} = M_{total} B_{QTor} f_{QTor}/(1\text{-}f_{total}) = 0.000 \pm 1.616$ ppm.

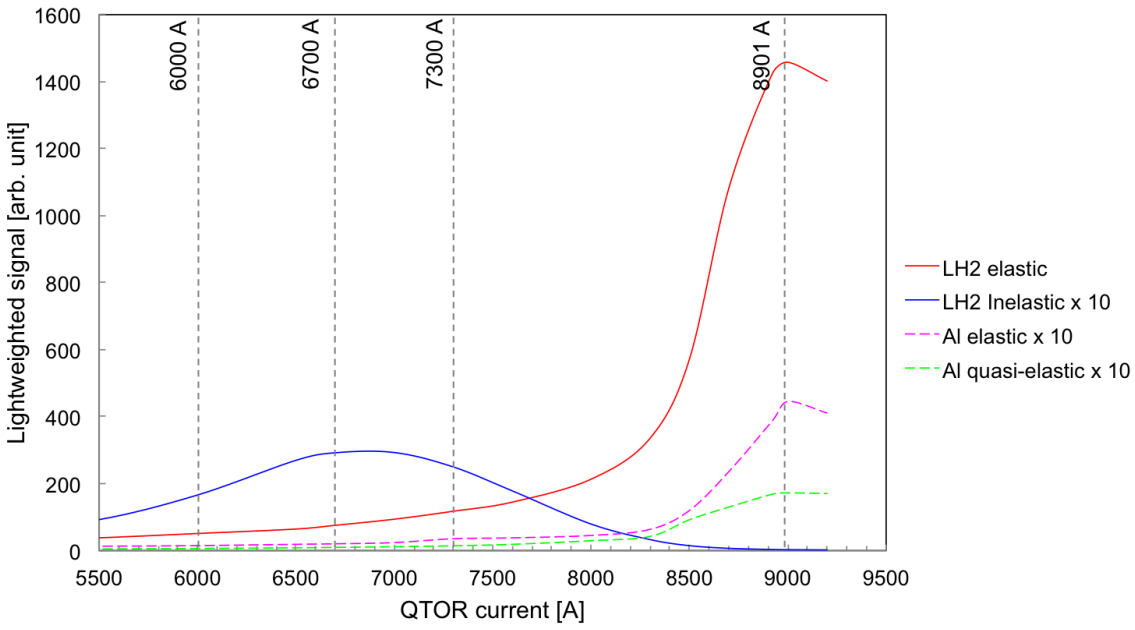

Figure 6.13 Simulation of contributions from elastic and inelastic electron-proton, and elastic electron-Al scattering from upstream (US) and downstream (DS) target windows [13]. All but elastic electron-proton events have been multiplied by 10 for better visualization.

6.6.2.4 Elastic Radiative Tail

The largest background correction comes from the elastic radiative tail ($b4$). The polarization corrected measured elastic transverse asymmetry was B_T^{el} = -5.345 ± 0.067 (stat) ± 0.076 (sys) ppm [168]. The elastic physics asymmetry from the LH_2-cell is similar in magnitude to the inelastic asymmetry but has the opposite sign. The elastic asymmetry was measured at $Q^2_{el} = 0.0250 \pm 0.0006$ (GeV/c)^2 [169] where as inelastic measurement was at $Q^2_{in} = 0.0209 \pm 0.0005$ (GeV/c)^2 (shown in Figure 6.16), hence it is necessary to scale it to the inelastic peak. The transverse asymmetry is proportional to $\sqrt{Q^2}$ [160,161]. The polarization and $\sqrt{Q^2}$ corrected elastic asymmetry is given by $B_{el} = \sqrt{\frac{Q^2_{in}}{Q^2_{el}}} B_T^{el}$ = -4.885 ± 0.093 ppm.

As ∼70% of the total signal in the inelastic peak was from elastic radiative tail (Figure 6.13), it was important to tackle it carefully. A GEANT simulation was used to extract elastic dilution. Dedicated measurements were taken at both sides of the inelastic peak (at QTor current 6000 A and 7300 A) to check the simulation. A ∼10% discrepancy was observed between current mode data and GEANT simulated signal at the inelastic peak, as shown in Figure 6.14. In order to incorporate this discrepancy, a 10% systematic uncertainty was assigned to the elastic dilution for this preliminary analysis. A more detailed simulation is ongoing to explore this difference. The signal size for inelastic transverse is ∼2-3 times smaller than that of the elastic signal. Although the signal reduces for inelastic, the nonlinearity in the detector remains the same and might be responsible for this discrepancy. The simulated elastic dilution factor is given by $f_{el} = 0.701 \pm 0.070$ [13,170].

The correction to the physics asymmetry due to the elastic radiative tail is $c_{el} = M_{total} B_{el} f_{el}/(1 - f_{total})$ = -17.063 ±7.304 ppm.

6.6.3 Other Corrections

Another set of corrections is used to remove all the experimental bias from the measured asymmetry before extracting BNSSA. The measured asymmetry is corrected for the electromagnetic (EM) radiative corrections, light weighting on the Čerenkov detector, and Q^2 precision. These corrections are considered as independent factors and are applied to the measured asymmetry.

6.6.3.1 Radiative Correction

The energy loss and depolarization of the electrons is a result of electromagnetic (EM) radiation [171]. The measured asymmetry needs to be corrected for these EM radiative effects to obtain the beam normal single spin asymmetry at the effective Q^2 and beam polarization.

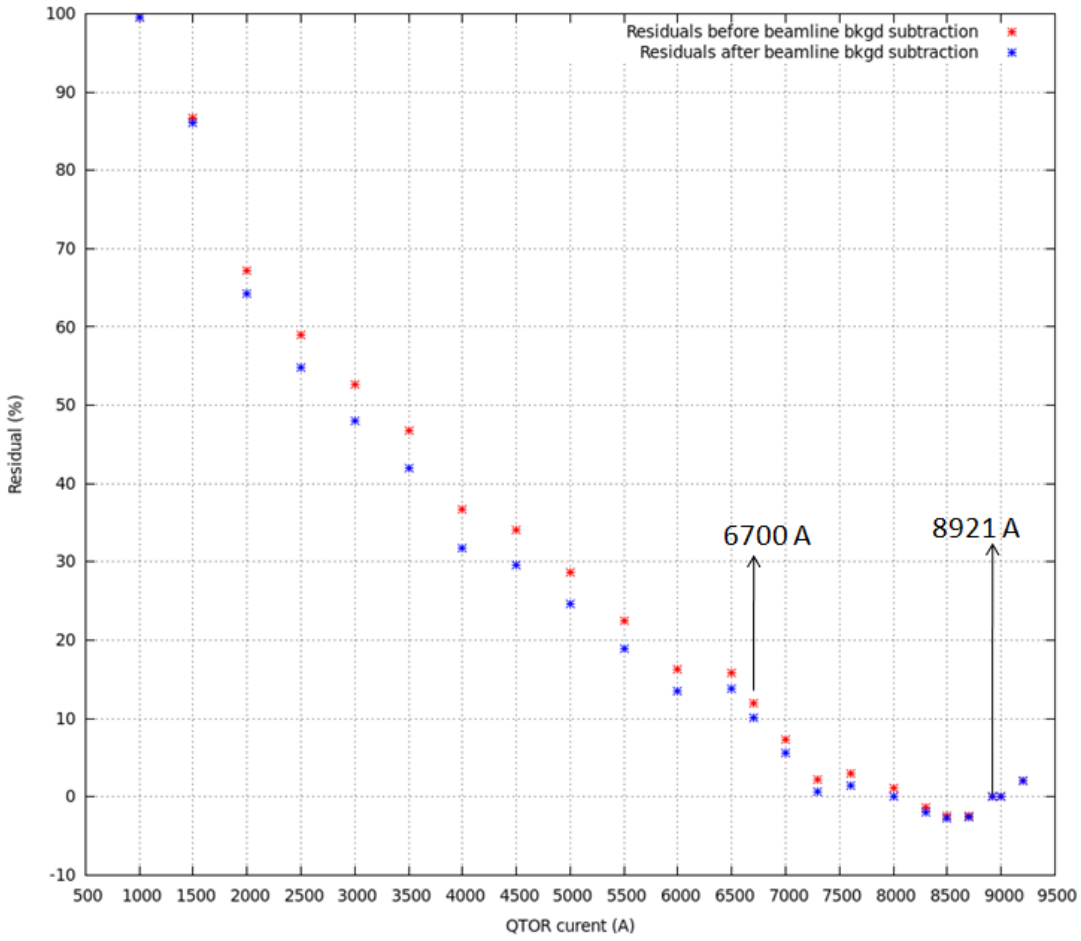

Figure 6.14 The residual of yield using Data and simulation from GEANT 3 [13] are shown in the figure. A ∼10% discrepancy was observed at inelastic peak (6700 A) between data and simulation for matching them at elastic peak (8921 A). Beamline background correction to the yield did not improve the discrepancy.

The deduced radiative correction for elastic electron-proton scattering from simulations with and without bremsstrahlung, using methods described in Refs. [172, 173], was found to be $M_{RC} = 1.010 \pm 0.010$ [19]. The same radiative correction was used for this data set as there were no existing simulations available for inelastic electron-proton scattering. This correction does not have a significant impact in the final asymmetry, hence it was not unreasonable to use the existing elastic simulation result.

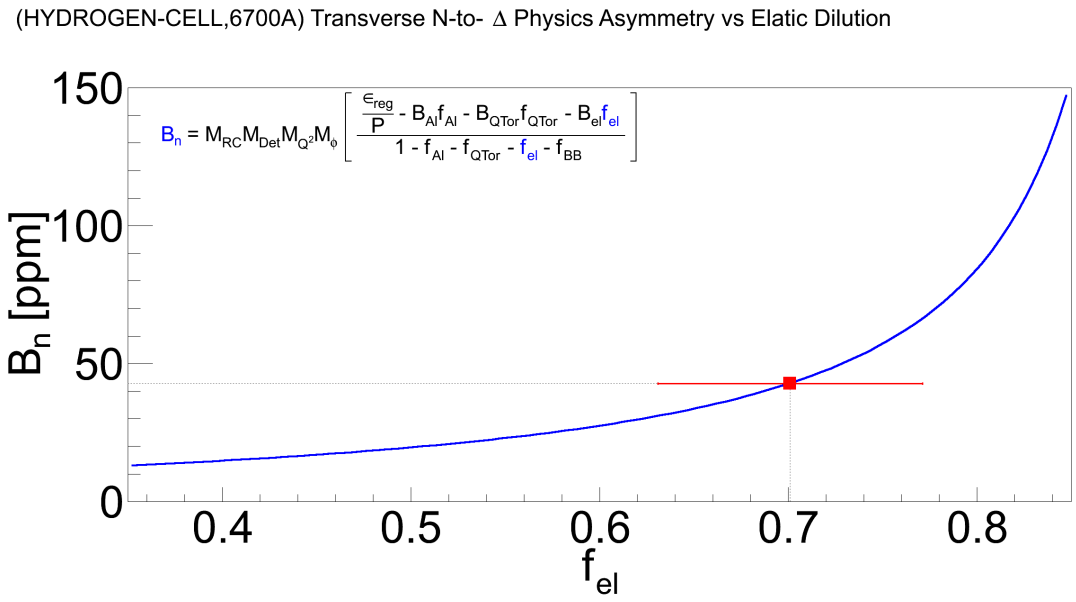

Figure 6.15 The variation of beam normal single spin asymmetry with elastic dilution.

6.6.3.2 Detector Bias Correction

The correction between light yield and Q^2 across the detector bars affects the measured asymmetry and needs to be accounted for in the final BNSSA extraction. The multiplicative correction factor to be applied to the data is

$$M_{Det} = \frac{\epsilon^{\rm sim}_{\rm no-bias}}{\epsilon^{\rm sim}_{\rm bias}} = \sqrt{\frac{(Q^2)^{\rm sim}_{\rm no-bias}}{(Q^2)^{\rm sim}_{\rm bias}}}. \tag{6.6.2}$$

Here, $\epsilon^{\rm sim}_{\rm bias}$ and $\epsilon^{\rm sim}_{\rm no-bias}$ are the simulated asymmetries with and without light-collection bias, respectively. The detector bias correction used for this analysis is $M_{Det} = 0.998 \pm 0.002$ and is obtained using transverse simulation results [19, 174].

6.6.3.3 Q^2 Precision

The Q^2 for inelastic electron-proton scattering was determined using GEANT 3 simulation and was found to be 0.0209 ± 0.0005 (GeV/c)^2 [14], as shown in Figure 6.16. Internal bremsstrahlung was not included in the simulation. The simulation was benchmarked by the tracking mode experimental data to represent the geometry of the experimental setup, collimation, and magnetic spectrometer. The cross section weighted Q^2 was simulated at main detector using the reaction $e + p \rightarrow e + n +$

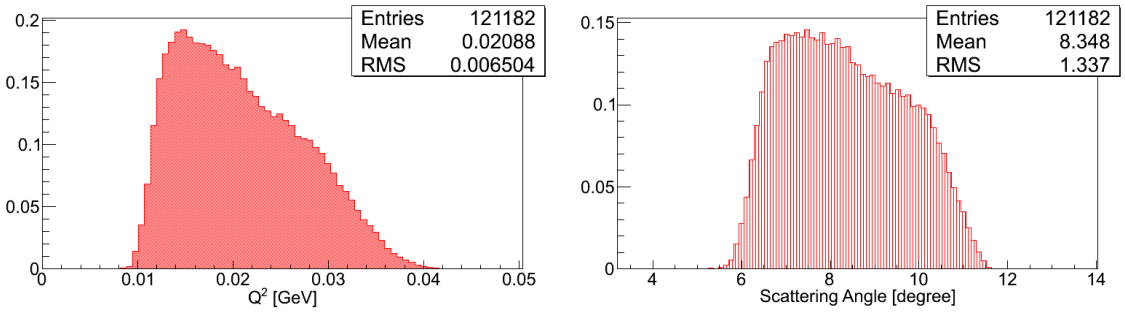

Figure 6.16 The Q^2 from GEANT 3 simulation [14]. The Q^2 was weighted by cross section and did not include any internal bremsstrahlung in the simulation (left panel). The simulated scattering angle is also shown in the right panel.

π^+ [14]. The two-body scattering process, and energy and momentum conservation were used to do the calculation. The scattered electron energy, and Q^2 are expressed as

$$\begin{aligned} E' &= RANDOM() \times (E_{in} - M_e) + M_e \\ Q^2 &= 4EE' \sin^2\theta, \end{aligned} \tag{6.6.3}$$

where E_{in} is the incident beam, M_e is electron mass, and θ is scattering angle. It was important to propagate the precision of Q^2 in the final physics asymmetry. Based on theory [175], the transverse beam spin asymmetries A_N at low Q^2 behave like

$$B_n \approx \sqrt{Q^2} = m\sqrt{Q^2}. \tag{6.6.4}$$

$$dB_n = \pm\frac{1}{2}\frac{m}{\sqrt{Q^2}}dQ^2 = \pm\frac{1}{2}\frac{34.7}{\sqrt{0.02078}}0.0005 = 0.0601 \text{ ppm}. \tag{6.6.5}$$

Using Equation 6.6.4 on Q^2 and a 5 ppm measured asymmetry, the proportionality constant in the above relation can be calculated as 34.7 ppm/(GeV/c). The estimated uncertainty on the measured asymmetry due to the uncertainty in determining Q^2 is 0.061 ppm (Equation 6.6.5). A correction of $M_{Q^2} = 1.000 \pm 0.012$ was applied to include the precision in calibrating the central value of Q^2.

6.6.3.4 Azimuthal Acceptance Correction

The acceptance of a single Q-weak Čerenkov detector is only 49% of an octant (section 3.1), so the reported asymmetry from a detector is an average over 22° azimuthal angle (ϕ). Each detector bar measures an average asymmetry over a range of ϕ selected by the collimators (details in [19,176]). The effect of averaging cosines for a variable of the form $y(\phi) = \epsilon\cos(\phi+\delta)$ over the azimuthal angle yields

$$AVG[y(\phi)] = \frac{\epsilon\int_{\phi_0-\Delta\phi}^{\phi_0+\Delta\phi}\cos(\phi+\delta)\,\mathrm{d}\phi}{(\phi_0+\Delta\phi)-(\phi_0-\Delta\phi)} = \epsilon\cos(\phi_0+\delta)\times\frac{\sin\Delta\phi}{\Delta\phi}, \tag{6.6.6}$$

where ϕ_0 is the nominal azimuthal location of the detector with $\Delta\phi$ coverage. Similarly, for sines, $AVG[y(\phi)] = \epsilon\sin(\phi_0+\delta)\times\frac{\sin\Delta\phi}{\Delta\phi}$. So the measured asymmetry from each detector needs to be scaled by a factor of $M_\phi = 1/\frac{\sin\Delta\phi}{\Delta\phi}$ to correct for the acceptance[2]. $\Delta\phi = 11.025°$ yields the scale factor to be $M_\phi = 1/0.9938 = 1.006 \pm 0.006$. A conservative 100% uncertainty was used for the correction.

6.6.4 Beam Normal Single Spin Asymmetry in LH_2

Summary of required quantities to extract the beam normal single spin asymmetry from the transverse data set presented so far using

$$B_n = M_{RC}M_{Det}M_{Q^2}M_\phi\left[\frac{\left(\frac{\epsilon_{reg}}{P}\right)-B_{Al}f_{Al}-B_{QTor}f_{QTor}-B_{el}f_{el}}{1-f_{Al}-f_{BB}-f_{QTor}-f_{el}}\right] \tag{6.6.7}$$

is shown in Table 6.8. Equation 6.6.1 has been expanded to obtain Equation 6.6.7. Using all the input values in Equation 6.6.7 gives the beam normal single spin asymmetry in inelastic electron-proton scattering

$$B_n = 42.82 \pm 2.45\ (\text{stat}) \pm 16.07\ (\text{sys})\ \text{ppm} \tag{6.6.8}$$

for the effective kinematics of acceptance averaged electron energy $\langle E_{beam}\rangle = 1.155 \pm 0.003$ GeV, $\langle Q^2\rangle = 0.0209 \pm 0.0005$ (GeV/c)^2, an average scattering angle $\langle\theta\rangle = 8.3°$, and missing mass $W = 1.204$ GeV. The contributions from the different uncertainty sources into the final measurement are summarized in Figure 6.17. The dominant correction to the asymmetry comes from the elastic dilution tail whereas the dominant uncertainty on the measured asymmetry comes from statistics.

[2]Here, the collimator is assumed to remove 49% of the octant acceptance (i.e 49% of 45°)

Table 6.8 Summary of input quantities to extract the BNSSA. The measured regressed asymmetry is corrected for detector acceptance using the factor provided in the table. The table shows the contributions of normalization factors on ϵ_{reg}, then the properly normalized contributions from other sources. Background corrections listed here include $M_{\text{total}} B_{bi} f_{bi}/(1 - f_{total})$. Uncertainties in BNSSA due to dilution fraction and background asymmetry uncertainties are noted separately.

Input parameters			
Measured asymmetry (ϵ_{reg})	5.095 ± 0.455 ppm		
Beam polarization (P)	0.875 ± 0.008		
Background corrections			
Quantity	Asymmetry (B_{bi}) [ppm]	Dilution (f_{bi})	Correction $c_{bi} = B_{bi} f_{bi}/(1 - f_{total})$ [ppm]
Target windows (Al)	9.185 ± 1.409	0.033 ± 0.002	1.416 ± 0.246
Other neutral bkg. (QTor)	0.000 ± 10.000	0.034 ± 0.010	0.000 ± 1.616
Elastic asymmetry (el)	-4.885 ± 0.093	0.701 ± 0.070	-17.063 ± 7.304
Beamline background (BB)		0.018 ± 0.009	
Other corrections			
Radiative correction (M_{RC})	1.010 ± 0.010		
Detector bias (M_{Det})	0.998 ± 0.002		
Q^2 acceptance (M_{Q^2})	1.000 ± 0.012		
Azimuthal acceptance (M_ϕ)	1.006 ± 0.006		

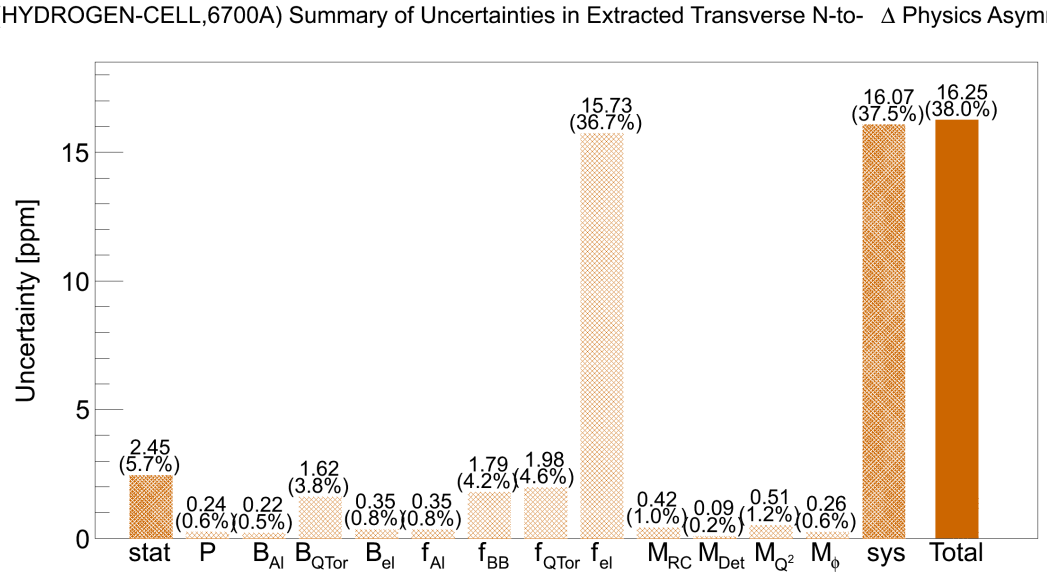

Figure 6.17 Summary of uncertainties in inelastic beam normal single spin asymmetry extraction. Measurement systematic contains the systematic uncertainties related to the extraction of the physics asymmetry such as regression, nonlinearity and acceptance averaging. The uncertainties are in ppm and the corresponding relative uncertainties are shown in parentheses.

6.7 Comparison With Model Calculation

No existing model calculation for beam normal single spin asymmetry was available at Q-weak kinematics during this analysis. Pasquini et al. [7] presented beam asymmetry in inelastic electron scattering (as shown in Figure 2.6, chapter 2) for large scattering angle at energies E = 0.424, 0.570, 0.855 GeV. The BNSSA were calculated separately for Δ and N intermediate states. The total asymmetry was the sum of these two intermediate states. Relatively large asymmetries were observed in the forward region; these are dominated by quasi Virtual Compton Scattering (VCS) kinematics where one exchanged photon becomes quasi-real. These asymmetries are sensitive to $\gamma^*\Delta\Delta$ form factors and can be a unique tool to study it [56].

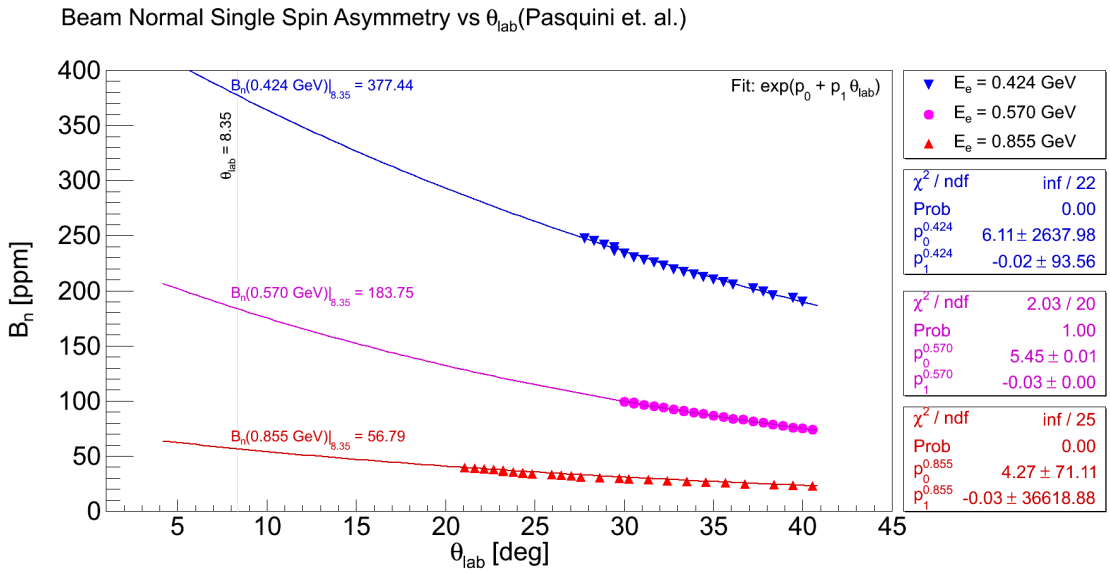

Figure 6.18 BNSSA calculation from Pasquini et al. The points are taken from [7]. Then, the calculation is fitted with a function of the form $f(\theta_{\rm lab}) = exp(p_0 + p_1\theta_{\rm lab})$ and extrapolated to Q-weak $\theta_{\rm lab}$ value.

These asymmetries were extrapolated to forward angle down to $\theta_{\rm lab}$<5° using a suitable fit for all available three energies from [7], as shown in Figure 6.18. The asymmetries were obtained at $\theta_{\rm lab}$ = 8.35° for three energies and extrapolated to Q-weak energy E_{beam} = 1.155 GeV in Figure 6.19. Using this hand waving toy model, the obtained BNSSA is B_n[model] = 12.15 ppm at Q-weak kinematics. The asymmetry from this analysis, $B_n[{\rm Q-weak}] = 42.82 \pm 16.25$ ppm is also shown in the Figure 6.19. The extrapolation uncertainties are large but can not be realistically estimated. New calculation are in progress.

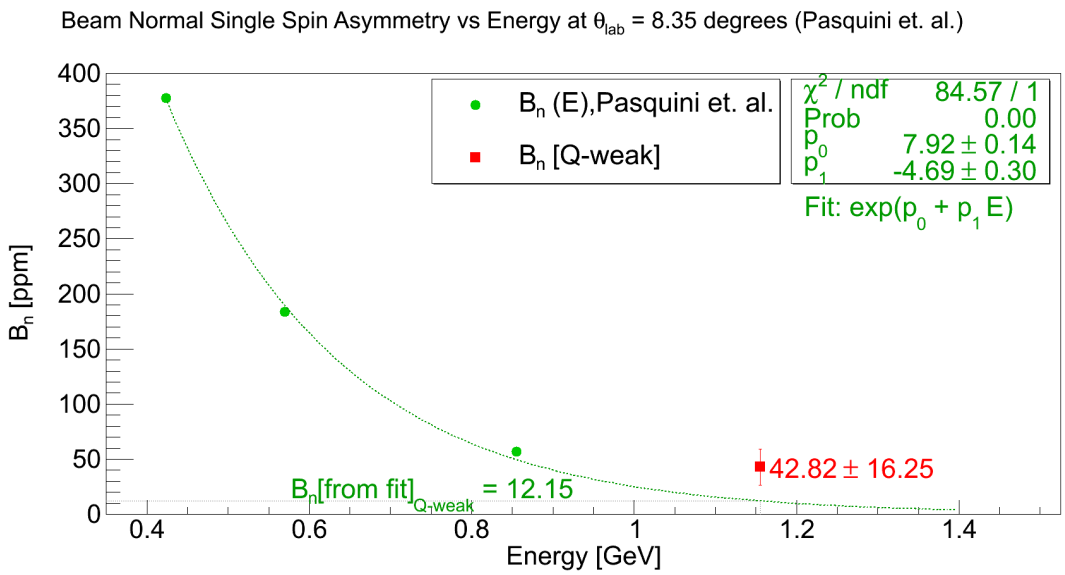

Figure 6.19 BNSSA asymmetry calculation from Pasquini et al. and its extension. The asymmetries from Figure 6.18 at $\theta_{\rm lab} = 8.35°$ are plotted here. A fit function of the form $f(E) = exp(p_0 + p_1 E)$ is used to extrapolate the asymmetry to the desired Q-weak kinematic region ($E = 1.155$ GeV).

6.8 BNSSA in LH_2 at Both Sides of the Inelastic Peak

Data on both sides of the inelastic peak (at QTor current 6000 A and 7300 A) were taken to better constrain the elastic dilution. The same prescription was used, as described in section 6.6, to extract the off peak physics asymmetries. The measured five-parameter regressed asymmetries are $\epsilon_M^{6000A} = 7.198 \pm 0.688$ (stat) ± 0.163 (sys) ppm, and $\epsilon_M^{7300A} = 0.717 \pm 0.476$ (stat) ± 0.252 (sys) ppm at QTor current 6000 A, and 7300 A, respectively (more details about the systematic studies are in APPENDIX D). Data were taken on the 4% downstream aluminum alloy target to determine the background contributions to the measured asymmetry at QTor current 7300 A, but there was no measurement at 6000 A. The measured regressed Al asymmetry at QTor current 7300 A is ϵ_M^{DSAl} = -0.108 $\pm$ 1.083 (stat) $\pm$ 1.140 (sys) ppm. After correcting for the acceptance difference between the upstream and downstream target windows, and the beam polarization, the background windows correction asymmetry becomes B_{Al}^{7300A} = -0.120 $\pm$ 1.791 ppm. A scaled Al windows asymmetry from the inelastic peak was used at 6000 A, where the LH_2 asymmetry was used to scale the Al asymmetry. The acceptance and polarization corrected asymmetry for windows correction is B_{Al}^{6000A} = 12.937 $\pm$ 2.709 ppm. The same dilution for the windows correction was used (see section 6.6.2.1) for both datasets. The correction from other neutral background, and beamline scattering were

same as inelastic peak dataset. The same elastic asymmetry was used for both datasets, whereas the dilutions were obtained using simulation as $f_{el}^{6000A} = 0.732 \pm 0.095$ and $f_{el}^{7300A} = 0.797 \pm 0.020$. The discrepancy between the data and simulation was larger for the left side of the inelastic peak, as shown in Figure 6.14, which contributed to the uncertainty in the dilution. The extracted beam normal single spin asymmetries at QTor current 6000 A and 7300 A are $B_n^{6000A} = 63.71 \pm 4.45$ (stat) $\pm$ 36.17 (sys) ppm, and $B_n^{7300A} = 42.17 \pm 5.26$ (stat) $\pm$ 9.85 (sys) ppm, respectively (see Figure 6.20).

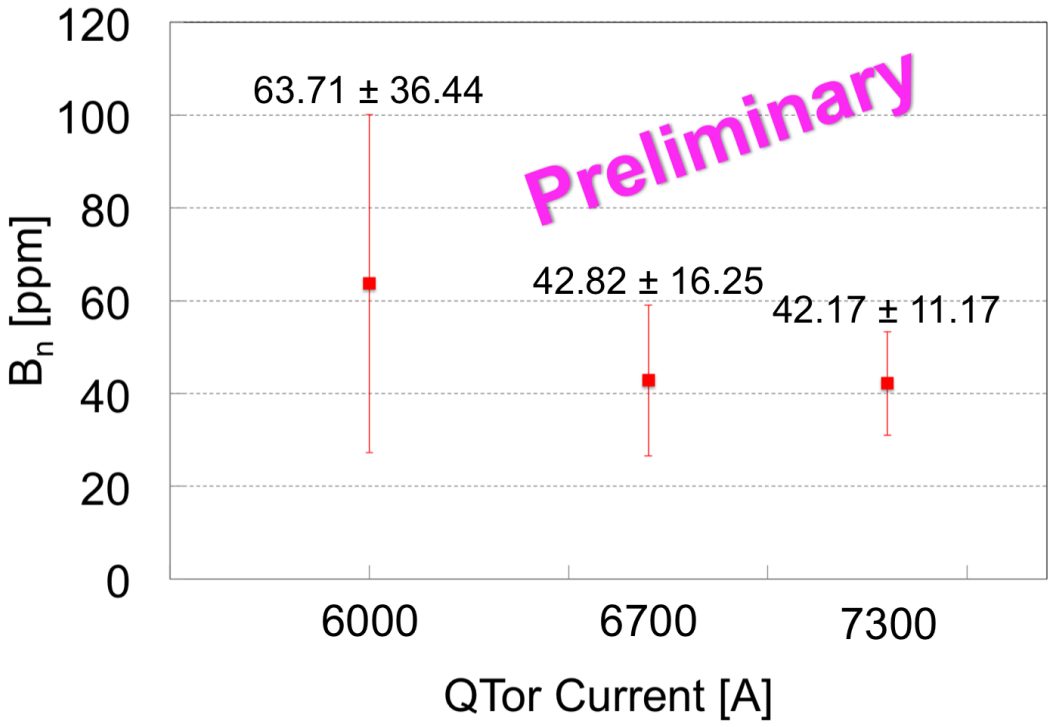

Figure 6.20 BNSSA at N→ Δ peak and off peak asymmetries in LH_2. The QTor current was changed to 6000 A, and 7000 A from 6700 A to cover the both sides of the N→ Δ peak. The missing mass, W, at the inelastic peak (6700 A) is 1.2 GeV. The uncertainty in the asymmetry is the total uncertainty and is the quadrature sum of the statistical and systematic uncertainties. The total uncertainty is dominated by the systematic uncertainty from elastic radiative tail.

6.9 BNSSA in Nuclear Targets

In this chapter, the inelastic beam normal single spin asymmetry measurements in e-p scattering have been discussed. In addition to the inelastic data from the proton, Q-weak has data on the beam normal single spin asymmetry measurements from several other physics processes. Few of

these measurements are the first of their kind and carry interesting physics. The measured regressed five-parameter asymmetries on liquid hydrogen cell, 4% thick downstream aluminum alloy, and a 1.6% thick downstream carbon foil are summarized in Table 6.9. The relative statistical precision of the measurements are also shown. The analysis of these data is ongoing and expected to test model calculations of beam normal single spin asymmetry.

Table 6.9 Measured regressed five-parameter asymmetries in inelastic electron-nucleon scattering for transverse polarized beam. Horizontal and vertical transverse data set are shown separately. The combined (error weighted average) asymmetries are also noted. The inelastic peak is at QTor current 6700 A. The other QTor currents were taken to improve the simulation for elastic radiative tail. The first uncertainty represents statistical contribution, whereas second represents systematic contribution. The missing mass, W, at the inelastic peak (6700 A) is 1.2 GeV.

Pol.	Asymmetry [ppm]		
	QTor currents		
	6000 A	6700 A	7300 A
		LH_2	
Hor.	7.198 ± 0.688 ± 0.163	5.303 ± 0.533 ± 0.092	0.717 ± 0.476 ± 0.252
Ver.		4.457 ± 0.807 ± 0.117	
Both	7.198 ± 0.688 (9.5%)	5.047± 0.444 (8.7%)	0.717 ± 0.476 (49.3%)
		Al	
Hor.		7.911 ± 1.187 ± 0.482	-0.108 ± 1.083 ± 1.140
Ver.		9.533 ± 1.759 ± 0.870	
Both		8.419 ± 0.984 ± 0.603 (11.7%)	-0.108 ± 1.083 ± 1.140 (87.3%)
		^{12}C	
Hor.		9.869 ± 1.870 ± 0.549 (18.3%)	

6.10 Conclusion

The Q-weak collaboration has made a 35% relative measurement of the beam normal single spin asymmetry of $B_n = 42.82 \pm 2.45$ (stat) ± 16.07 (sys) ppm using transversely polarized 1.155 GeV electrons scattering in-elastically from protons with an average Q^2 of 0.0209 $(\text{GeV/c})^2$, an average scattering angle of 8.3°, and missing mass of 1.204 GeV. This is the first measurement of the beam normal single spin asymmetry in inelastic electron-proton scattering. This measurement would be an excellent test of theoretical calculations. Unfortunately, at the time of this analysis, there was no existing theoretical calculation or model to compare with the data. Hopefully this thesis will encourage theoreticians to produce new calculations.

SECTION 7
SUMMARY OF CONTRIBUTIONS AND CONCLUSIONS

This dissertation presents the highlights of my Ph.D. research work in the context of the Q-weak experiment. This chapter summarizes the results and conclusions presented so far. My contributions towards the measurement of the weak charge of the proton can be summarized under three categories: the beam modulation system, the beamline optics and false asymmetries, and the beam normal single spin asymmetry measurement in inelastic electron-proton scattering. The experience gained during this experiment will help the future precision parity violating measurements at the Jefferson Lab such as the Møller experiment [133].

7.1 Beam Modulation

The electron-proton scattering rate largely depends on the five beam parameters: horizontal position, horizontal angle, vertical position, vertical angle, and energy. Changes in these beam parameters when the beam polarization is reversed create false asymmetries. Although attempts have been made to keep changes in beam parameters during reversal as small as possible, it is necessary to correct for such false asymmetries. To make this correction precisely, I implemented a beam modulation system to induce small position, angle, and energy changes at the target to characterize detector response to the beam jitter. The beam modulation system modulated position and angle using two pairs of air-core dipoles separated by ∼10 m and pulsing one pair at a time to produce relatively pure position or angle changes at the target. The beam energy was modulated using an SRF cavity. The system has been commissioned using the simulated optics from OptiM [82] and collected data during the experiment. The beam modulation system was designed for sinusoidal modulation up to 250 Hz which was robust and well-suited for the experiments measuring small parity violating asymmetries like the Q-weak experiment. At the cost of 1% of beam time for one parameter, the system was able to measure all sensitivities up to 10% accuracy each day. The pairs of coils were tuned to deliver relatively pure positions or angle modulations, making it much less likely that singular matrices are encountered when solving for the sensitivities. The ratio of coil currents was adjusted to incorporate any optics change in the beamline compare to move the coils physically, which made the system independent of the design optic. For 1.165 GeV electron beam, using 125 Hz sinusoidal drive signal, the Trim power amplifier was able to provide the desired beam modulation amplitudes with existing air-core MAT coils. The modulation system worked quite well for the

span of two years during the Q-weak experiment and collected data noninvasively with production running. Preliminary detector sensitivities were extracted which helped to reduce the width of the measured asymmetry. The beam modulation system also has proven valuable for tracking changes in the optics, such as dispersion at the target and beam position coupling [177]. The system has also helped to track some of the hardware and software problems in the BPMs in the Hall-C beamline.

7.2 Beamline Work

The beam position monitors (BPMs) in front of the target were used for the linear regression, and hence, it was necessary to know their position and angle resolutions. We developed and simulated the concept of the virtual BPM to determine the position and angle at the target. I extracted the position resolution of the BPM in front of the target by observing the residual of beam position differences (between two helicity states) on any BPM and the orbit projected from the virtual target BPM. Using selective data samples from the commissioning phase of the experiment, the average BPM resolution was 0.70 μm and 0.77 μm for X and Y, respectively. The target BPM angle resolution was simulated using OptiM [82]. A relatively pure position measurement, which corresponds to pure angle measurement at target, was chosen to be at BPM 3P02A from the simulation to extract the angle resolution. Assuming 0.90 (0.96) μm X(Y)-position resolutions, the estimated target BPM angle resolutions at 180 μA are 0.048 μrad, and 0.060 μrad for X' and Y', respectively. A new least square linear regression scheme was developed based on my BPM study.

I surveyed the helicity correlated pedestals to improve the false asymmetry contribution for the entire data set of the experiment. No helicity correlated pickups were seen for most of the detector channels and were at $\mathcal{O}(1)$ ppb. Electronic noise levels were generally acceptable, though potentially marginal for the upstream luminosity (USLumi) monitor channels near the end of Run 1 but improving during Run 2. Nonlinearity due to pedestal errors for main detectors were extremely small whereas USLumi had a nonlinearity of few percent. There is a scope for improvement in USLumi pedestal. Nonlinearity could be very large for low-yield production running on aluminum and N$\rightarrow \Delta$ but still be under 1%. Resolutions for all the detectors were reasonably stable.

7.3 Beam Normal Single Spin Asymmetry in Inelastic e+p Scattering

The objective of the Q-weak experiment is to challenge the predictions of the Standard Model in low Q^2 range and search for new physics at the TeV scale through a 4% measurement of the weak charge of the proton *via* the parity-violating asymmetry ($\sim$250 ppb) in elastic electron-proton

scattering [16]. One of the potential corrections for the PV asymmetry comes from the residual transverse polarization in the beam. There is a parity conserving beam normal single spin asymmetry or transverse asymmetry (B_n) on H_2 with a $\sin(\phi)$ like dependence due to two-photon exchange. The size of B_n is few ppm. So, a few percent residual transverse polarization in the beam, in addition to potentially small broken azimuthal symmetries in the detector, might lead to few ppb corrections to the Q-weak data. As part of a program of B_n background studies, we made the first measurement of B_n in the N$\rightarrow \Delta$ transition using the Q-weak apparatus. B_n provides direct access to the imaginary part of the two-photon exchange amplitude. The magnitude of B_n in the N$\rightarrow \Delta$ transition has never been measured before. The B_n from electron-nucleon scattering is also a unique tool to study the $\gamma^*\Delta\Delta$ form factors [178].

The Q-weak collaboration has made the first measurement of the beam normal single spin asymmetry in the N-to-$\Delta(1232)$ transition. After correcting for backgrounds and beam polarization, I extracted the final transverse asymmetry $B_n = 42.82 \pm 2.45$ (stat) $\pm$ 16.07 (sys) ppm using transversely polarized 1.155 GeV electrons scattering in-elastically from protons with a Q^2 of 0.0209 $(\mathrm{GeV/c})^2$ and missing mass of 1.204 GeV. This measurement would be an excellent test of theoretical calculations. In addition to the inelastic data from the proton, Q-weak has data on the B_n measurements from several other physics processes. The asymmetries were measured on liquid hydrogen cell, 4% thick downstream aluminum alloy, and a 1.6% thick downstream carbon foil. Some of these measurements are the first of their kind and carry interesting physics. The analysis of these data is ongoing and expected to test the theoretical models on beam normal single spin asymmetry and thereby our understanding of the doubly virtual Compton scattering process. Unfortunately, at the time of this analysis, there was no existing theoretical calculation or model to compare with the data. Hopefully this thesis will encourage theoreticians to produce new calculations.

APPENDICES

APPENDIX A
BEAM MODULATION

A.1 Beam Modulation

$$dA = \frac{1}{\sqrt{N}} = 1 \times 10^{-6} = 1\ ppm \tag{A.1.1}$$

$$N = 10^{12}\ \text{counts} = Rt \tag{A.1.2}$$

$$t = \frac{N}{R} = \frac{10^{12}}{8 \times 800 \times 10^{6}\ Hz} = 156.25\ s \tag{A.1.3}$$

Table A.1 The components of beam modulation bench test.

The Components	Quantity
Signal Generator	1
TRIM-II	2
MAT Coil	2
LEM	1
Ammeter	2
Power Supply	1
Tesla Meter	1

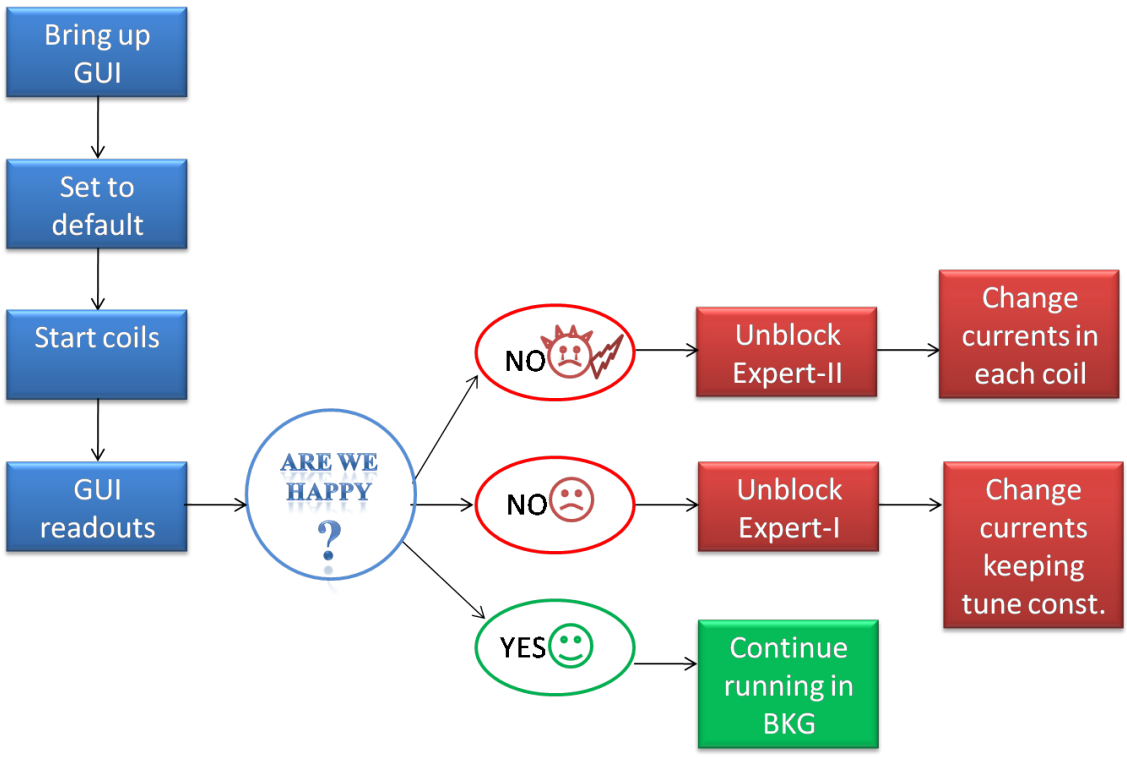

Figure A.1 BMod GUI design flow chart.

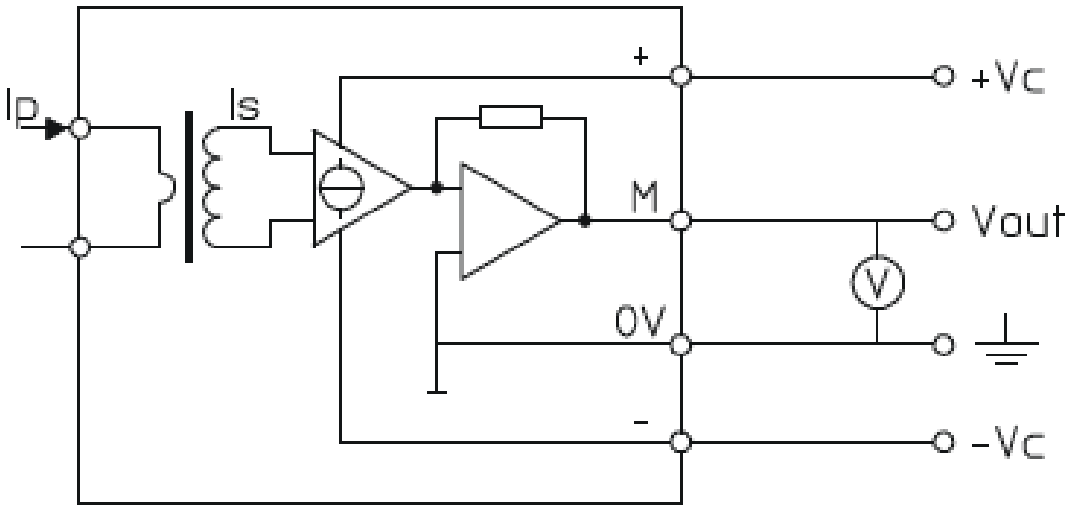

Figure A.2 The circuit design of the LEM current transducer used to measure the current through the beam modulation magnet.

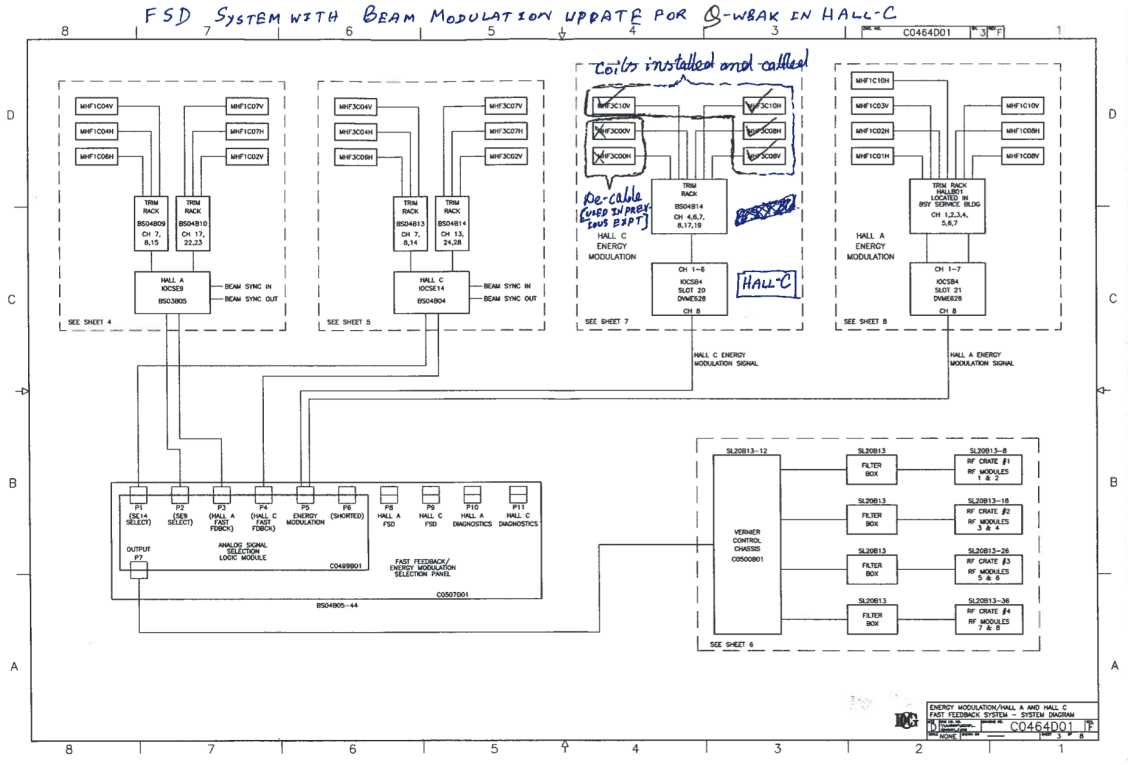

Figure A.3 Fast shut down circuit diagram for Q-weak. The modification shown are implemented before the experiment.

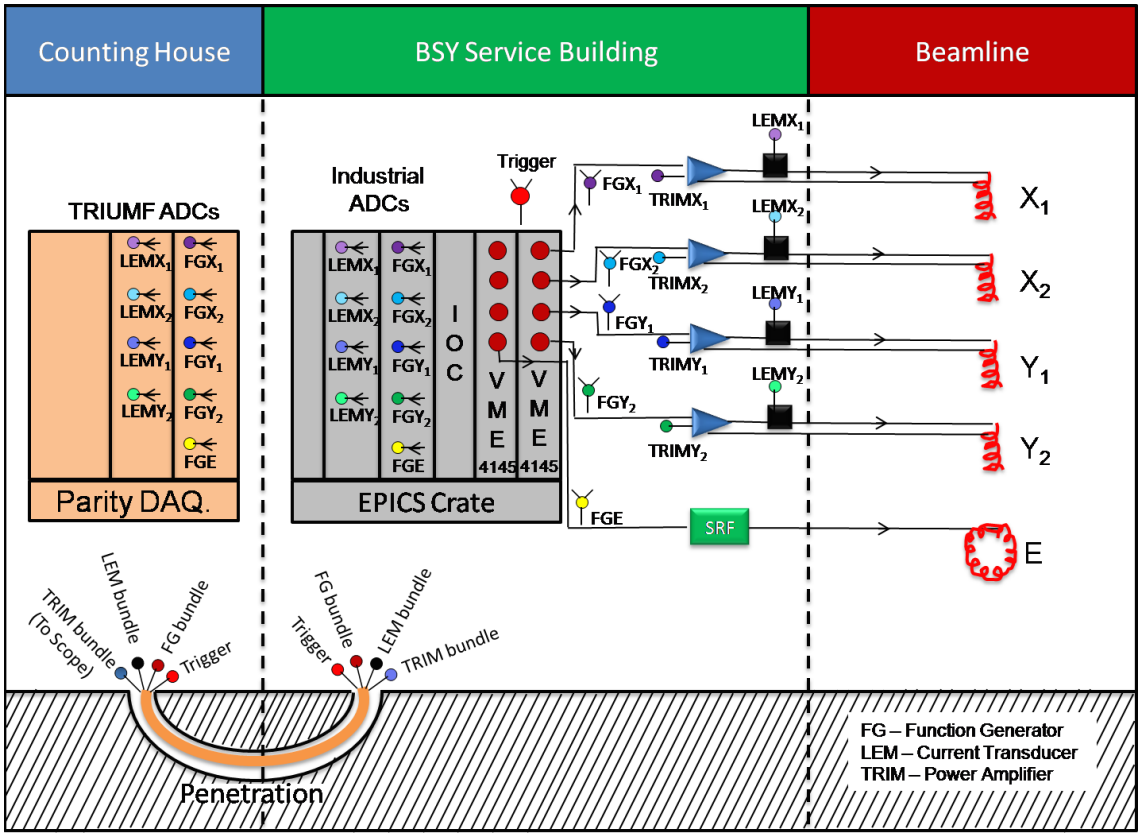

Figure A.4 The cable path for the modulation system. The components are spanned into counting house Hall-C and beamline.

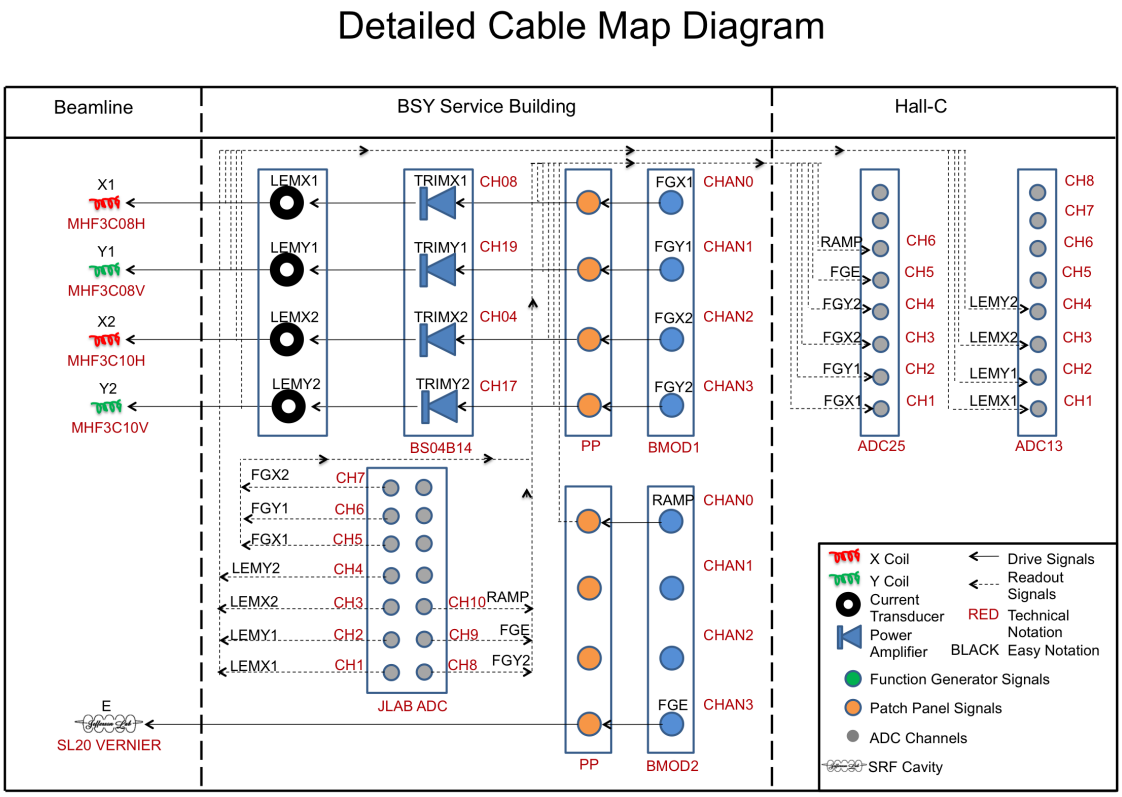

Figure A.5 The cable map for the modulation system.

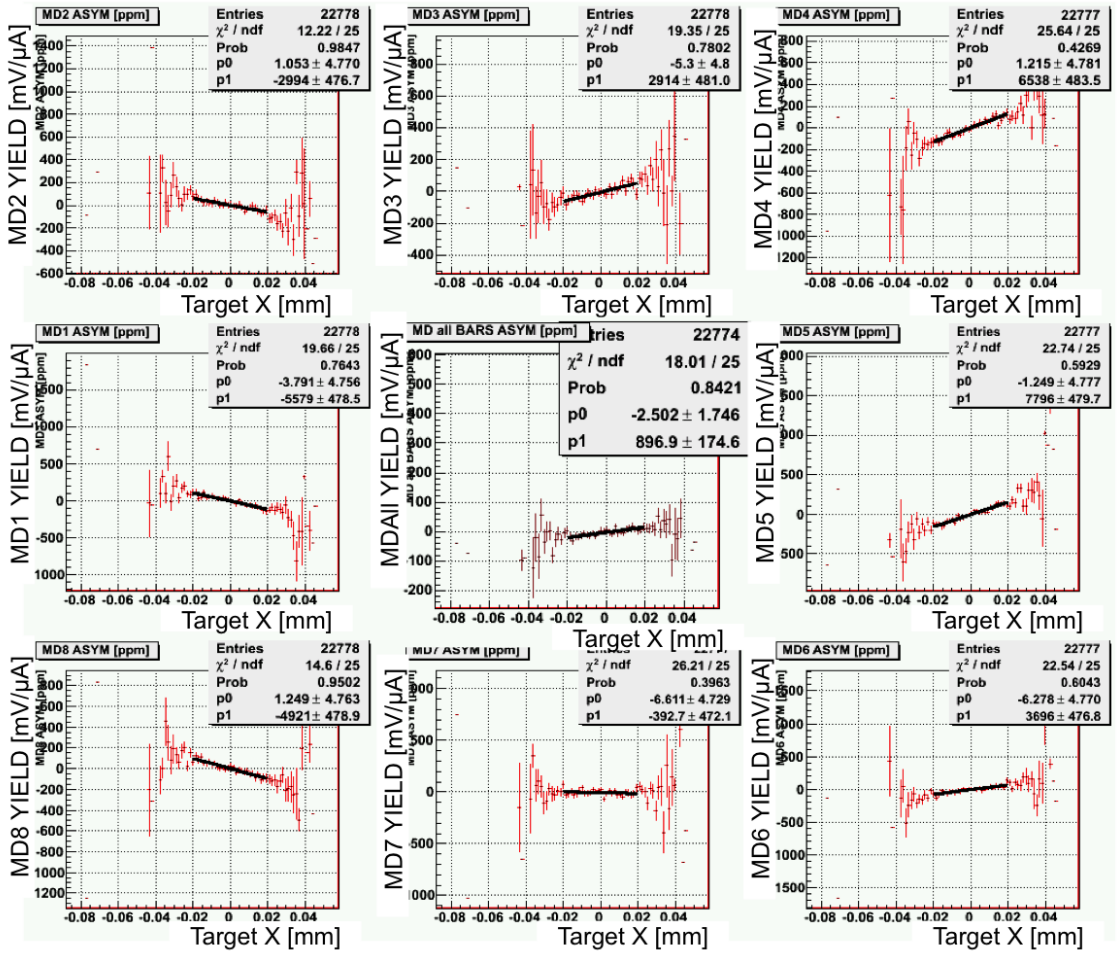

Figure A.6 Main detector sensitivities with respect to target BPM X position for X modulation. The eight octants along with combined sensitivities are shown.

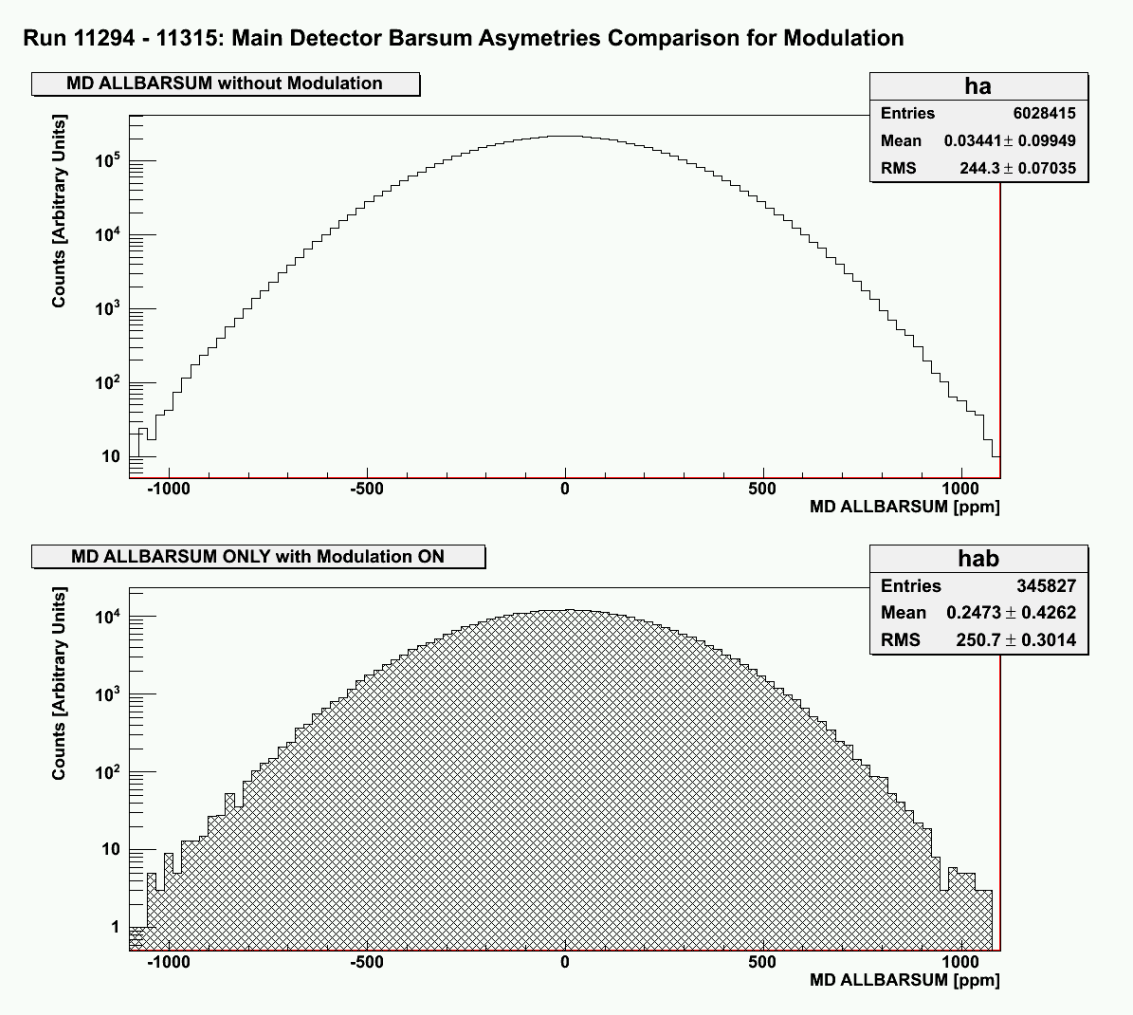

Figure A.7 Effect of beam modulation on main detector asymmetry. Comparison of main detector asymmetry when modulation is OFF (top) and modulation is ON (bottom) are shown here.

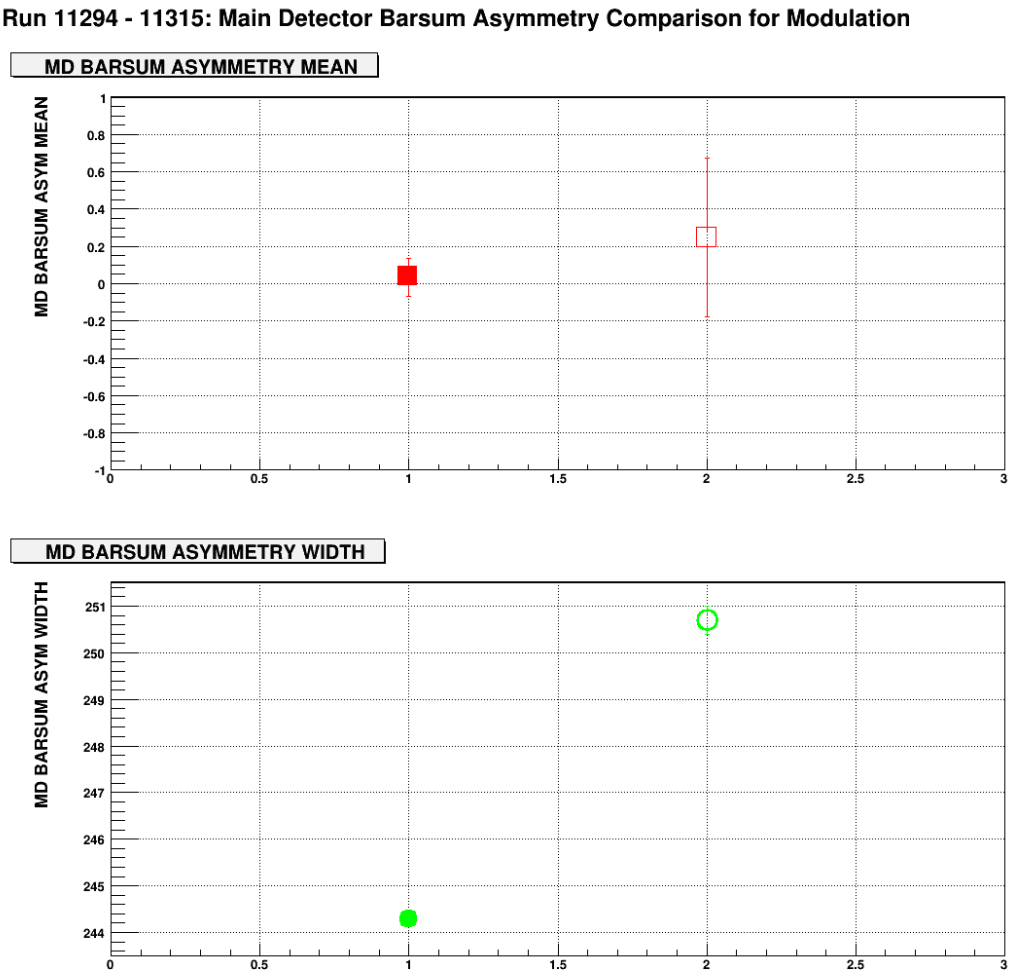

Figure A.8 Effect of beam modulation on main detector asymmetry. Main detector asymmetry mean when modulation is OFF and ON (top) and asymmetry width (bottom) are compared here.

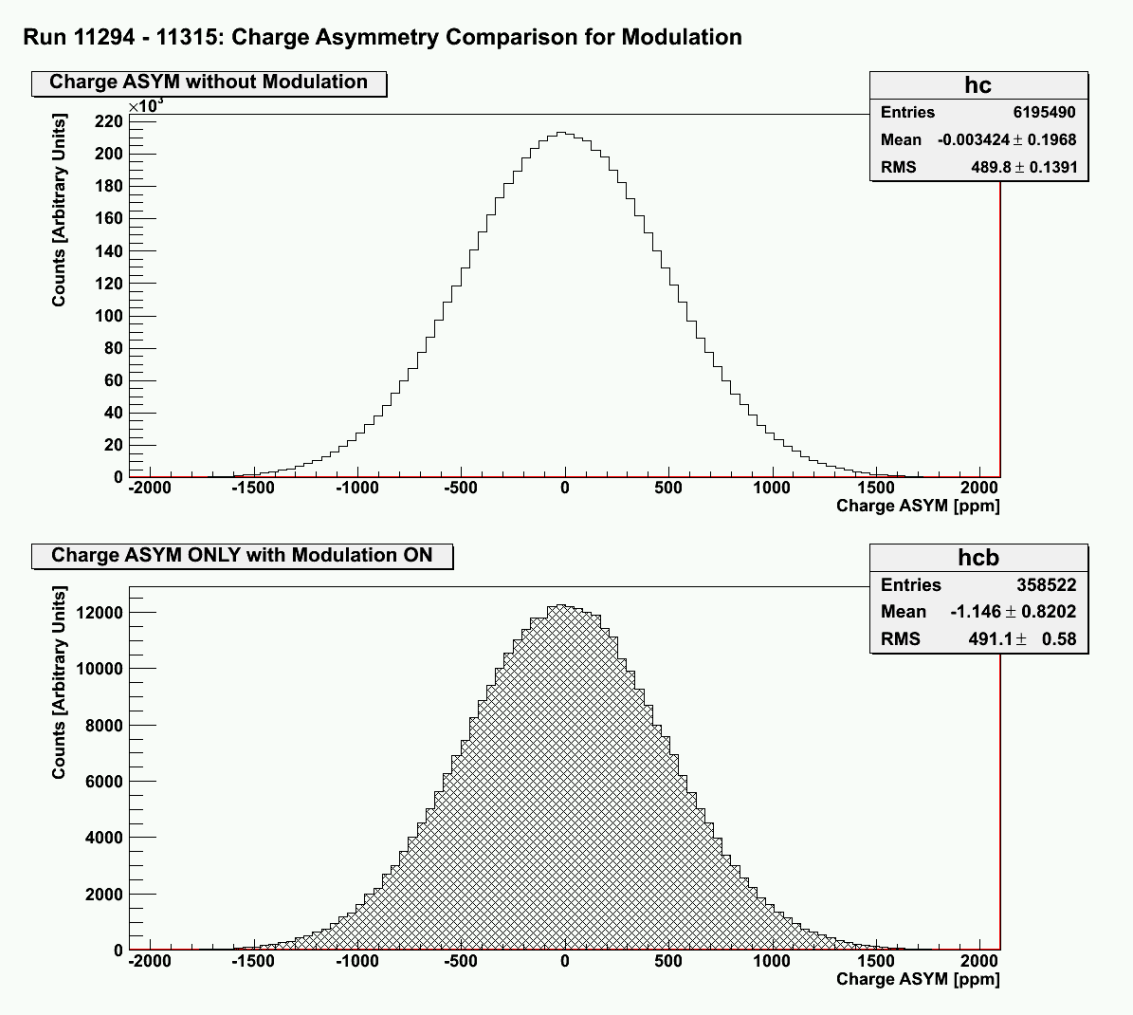

Figure A.9 Effect of beam modulation on charge asymmetry. Comparison of charge asymmetry when modulation is OFF (top) and modulation is ON (bottom) are shown here.

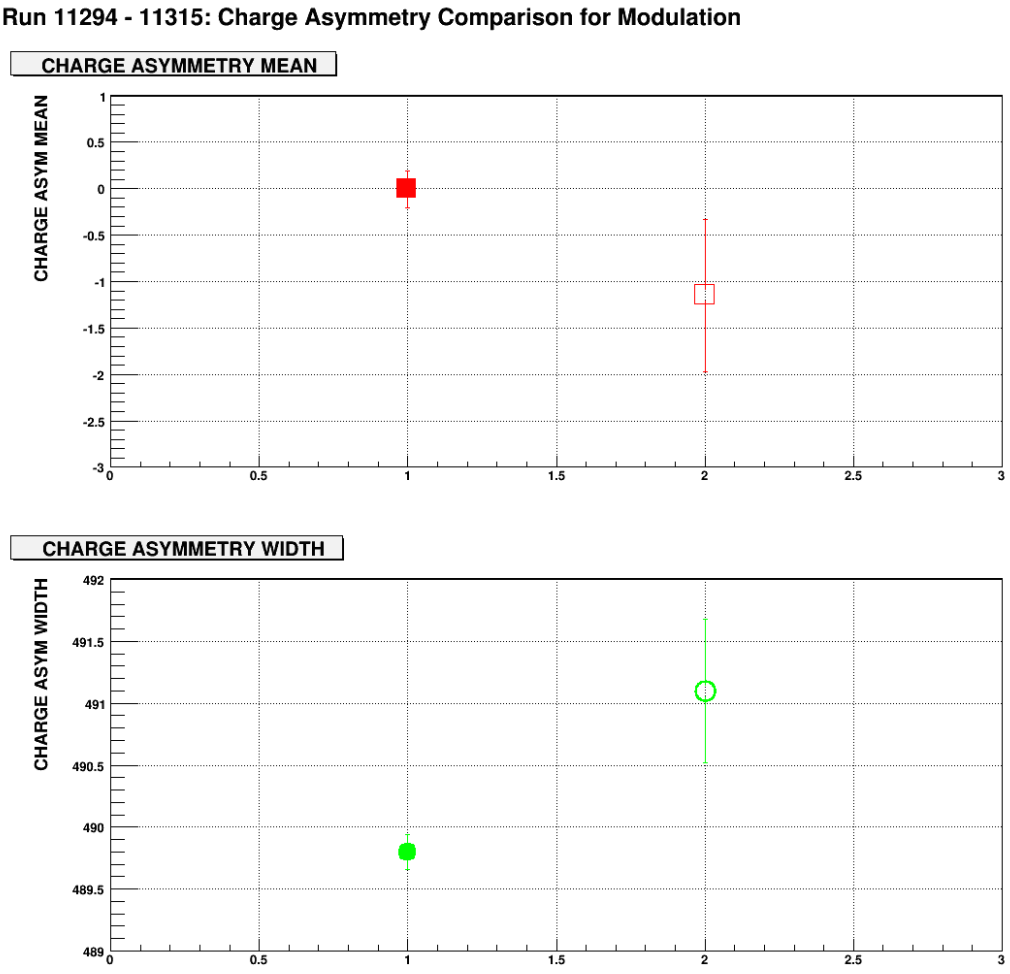

Figure A.10 Effect of beam modulation on charge asymmetry. Comparison of charge asymmetry without modulation with charge asymmetry only during modulation ON.

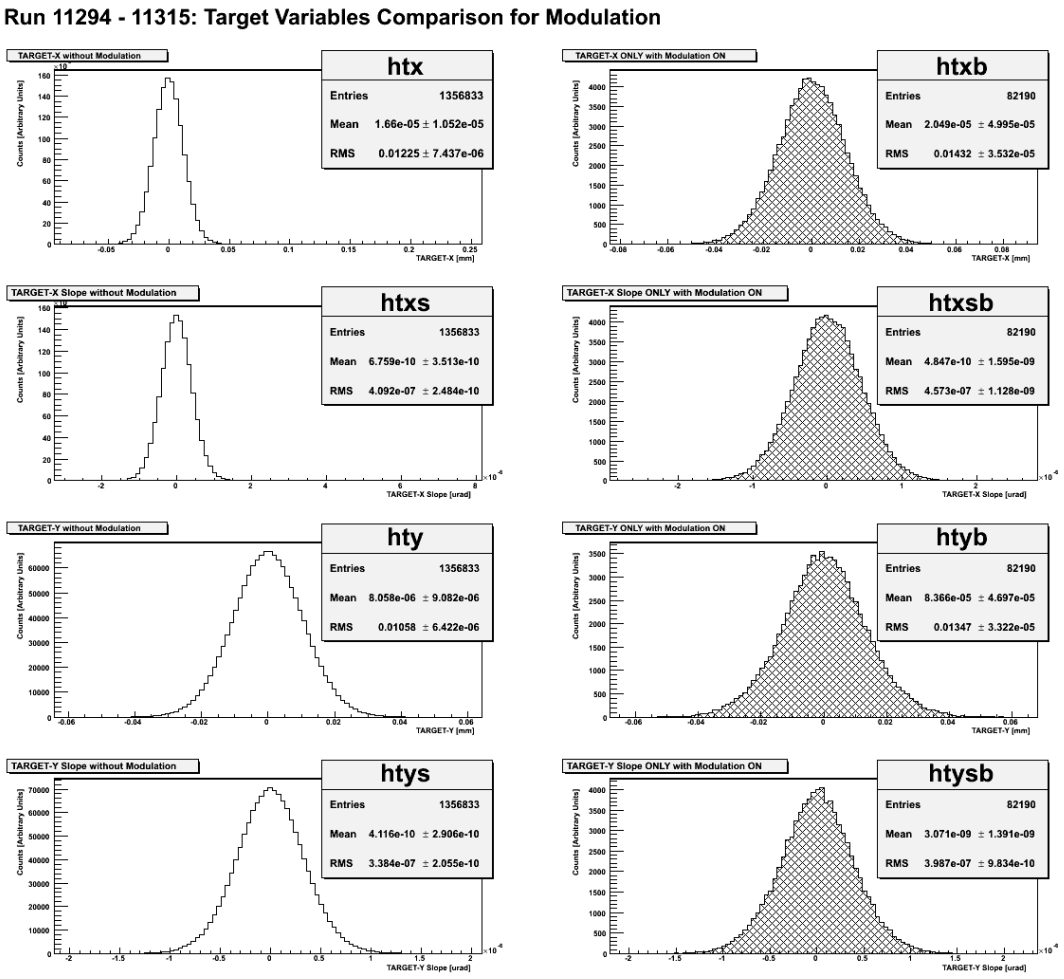

Figure A.11 Effect of beam modulation on target BPM. Comparison of target BPM differences when modulation is OFF (left) and modulation is ON (right) are shown here.

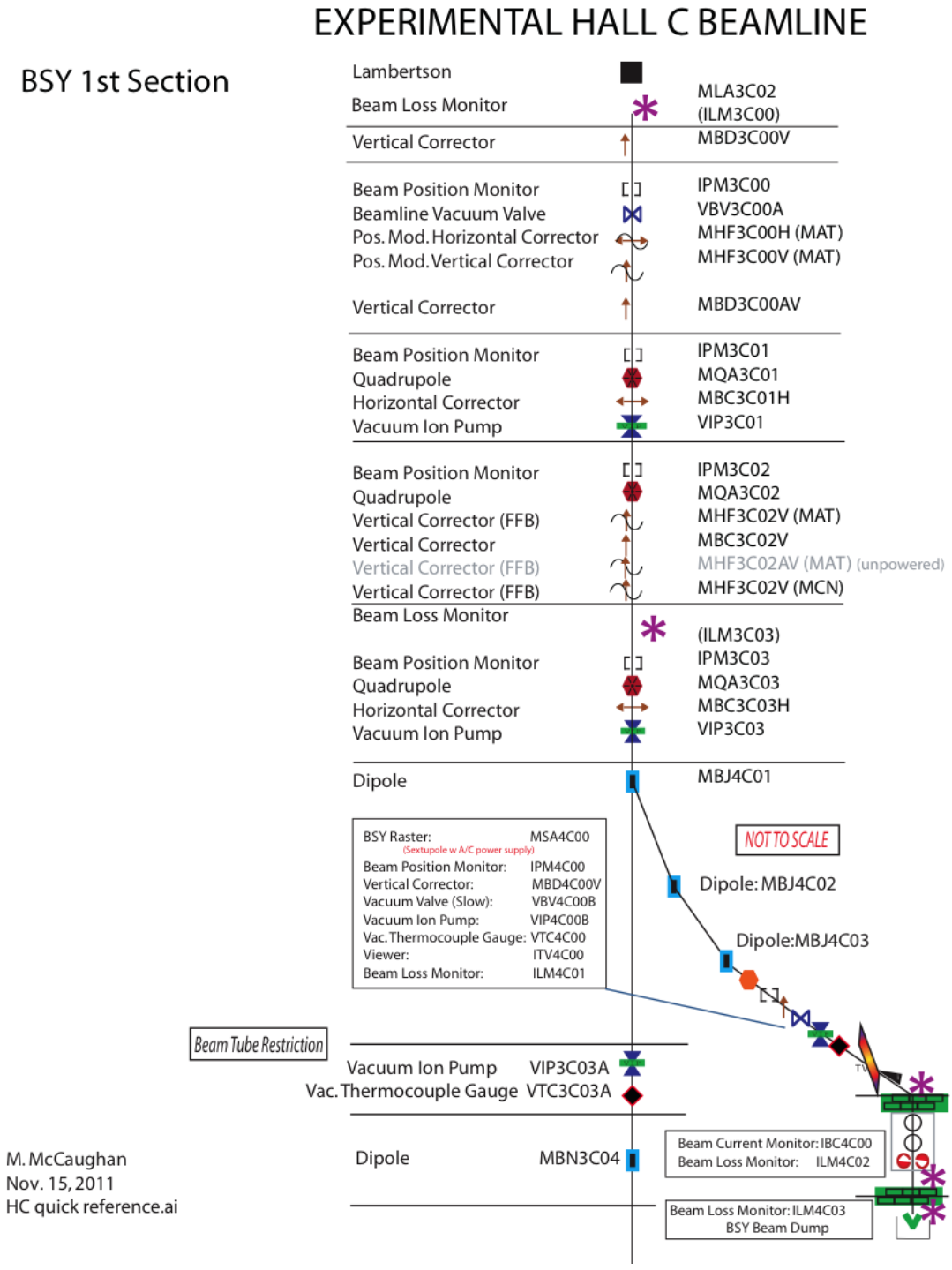

Figure A.12 Beamline drawing 1.

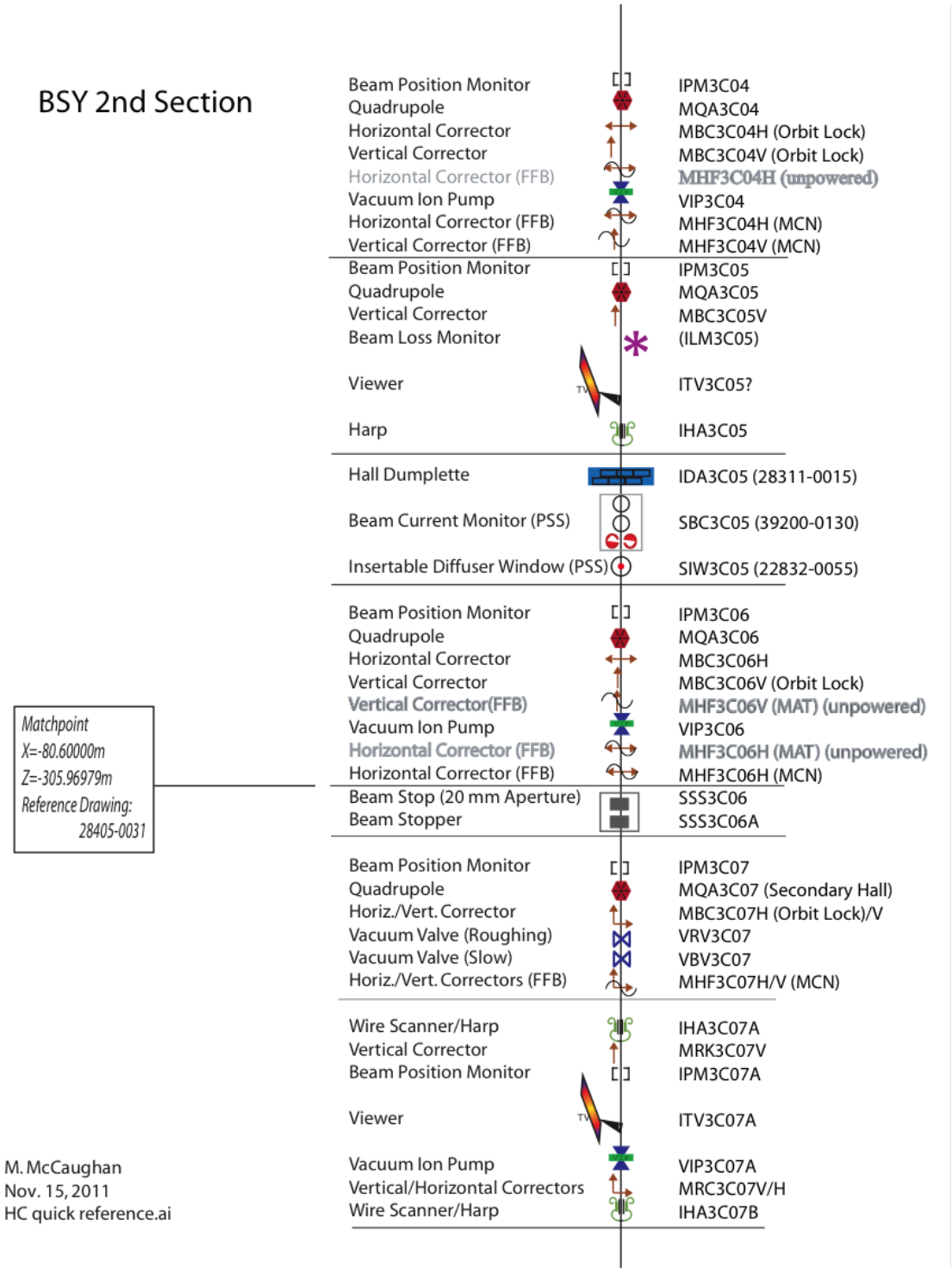

Figure A.13 Beamline drawing 2.

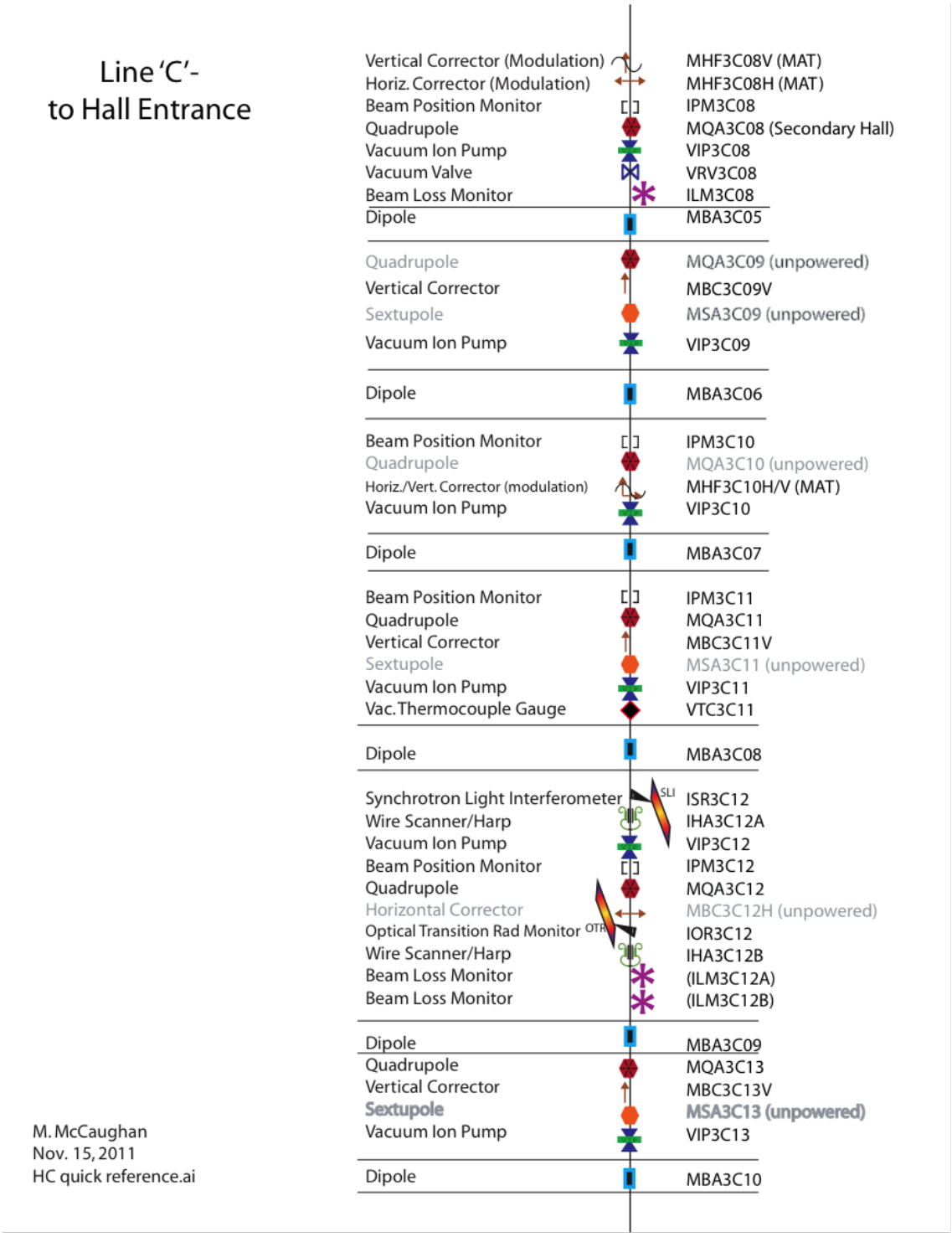

Figure A.14 Beamline drawing 3.

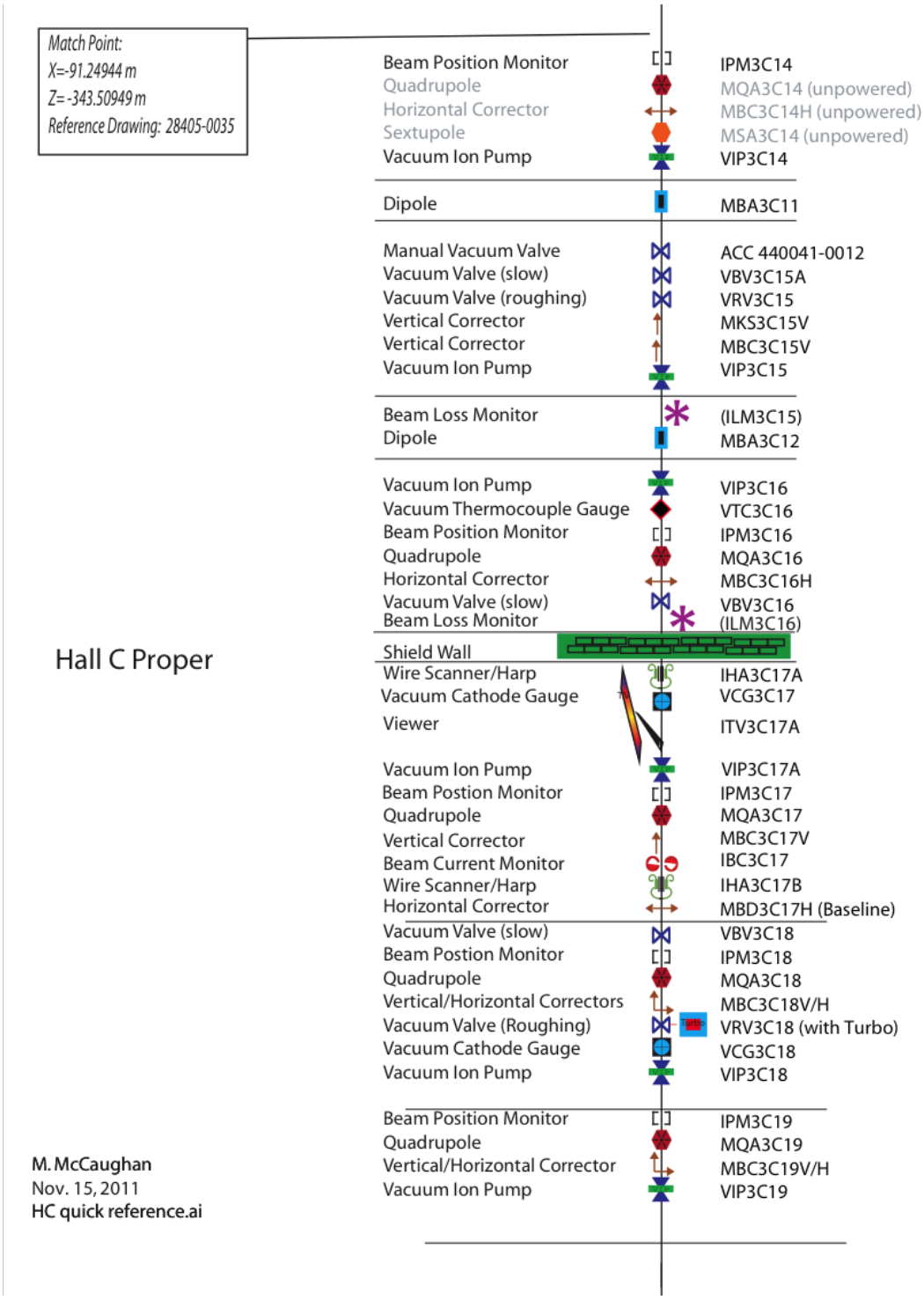

Figure A.15 Beamline drawing 4.

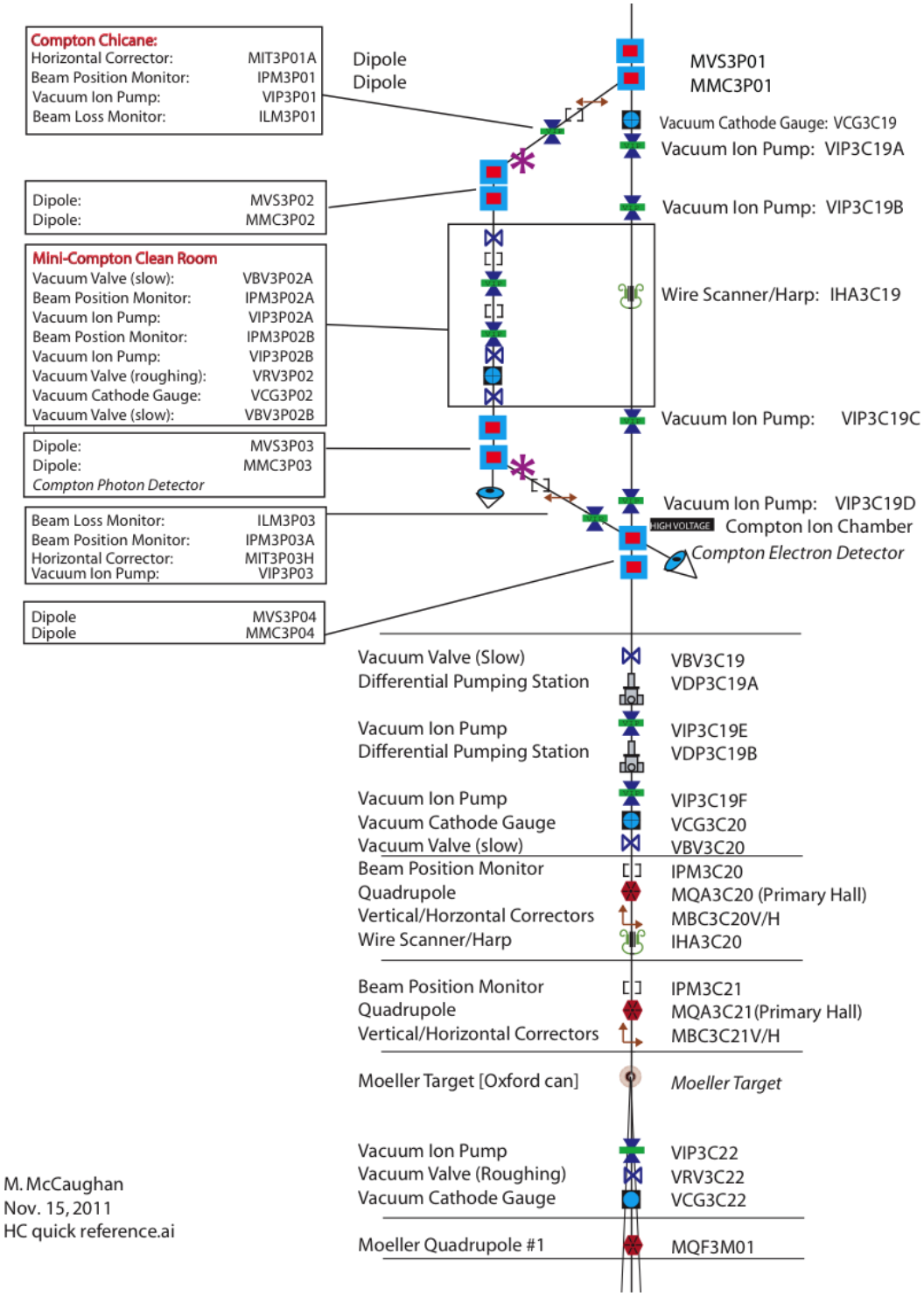

Figure A.16 Beamline drawing 5.

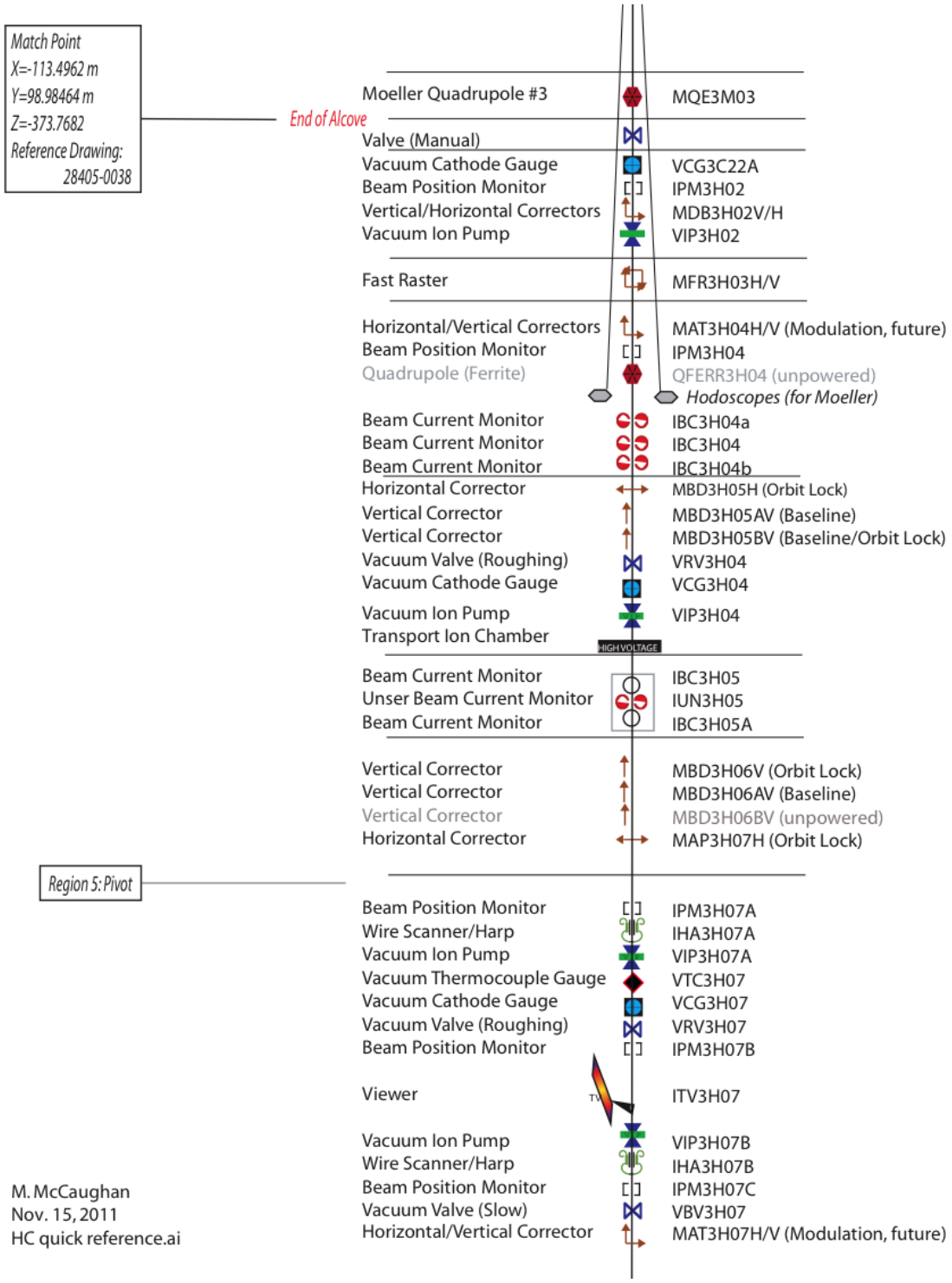

Figure A.17 Beamline drawing 6.

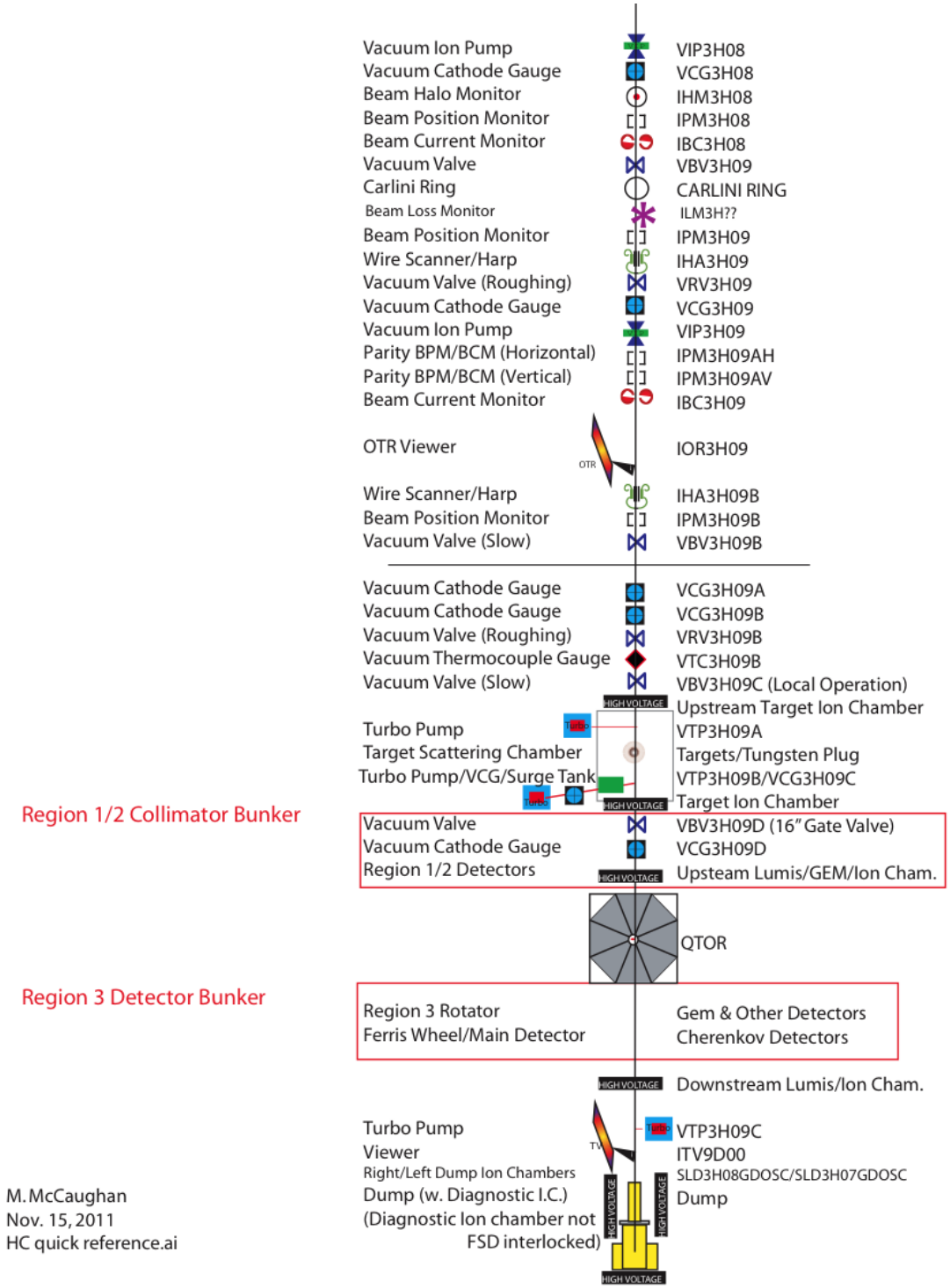

Figure A.18 Beamline drawing 7.

APPENDIX B
QTOR

B.1 Hall Probe

The QTor Hall probes were hooked up to a Lakeshore controller, taken from the old HMS hut. The VME IOC inside the HMS hut was also moved to the doghouse and was connected to the Lakeshore controller. After restoring some boot information on the CPU (vmec18), the EPICS controls was used to to control the system. The EPICS names for the Lakeshore controller outputs were Q1HallP, Q2HallP and Q3HallP. The hall probes can be read from the cdaq machines with the commands:

```
caget Q1HallP
caget Q2HallP
caget Q3HallP.
```

These channels were also added to the QTor GUI, that controlled the QTor power supply. There are EPICS commands to zero the probes:

```
caput Q1ZeroP
caput Q2ZeroP
caput Q3ZeroP.
```

These will send the command "ZCAL" to the Lakeshore for the specified probe. In addition, the IOC for the Hall probe was also accessed via the portserver.

B.2 QTor Corrector Magnet

The idea of this analysis is to estimate beam steering due to QTOR fringe field assuming a field of 4500 Gauss-cm along the beam axis using OPTIM.

Recently we discovered QTOR steers the forward beam. We tried to examine whether this steering is due to expected QTOR fringe field along the beam axis, or it indicates misalignment or motion of any QTOR coils. The steering implies a field integral of 4500 Gauss-cm. See more details in [1]. In this analysis we tried to predict the effect of QTOR fringe field (4500 Gauss-cm) along the beam axis Using OPTIM simulation.

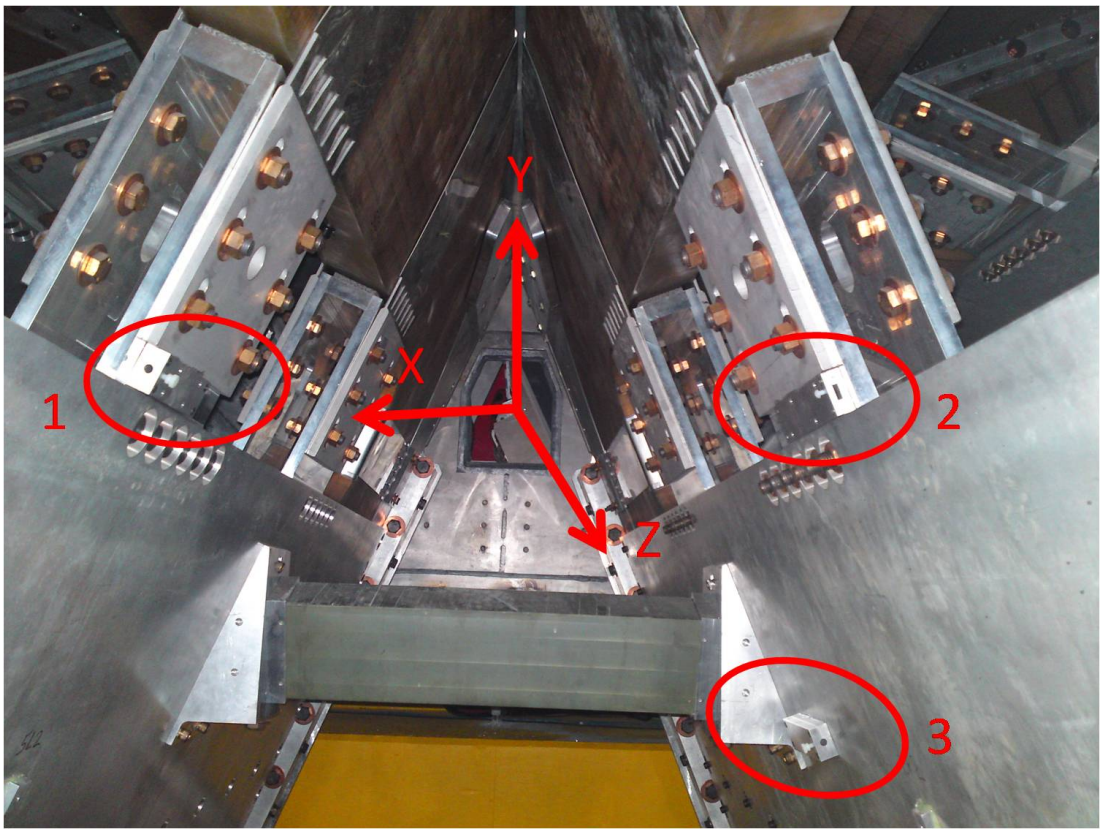

Figure B.1 QTor hall probe mounts and their locations inside the QTor are shown here.

B.2.1 TOSCA

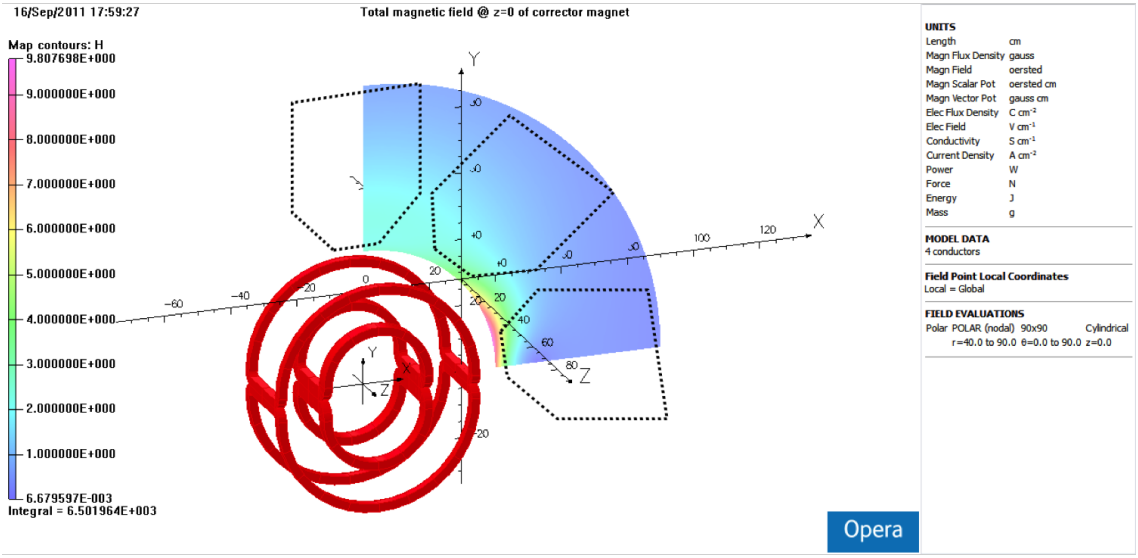

Figure B.2 The QTor corrector magnet design and magnetic field for an octant at Z=0. The primary collimator openings are also shown in the figure. The magnetic fields along the collimator openings are simulated.

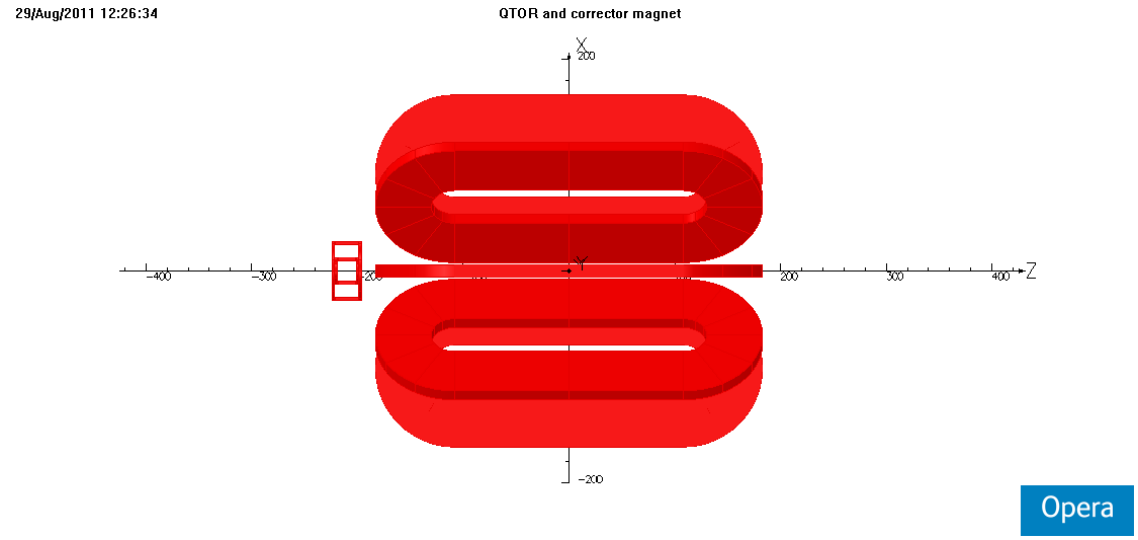

Figure B.3 The QTor with its corrector magnet from side view.

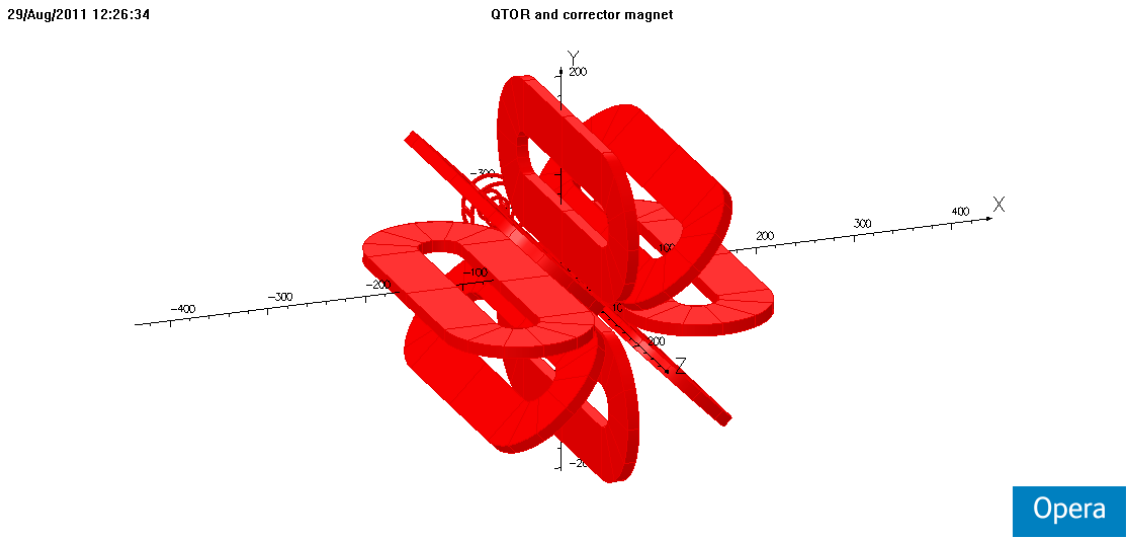

Figure B.4 A three-dimensional view of the QTor with its corrector magnet.

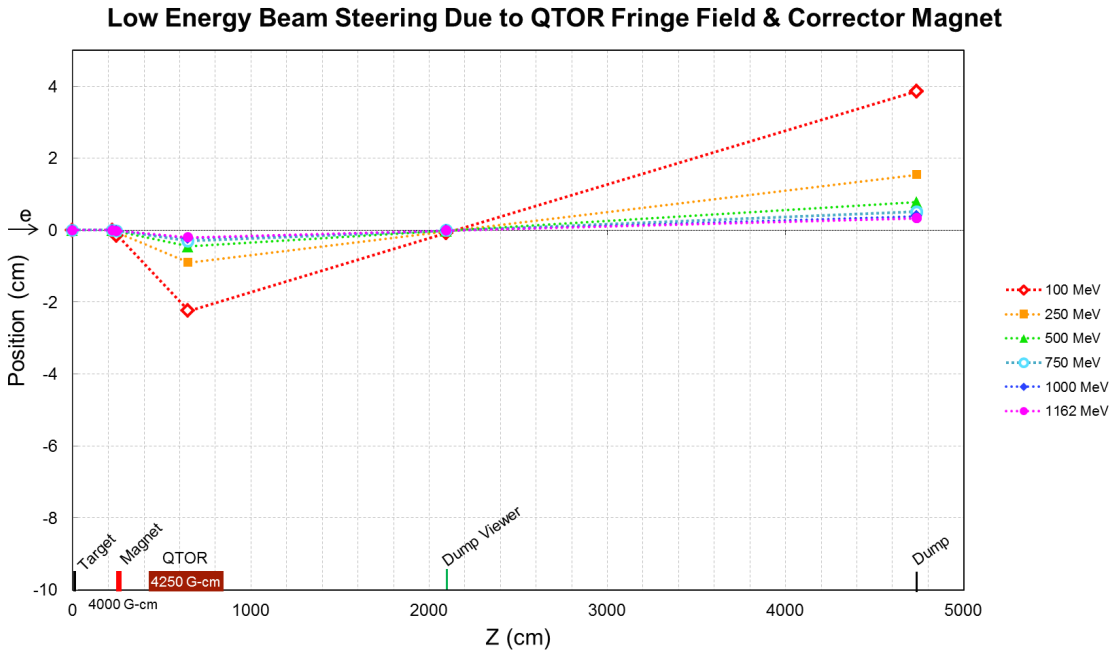

Figure B.5 The trajectory of scattered electrons 4000Gcm QTor fringe field at the dump viewer.

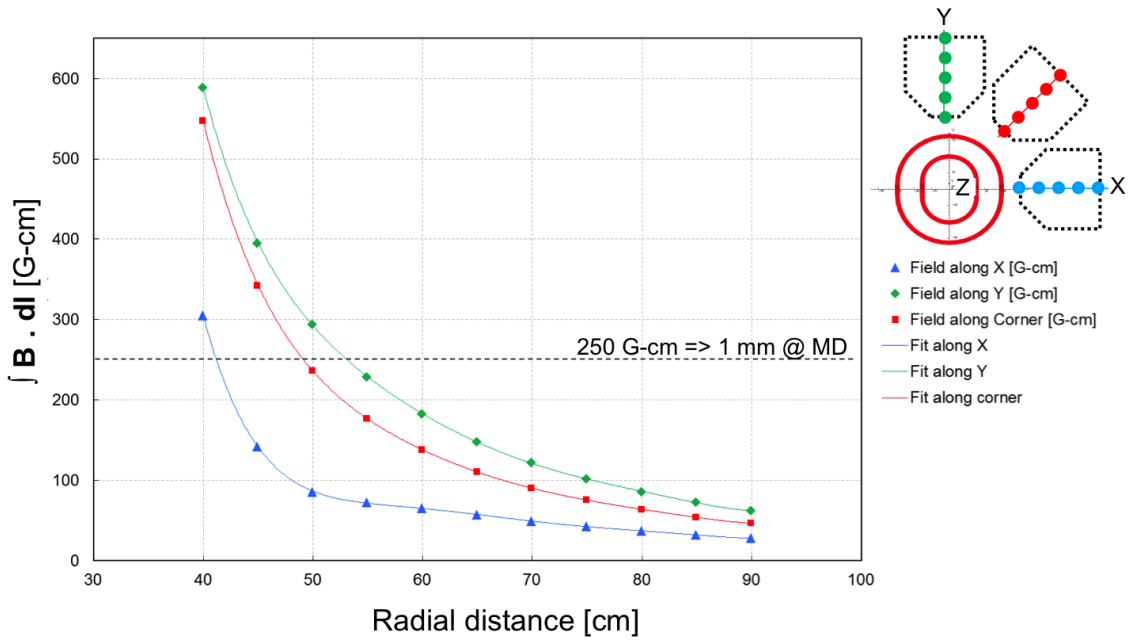

Figure B.6 The QTor corrector field integral variation along the radial direction.

QTOR Corrector Magnet Basic Calculation

Half Length along Z	Radius	Cross-section	Current	No. of turns	Length per turn	Total Length	Mass	Current per turn	Current Density	Wire Resistance	Block Resistance	Wire Power	Block Power	Voltage	Temperature
b	r	A	I	N	L = 2(2b+πr) + Δ	LT = 1.1*L*N	m = ρ-Cu*V	It = I/N	σ = I/A	Rt = N^2 ρL/A	R = ρL/A	Pt = It^2Rt	P = I^2R	V = IR	T = P/m.C
[cm]	[cm]	[cm^2]	[A-turns]	[turns]	[cm]	[cm]	[kg]	[A]	[A/cm^2]	[Ω]	[Ω]	[W]	[W]	[V]	[K/s]
8	14	10	2600	240	132.48	34946.76	11.87	10.84	260.00	1.27	2.21E-05	149.56	149.56	13.79	3.23E-02
10	28	6.25	1000	150	240.96	39726.62	13.49	6.67	160.00	1.45	6.44E-05	64.38	64.38	9.65	1.22E-02

Constant Table

Resistivity	Cu-Density	Specific Heat	Wire Area
ρ	ρ-Cu	C	WA
[Ω-m]	[kg/m^3]	[J/kg.K]	[cm^2]
1.67E-08	8960	390	0.0417

Available conductors

BC Coil					
20	10	56	225	60.00	13500.00
15	8	56	225	46.00	10350.00
Coil Spool					30096
Total Wire	Required				149346.7626

Figure B.7 The QTor corrector magnet power dissipation calculation.

Sensitivity of QTOR Corrector Magnet

Inner Coils Moved	Inner Coils Moved	Inner Coils Moved	Inner Coils Moved	Inner Coils Moved	Outer Coils Moved	Outer Coils Moved	Outer Coils Moved	Outer Coils Moved	Outer Coils Moved	B	B	B	ΔB(%)	ΔB(%)	ΔB(%)
X	Y	Z	θ	φ	X	Y	Z	θ	φ	X=40	Y=40	Center	X=40	Y=40	Center
[cm]	[cm]	[cm]	[degree]	[degree]	[cm]	[cm]	[cm]	[degree]	[degree]	[G-cm]	[G-cm]	[G-cm]	[G-cm]	[G-cm]	[G-cm]
1	0	0	0	0	0	0	0	0	0	296.29	590.12	4301.73	2.77	-0.24	-0.38
0	1	0	0	0	0	0	0	0	0	304.94	594.13	4219.97	-0.07	-0.92	1.52
0	0	1	0	0	0	0	0	0	0	306.33	596.18	4302.79	-0.53	-1.27	-0.41
0	0	0	1	0	0	0	0	0	0	305.22	588.93	4286.01	-0.16	-0.03	-0.02
0	0	0	0	1	0	0	0	0	0	301.87	588.75	4285.1	0.94	0.00	0.00
0	0	0	0	0	1	0	0	0	0	350.14	589.39	4284.95	-14.90	-0.11	0.01
0	0	0	0	0	0	1	0	0	0	307.03	673.84	4292.93	-0.75	-14.46	-0.18
0	0	0	0	0	0	0	1	0	0	307.94	588.66	4286.08	-1.05	0.01	-0.02
0	0	0	0	0	0	0	0	1	0	306.21	588.65	4285.21	-0.49	0.01	0.00
0	0	0	0	0	0	0	0	0	1	306.63	588.69	4285.31	-0.62	0.01	0.00
1	0	0	0	0	1	0	0	0	0	337.39	587.92	4300.02	-10.72	0.14	-0.34
0	1	0	0	0	0	1	0	0	0	300.28	653.47	4225.01	1.46	-11.00	1.41
0	0	1	0	0	0	0	1	0	0	305.72	588.66	4299.42	-0.32	0.01	-0.33
1	0	0	0	0	-1	0	0	0	0	271.64	593.25	4302.65	10.86	-0.77	-0.41
0	1	0	0	0	0	-1	0	0	0	317.54	574.78	4215.71	-4.20	2.37	1.62
0	0	1	0	0	0	0	-1	0	0	304.73	588.73	4285.25	0.00	0.00	0.00
0	0	0	1	0	0	0	0	1	0	305.28	588.68	4286.09	-0.18	0.01	-0.02
0	0	0	0	1	0	0	0	0	1	301.08	588.69	4285.09	1.20	0.01	0.00
0	0	0	1	0	0	0	0	-1	0	307.82	589.03	4286	-1.01	-0.05	-0.02
0	0	0	0	1	0	0	0	0	-1	316.08	588.73	4285.24	-3.72	0.00	0.00
Nominal Field															
0	0	0	0	0	0	0	0	0	0	304.73	588.73	4285.25			

Figure B.8 The QTor corrector magnet sensitivities to the position and angle change.

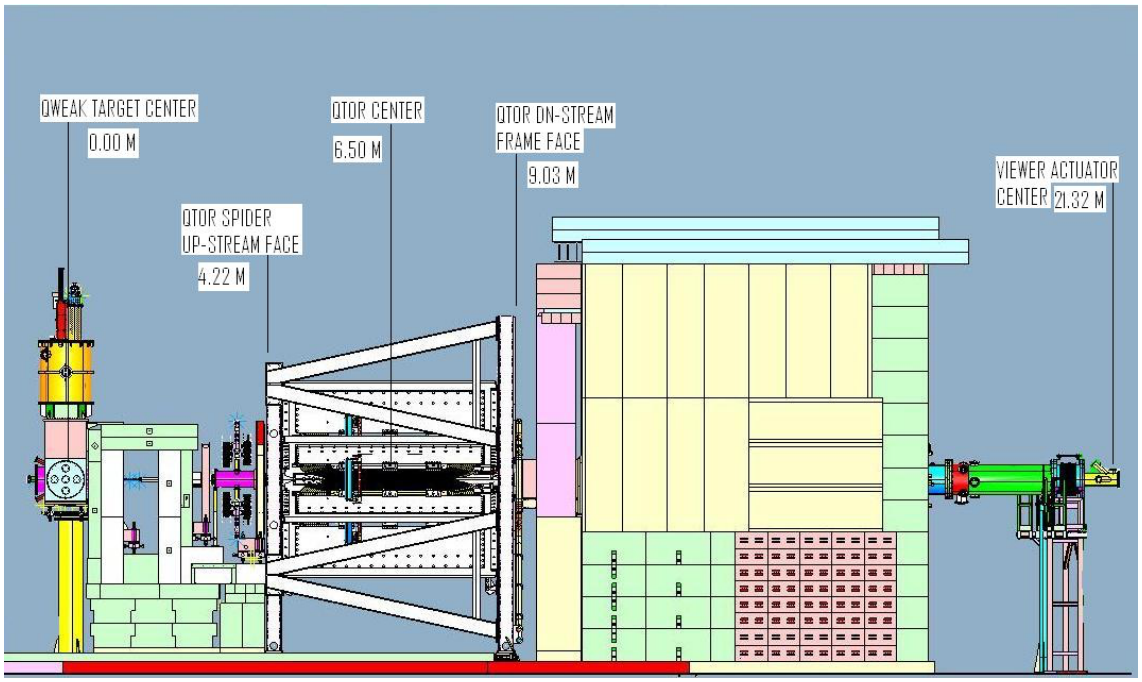

Figure B.9 A Computer-aided design (CAD) of the QTor and nearby region.

APPENDIX C

HELICITY CORELATED PEDESTAL ANALYSIS

C.1 Helicity Corelated Pedestal Analysis

Helicity is the projection of the spin $\vec{S}$ onto the direction of momentum.

$$\vec{h} = \vec{J} \cdot \hat{p} = \vec{L} \cdot \hat{p} + \vec{S} \cdot \hat{p} = \vec{S} \cdot \hat{p} \tag{C.1.1}$$

C.1.1 Condition of Experimental Data Taking

- Dedicated pedestal runs: Typically 5 minutes dedicated beam off pedestal run were taken with production running once a day during Run 1 and once a shift during Run 2. There were also ∼1 hour long beam off pedestal runs taken throughout, whenever there was an opportunity.
- Target - LH2 , Al, No target: Most of the pedestal runs are with LH2 target, but there were significant number of Al pedestal runs. There were few runs without target and while the target was moving.
- Beam OFF: Only beam off pedestal runs were included in this analysis. There were several runs marked as pedestal in the HCLOG that didn't pass the standard beam current cuts (details in C.1.2), meaning they had some beam and hence were excluded from this analysis. More details has been presented in [179, 180].

C.1.2 Condition of This Analysis

- Analyzer version: 4024 (12th February 2012 14:06:42).
- Beam current cut (global): -10 to 1 μA.
- Effective charge cut (global) on BPM 3h09 and 3c12: -100000 to 25000.
- Turned OFF normalization: The main detectors and luminosity monitors are normalized to the charge monitors for nominal parity analysis so it is important that neither have any evidence of helicity correlated pedestal differences. Hence, MD and Lumi normalization were turned off during pedestal analysis.
- Hel_Tree and Mps_Tree: Helicity correlated differences were taken from Hel_Tree and raw pedestal signal from Mps_Tree.
- Turned OFF Data Base update.
- Turned OFF blinding factor for this analysis keeping the integrity of the experiment. [181]

C.1.3 Configuration

The following command has been used for this analysis using standard Q-weak analyzer.

```
qwparity -r 18974 -c pedestal_ifarm.conf
```
(C.1.2)

Here, 18974 is the run number and pedestal_ifarm.conf is the configuration file and has following configurations:

```
chainfiles = yes
single-output-file = yes
detectors = detectors_pedestal.map
codafile-stem = QwRun_
codafile-ext = log
QwMainCerenkovDetector.normalize = no
QwLumi.normalize = no
rootfile-stem = Qweak_Hel_Ped_Ana_
enable-differences = yes
disable-histos = yes
blinder.force-target-out = yes
disable-slow-tree = yes
disable-burst-tree = yes
disable-by-type = QwScanner
disable-by-type = QwBeamMod
enable-tree-trim = yes
QwDatabase.accesslevel = OFF
```

C.1.4 List of Variables

The list of variables included in this analysis are shown below. The variables are from the Hel_Tree of the standard analyzed rootfiles, and has the following nomenclature “diff_qwk_VARIABLE_NAME”.

C.1.4.1 Main Cerenkov Detector(17)

mdallbars, md1pos, md2pos, md3pos, md4pos, md5pos, md6pos, md7pos, md8pos, md1neg, md2neg, md3neg, md4neg, md5neg, md6neg, md7neg, md8neg.

C.1.4.2 Downstream Luminosity Detector(9)

dslumi_sum, dslumi1, dslumi2, dslumi3, dslumi4, dslumi5, dslumi6, dslumi7, dslumi8.

C.1.4.3 Uptream Luminosity Detector(9)

uslumi_sum, uslumi1pos, uslumi3pos, uslumi5pos, uslumi7pos, uslumi1neg, uslumi3neg, uslumi5neg, uslumi7neg.

C.1.4.4 Beam Current Monitor(9)

charge[1], bcm1, bcm2, bcm5, bcm6, bcm7, bcm8, bcmgl1, bcmgl2.

C.1.5 List of Runs

The list of dedicated pedestal runs included in this analysis are shown in following subsections. The data taken during 31 January 2011 - 17 May 2012.

C.1.5.1 Wien 0

9593 9546 9539 9510 9483 9469 9456 9436 9407 9394 9354 9353 9352 9314 9303 9288 9205 9131 9129 9098 9095 9067 9028 9027 9026

C.1.5.2 Wien 1

10182 10168 10150 10133 10105 10092 10087 10083 10082 10077 10066 10060 10026 9979 9972 9970

C.1.5.3 Wien 2

11123 11106 11089 11067 11066 11053 11050 11049 11032 10997 10974 10969 10954 10953 10945 10920 10916 10902 10892 10891 10890 10889 10887 10886 10822 10805 10802 10799 10797 10782

[1] charge = bcm1+bcm2 for Run-I and = bcm8 for most of Run-II.

10781 10743 10730 10720 10716 10711 10708 10705 10702 10699 10288 10287 10252 10239 10229 10201

C.1.5.4 Wien 3

11380 11343 11304 11289 11285 11274 11264 11255 11246 11238 11229 11215 11211 11206 11189 11177 11166 11164 11160 11146 11131

C.1.5.5 Wien 4

11691 11690 11670 11668 11661 11648 11633 11608 11585 11574 11555 11529 11444 11422

C.1.5.6 Wien 5

11715 11712 11691 11690 11670 11668 11661 11648 11633 11608 11585 11574 11555 11529 11444 11422 11380 11343 11304 11289 11285 11274 11264 11255 11246 11238 11229 11215 11211 11206 11189 11177 11166 11164 11160 11146 11131 11130 11123

C.1.5.7 Wien 6

14209 14206 14205 14147 14125 14124 14120 14102 14091 14064 14063 14062 14061 14060 14059 14058 14057 14041 14040 14039 14038 14037 14036 14035 14034 14025 13987 13986 13971 13969 13968 13967 13966 13928 13927 13926 13925 13924 13914 13895 13888 13886 13859 13858

C.1.5.8 Wien 7

14683 14675 14674 14669 14631 14595 14568 14567 14564 14561 14552 14530 14529 14528 14527 14524 14466 14464 14452 14449 14440 14430 14384 14326 14325 14324 14322 14308

C.1.5.9 Wien 8

15980 15919 15913 15904 15888 15887 15877 15876 15817 15797 15766 15746 15708 15706 15699 15694 15676 15660 15659 15658 15657 15656 15645 15639 15638 15637 15624 15623 15618 15599 15591 15515 15514 15493 15488 15487 15420 15418 15417 15401 15400 15396 15395 15362 15359 15349 15338 15337 15321 15313 15311 15227 15247 15228 15214 15213 15176 15169

C.1.5.10 Wien 9

16207 16259 16329 16330 16368 16374 16387 16388 16391 16394 16395 16397 16398 16399 16400 16403 16404 16407 16420 16424 16425 16428 16446 16449 16454 16460 16465 16517 16518 16519

16520 16521 16522 16523 16581 16582 16583 16593 16595 16598 16606 16616 16619 16620 16626
16642 16643 16644 16719 16721 16736 16738 16739 16740 16742 16743 16764 16785 16797 16799
16810 16813 16814 16815 16816 16817 16818 16819 16830 16890 16907 16908 16909 16910 16911
16915 16921 16926 16934 16945 16950 16966 16967 16981 16988 16989 17000 17001 17002 17003
17004 17005 17006 17007 17018 17020 17021 17022 17023 17024 17028 17042 17043 17044 17045
17046 17047 17048 17049 17050 17051 17052 17093 17094 17095 17096 17097 17098 17099 17102
17103 17104 17105 17106 17107 17108 17109 17110 17144 17145 17146 17160 17165 17167 17173
17174 17190 17193 17194 17195 17200 17204 17222 17257 17284 17310 17332 17333 17346 17347
17348 17349 17350 17351 17352 17353 17354 17355 17356 17357 17358 17359 17360 17361 17362
17363 17364 17365 17366 17367 17368 17369 17374 17375 17399 17414 17460 17462 17464 17467
17469 17470 17631 17633 17634 17635 17636 17646 17650 17677 17682 17696 17708 17711 17715
17718 17723 17753 17801 17868 17869 17870 17890 17891 17957 17958 18001 18002 18003 18005
18028 18031 18043 18045 18069 18103 18115 18137 18150 18155 18160 18170 18179 18192 18206
18227 18230 18237 18259 18281 18288 18321 18327 18330 18373 18419 18422 18447 18448

C.1.5.11 Wien 10

18587 18588 18589 18590 18606 18611 18612 18644 18676 18677 18678 18679 18680 18681 18682
18683 18684 18685 18713 18719 18724 18727 18730 18733 18736 18739 18742 18743 18801 18815
18818 18831 18832 18847 18848 18851 18852 18855 18856 18863 18864 18865 18868 18869 18870
18871 18872 18874 18875 18876 18877 18878 18879 18880 18881 18885 18899 18900 18902 18909
18910 18928 18930 18935 18942 18944 18951 18952 18953 18972 18973 18974

C.2 Background Detectors

The helicity correlated differences from Hel_Tree and pedestal subtracted signals from Mps_Tree for background detectors are shown here. All other plots for individual channels, and run by run plots grouped by Wien can be found in [182].

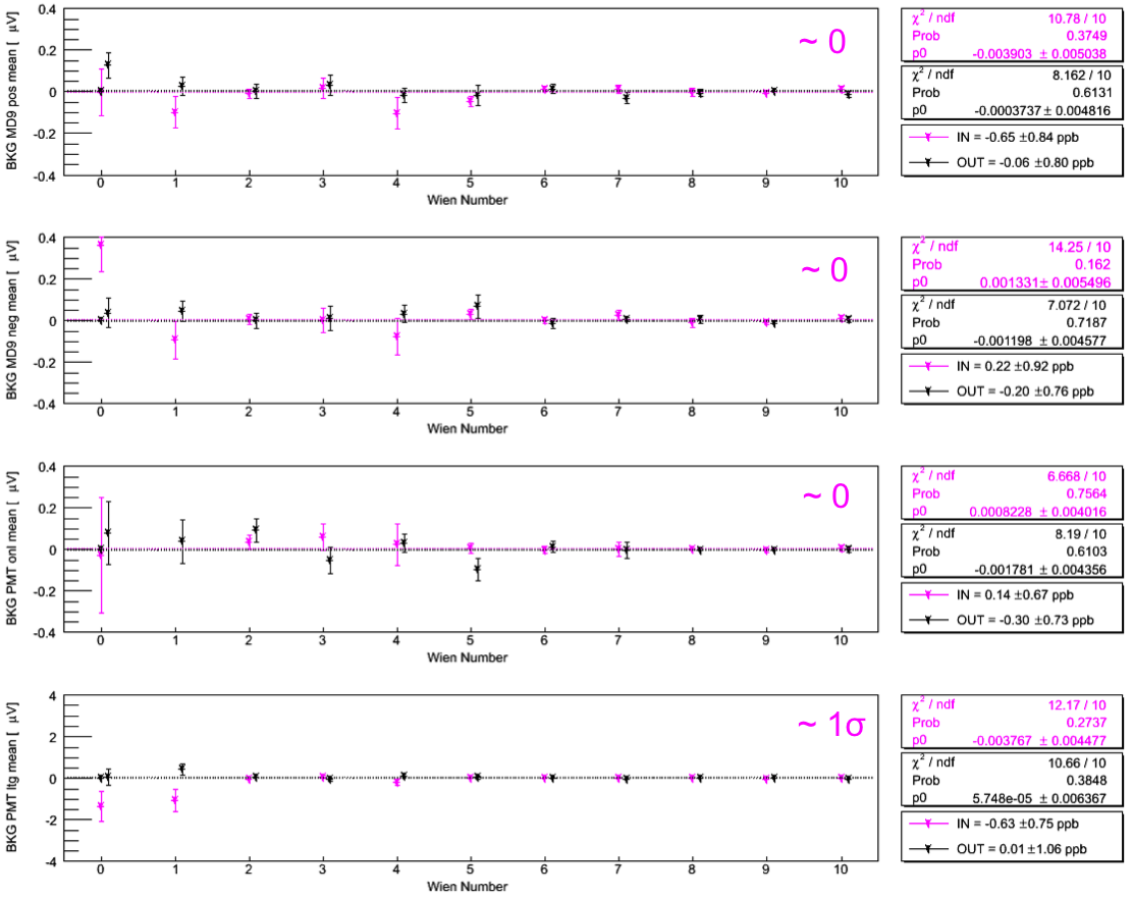

Figure C.1 Mean of the helicity correlated differences for MD9 pos, MD9 neg, PMT onl, and PMT ltg are shown in the figure (top to bottom). Helicity correlated differences for these important background detectors from Hel_Tree are zero within $\sim 1\sigma$ for averaged over each wien.

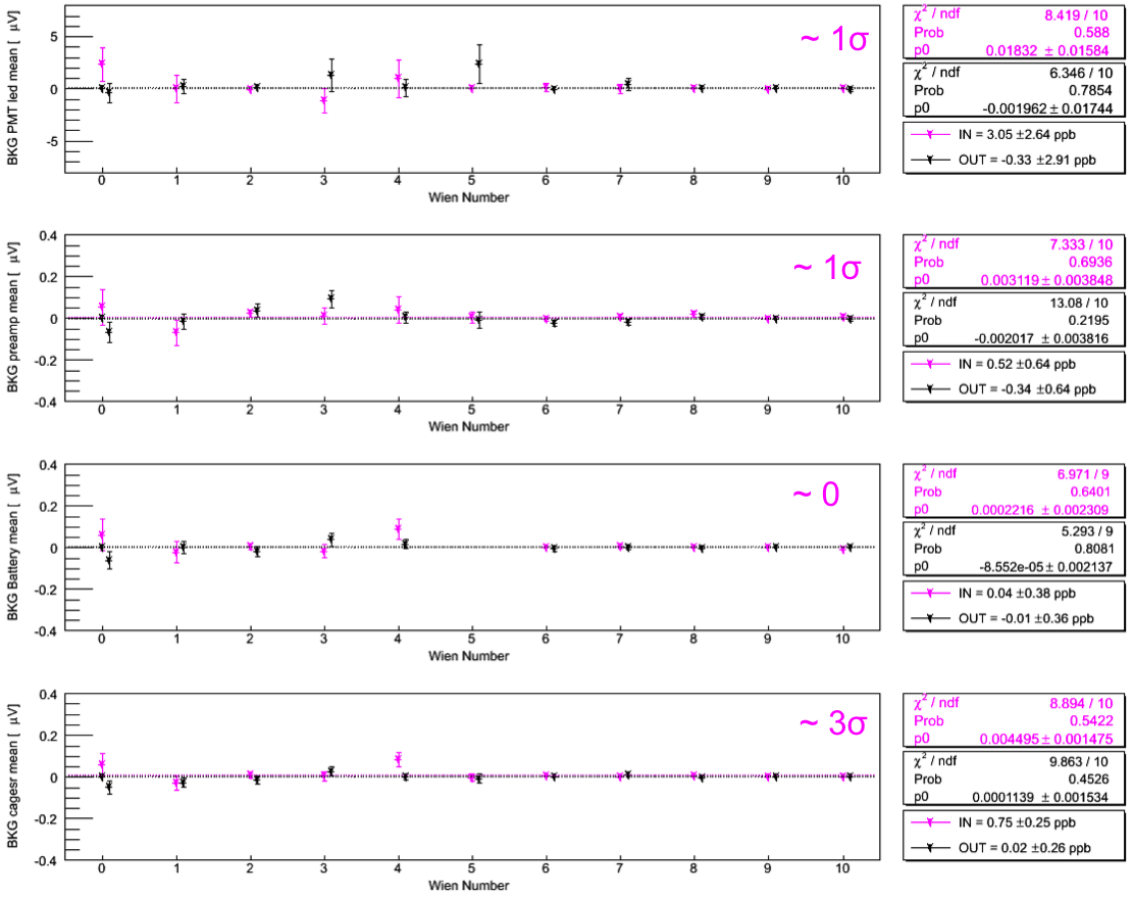

Figure C.2 Mean of the helicity correlated differences for PMT led, preamp, battery, and cages source are shown in the figure (top to bottom). Helicity correlated differences for these important background detectors from Hel_Tree are zero within $\sim 3\sigma$ for averaged over each wien.

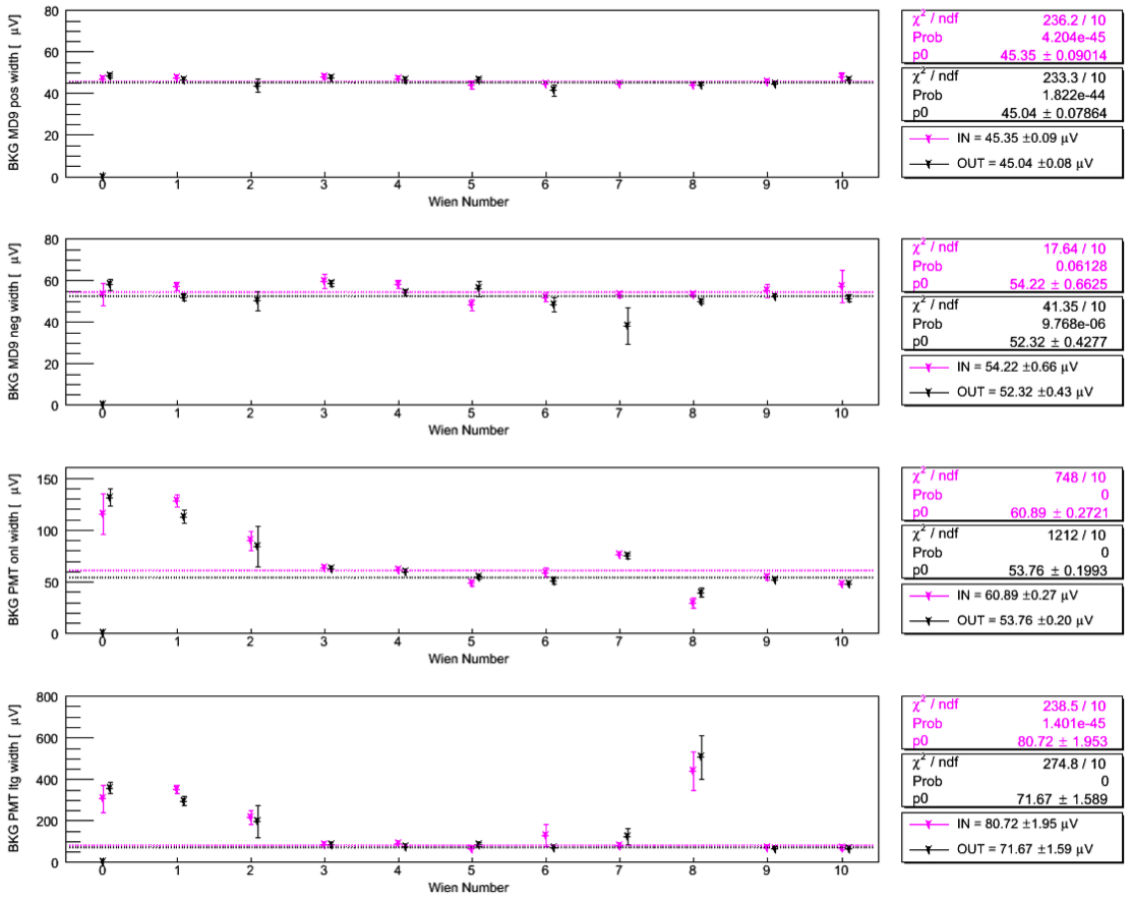

Figure C.3 Width of the helicity correlated differences for MD9 pos, MD9 neg, PMT onl, and PMT ltg are shown in the figure (top to bottom).

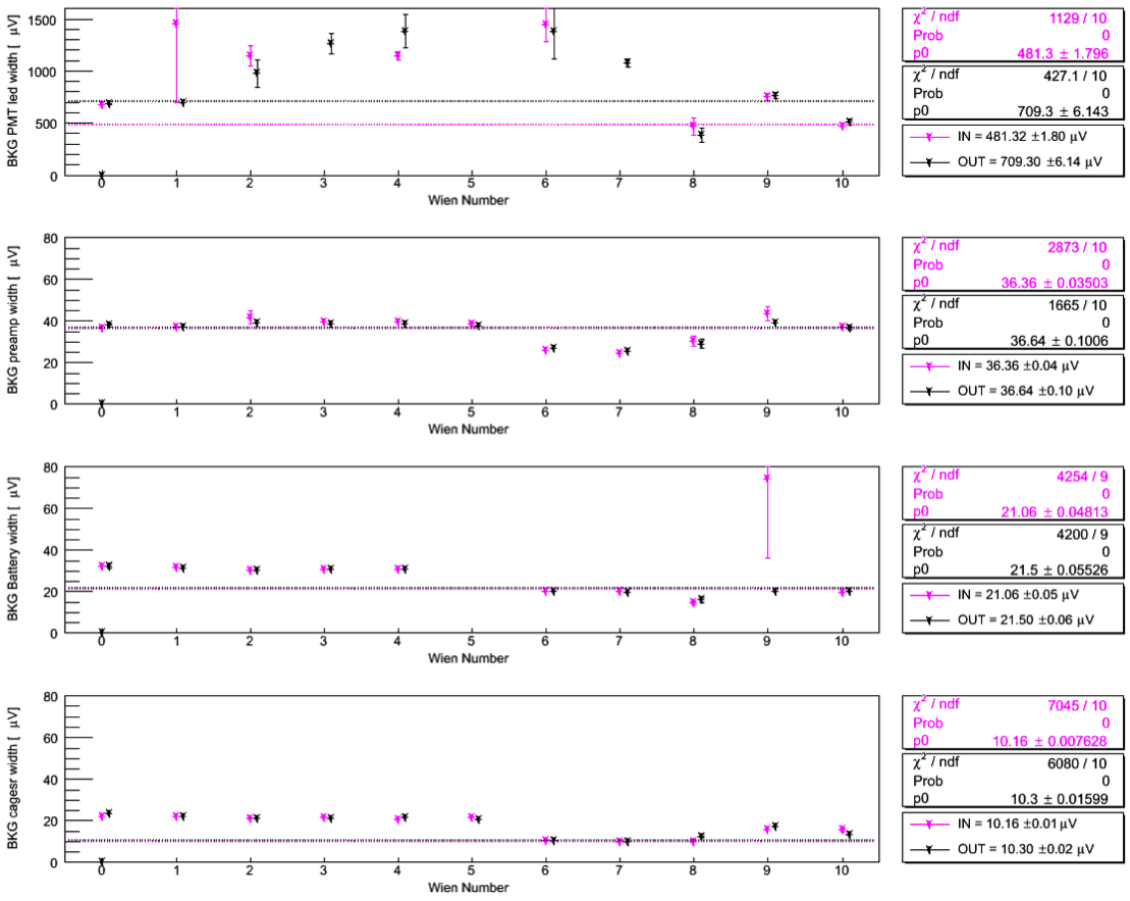

Figure C.4 Width of the helicity correlated differences for PMT led, preamp, battery, and cages source are shown in the figure (top to bottom).

APPENDIX D
BEAM NORMAL SINGLE SPIN ASYMMETRY IN INELASTIC E-P SCATTERING

D.1 Condition of Experimental Data Taking

Run Conditions:

- Transverse N-to-Δ production runs: Typically one hour dedicated transverse run were taken with production running condition during Run 2.
- Target - LH_2, 4% DS Al, Carbon: Most of the production runs are with LH_2 target, but there were significant number of Aluminum and few Carbon runs. The existing data set are shown in Table 6.1.
- Beam current:
  - For LH_2: 180 μA.
  - For 4% DS Al: 60 μA.
  - For Carbon :75 μA.
- QTor current settings: 6000, 6700†, 7300 A.
- Beam raster dimension: 4x4 mm^2.
- Beam energy: 1.155 GeV.

Analysis Conditions:

- From run2_pass5 data base.
- Standard data base cuts: Only declared GOOD data, no additional cuts applied.
- Regressed with std, 5+1, set3, set4, set7, set8, set9, set10 and set11 schemes. (md9 regression failed for LH_2 horizontal transverse)

This analysis includes:

- Data taken: 16 February 2012 - 20 February 2012
- Preliminary main detector asymmetries, sensitivities, yields, position, angle, energy, differences. charge asymmetries.

D.2 Weight Calculation for Main Detector Yields

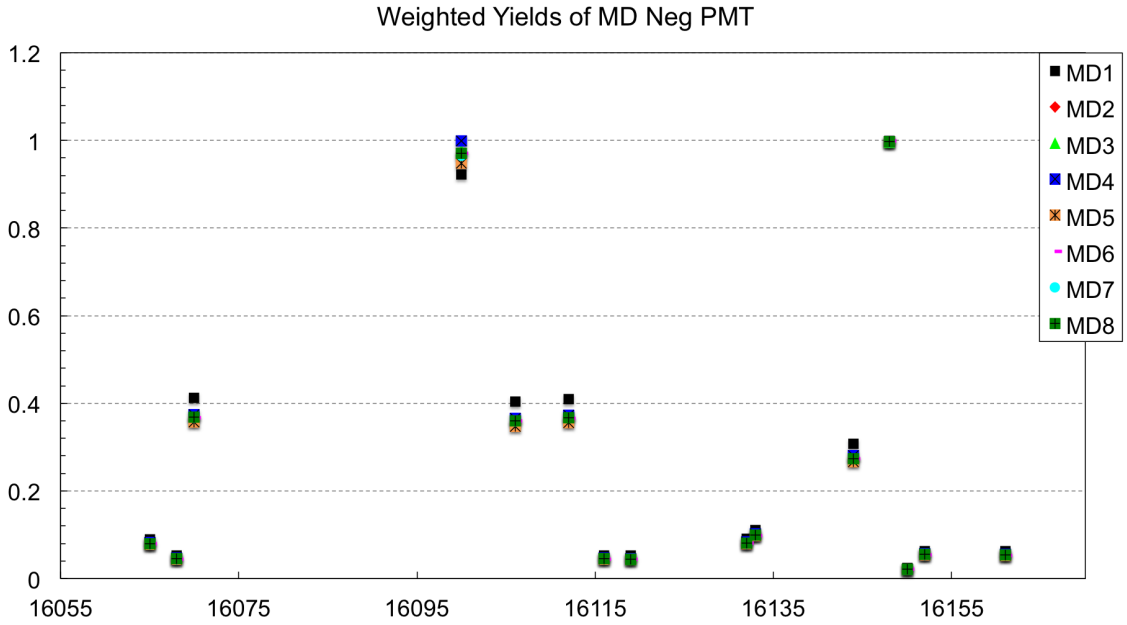

Figure D.1 Transverse N→ Δ run by run old weighted yields for negative PMT.

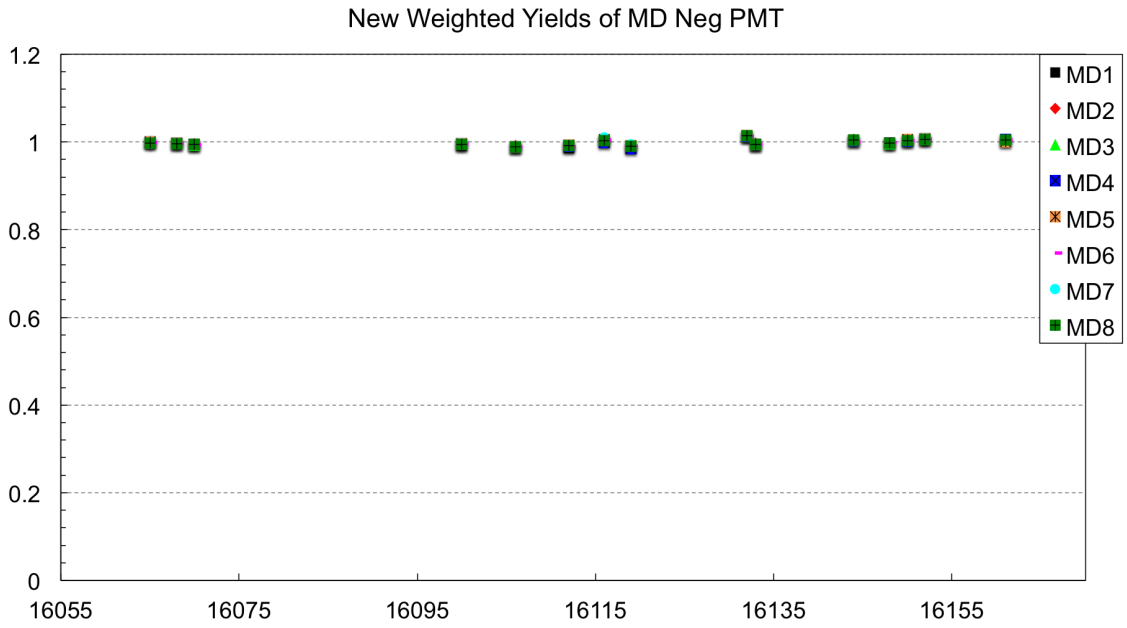

Figure D.2 Transverse N→ Δ run by run new weighted yields for negative PMT.

New weights for Run 2 transverse N→ Δ were calculated to better match the PMT gains of the main detectors [183].

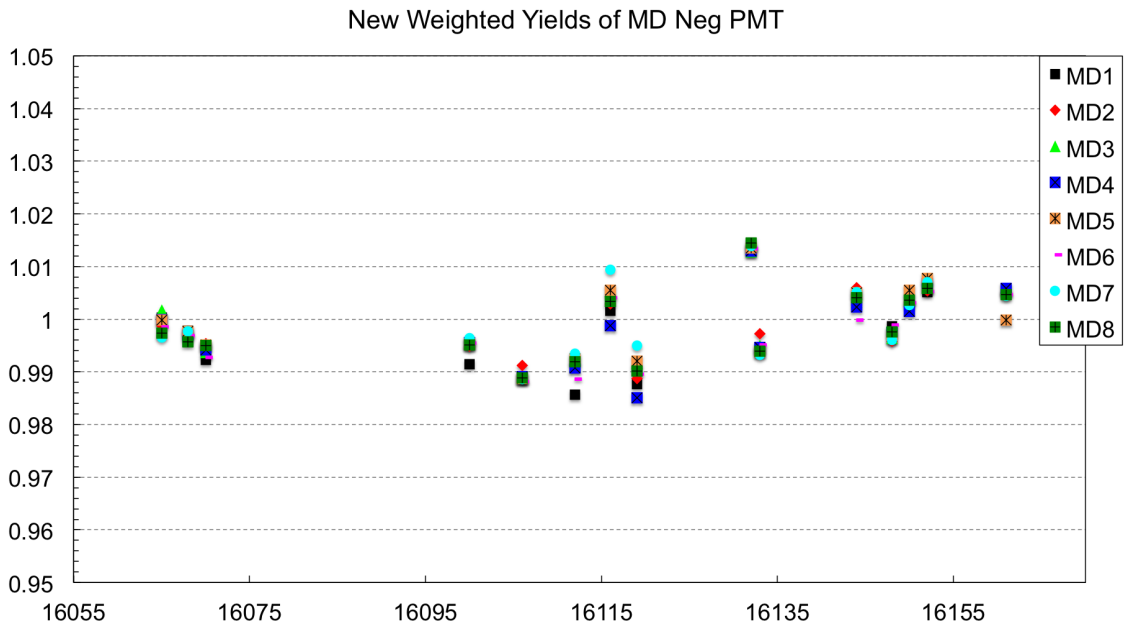

Figure D.3 Transverse N→ Δ run by run new weighted yields for negative PMT with a zoomed view.

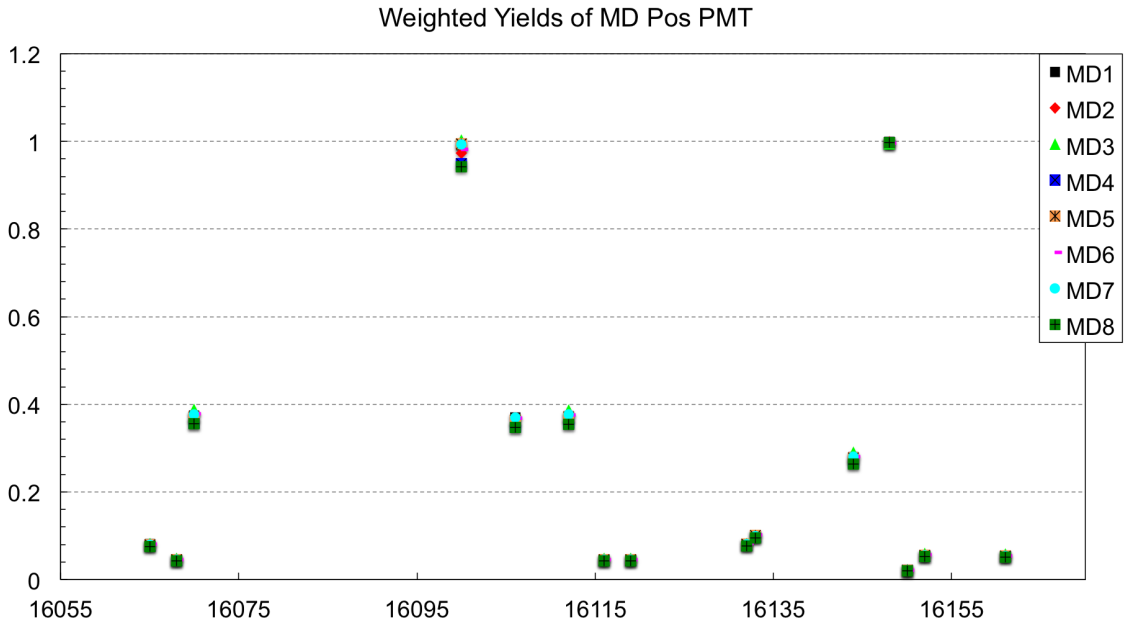

Figure D.4 Transverse N→ Δ run by run old weighted yields for positive PMT.

Inelastic (N→ Δ) hydrogen : new weights for range 16065-16066 from run 16065. Used in map file qweak_maindet.16065-16066.map

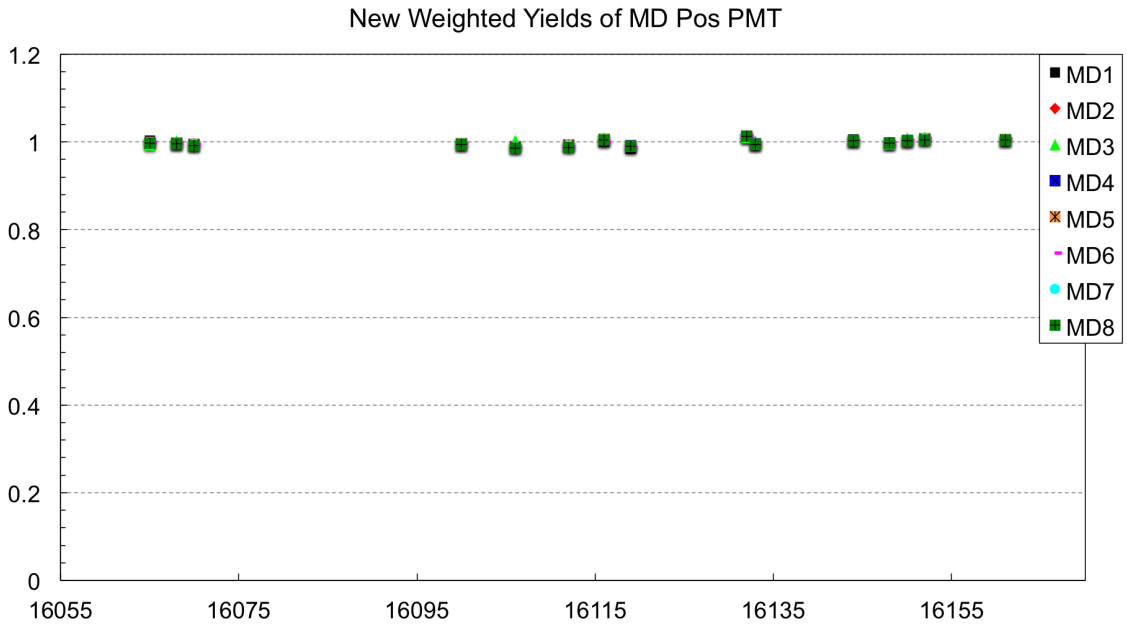

Figure D.5 Transverse N→ Δ run by run new weighted yields for positive PMT.

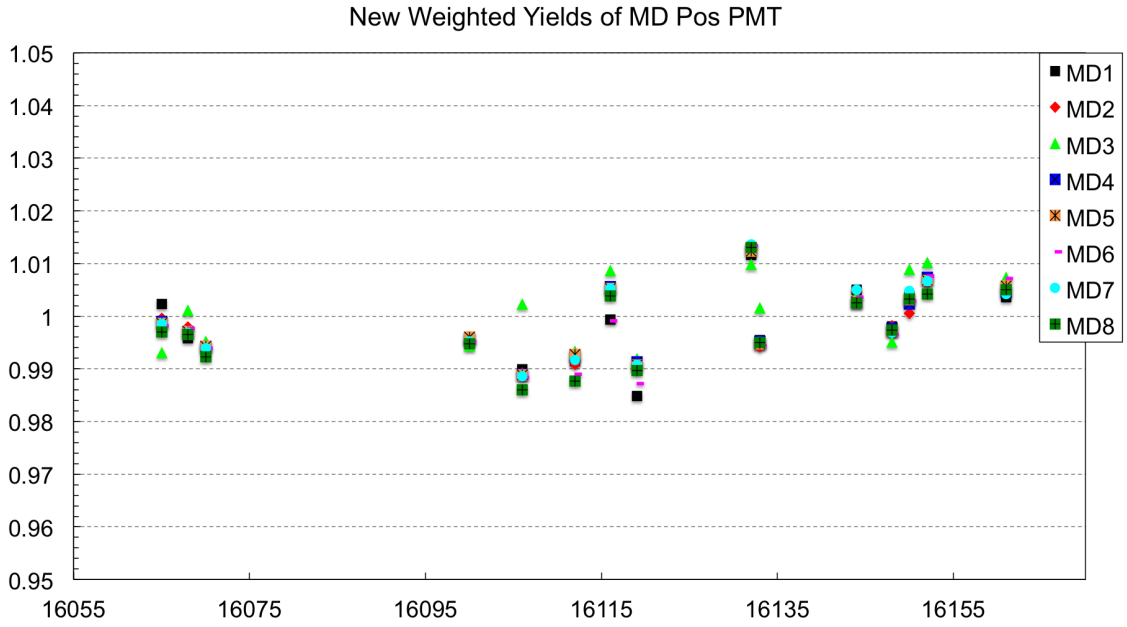

Figure D.6 Transverse N→ Δ run by run new weighted yields for positive PMT with a zoomed view.

Table D.1 Inelastic N→ Δ hydrogen: new weights for range 16065-16066 from run 16065. Used in map file qweak_maindet.16065-16066.map.

Detector	Yield	Inverse Yield
qwk_md1neg	0.0030	330.5330
qwk_md1pos	0.0031	321.5347
qwk_md2neg	0.0022	445.5271
qwk_md2pos	0.0036	279.2840
qwk_md3neg	0.0035	287.5661
qwk_md3pos	0.0019	516.7349
qwk_md4neg	0.0021	483.8969
qwk_md4pos	0.0030	336.5697
qwk_md5neg	0.0028	356.8381
qwk_md5pos	0.0036	275.7896
qwk_md6neg	0.0031	325.2310
qwk_md6pos	0.0027	375.7575
qwk_md7neg	0.0025	397.9348
qwk_md7pos	0.0030	333.9648
qwk_md8neg	0.0032	314.0859
qwk_md8pos	0.0033	298.7560
qwk_md9neg	saturating	
qwk_md9pos	0.0227	43.9706

Table D.2 Inelastic N→ Δ hydrogen: new weights for range 16129-16132 from run 16132. Used in map file qweak_maindet.16129-16132.map.

Detector	Yield	Inverse Yield
qwk_md1neg	0.0030	331.4473
qwk_md1pos	0.0031	322.9721
qwk_md2neg	0.0022	444.7867
qwk_md2pos	0.0036	279.1371
qwk_md3neg	0.0035	286.4275
qwk_md3pos	0.0019	523.1008
qwk_md4neg	0.0021	484.0794
qwk_md4pos	0.0030	335.8389
qwk_md5neg	0.0028	356.5254
qwk_md5pos	0.0036	275.1948
qwk_md6neg	0.0031	324.6119
qwk_md6pos	0.0027	375.2064
qwk_md7neg	0.0025	396.6083
qwk_md7pos	0.0030	333.4368
qwk_md8neg	0.0032	313.4542
qwk_md8pos	0.0034	298.3221
qwk_md8pos	0.0034	297.3187
qwk_md9neg	saturating	
qwk_md9pos	0.0228	43.9544

Table D.3 Inelastic N$\rightarrow \Delta$ hydrogen: new weights for range 16133-16137 from run 16135. Used in map file qweak_maindet.16133-16137.map.

Detector	Yield	Inverse Yield
qwk_md1neg	0.0038	266.1529
qwk_md1pos	0.0039	258.2914
qwk_md2neg	0.0028	355.5812
qwk_md2pos	0.0045	222.2689
qwk_md3neg	0.0044	228.4396
qwk_md3pos	0.0024	424.9694
qwk_md4neg	0.0026	386.2623
qwk_md4pos	0.0037	268.6043
qwk_md5neg	0.0035	284.2996
qwk_md5pos	0.0046	219.4513
qwk_md6neg	0.0039	259.7001
qwk_md6pos	0.0033	300.1012
qwk_md7neg	0.0032	316.8244
qwk_md7pos	0.0038	266.0677
qwk_md8neg	0.0040	249.5169
qwk_md8pos	0.0042	237.6253
qwk_md9neg	0.3794	2.6358
qwk_md9pos	0.0887	11.2772

Table D.4 Inelastic N→ Δ hydrogen: new weights for range 16152-16158, from run 16152. Used in map file qweak_maindet.16152-16158.map.

Detector	Yield	Inverse Yield
qwk_md1neg	0.0021	477.6794
qwk_md1pos	0.0021	472.5407
qwk_md2neg	0.0016	644.8716
qwk_md2pos	0.0025	404.0438
qwk_md3neg	0.0024	415.0359
qwk_md3pos	0.0014	728.0065
qwk_md4neg	0.0014	704.6771
qwk_md4pos	0.0021	487.6773
qwk_md5neg	0.0019	517.9050
qwk_md5pos	0.0025	401.9060
qwk_md6neg	0.0021	474.0913
qwk_md6pos	0.0018	546.7656
qwk_md7neg	0.0017	576.2694
qwk_md7pos	0.0021	486.3954
qwk_md8neg	0.0022	456.6464
qwk_md8pos	0.0023	435.2565
qwk_md9neg	0.0498	20.0761
qwk_md9pos	0.0122	81.7203

Table D.5 Inelastic N→ Δ aluminum: new weights for ranges 16067-16069 and 16115-16124 from run 16067. Used in map files qweak_maindet.16067-16069.map and qweak_maindet.16115-16124.map.

Detector	Yield	Inverse Yield
qwk_md1neg	0.0018	563.1134
qwk_md1pos	0.0018	567.0229
qwk_md2neg	0.0013	791.2187
qwk_md2pos	0.0020	494.0402
qwk_md3neg	0.0020	508.6698
qwk_md3pos	0.0011	887.0735
qwk_md4neg	0.0012	854.3876
qwk_md4pos	0.0017	595.1733
qwk_md5neg	0.0016	632.2300
qwk_md5pos	0.0020	488.4802
qwk_md6neg	0.0017	577.2902
qwk_md6pos	0.0015	662.4486
qwk_md7neg	0.0014	691.0762
qwk_md7pos	0.0017	582.1006
qwk_md8neg	0.0018	552.0701
qwk_md8pos	0.0019	528.0746
qwk_md9neg	saturating	
qwk_md9pos	0.0114	87.7754

A brief weighted yield and relative weighted yield for the entire parity-violating production dataset are shown in Figure E.5 and Figure E.6 (APPENDIX E).

Table D.6 Inelastic N→ Δ aluminum: new weights for range 16160-16161, from run 16160. Used in map file qweak_maindet.16160-16161.map.

Detector	Yield	Inverse Yield
qwk_md1neg	0.0021	476.9109
qwk_md1pos	0.0021	474.5462
qwk_md2neg	0.0015	665.1318
qwk_md2pos	0.0024	415.4953
qwk_md3neg	0.0023	428.0483
qwk_md3pos	0.0013	746.6703
qwk_md4neg	0.0014	723.3967
qwk_md4pos	0.0020	501.2203
qwk_md5neg	0.0019	530.5362
qwk_md5pos	0.0024	411.7435
qwk_md6neg	0.0021	487.6173
qwk_md6pos	0.0018	565.3161
qwk_md7neg	0.0017	582.9472
qwk_md7pos	0.0020	489.5450
qwk_md8neg	0.0022	464.5394
qwk_md8pos	0.0022	444.8808
qwk_md9neg	0.1340	7.4654
qwk_md9pos	0.0322	31.0311

Table D.7 Inelastic N→ Δ carbon: new weights for range 16148-16151, from run 16148.Used in map file qweak_maindet.16148-16151.map.

Detector	Yield	Inverse Yield
qwk_md1neg	0.0008	1205.9293
qwk_md1pos	0.0008	1216.4200
qwk_md2neg	0.0006	1681.8313
qwk_md2pos	0.0010	1050.1477
qwk_md3neg	0.0009	1081.4484
qwk_md3pos	0.0005	1888.8651
qwk_md4neg	0.0005	1818.8889
qwk_md4pos	0.0008	1251.2483
qwk_md5neg	0.0007	1343.7638
qwk_md5pos	0.0010	1039.5739
qwk_md6neg	0.0008	1219.9163
qwk_md6pos	0.0007	1415.7069
qwk_md7neg	0.0007	1473.6067
qwk_md7pos	0.0008	1250.6393
qwk_md8neg	0.0008	1183.1535
qwk_md8pos	0.0009	1127.1379
qwk_md9neg	0.0310	32.2814
qwk_md9pos	0.0071	141.5792

D.3 Uncertainty in Physics Asymmetries

$$(dB_n)_{\epsilon_{reg}} = M_{RC}M_{Det}M_{Q^2}M_\phi\frac{d\epsilon_{reg}}{P}\left[\frac{1}{1-f_{Al}-f_{BB}-f_{QTor}-f_{el}}\right] \tag{D.3.1}$$

$$(dB_n)_P = M_{RC}M_{Det}M_{Q^2}M_\phi\frac{\epsilon_{reg}}{P}\frac{dP}{P}\left[\frac{1}{1-f_{Al}-f_{BB}-f_{QTor}-f_{el}}\right] \tag{D.3.2}$$

$$(dB_n)_{B_{Al}} = M_{RC}M_{Det}M_{Q^2}M_\phi\left[\frac{-dB_{Al}f_{Al}}{1-f_{Al}-f_{BB}-f_{QTor}-f_{el}}\right] \tag{D.3.3}$$

$$(dB_n)_{B_{QTor}} = M_{RC}M_{Det}M_{Q^2}M_\phi\left[\frac{-dB_{QTor}f_{QTor}}{1-f_{Al}-f_{BB}-f_{QTor}-f_{el}}\right] \tag{D.3.4}$$

$$(dB_n)_{B_{el}} = M_{RC}M_{Det}M_{Q^2}M_\phi\left[\frac{-dB_{el}f_{el}}{1-f_{Al}-f_{BB}-f_{QTor}-f_{el}}\right] \tag{D.3.5}$$

$$(dB_n)_{f_{Al}} = M_{RC}M_{Det}M_{Q^2}M_\phi df_{Al}\left[\frac{\frac{\epsilon_{reg}}{P}-B_{Al}(1-f_{BB}-f_{QTor}-f_{el})-B_{QTor}f_{QTor}-B_{el}f_{el}}{(1-f_{Al}-f_{BB}-f_{QTor}-f_{el})^2}\right] \tag{D.3.6}$$

$$(dB_n)_{f_{BB}} = M_{RC}M_{Det}M_{Q^2}M_\phi df_{BB}\left[\frac{\frac{\epsilon_{reg}}{P}-B_{Al}f_{Al}-B_{QTor}f_{QTor}-B_{el}f_{el}}{(1-f_{Al}-f_{BB}-f_{QTor}-f_{el})^2}\right] \tag{D.3.7}$$

$$(dB_n)_{f_{QTor}} = M_{RC}M_{Det}M_{Q^2}M_\phi df_{QTor}\left[\frac{\frac{\epsilon_{reg}}{P}-B_{Al}f_{Al}-B_{QTor}(1-f_{Al}-f_{BB}-f_{el})-B_{el}f_{el}}{(1-f_{Al}-f_{BB}-f_{QTor}-f_{el})^2}\right] \tag{D.3.8}$$

$$(dB_n)_{f_{el}} = M_{RC}M_{Det}M_{Q^2}M_\phi df_{el}\left[\frac{\frac{\epsilon_{reg}}{P}-B_{Al}f_{Al}-B_{QTor}f_{QTor}-B_{el}(1-f_{Al}-f_{BB}-f_{QTor})}{(1-f_{Al}-f_{BB}-f_{QTor}-f_{el})^2}\right] \tag{D.3.9}$$

Table D.8 Systematic error table.

Error from	Uncertainty [ppm]	Relative uncertainty [%]
ϵ_{reg}	2.36	5.9
P	0.26	0.7
B_{Al}	0.17	0.4
B_{QTor}	0.02	0.1
B_{el}	0.47	1.2
f_{Al}	0.30	0.7
f_{BB}	0.13	0.3
f_{QTor}	1.70	4.3
f_{el}	13.96	35.2
M_{RC}	0.00	0.0
M_{Det}	0.00	0.0
M_{Q^2}	1.19	3.0
M_{ϕ}	0.00	0.0
Total	14.33	36.1

D.4 Corrections

D.5 Barsum vs PMTavg Asymmetries

Different ways to calculate the asymmetries. In case of barsum asymmetries we match gain of PMTs and then sum their yields and form asymmetries, whereas PMTavg asymmetries were formed as individual PMT asymmetries and then averaged. PMTavg and barsum asymmetries are shown in section 6.4 and Figures D.12, D.13, respectively. Barsum and PMTavg asymmetries match within ~ 0.0005 ppm.

Table D.9 Barsum and PMTavg asymmetries.

Asymmetries	Barsum [ppm]	PMTavg [ppm]	Difference [ppm]
ϵ_{reg}^{H}	5.34291	5.34293	0.00002
ϵ_{reg}^{V}	4.52568	4.52522	0.00046

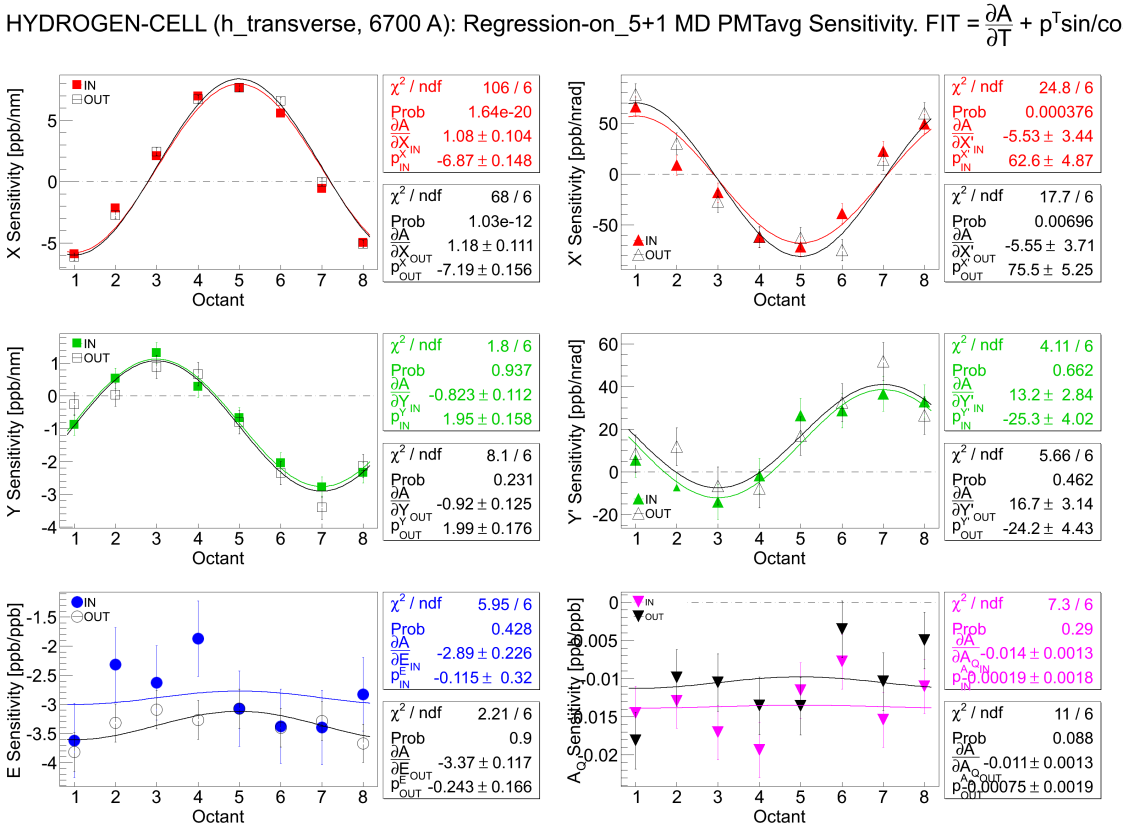

Figure D.7 Azimuthal dependence of the main detector sensitivities to HCBA for the "5+1" regression scheme in the horizontal LH_2 transverse data set are shown here. Sensitivities for beam positions and angles have sinusoidal dependence with octant. No such strong dependence is seen for energy and charge. Two IHWP states are shown separately for each beam parameter. Fit functions used to fit the parameters are shown on the plot. The constant in the fit gives the error weighted average of the sensitivities.

Table D.10 MD Sensitivities for X and Y.

Detector	$\frac{\partial\epsilon}{\partial X}$ [ppb/nm]		$\frac{\partial\epsilon}{\partial Y}$ [ppb/nm]	
	HWP-IN	HWP-OUT	HWP-IN	HWP-OUT
MD1	-5.91±0.29	-6.13±0.31	-0.88±0.29	-0.25±0.35
MD2	-2.16±0.29	-2.74±0.31	0.53±0.29	0.04±0.35
MD3	2.10±0.29	2.44±0.31	1.32±0.29	0.89±0.35
MD4	6.98±0.30	6.74±0.32	0.29±0.30	0.67±0.36
MD5	7.66±0.30	7.66±0.32	-0.67±0.30	-0.80±0.36
MD6	5.57±0.29	6.58±0.31	-2.05±0.30	-2.35±0.35
MD7	-0.58±0.30	-0.01±0.31	-2.79±0.30	-3.41±0.35
MD8	-4.98±0.29	-5.08±0.31	-2.34±0.29	-2.14±0.35

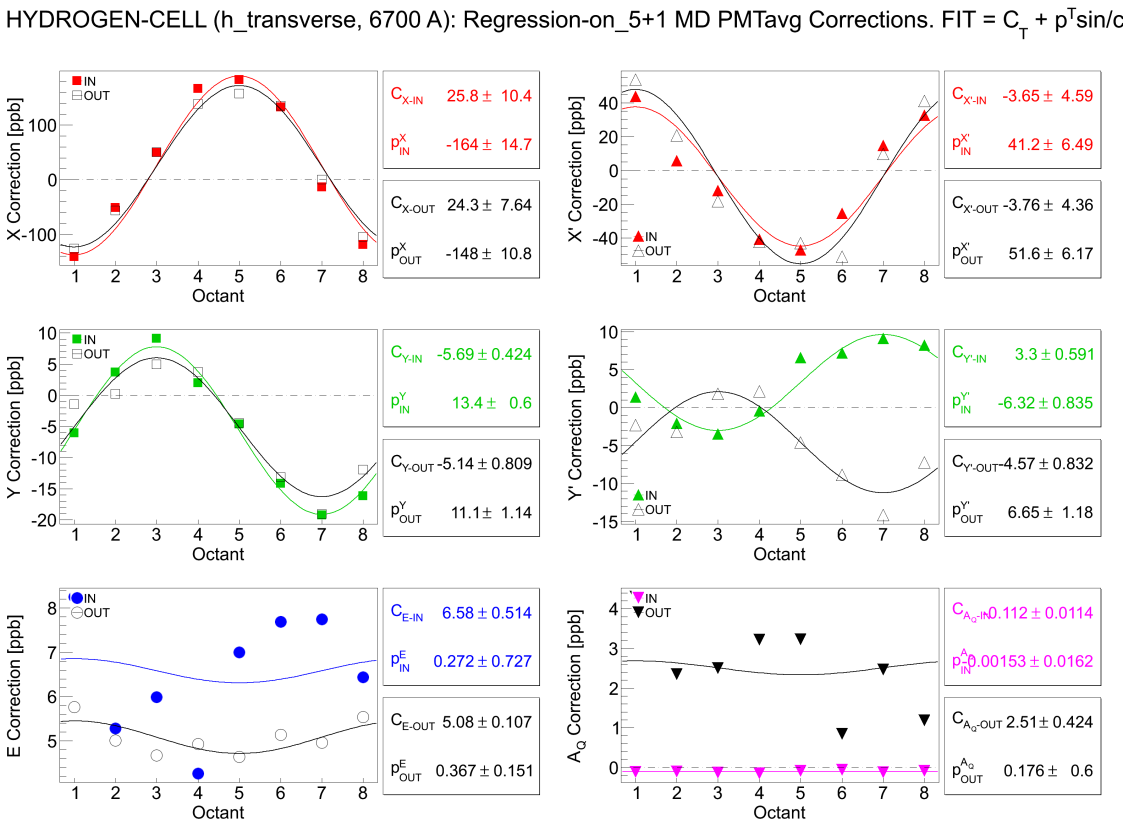

Figure D.8 Main detector corrections (using sensitivities from "5+1" regression scheme) vs octant for horizontal LH_2 transverse data set are shown here. Beam positions and angles have sinusoidal dependence with octant inherited from the sensitivities. No such dependence is seen for energy and charge. Both IHWP states are shown separately for each beam parameter.

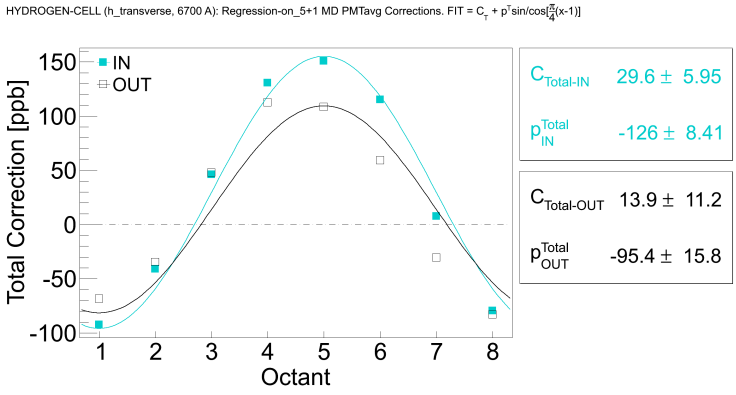

Figure D.9 Total corrections in "5+1" regression scheme vs octant for horizontal LH_2 transverse data set are shown here. The total correction is the sum of all the corrections (with sign) shown in Figure D.8.

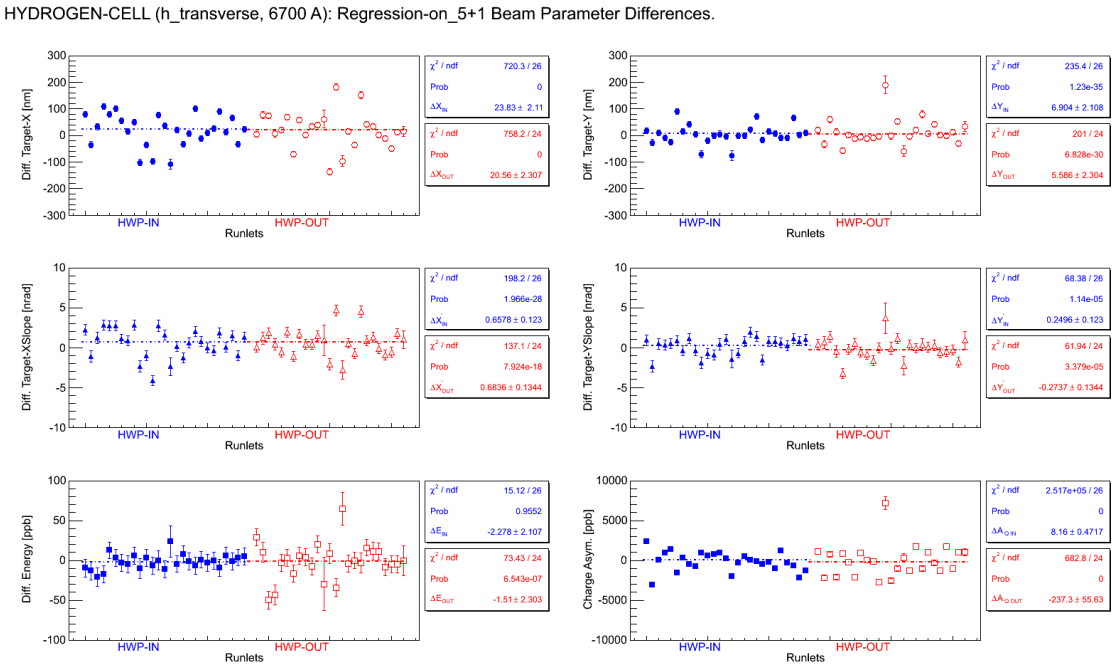

Figure D.10 Beam position differences for horizontal transverse data set.

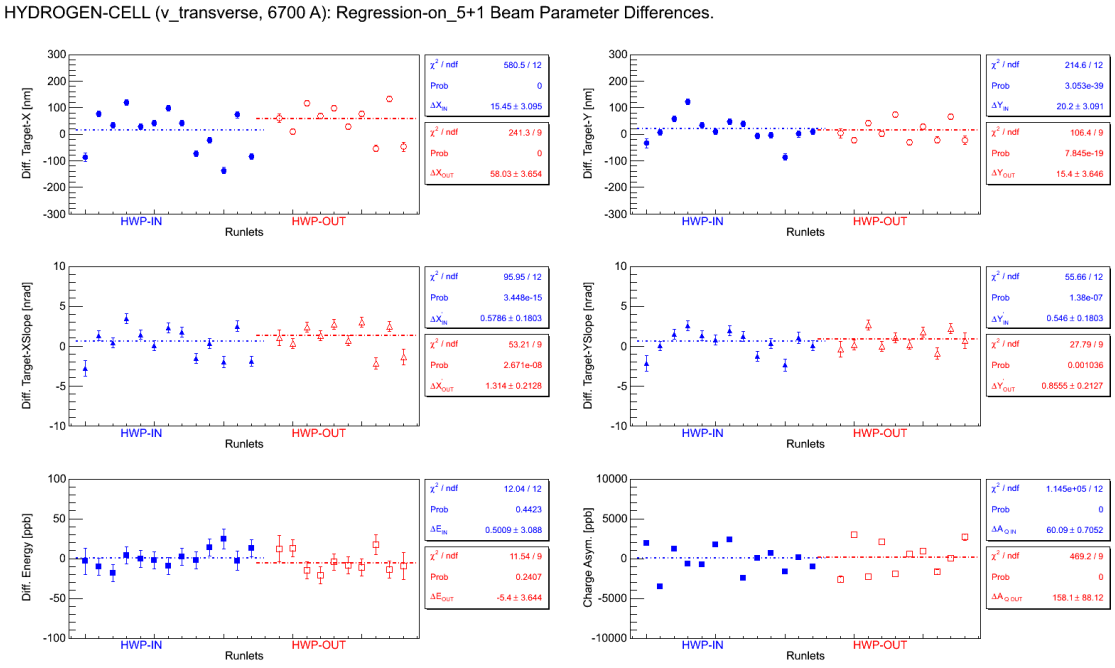

Figure D.11 Beam position differences for vertical transverse data set.

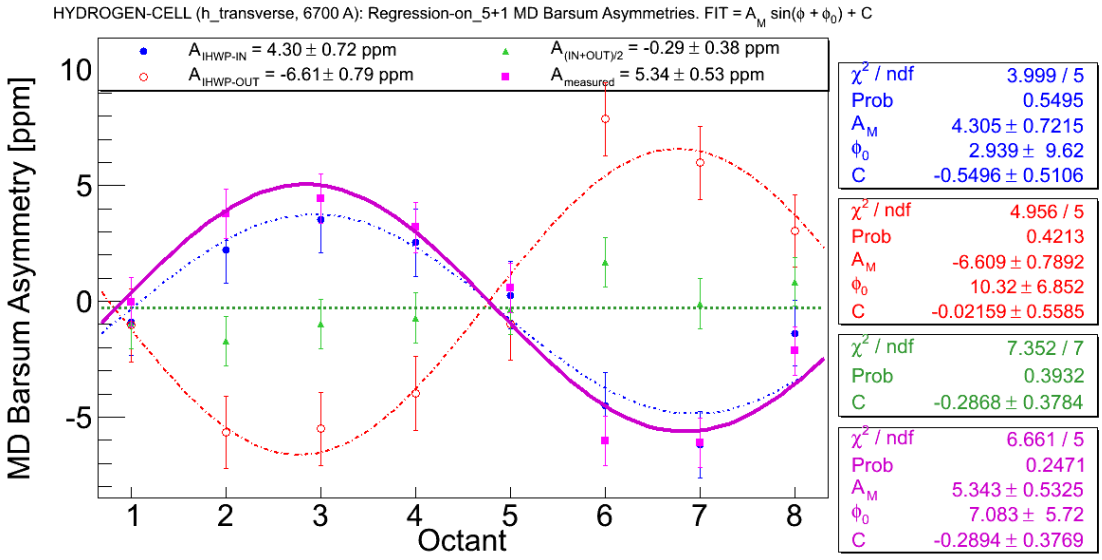

Figure D.12 Main detector barsum asymmetry for horizontal transverse at inelastic peak. For comparison, asymmetries for IN and OUT data are also shown separately. The regressed asymmetries change sign with the insertion of the IHWP with comparable amplitudes.

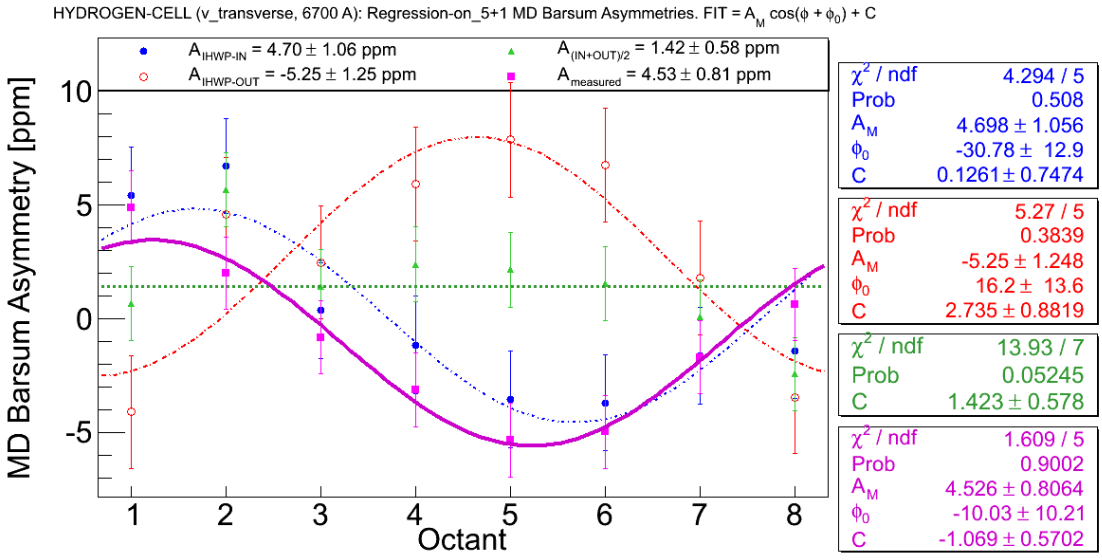

Figure D.13 Main detector barsum asymmetry for vertical transverse at inelastic peak. For comparison, asymmetries for IN and OUT data are also shown separately. The regressed asymmetries change sign with the insertion of the IHWP with comparable amplitudes.

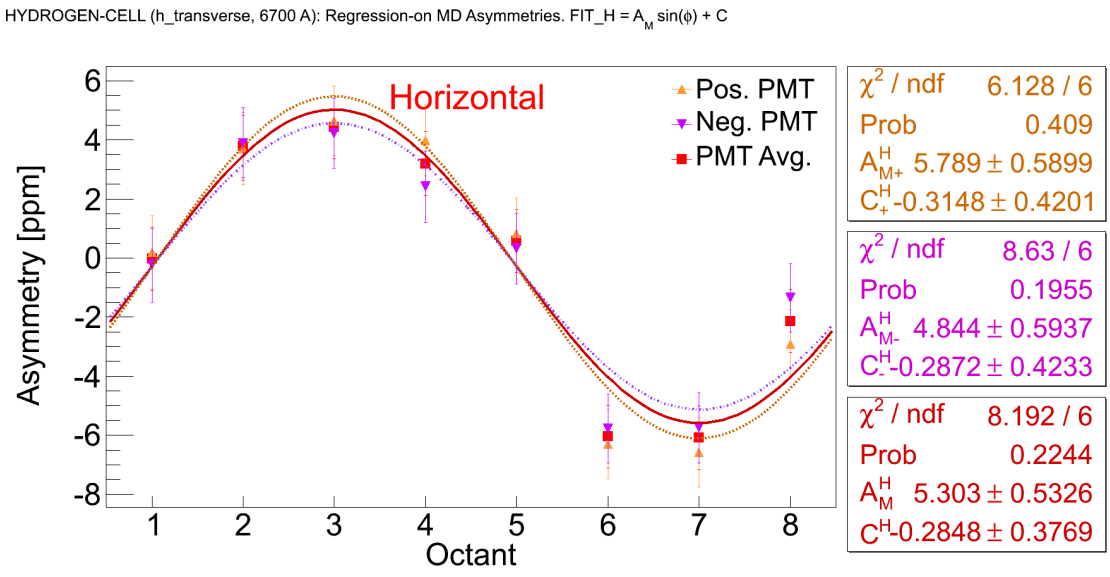

Figure D.14 The individual fits over POS, NEG PMTs and PMTavg asymmetries vs octant for inelastic horizontal transverse dataset [15].

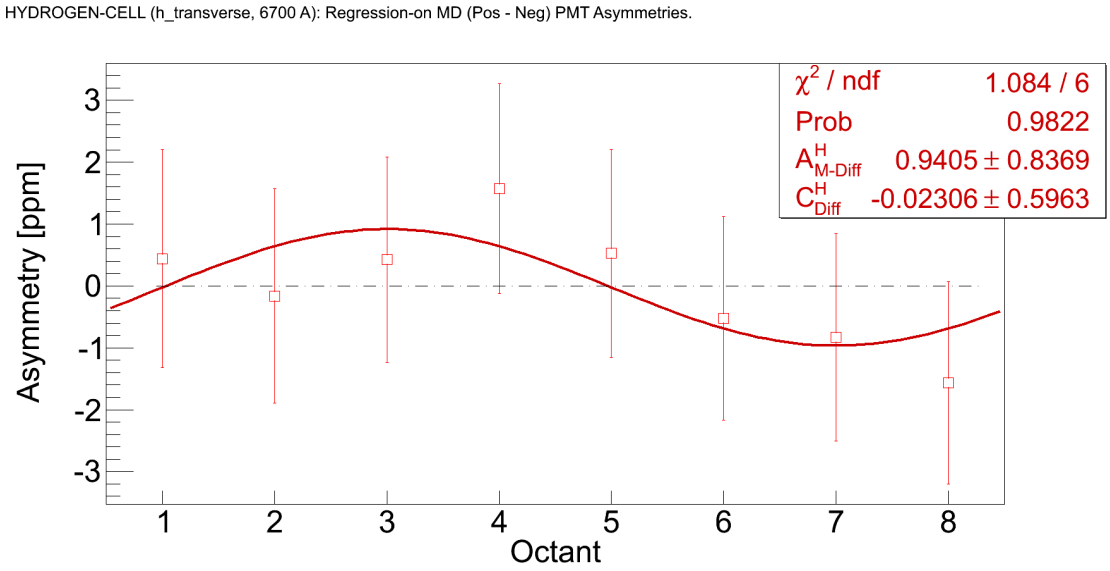

Figure D.15 Difference between POS-NEG asymmetries vs octant for inelastic horizontal transverse dataset. The error here is the quadrature sum of the POS and NEG asymmetry errors. See Table 1 for the values [15].

D.6 PMT Asymmetries

D.7 Detector Sensitivities

D.8 Regression Scheme Dependence

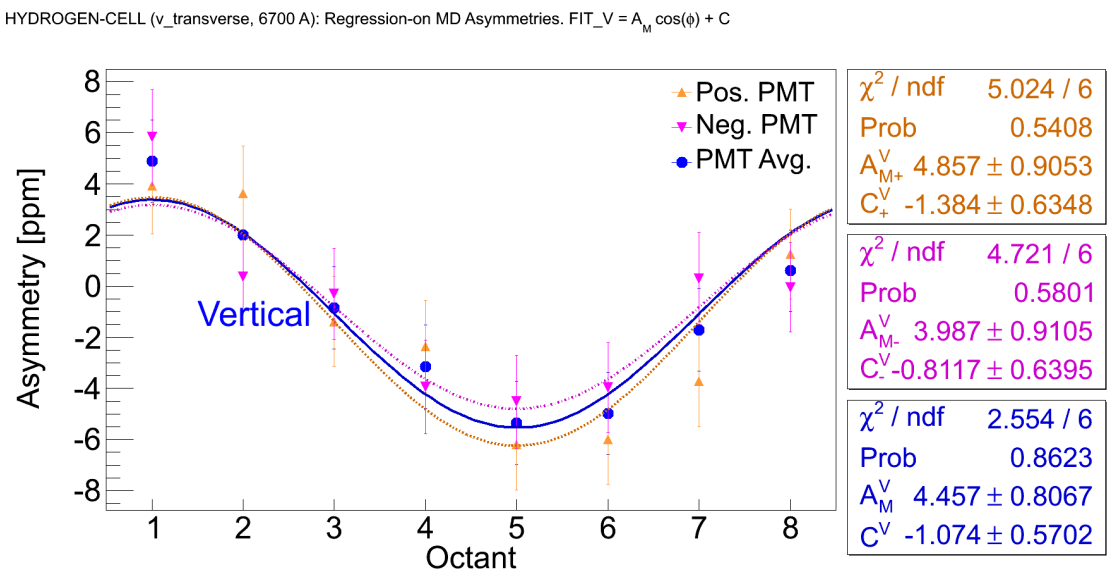

Figure D.16 The individual fits over POS, NEG PMTs and PMTavg asymmetries vs octant for inelastic vertical transverse dataset [15].

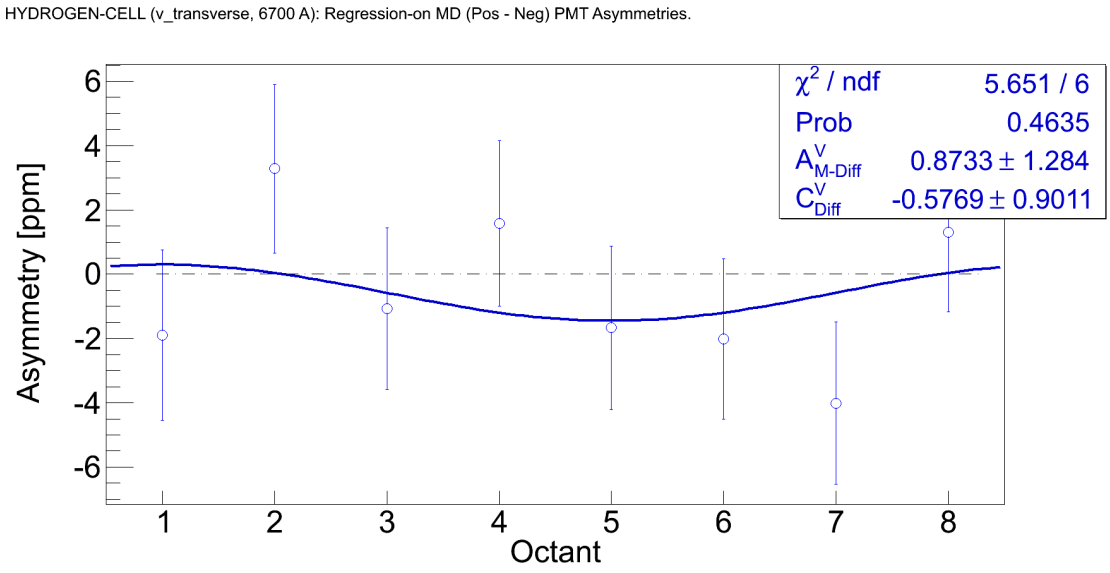

Figure D.17 Difference between POS-NEG asymmetries vs octant for inelastic vertical transverse dataset. The error here is the quadrature sum of the POS and NEG asymmetry errors. See Table 1 for the values [15].

Table D.11 MD Sensitivities for X′ and Y′.

Detector	$\frac{\partial\epsilon}{\partial X'}$ [ppb/nrad]		$\frac{\partial\epsilon}{\partial Y'}$ [ppb/nrad]	
	HWP-IN	HWP-OUT	HWP-IN	HWP-OUT
MD1	66.31±9.71	78.33±10.48	5.54±8.03	8.56±8.85
MD2	8.61±9.67	30.13±10.44	-8.33±8.00	11.81±8.82
MD3	-18.33±9.71	-26.87±10.50	-14.08±8.032	-6.59±8.87
MD4	-62.14±9.83	-61.88±10.58	-1.82±8.13	-7.78±8.94
MD5	-71.83±9.82	-63.13±10.60	26.31±8.12	16.87±8.95
MD6	-38.80±9.71	-74.72±10.48	28.69±8.03	32.50±8.85
MD7	22.40±9.76	14.19±10.53	36.49±8.068	51.75±8.90
MD8	49.43±9.62	59.98±10.39	32.82±7.96	26.52±8.78

Table D.12 MD Sensitivities for E and A_Q.

Detector	$\frac{\partial\epsilon}{\partial E}$ [ppb/ppb]		$\frac{\partial\epsilon}{\partial A_Q}$ [ppb/ppb]	
	HWP-IN	HWP-OUT	HWP-IN	HWP-OUT
MD1	-3.62±0.64	-3.82±0.33	-0.0146±0.0036	-0.0181±0.0037
MD2	-2.32±0.64	-3.32±0.33	-0.0129±0.0036	-0.0099±0.0037
MD3	-2.63±0.64	-3.09±0.33	-0.0171±0.0036	-0.0105±0.0037
MD4	-1.87±0.65	-3.27±0.33	-0.0194±0.0036	-0.0135±0.0038
MD5	-3.07±0.65	-3.07±0.33	-0.0116±0.0036	-0.0136±0.0038
MD6	-3.38±0.64	-3.40±0.33	-0.0078±0.0036	-0.0036±0.0037
MD7	-3.40±0.64	-3.28±0.33	-0.0154±0.0036	-0.0104±0.0038
MD8	-2.83±0.63	-3.67±0.33	-0.0110±0.0035	-0.0050±0.0037

Table D.13 Regression scheme dependence of measured main detector transverse asymmetry from Run 2 Pass 5 for vertical transverse polarization.

Regression scheme	ϵ_{reg} [ppm]	ϕ_0 [degree]	C [ppm]	χ^2/DOF	Prob.
UnReg	4.602 ± 0.807	-9.660 ± 10.042	-1.078 ± 0.571	0.316	0.904
std	4.524 ± 0.806	-9.945 ± 10.211	-1.073 ± 0.570	0.323	0.899
5+1	4.525 ± 0.806	-10.016 ± 10.208	-1.069 ± 0.570	0.321	0.900
set3	4.525 ± 0.806	-10.016 ± 10.208	-1.069 ± 0.570	0.321	0.900
set4	4.527 ± 0.806	-10.017 ± 10.205	-1.068 ± 0.570	0.322	0.900
set7	4.529 ± 0.806	-9.899 ± 10.199	-1.069 ± 0.570	0.320	0.901
set8	4.531 ± 0.806	-9.969 ± 10.196	-1.065 ± 0.570	0.319	0.902
~~set9~~	~~4.534 ± 0.806~~	~~-9.872 ± 10.185~~	~~-1.612 ± 0.570~~	~~0.317~~	~~0.903~~
set10	4.526 ± 0.806	-10.013 ± 10.208	-1.069 ± 0.570	0.321	0.900
set11	4.524 ± 0.806	-9.945 ± 10.211	-1.073 ± 0.570	0.323	0.899

Table D.14 Regression scheme dependence of measured main detector transverse asymmetry from Run-II Pass5 for horizontal transverse polarization.

Regression scheme	ϵ_{reg} [ppm]	ϕ_0 [degree]	C [ppm]	χ^2/DOF	Prob.
UnReg	5.339 ±0.533	6.826 ±5.729	-0.287 ±0.377	1.320	0.252
std	5.343 ±0.533	7.089 ±5.720	-0.289 ±0.377	1.333	0.247
5+1	5.343 ±0.532	7.081 ±5.720	-0.289 ±0.377	1.332	0.247
set3	5.343 ±0.532	7.081 ±5.720	-0.289 ±0.377	1.332	0.247
set4	5.343 ±0.532	7.088 ±5.720	-0.289 ±0.377	1.332	0.247
set7	5.347 ±0.533	7.007 ±5.716	-0.288 ±0.377	1.334	0.246
set8	5.346 ±0.532	6.999 ±5.716	-0.288 ±0.377	1.334	0.246
~~set9~~	~~5.343 ±0.532~~	~~7.154 ±5.719~~	~~-0.376 ±0.377~~	~~1.343~~	~~0.243~~
set10	5.343 ±0.532	7.085 ±5.720	-0.289 ±0.377	1.332	0.247
set11	5.343 ±0.533	7.089 ±5.720	-0.289 ±0.377	1.333	0.247

Table D.15 Correction on measured main detector transverse asymmetry from Run 2 Pass5 due to regression scheme dependence.

Regression scheme	Vertical Correction [ppm]	Horizontal Correction [ppm]
std	0.078	0.004
5+1	0.077	0.004
set3	0.077	0.004
set4	0.076	0.004
set7	0.073	0.007
set8	0.072	0.007
~~set9~~	~~0.069~~	~~0.003~~
set10	0.077	0.003
set11	0.078	0.004
Max-Min	0.006	0.004

Table D.16 Regression time dependence.

Polarization	Runlet based ϵ_{reg}^{runlet} [ppm]	Slug based ϵ_{reg}^{slug} [ppm]	ϵ_{reg}^{runlet} - ϵ_{reg}^{slug} [ppm]
Horizontal	5.3432	5.3492	0.0060
Vertical	4.5252	4.5171	0.0081

Table D.17 Cut dependence.

Cut	Horizontal		Vertical	
	Allowed Statistical Shift [ppm]	ϵ_{reg}^{H} Cut - NoCut [ppm]	Allowed Statistical Shift [ppm]	ϵ_{reg}^{V} Cut - NoCut [ppm]
7,6,5,4σ	0.000	0.000	0.000	0.000
3σ	0.001	0.024	0.000	0.000
2.5σ	0.026	-0.064	0.021	-0.068
2σ	0.082	0.107	0.142	0.367

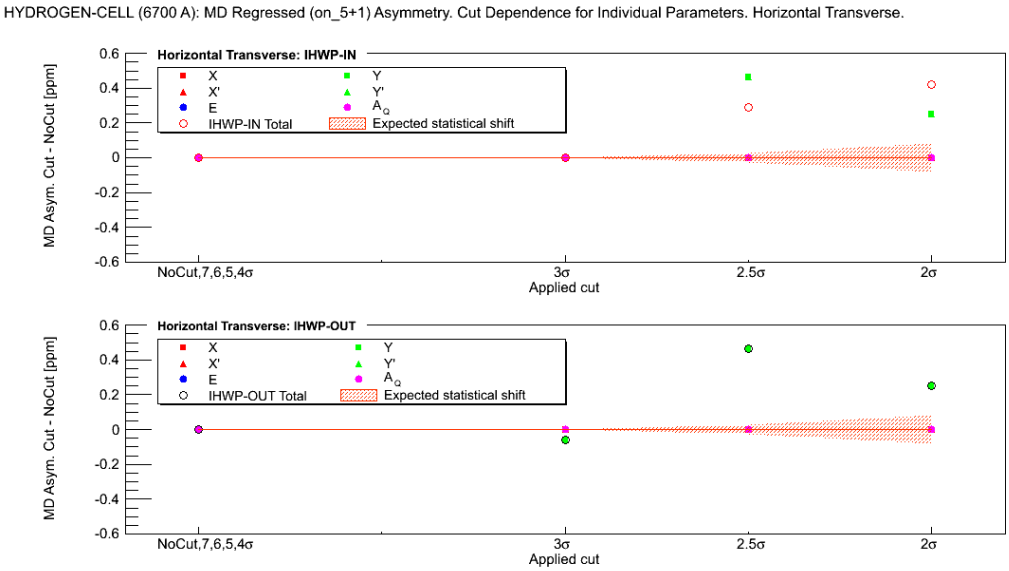

Figure D.18 Cut dependence for horizontal transverse.

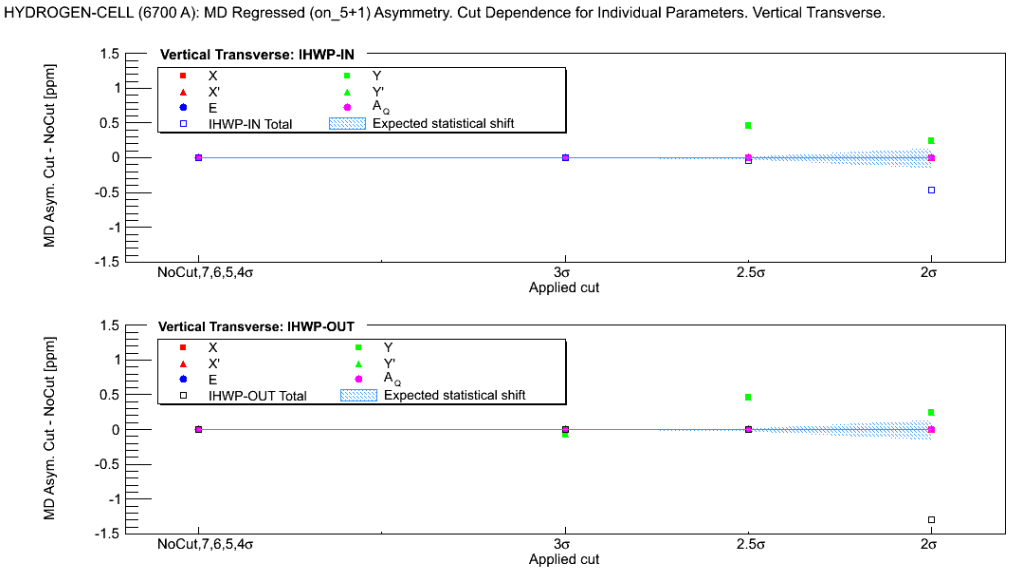

Figure D.19 Cut dependence for vertical transverse.

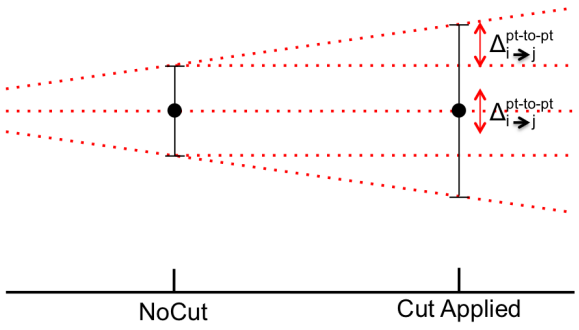

Figure D.20 Cut dependence cartoon.

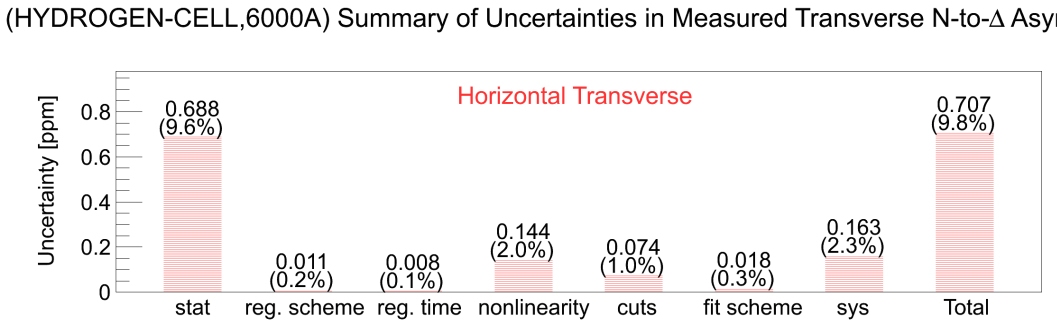

Figure D.21 Summary of uncertainties on measured asymmetry for transverse data set in LH_2 at QTor current 6000 A.

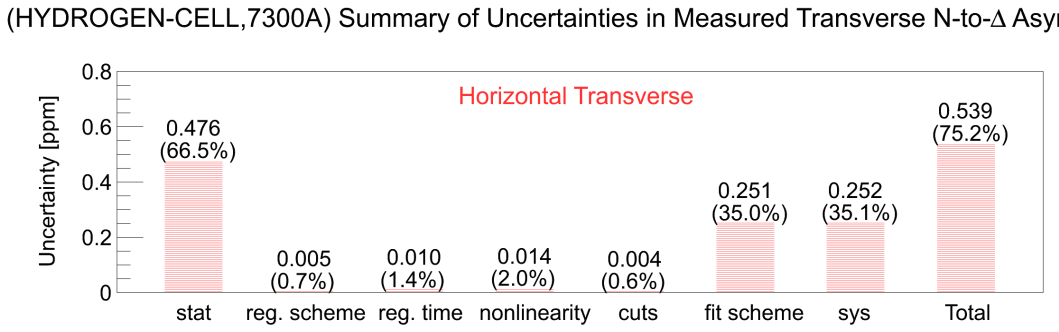

Figure D.22 Summary of uncertainties on measured asymmetry for transverse data set in LH_2 at QTor current 7300 A.

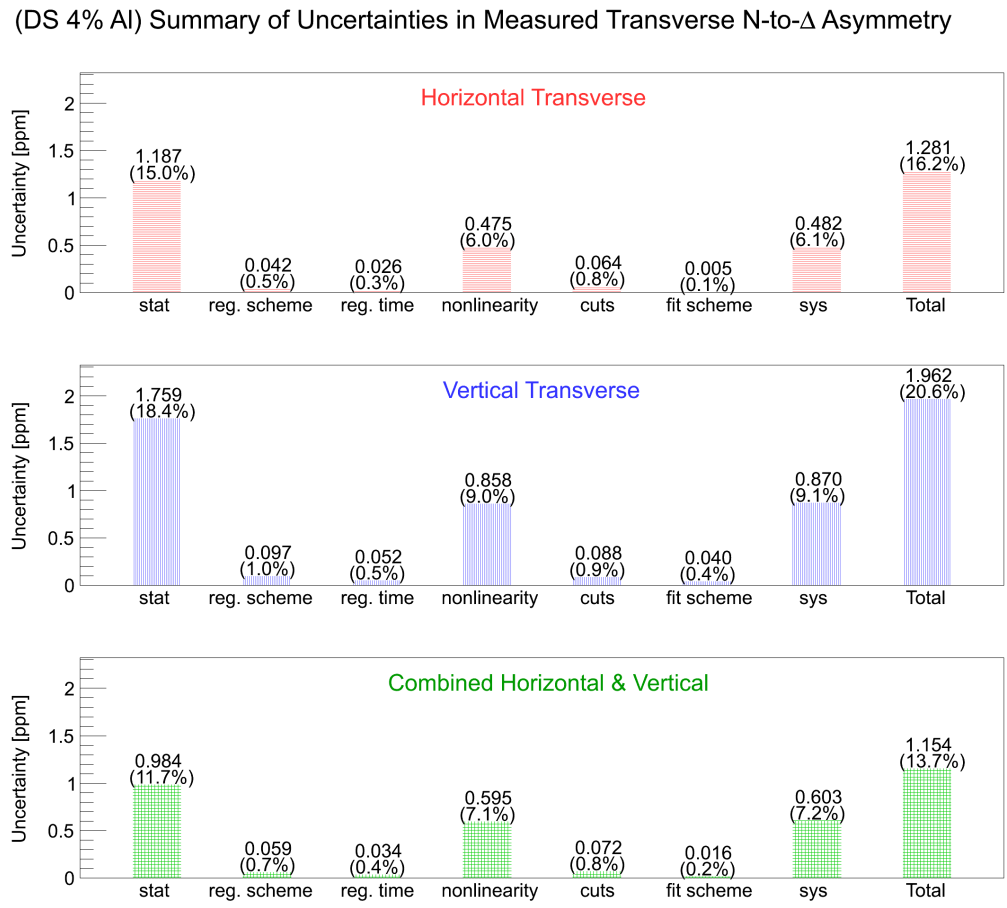

Figure D.23 Summary of uncertainties on measured asymmetry for transverse data set in 4% DS Al at QTor current 6700 A.

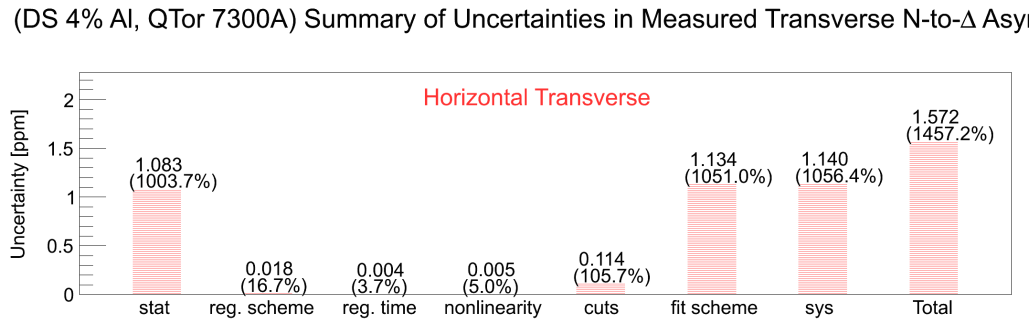

Figure D.24 Summary of uncertainties on measured asymmetry for transverse data set in 4% DS Al at QTor current 7300 A.

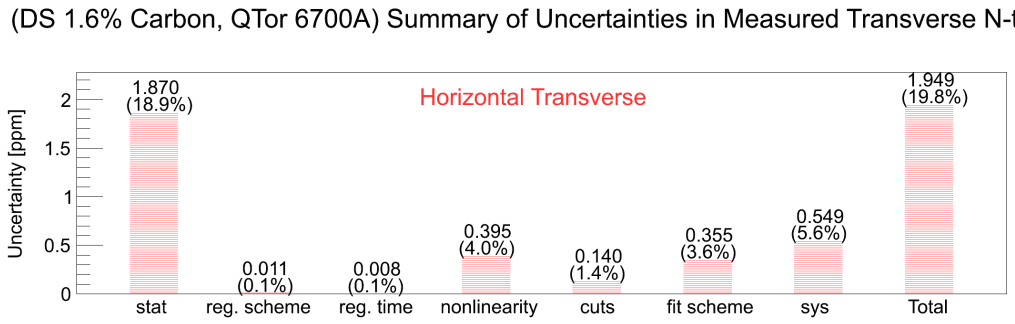

Figure D.25 Summary of uncertainties on measured asymmetry for transverse data set in Carbon at QTor current 6700 A.

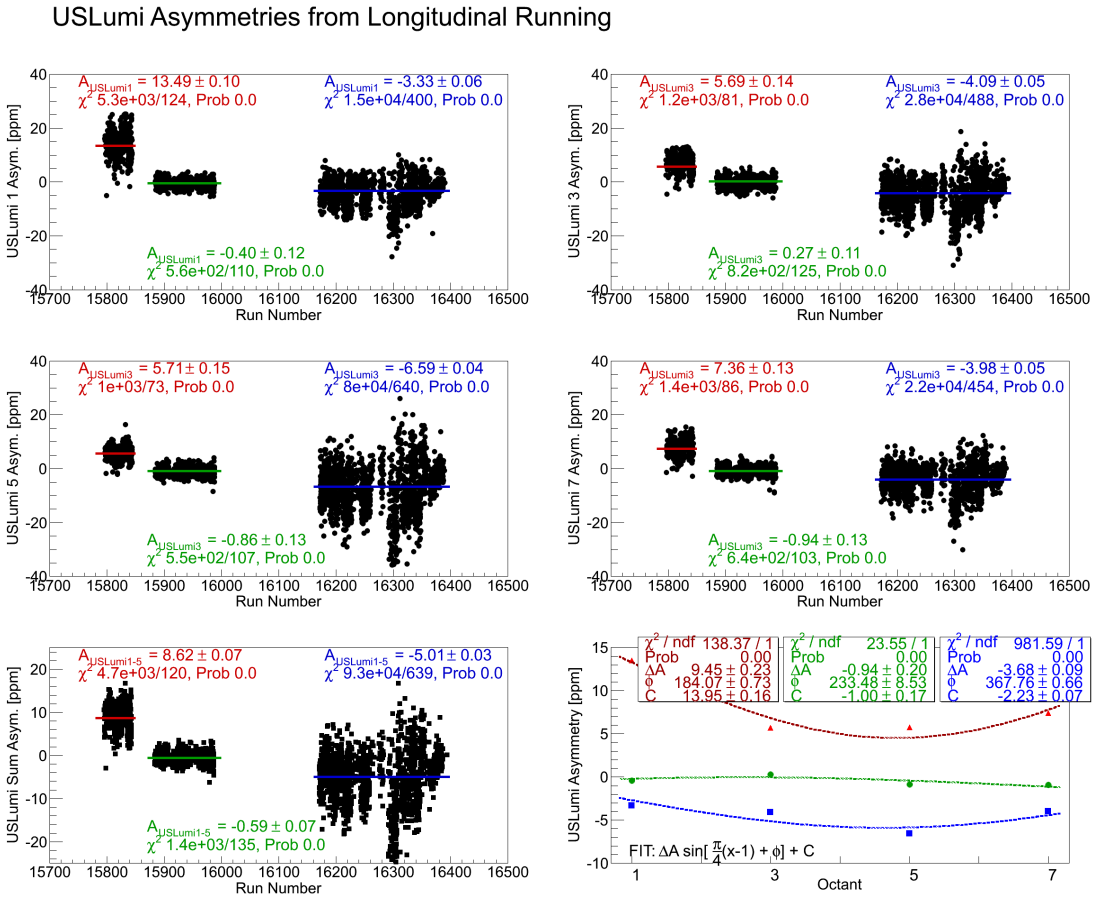

Figure D.26 Regressed "5+1" USLumi asymmetries longitudinal running for octant 1, 3, 5, and 7 are shown in panel 1-4. USLumi sum asymmetry is shown in panel 5. Each point is a runlet. The average asymmetries vs octant for each time period are shown in panel 6.

APPENDIX E

MISCELLANEOUS

E.1 Target BPM Angle Resolution

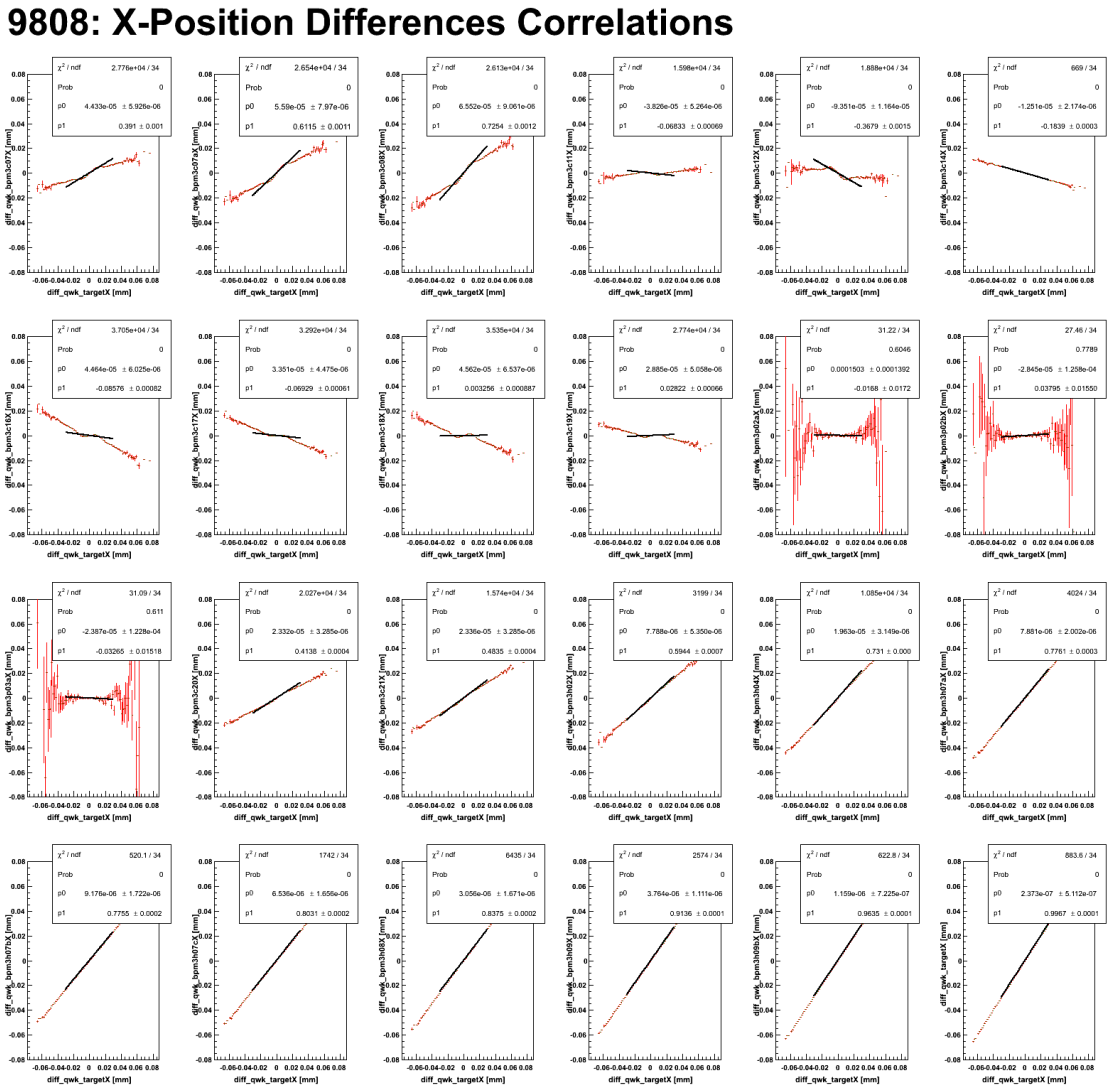

Figure E.1 The BPM target X correlation with other upstream BPMs for a run during Wien 0.

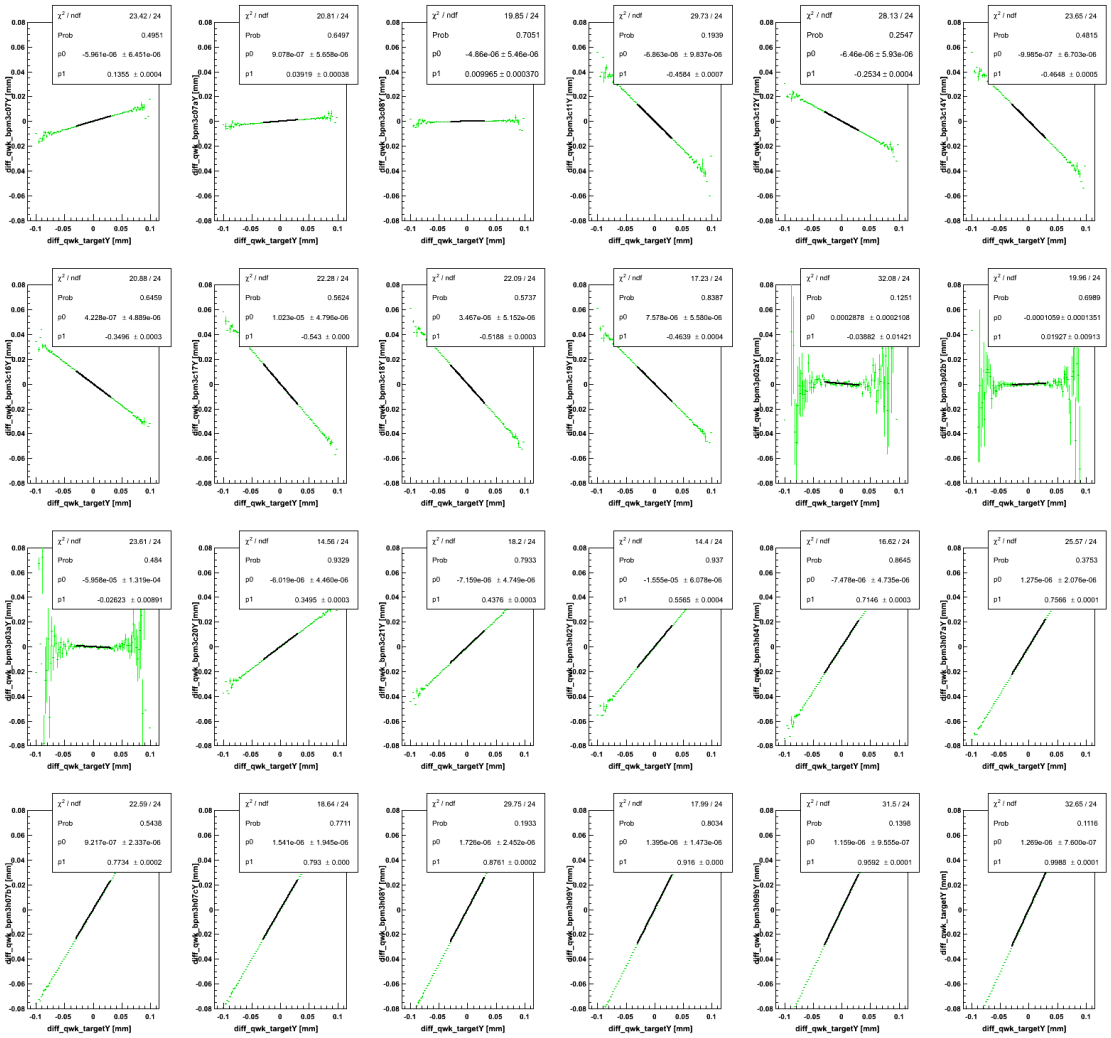

Figure E.2 The BPM target Y correlation with other upstream BPMs for a run during Wien 0.

E.2 Regression Independent Variable Correlation

E.3 Relative Weighted Yield Stability for Q-weak

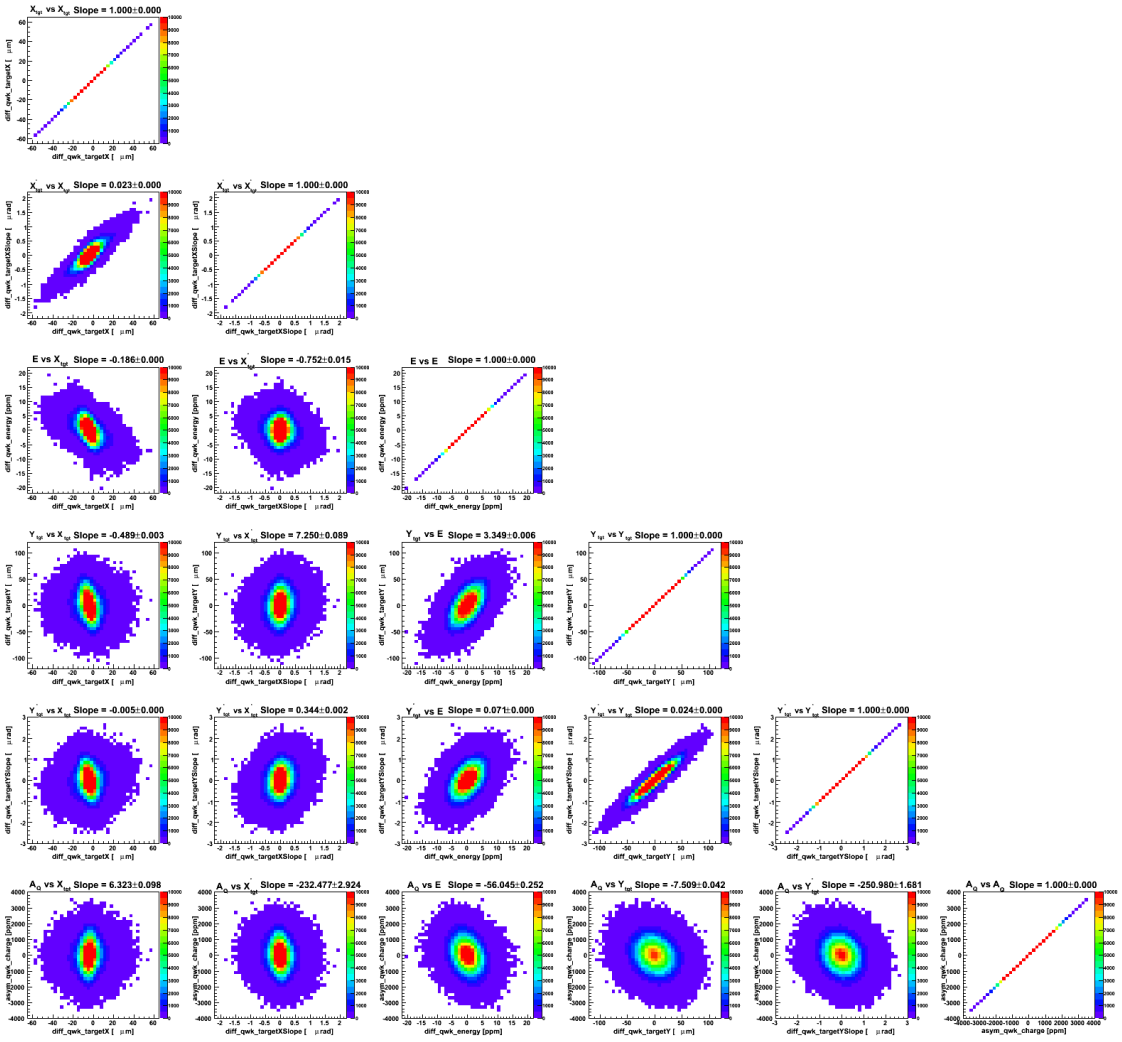

Figure E.3 The correlation between regression variables for a run during Wien 0.

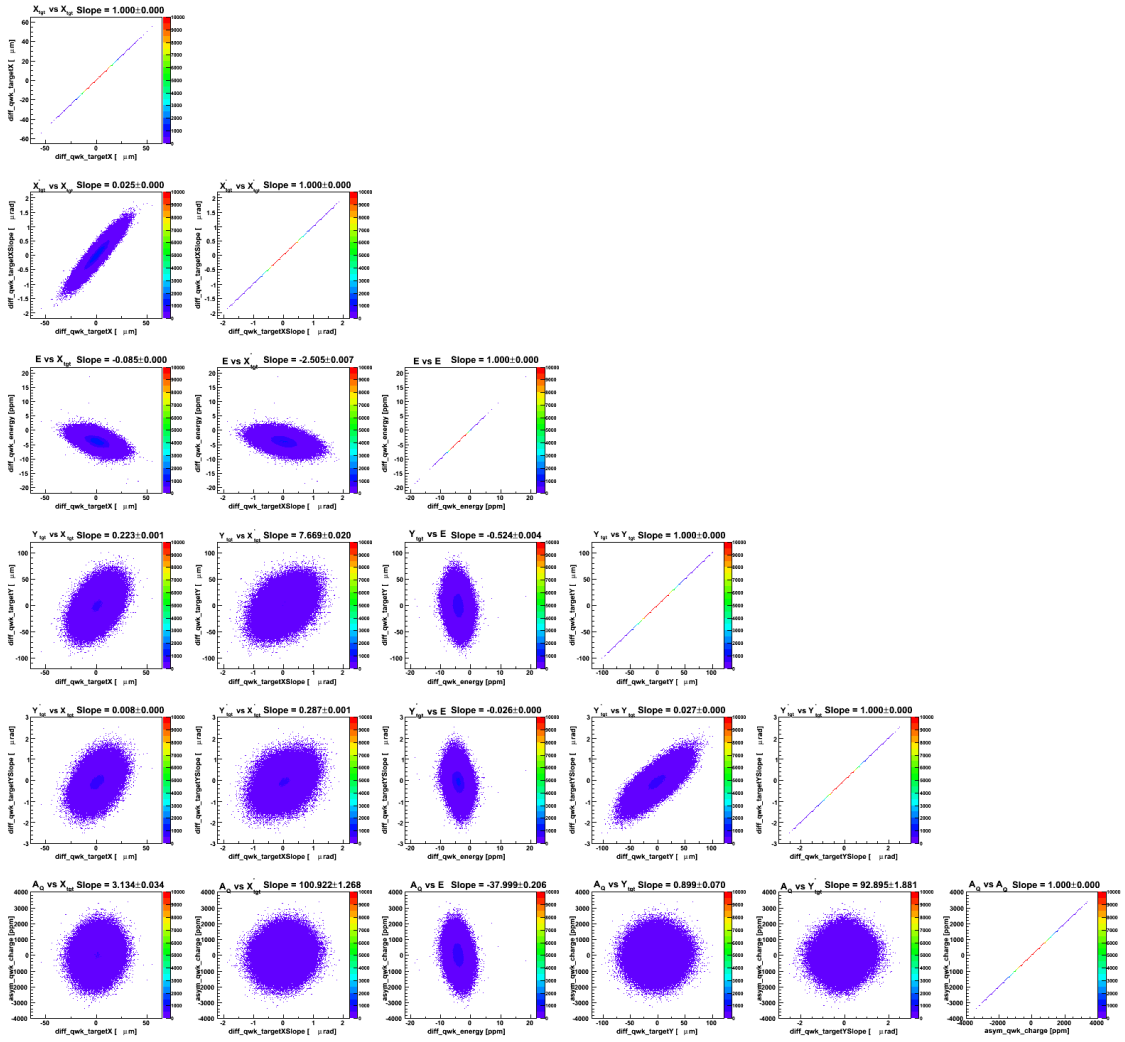

Figure E.4 The correlation between regression variables for a run during Run 2.

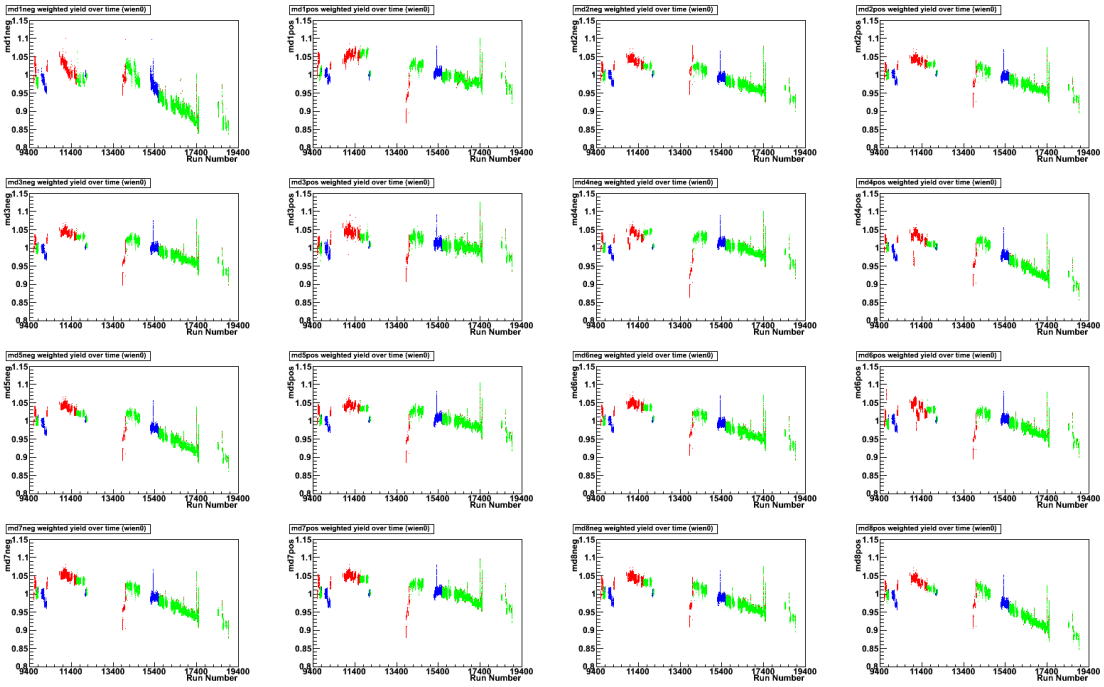

Figure E.5 The weighted yield for each PMT tube in the main detector and can be expressed as $w_i \times Y_i = Y_i / < Y_i >$. Ideally expect to be equal to 1. The weights are equal to the yields at about the 5% level for run1. One can see drifts during Run 2. Each data point is a runlet and the plot was made using the database rootfiles. The weights used for a given runlet to calculate the relative weighted yield are those appropriate for that time based on the mapfile names.

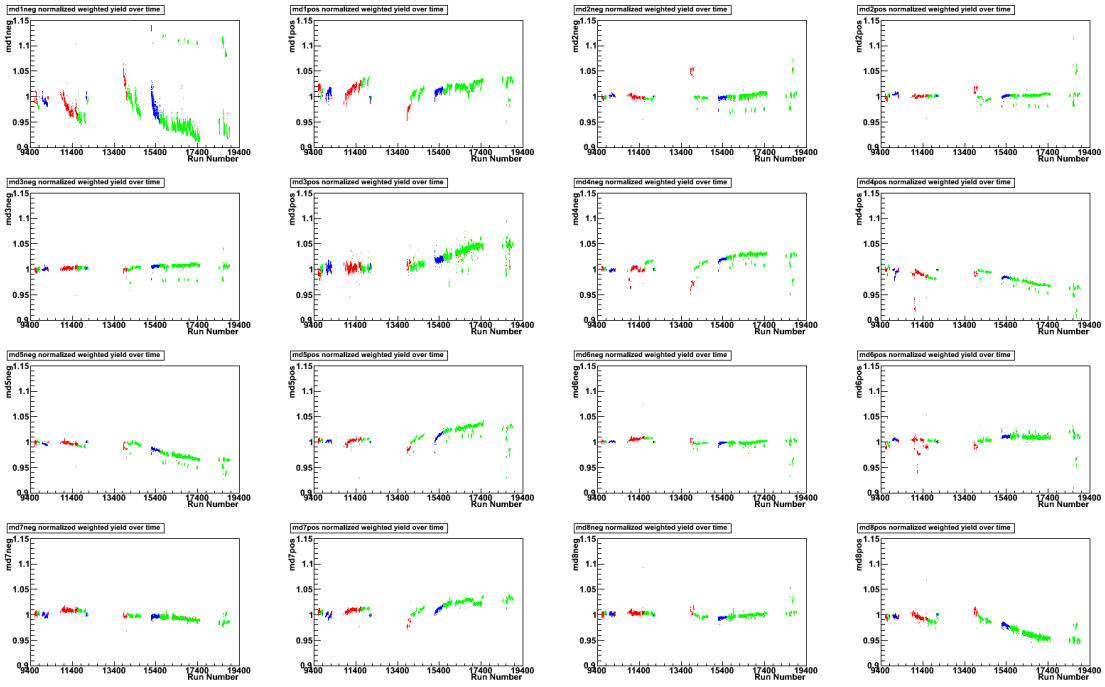

Figure E.6 The relative weighted yield for each PMT tube in the main detector and can be expressed as $w_i \times Y_i / \sum(w_i \times Y_i/16)$. Color transitions mark the beginning of a weighting period defined by the mapfiles.

APPENDIX F

DATABASE STRESS TEST

F.1 Database Stress Test

The motivation behind this analysis was to perform quality checks of the analyzer and database. In order to do such an analysis, a dataset of N→ Δ measurement from Run 1, slug 3 and 4 was chosen for its strange behavior. This section will focus on different quality checks performed on the dataset.

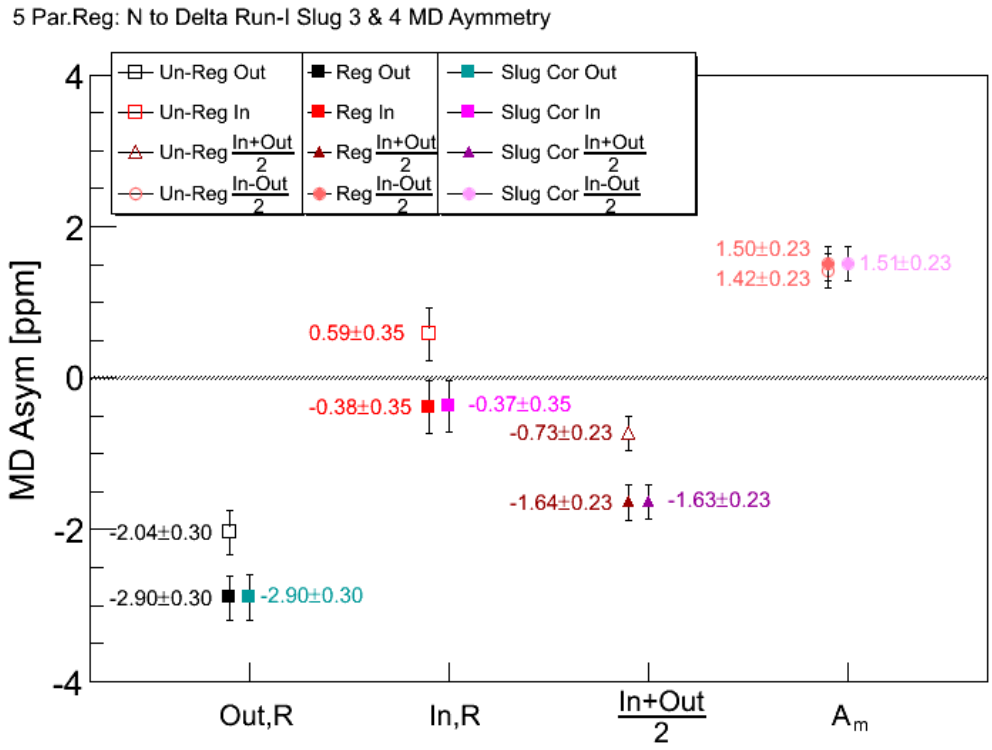

Figure F.1 Main detector asymmetries for PV e-p scattering in N→ Δ dataset from Run 1 pass 4b database for slugs 3 and 4.

F.1.1 Database Stress Test

The regression stress test was performed on the parity violating electron-proton scattering in N→ Δ region dataset from Run 1 pass 3 database for slugs 3 and 4. A closer look revealed a discrepancy

between runlet numbers between un-regressed and regressed asymmetries in the database for pass 3, which was then fixed during the pass 4b. The weighted, un-weighted octant averaged asymmetries, and MDall asymmetries were similar. The asymmetries averaged over runlet yielded a different asymmetry compared to run averaged asymmetry. The different noise suppression in runlet and run level averaging might have created this discrepancy. The un-regressed IHWP-IN and correction are significantly different from this analysis, compared to an independent analysis by J. Leacock [3]. The regressed MD all asymmetries in Run 1 pass4b database were consistent with [3]. The regression did not improve χ^2/DOF or probability, but improved the main detector asymmetry widths by few ppm. Normalizing the asymmetry width with beam current didn't improve the result. The regression also helped to remove the dipole. The $\sim 7\sigma$ (IN+OUT)/2 problem persists in pass4b 5 parameter regression for the dataset. The slug averaged sensitivities give similar results. The sensitivity vs octant looks nice.

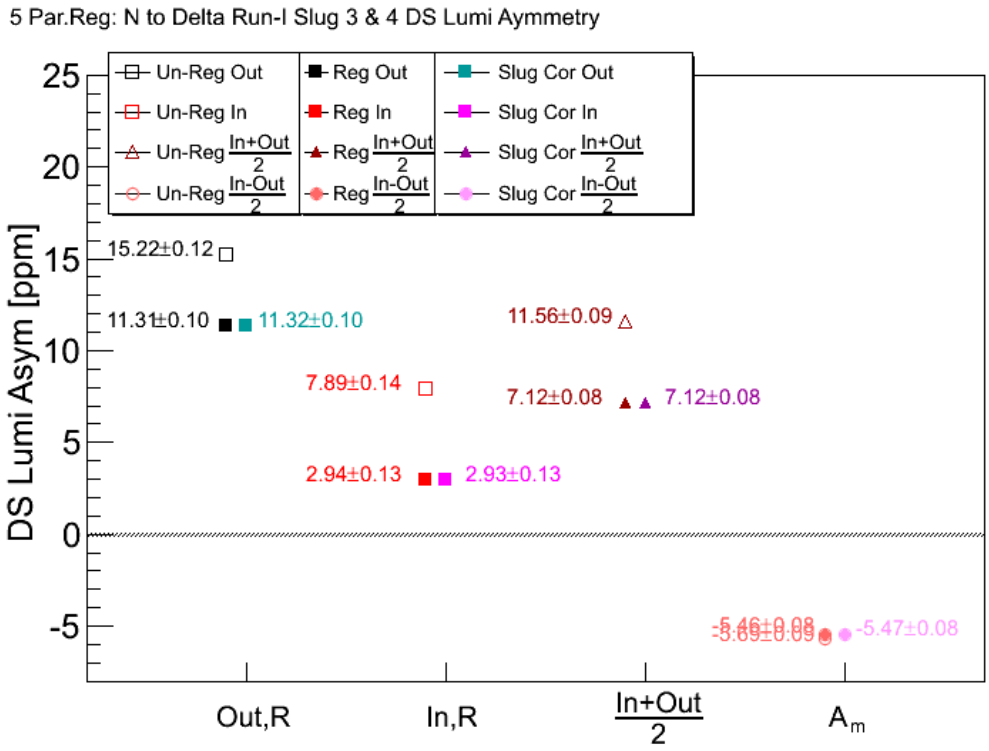

Figure F.2 The downstream luminosity monitor asymmetries for PV e-p scattering in N→ Δ dataset from Run 1 pass 4b database for slugs 3 and 4.

The same analysis was performed on DS Lumi. The slug average sensitivities give similar answer within ∼8 ppb level. The DS Lumi sensitivities are fairly stable but high compared to main

detector. The slug averaged sensitivity reduce the noise but don't improve as main detector. The regression improve widths by 28 ppm. The octant averaged asymmetries didn't match DS lumi sum. The normalized octant yields are different. Problem found in the DS Lumi sum calculation. The regression didn't remove dipole completely and the dipole was too big to be transverse. Some significant slopes remaining after regression in few cases. The charge sensitivity was 20%.

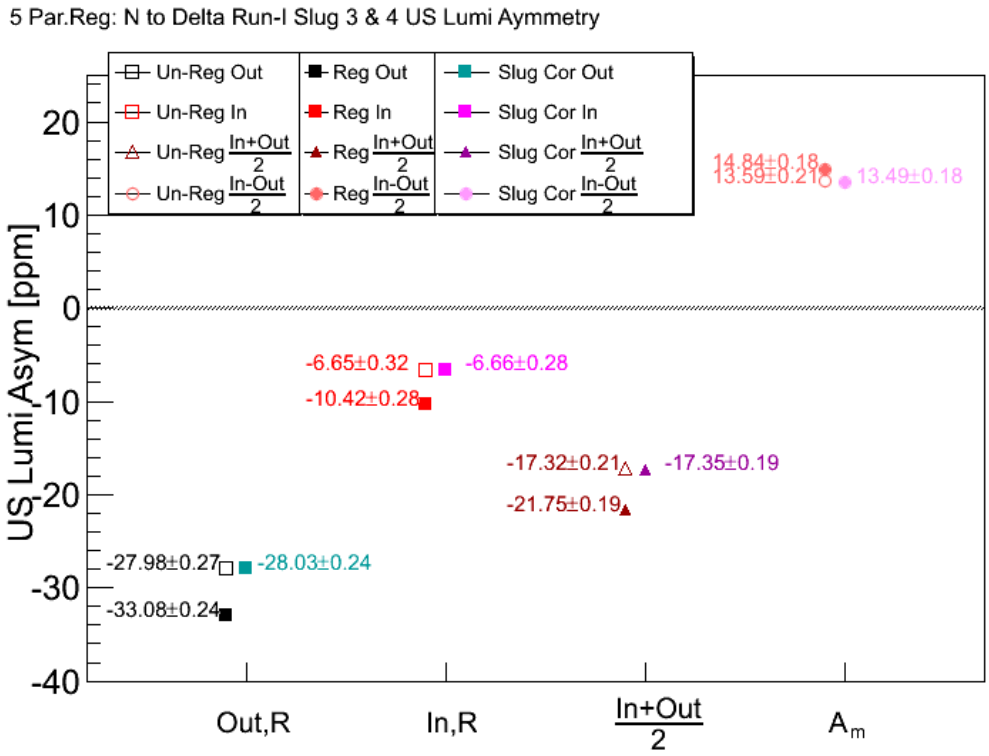

Figure F.3 The upstream luminosity monitor asymmetries for PV e-p scattering in N→ Δ dataset from Run 1 pass 4b database for slugs 3 and 4.

APPENDIX G

REGRESSION SCHEMES

The regression schemes for the Q-weak experiment are shown in Table G.1.

Table G.1 Summary of the variables used in different regression schemes used [21].

std	**on_5+1**	**set3**
diff_qwk_targetX	diff_qwk_targetX	diff_qwk_targetX
diff_qwk_targetY	diff_qwk_targetY	diff_qwk_targetY
diff_qwk_targetXSlope	diff_qwk_targetXSlope	diff_qwk_targetXSlope
diff_qwk_targetYSlope	diff_qwk_targetYSlope	diff_qwk_targetYSlope
diff_qwk_energy	diff_qwk_energy	diff_qwk_bpm3c12X
	asym_qwk_charge	asym_qwk_charge

set4	**set5**	**set6**
diff_qwk_targetX	diff_bpm_9b_p_4X	diff_bpm_9b_p_4X
diff_qwk_targetY	diff_bpm_9b_p_4Y	diff_bpm_9b_p_4Y
diff_qwk_targetXSlope	diff_bpm_9b_m_4X	diff_bpm_9b_m_4X
diff_qwk_targetYSlope	diff_bpm_9b_m_4Y	diff_bpm_9b_m_4Y
diff_qwk_energy	diff_qwk_bpm3c12X	diff_qwk_bpm3c12X
asym_qwk_bcm5		asym_qwk_charge

set7	**set8**	**set9**
diff_bpm_9_p_4X	diff_bpm_9_p_4X	diff_qwk_targetX
diff_bpm_9_p_4Y	diff_bpm_9_p_4Y	diff_qwk_targetY
diff_bpm_9_m_4X	diff_bpm_9_m_4X	diff_qwk_targetXSlope
diff_bpm_9_m_4Y	diff_bpm_9_m_4Y	diff_qwk_targetYSlope
diff_qwk_bpm3c12X	diff_qwk_bpm3c12X	diff_qwk_energy
	asym_qwk_charge	asym_qwk_charge
		asym_uslumi_sum

set10	**set11**	**set12**
diff_qwk_targetX	diff_qwk_targetX	diff_qwk_target_plus4X
diff_qwk_targetY	diff_qwk_targetY	diff_qwk_target_plus4Y
diff_qwk_targetXSlope	diff_qwk_targetXSlope	diff_qwk_target_plus4XSlope
diff_qwk_targetYSlope	diff_qwk_targetYSlope	diff_qwk_target_plus4YSlope
diff_qwk_energy	diff_qwk_bpm3c12X	diff_qwk_bpm3c12X
asym_qwk_bcm6		

The notation in "set5" and "set6" of "diff_bpm_9b_p(m)_4" for X and Y is given as:

diff_bpm_9b_p_4 ≡ diff_qwk_bpm3h09b + diff_qwk_bpm3h04 (position-like),

diff_bpm_9b_m_4 ≡ diff_qwk_bpm3h09b - diff_qwk_bpm3h04 (direction/angle-like).

The prefix *diff* is used to denote the helicity correlated difference, except for the energy variable which is $\frac{dp}{p}$. The acronym used for the asymmetry is "asym" and "qwk" is for Q-weak. The position variables at the target are shown by "targetX" and "targetY", whereas angles are shown by "tar-

getXSlope" and "targetYSlope". The horizontal BPM position measurement at 3C12, "bpm3c12X", at the highest dispersive region of the beamline is used as an alternate measure of the energy of the electron beam.

APPENDIX H

Q-WEAK COLLABORATION

D. Armstrong[1], A. Asaturyan[14], T. Averett[1], R.Beminiwattha[c,18], J. Benesch[10], J. Birchall[8], P. Bosted[10], A. Bruell, C. Capuano[1], R. D. Carlini[a,10] (Principal Investigator), G. Cates[21], C. Carrigee, S. Chattopadhyay, S. Covrig[13], M. Dalton[21], C. A. Davis[12], W. Deconinck[9], X. Deng[21], K. Dow[9], J. Dunne[15], D. Dutta[15], R. Ent[10], J. Erler, W. Falk[8], H. Fenker[10], T. A. Forest, W. Franklin[9], D. Gaskell[10], M. Gericke[8], J. Grames[10], K. Grimm, F.W. Hersman, D. Higinbotham[10], M. Holtrop[13], J.R. Hoskins[c,1], K. Johnston, E. Ihloff[9], D. Jones[21], M. Jones[10], R. Jones, K. Joo, J. Kelsey[9], C. Keppel[19], M. Khol[19], P. King[18], E. Korkmaz, S. Kowalski[a,9], J. Leacock[c,11], J.P. Leckey[c,1], J. H. Lee[1,18], L. Lee[12], A. Lung[10], S. MacEwan[8], D. Mack[10], R. Mahurin[8], S. Majewski, J. Mammei[11], J. Martin[20], D. Meekins[10], A. Micherdzinska[22], A. Mkrtchyan[14], H. Mkrtchyan[14], N. Morgan[11], K. E. Myers[c,22], A. Narayan[c,15], Nuruzzaman[c,19], A. K. Opper[22], S. Page[a,8], J. Pan[c,8], K. Paschke[21], S. Phillips[13], M. Pitt[11], M. Poelker[10], T. Porcelli, Y. Prok, W. D. Ramsay[8], M. Ramsey-Musolf, J. Roche[18], B. Sawatzky[10], N. Simicevic, G. Smith[b,10], T. Smith, P. Solvignon[10], P. Souder[23], D. Spayde[6], B. E. Stokes, R. Subedi[21], R. Suleiman[10], V. Tadevosyan, E. Tsentalovich[9], W.T.H. van Oers[8], W. Vulcan[10], B. Waidyawansa[c,18], D. Wang[21], P. Wang[c,8], S. Wells, S. A. Wood[10], S. Yang[c,1], R. Young, H. Zhu, X. Zheng[21], C. Zorn[10].

a Spokespersons *b* Project Manager *c* Graduate Student

[1]College of William and Mary, Williamsburg, VA, USA.
[2]University of Connecticut.
[3]Instituto de Fisica.
[4]Universidad Nacional Autonoma de Mexico.
[5]University of Wisconsin.
[6]Hendrex College.
[7]Louisiana Tech University.
[8]University of Manitoba.
[9]Massachusetts Institute of Technology, Massachusetts, VA, USA.
[10]Thomas Jefferson National Accelerator Facility, Newport News VA, USA.
[11]Virginia Polytechnic Institute & State University
[12]TRIUMF, Vancouver, British Columbia, Canada.
[13]University of New Hampshire.
[14]Yerevan Physics Institute, Yerevan, Armenia.
[15]Mississippi State University, Mississippi State, VA, USA.
[16]University of Northern British Columbia.
[17]Cockroft Institute of Accelerator Science and Technology.
[18]Ohio University, Athens, OH, USA.
[19]Hampton University, Hampton, VA, USA.
[20]University of Winnipeg.
[21]University of Virginia, Charlottesville, VA, USA.
[22]George Washington University, VA, USA.
[23]Syracuse University
[24]Idaho State University.
[25]University of Connecticut.
[26]Christopher Newport University, Newport News, VA, USA.

Note: The details about the collaboration can be found in reference [184].

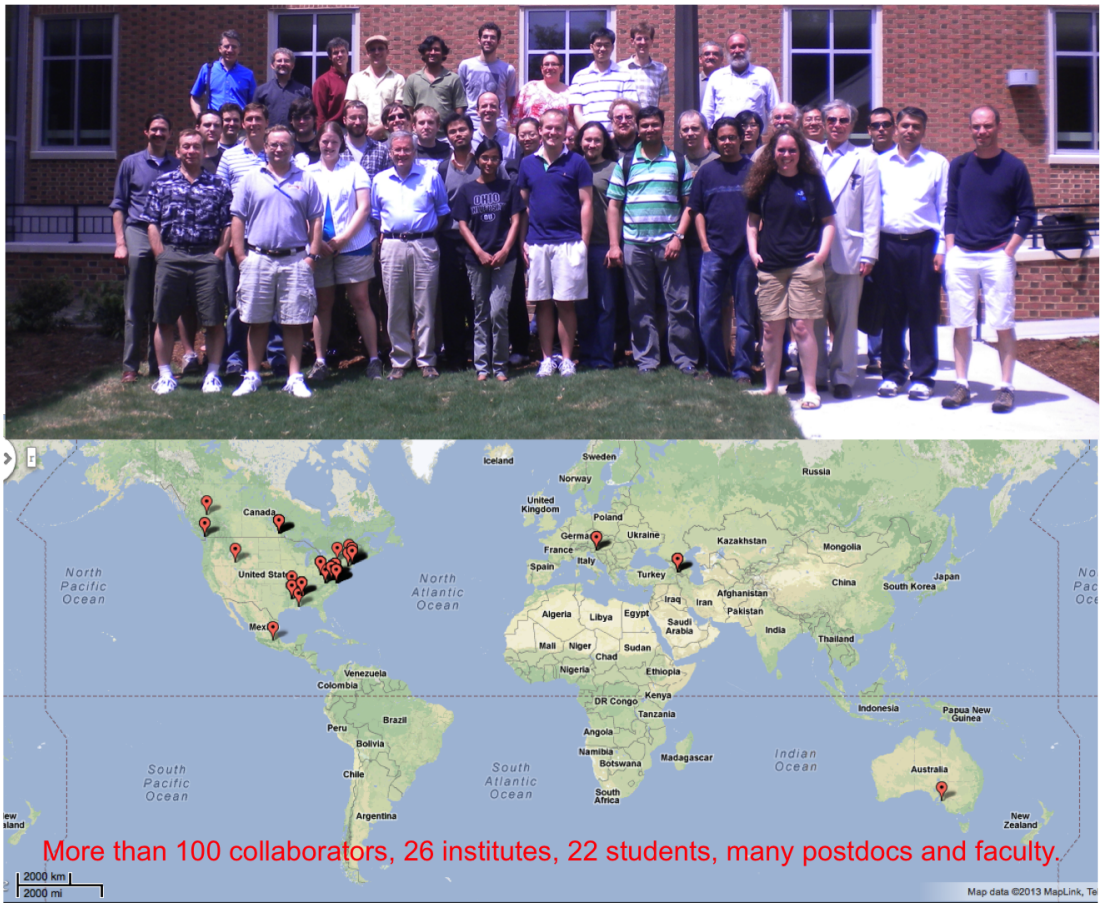

Figure H.1 The Q-weak collaboration during meeting at College of W&M 2011.

REFERENCES

[1] MissMJ. Standard model of elementary particles. (free to use, original file created by user) Own work by uploader, PBS NOVA, Fermilab, Office of Science, United States Department of Energy, Particle Data Group. Licensed under Creative Commons Attribution 3.0 via Wikimedia Commons -http://commons.wikimedia.org/wiki/File:Standard_Model_of_Elementary_Particles.svg#mediaviewer/File:Standard_Model_of_Elementary_Particles.svg, 2014. (Cited on pages xvi and 3.)

[2] Kent Paschke. Overview of Parity-Viola1ng Electron Scattering. CREX Workshop, https://www.jlab.org/conferences/crex/sun/Paschke_CREX_IntroPVES.pdf, March 2013. (Cited on pages xvi and 4.)

[3] John Leacock. *Measuring the Weak Charge of the Proton and the Hadronic Parity Violation of the $N \rightarrow \Delta$ Transition.* PhD thesis, Virginia Polytechnic Institute & State University, Blacksburg, VA 24061-0002, USA, October 2012. (Cited on pages xvi, 9, 41, 93, 118, and 196.)

[4] J. Arrington, W. Melnitchouk, and J. A. Tjon. Global analysis of proton elastic form factor data with two-photon exchange corrections. *Phys. Rev. C*, 76:035205, Sep 2007. (Cited on pages xvi and 13.)

[5] B. Pasquini and M. Vanderhaeghen. Resonance estimates for single spin asymmetries in elastic electron-nucleon scattering. *Phys. Rev. C*, 70:045206, Oct 2004. (Cited on pages xvi and 16.)

[6] B. Pasquini and M. Vanderhaeghen. Single spin asymmetries in elastic electron-nucleon scattering. *Eur Phys J*, 24:29–32, 2005. (Cited on pages xvi and 16.)

[7] Barbara Pasquini. Two-Photon Physics: Theory. MAMI and Beyond: http://wwwkph.kph.uni-mainz.de/T//MAMIandBeyond/02%20Dienstag/08%20Pasquini.pdf, April 2009. (Cited on pages xvi, xxiv, 17, 18, and 126.)

[8] Kathrine Myers. *The First Determination of the Proton's Weak Charge Through Parity-Violating Asymmetry Measurements in Elastic e+p and e+Al Scattering.* PhD thesis, The George Washington University, Washington, DC 20052, USA, May 2012. (Cited on pages xvii, 25, 29, 34, 35, and 118.)

[9] Peiqing Wang. Simulated elastic flux images on main bars. ELOG-Analysis-588: https://qweak.jlab.org/elog/Analysis+&+Simulation/588, May 2012. (Cited on pages xvii and 39.)

[10] Jie Pan. *Towards a Precision Measurement of Parity-Violating e-p Elastic Scattering at Low Momentum Transfer*. PhD thesis, University of Manitoba, Winnipeg, Manitoba, Canada, June 2012. (Cited on pages xvii, 39, 40, and 42.)

[11] David Armstrong. BMod energy modulation: indeed, needs FFB paused. HCLOG-249809: https://hallcweb.jlab.org/hclog/1201_archive/120124094154.html, January 2012. (Cited on pages xix and 59.)

[12] T. Allison et al. The Q˙weak Experimental Apparatus. 2014. (Cited on pages xx, xxix, 74, 75, and 76.)

[13] Adesh Subedi. Simulation of QTor scans using QWGEANT3. ELOG-Analysis-837: https://qweak.jlab.org/elog/Analysis+&+Simulation/837, December 2012. (Cited on pages xxiii, 119, 120, and 121.)

[14] Nuruzzaman. Q^2 for transverse N-to-Delta from GEANT-III. ELOG-Ancillary-44: https://qweak.jlab.org/elog/Ancillary/44, July 2013. (Cited on pages xxiii, 122, and 123.)

[15] Nuruzzaman. PMT Asymmetries for Inelastic Transverse Dataset on LH2. ELOG-Ancillary-145: https://qweak.jlab.org/elog/Ancillary/145, November 2014. (Cited on pages xxvi, 181, and 182.)

[16] Q weak Collaboration. The Q-weak Experiment: "A Search for New Physics at the TeV Scale via a Measurement of the Proton's Weak Charge". Technical Report E05-008 Jeopardy proposal, December 2007. (Cited on pages xxviii, 6, 7, 17, 19, 21, 91, 101, and 132.)

[17] D. Androic et al. First Determination of the Weak Charge of the Proton. 2013. (Cited on pages xxviii and 21.)

[18] Nuruzzaman. Qweak: First direct measurement of the weak charge of the proton. *EPJ Web of Conferences*, 71:00100, 2014. (Cited on pages xxviii and 21.)

[19] Buddhini Waidyawansa. *A 3% Measurement of the Beam Normal Single Spin Asymmetry in Forward Angle Elastic Electron-Proton Scattering using the Qweak Setup*. PhD thesis, Ohio

University, Athens OH 45701, USA, August 2013. (Cited on pages xxviii, 27, 42, 44, 87, 91, 121, 122, and 124.)

[20] Joshua Magee. The Qweak Run 2 Moller Polarimetry Analysis. Technical Report Qweak-DocDB-1955, January 2014. (Cited on pages xxix and 116.)

[21] Nuruzzaman. Q-weak regression scheme. ELOG-Management-5: https://qweak.jlab.org/elog/Management/5, April 2012. (Cited on pages xxx and 198.)

[22] Francis Halzen and Alan D. Martin. *Quarks and Leptones: An Introductory Course in Modern Particle Physics*. John Wiley and Sons, Inc., 1st edition, January 1984. (Cited on page 2.)

[23] C.Y. Prescott, W.B. Atwood, R.L.A. Cottrell, H. DeStaebler, Edward L. Garwin, A. Gonidec, R.H. Miller, L.S. Rochester, T. Sato, D.J. Sherden, C.K. Sinclair, S. Stein, R.E. Taylor, J.E. Clendenin, V.W. Hughes, N. Sasao, K.P. Schler, M.G. Borghini, K. Lbelsmeyer, and W. Jentschke. Parity non-conservation in inelastic electron scattering. *Physics Letters B*, 77(3):347 – 352, 1978. (Cited on page 2.)

[24] F.J. Hasert, S. Kabe, W. Krenz, J. Von Krogh, D. Lanske, J. Morfin, K. Schultze, H. Weerts, G.H. Bertrand-Coremans, J. Sacton, W. Van Doninck, P. Vilain, U. Camerini, D.C. Cundy, R. Baldi, I. Danilchenko, W.F. Fry, D. Haidt, S. Natali, P. Musset, B. Osculati, R. Palmer, J.B.M. Pattison, D.H. Perkins, A. Pullia, A. Rousset, W. Venus, H. Wachsmuth, V. Brisson, B. Degrange, M. Haguenauer, L. Kluberg, U. Nguyen-Khac, P. Petiau, E. Belotti, S. Bonetti, D. Cavalli, C. Conta, E. Fiorini, M. Rollier, B. Aubert, D. Blum, L.M. Chounet, P. Heusse, A. Lagarrigue, A.M. Lutz, A. Orkin-Lecourtois, J.P. Vialle, F.W. Bullock, M.J. Esten, T.W. Jones, J. McKenzie, A.G. Michette, G. Myatt, and W.G. Scott. Observation of neutrino-like interactions without muon or electron in the gargamelle neutrino experiment. *Physics Letters B*, 46(1):138 – 140, 1973. (Cited on page 2.)

[25] F.J. Hasert, H. Faissner, W. Krenz, J. Von Krogh, D. Lanske, J. Morfin, K. Schultze, H. Weerts, G.H. Bertrand-Coremans, J. Lemonne, J. Sacton, W. Van Doninck, P. Vilain, C. Baltay, D.C. Cundy, D. Haidt, M. Jaffre, P. Musset, A. Pullia, S. Natali, J.B.M. Pattison, D.H. Perkins, A. Rousset, W. Venus, H.W. Wachsmuth, V. Brisson, B. Degrange, M. Haguenauer, L. Kluberg, U. Nguyen-Khac, P. Petiau, E. Bellotti, S. Bonetti, D. Cavalli, C. Conta, E. Fiorini, M. Rollier, B. Aubert, L.M. Chounet, P. Heusse, A. Lagarrigue, A.M. Lutz, J.P. Vialle, F.W. Bullock, M.J. Esten, T. Jones, J. McKenzie, A.G. Michette, G. Myatt, J. Pinfold, and W.G.

Scott. Search for elastic muon-neutrino electron scattering. *Physics Letters B*, 46(1):121 – 124, 1973. (Cited on page 2.)

[26] F.J. Hasert, S. Kabe, W. Krenz, J. Von Krogh, D. Lanske, J. Morfin, K. Schultze, H. Weerts, G. Bertrand-Coremans, J. Sacton, W. Van Doninck, P. Vilain, R. Baldi, U. Camerini, D.C. Cundy, I. Danilchenko, W.F. Fry, D. Haidt, S. Natali, P. Musset, B. Osculati, R. Palmer, J.B.M. Pattison, D.H. Perkins, A. Pullia, A. Rousset, W. Venus, H. Wachsmuth, V. Brisson, B. Degrange, M. Haguenauer, L. Kluberg, U. Nguyen-Khac, P. Petiau, E. Bellotti, S. Bonetti, D. Cavalli, C. Conta, E. Fiorini, M. Rollier, B. Aubert, D. Blum, L.M. Chounet, P. Heusse, A. Lagarrigue, A.M. Lutz, A. Orkin-Lecourtois, J.P. Vialle, F.W. Bullock, M.J. Esten, T.W. Jones, J. McKenzie, A.G. Michette, G. Myatt, and W.G. Scott. Observation of neutrino-like interactions without muon or electron in the gargamelle neutrino experiment. *Nuclear Physics B*, 73(1):1 – 22, 1974. (Cited on page 2.)

[27] G. W. Bennett, B. Bousquet, H. N. Brown, G. Bunce, R. M. Carey, P. Cushman, G. T. Danby, P. T. Debevec, M. Deile, H. Deng, S. K. Dhawan, V. P. Druzhinin, L. Duong, F. J. M. Farley, G. V. Fedotovich, F. E. Gray, D. Grigoriev, M. Grosse-Perdekamp, A. Grossmann, M. F. Hare, D. W. Hertzog, X. Huang, V. W. Hughes, M. Iwasaki, K. Jungmann, D. Kawall, and B. I. Khazin. Measurement of the negative muon anomalous magnetic moment to 0.7 ppm. *Phys. Rev. Lett.*, 92(16):161802, Apr 2004. (Cited on page 3.)

[28] E. Klempt. Baryon resonances and strong QCD. 2002. (Cited on page 8.)

[29] Nimai C. Mukhopadhyay, M.J. Ramsey-Musolf, Steven J. Pollock, Jn Lu, and H.-W. Hammer. Parity-violating excitation of the $\delta(1232)$: hadron structure and new physics. *Nuclear Physics A*, 633(3):481 – 518, 1998. (Cited on page 9.)

[30] Shi-Lin Zhu, C. M. Maekawa, G. Sacco, B. R. Holstein, and M. J. Ramsey-Musolf. Electroweak radiative corrections to parity-violating electroexcitation of the δ. *Phys. Rev. D*, 65:033001, Dec 2001. (Cited on page 9.)

[31] J. Arrington, P.G. Blunden, and W. Melnitchouk. Review of two-photon exchange in electron scattering. *Progress in Particle and Nuclear Physics*, 66(4):782 – 833, 2011. (Cited on pages 10 and 13.)

[32] M. K. Jones, K. A. Aniol, F. T. Baker, J. Berthot, P. Y. Bertin, W. Bertozzi, A. Besson, L. Bimbot, W. U. Boeglin, E. J. Brash, D. Brown, J. R. Calarco, L. S. Cardman, C.-C. Chang, J.-P.

Chen, E. Chudakov, S. Churchwell, E. Cisbani, D. S. Dale, R. De Leo, A. Deur, B. Diederich, J. J. Domingo, M. B. Epstein, L. A. Ewell, K. G. Fissum, A. Fleck, H. Fonvieille, S. Frullani, J. Gao, F. Garibaldi, A. Gasparian, G. Gerstner, S. Gilad, R. Gilman, A. Glamazdin, C. Glashausser, J. Gomez, V. Gorbenko, A. Green, J.-O. Hansen, C. R. Howell, G. M. Huber, M. Iodice, C. W. de Jager, S. Jaminion, X. Jiang, W. Kahl, J. J. Kelly, M. Khayat, L. H. Kramer, G. Kumbartzki, M. Kuss, E. Lakuriki, G. Lavessière, J. J. LeRose, M. Liang, R. A. Lindgren, N. Liyanage, G. J. Lolos, R. Macri, R. Madey, S. Malov, D. J. Margaziotis, P. Markowitz, K. McCormick, J. I. McIntyre, R. L. J. van der Meer, R. Michaels, B. D. Milbrath, J. Y. Mougey, S. K. Nanda, E. A. J. M. Offermann, Z. Papandreou, C. F. Perdrisat, G. G. Petratos, N. M. Piskunov, R. I. Pomatsalyuk, D. L. Prout, V. Punjabi, G. Quéméner, R. D. Ransome, B. A. Raue, Y. Roblin, R. Roche, G. Rutledge, P. M. Rutt, A. Saha, T. Saito, A. J. Sarty, T. P. Smith, P. Sorokin, S. Strauch, R. Suleiman, K. Takahashi, J. A. Templon, L. Todor, P. E. Ulmer, G. M. Urciuoli, P. Vernin, B. Vlahovic, H. Voskanyan, K. Wijesooriya, B. B. Wojtsekhowski, R. J. Woo, F. Xiong, G. D. Zainea, and Z.-L. Zhou. g_{Ep}/g_{Mp} ratio by polarization transfer in e(pol.) p -> e p(pol.). *Phys. Rev. Lett.*, 84:1398–1402, Feb 2000. (Cited on pages 10, 11, and 12.)

[33] O. Gayou, K. A. Aniol, T. Averett, F. Benmokhtar, W. Bertozzi, L. Bimbot, E. J. Brash, J. R. Calarco, C. Cavata, Z. Chai, C.-C. Chang, T. Chang, J.-P. Chen, E. Chudakov, R. De Leo, S. Dieterich, R. Endres, M. B. Epstein, S. Escoffier, K. G. Fissum, H. Fonvieille, S. Frullani, J. Gao, F. Garibaldi, S. Gilad, R. Gilman, A. Glamazdin, C. Glashausser, J. Gomez, V. Gorbenko, J.-O. Hansen, D. W. Higinbotham, G. M. Huber, M. Iodice, C. W. de Jager, X. Jiang, M. K. Jones, J. J. Kelly, M. Khandaker, A. Kozlov, K. M. Kramer, G. Kumbartzki, J. J. LeRose, D. Lhuillier, R. A. Lindgren, N. Liyanage, G. J. Lolos, D. J. Margaziotis, F. Marie, P. Markowitz, K. McCormick, R. Michaels, B. D. Milbrath, S. K. Nanda, D. Neyret, Z. Papandreou, L. Pentchev, C. F. Perdrisat, N. M. Piskunov, V. Punjabi, T. Pussieux, G. Quéméner, R. D. Ransome, B. A. Raue, R. Roché, M. Rvachev, A. Saha, C. Salgado, S. Širca, I. Sitnik, S. Strauch, L. Todor, E. Tomasi-Gustafsson, G. M. Urciuoli, H. Voskanyan, K. Wijesooriya, B. B. Wojtsekhowski, X. Zheng, and L. Zhu. Measurement of G_{E_p}/G_{M_p} in e(pol)p->ep(pol) to $q^2 = 5.6\text{gev}^2$. *Phys. Rev. Lett.*, 88:092301, Feb 2002. (Cited on pages 10 and 11.)

[34] L. Andivahis, P. E. Bosted, A. Lung, L. M. Stuart, J. Alster, R. G. Arnold, C. C. Chang, F. S. Dietrich, W. Dodge, R. Gearhart, J. Gomez, K. A. Griffioen, R. S. Hicks, C. E. Hyde-Wright, C. Keppel, S. E. Kuhn, J. Lichtenstadt, R. A. Miskimen, G. A. Peterson, G. G. Petratos,

S. E. Rock, S. Rokni, W. K. Sakumoto, M. Spengos, K. Swartz, Z. Szalata, and L. H. Tao. Measurements of the electric and magnetic form factors of the proton from q^2=1.75 to 8.83 (gev/c)^2. *Phys. Rev. D*, 50:5491–5517, Nov 1994. (Cited on pages 10 and 11.)

[35] M. E. Christy, A. Ahmidouch, C. S. Armstrong, J. Arrington, R. Asaturyan, S. Avery, O. K. Baker, D. H. Beck, H. P. Blok, C. W. Bochna, W. Boeglin, P. Bosted, M. Bouwhuis, H. Breuer, D. S. Brown, A. Bruell, R. D. Carlini, N. S. Chant, A. Cochran, L. Cole, S. Danagoulian, D. B. Day, J. Dunne, D. Dutta, R. Ent, H. C. Fenker, B. Fox, L. Gan, H. Gao, K. Garrow, D. Gaskell, A. Gasparian, D. F. Geesaman, P. L. J. Guèye, M. Harvey, R. J. Holt, X. Jiang, C. E. Keppel, E. Kinney, Y. Liang, W. Lorenzon, A. Lung, P. Markowitz, J. W. Martin, K. McIlhany, D. McKee, D. Meekins, M. A. Miller, R. G. Milner, J. H. Mitchell, H. Mkrtchyan, B. A. Mueller, A. Nathan, G. Niculescu, I. Niculescu, T. G. O'Neill, V. Papavassiliou, S. F. Pate, R. B. Piercey, D. Potterveld, R. D. Ransome, J. Reinhold, E. Rollinde, P. Roos, A. J. Sarty, R. Sawafta, E. C. Schulte, E. Segbefia, C. Smith, S. Stepanyan, S. Strauch, V. Tadevosyan, L. Tang, R. Tieulent, A. Uzzle, W. F. Vulcan, S. A. Wood, F. Xiong, L. Yuan, M. Zeier, B. Zihlmann, and V. Ziskin. Measurements of electron-proton elastic cross sections for 0.4&$lt;Q^2$&$lt;$5.5 (GeVc)^2. *Phys. Rev. C*, 70:015206, Jul 2004. (Cited on page 10.)

[36] J. Arrington. New measurement of G(E) / G(M) for the proton. 2003. (Cited on page 10.)

[37] P. A. M. Guichon and M. Vanderhaeghen. How to reconcile the rosenbluth and the polarization transfer methods in the measurement of the proton form factors. *Phys. Rev. Lett.*, 91:142303, Oct 2003. (Cited on page 10.)

[38] Harleen Dahiya and Neetika Sharma. Electromagnetic form factors of the nucleon in the chiral constituent quark model. 2011. (Cited on page 11.)

[39] S. Kondratyuk, P. G. Blunden, W. Melnitchouk, and J. A. Tjon. δ resonance contribution to two-photon exchange in electron-proton scattering. *Phys. Rev. Lett.*, 95:172503, Oct 2005. (Cited on pages 11 and 12.)

[40] R. C. Walker, B. W. Filippone, J. Jourdan, R. Milner, R. McKeown, D. Potterveld, L. Andivahis, R. Arnold, D. Benton, P. Bosted, G. deChambrier, A. Lung, S. E. Rock, Z. M. Szalata, A. Para, F. Dietrich, K. Van Bibber, J. Button-Shafer, B. Debebe, R. S. Hicks, S. Dasu, P. de Barbaro, A. Bodek, H. Harada, M. W. Krasny, K. Lang, E. M. Riordan, R. Gearhart, L. W. Whitlow, and J. Alster. Measurements of the proton elastic form factors for $1 \leq Q^2 \leq$ 3 (gev/c)^2 at slac. *Phys. Rev. D*, 49:5671–5689, Jun 1994. (Cited on page 11.)

[41] I. A. Qattan, J. Arrington, R. E. Segel, X. Zheng, K. Aniol, O. K. Baker, R. Beams, E. J. Brash, J. Calarco, A. Camsonne, J.-P. Chen, M. E. Christy, D. Dutta, R. Ent, S. Frullani, D. Gaskell, O. Gayou, R. Gilman, C. Glashausser, K. Hafidi, J.-O. Hansen, D. W. Higinbotham, W. Hinton, R. J. Holt, G. M. Huber, H. Ibrahim, L. Jisonna, M. K. Jones, C. E. Keppel, E. Kinney, G. J. Kumbartzki, A. Lung, D. J. Margaziotis, K. McCormick, D. Meekins, R. Michaels, P. Monaghan, P. Moussiegt, L. Pentchev, C. Perdrisat, V. Punjabi, R. Ransome, J. Reinhold, B. Reitz, A. Saha, A. Sarty, E. C. Schulte, K. Slifer, P. Solvignon, V. Sulkosky, K. Wijesooriya, and B. Zeidman. Precision rosenbluth measurement of the proton elastic form factors. *Phys. Rev. Lett.*, 94:142301, Apr 2005. (Cited on page 11.)

[42] P. G. Blunden, W. Melnitchouk, and J. A. Tjon. Two-photon exchange and elastic electron-proton scattering. *Phys. Rev. Lett.*, 91:142304, Oct 2003. (Cited on page 11.)

[43] S. Kondratyuk, P.G. Blunden, W. Melnitchouk, and J.A. Tjon. Two-photon exchange in elastic and inelastic electron-proton scattering. *AIP Conf.Proc.*, 842:336–338, 2006. (Cited on page 11.)

[44] Megh Raj Niroula. *Beyond the Born Approximation: a Precise Comparison of e+p and e-p Elastic Scattering in the CEBAF Large Acceptance Spectrometer (CLAS).* PhD thesis, Old Dominion University, VA, May 2010. (Cited on page 12.)

[45] Gary K. Greenhut. Two-photon exchange in electron-proton scattering. *Phys. Rev.*, 184:1860–1867, Aug 1969. (Cited on page 12.)

[46] Raymond G. Arnold, Carl E. Carlson, and Franz Gross. Polarization transfer in elastic electron scattering from nucleons and deuterons. *Phys. Rev. C*, 23:363–374, Jan 1981. (Cited on page 12.)

[47] M. N. Rosenbluth. High energy elastic scattering of electrons on protons. *Phys. Rev.*, 79:615–619, Aug 1950. (Cited on page 12.)

[48] S. Kondratyuk and P. G. Blunden. Contribution of spin 1/2 and 3/2 resonances to two-photon exchange effects in elastic electron-proton scattering. *Phys. Rev. C*, 75:038201, Mar 2007. (Cited on page 13.)

[49] M. Gorchtein, P.A.M. Guichon, and M. Vanderhaeghen. Normal spin asymmetries in elastic electron-proton scattering. *Nuclear Physics A*, 755(0):273 – 276, 2005. Proceedings of the 10th International Conference on the Structure of Baryons. (Cited on page 14.)

[50] Juliette Mammei. *Parity-Violating Elastic Electron Nucleon Scattering: Measurement of the Strange Quark Content of the Nucleon and Towards a Measurement of the Weak Charge of the Proton.* PhD thesis, Virginia Polytechnic Institute & State University, Blacksburg, VA 24061-0002, USA, April 2010. (Cited on pages 14 and 35.)

[51] M Gorchtein, P.A.M Guichon, and M Vanderhaeghen. Beam normal spin asymmetry in elastic lepton-nucleon scattering. *Nuclear Physics A*, 741(0):234 – 248, 2004. (Cited on page 14.)

[52] Carl E. Carlson and Marc Vanderhaeghen. Two-photon physics in hadronic processes. *Annual Review of Nuclear and Particle Science*, 57(1):171–204, 2007. (Cited on pages 14 and 15.)

[53] M. Gorchtein. Beam normal spin asymmetry in the quasireal compton scattering approximation. *Phys. Rev. C*, 73:055201, May 2006. (Cited on page 16.)

[54] Jorge Segovia, Chen Chen, IanC. Clot, CraigD. Roberts, SebastianM. Schmidt, and Shaolong Wan. Elastic and transition form factors of the delta(1232). *Few-Body Systems*, 55(1):1–33, 2014. (Cited on page 17.)

[55] G. Ramalho, M. T. Peña, and A. Stadler. Shape of the δ baryon in a covariant spectator quark model. *Phys. Rev. D*, 86:093022, Nov 2012. (Cited on page 17.)

[56] Constantia Alexandrou, Tomasz Korzec, Giannis Koutsou, Cdric Lorc, John W. Negele, Vladimir Pascalutsa, Antonios Tsapalis, and Marc Vanderhaeghen. Quark transverse charge densities in the from lattice {QCD}. *Nuclear Physics A*, 825(1-2):115 – 144, 2009. (Cited on pages 17 and 126.)

[57] Carl Carlson. BSA.NΔ@Qweak. The Q-weak Collaboration Meeting, https://qweak.jlab.org/doc-private/ShowDocument?docid=2060, August 2014. (Cited on page 17.)

[58] Thomas Jefferson National Accelerator Facility. http://www.jlab.org/. (Cited on page 19.)

[59] Q weak Collaboration. The Q-Weak Experiment: A search for New Physics at the TeV Scale via a Measurement of the Proton's Weak Charge. Technical Report E02-020 proposal, December 2001. (Cited on page 19.)

[60] Q weak Collaboration. The Q-weak Experiment: "A Search for New Physics at the TeV Scale via a Measurement of the Proton's Weak Charge". Technical Report E05-008 Jeopardy proposal, December 2004. (Cited on page 19.)

[61] E.J. Beise, M.L. Pitt, and D.T. Spayde. The sample experiment and weak nucleon structure. *Progress in Particle and Nuclear Physics*, 54(1):289 – 350, 2005. (Cited on page 19.)

[62] D. S. Armstrong, J. Arvieux, R. Asaturyan, T. Averett, S. L. Bailey, G. Batigne, D. H. Beck, E. J. Beise, J. Benesch, L. Bimbot, J. Birchall, A. Biselli, P. Bosted, E. Boukobza, H. Breuer, R. Carlini, R. Carr, N. Chant, Y.-C. Chao, S. Chattopadhyay, R. Clark, S. Covrig, A. Cowley, D. Dale, C. Davis, W. Falk, J. M. Finn, T. Forest, G. Franklin, C. Furget, D. Gaskell, J. Grames, K. A. Griffioen, K. Grimm, B. Guillon, H. Guler, L. Hannelius, R. Hasty, A. Hawthorne Allen, T. Horn, K. Johnston, M. Jones, P. Kammel, R. Kazimi, P. M. King, A. Kolarkar, E. Korkmaz, W. Korsch, S. Kox, J. Kuhn, J. Lachniet, L. Lee, J. Lenoble, E. Liatard, J. Liu, B. Loupias, A. Lung, G. A. MacLachlan, D. Marchand, J. W. Martin, K. W. McFarlane, D. W. McKee, R. D. McKeown, F. Merchez, H. Mkrtchyan, B. Moffit, M. Morlet, I. Nakagawa, K. Nakahara, M. Nakos, R. Neveling, S. Niccolai, S. Ong, S. Page, V. Papavassiliou, S. F. Pate, S. K. Phillips, M. L. Pitt, M. Poelker, T. A. Porcelli, G. Quéméner, B. Quinn, W. D. Ramsay, A. W. Rauf, J.-S. Real, J. Roche, P. Roos, G. A. Rutledge, J. Secrest, N. Simicevic, G. R. Smith, D. T. Spayde, S. Stepanyan, M. Stutzman, V. Sulkosky, V. Tadevosyan, R. Tieulent, J. van de Wiele, W. van Oers, E. Voutier, W. Vulcan, G. Warren, S. P. Wells, S. E. Williamson, S. A. Wood, C. Yan, J. Yun, and V. Zeps. Strange-quark contributions to parity-violating asymmetries in the forward g0 electron-proton scattering experiment. *Phys. Rev. Lett.*, 95:092001, Aug 2005. (Cited on page 19.)

[63] K. A. Aniol, D. S. Armstrong, T. Averett, H. Benaoum, P. Y. Bertin, E. Burtin, J. Cahoon, G. D. Cates, C. C. Chang, Y.-C. Chao, J.-P. Chen, Seonho Choi, E. Chudakov, B. Craver, F. Cusanno, P. Decowski, D. Deepa, C. Ferdi, R. J. Feuerbach, J. M. Finn, S. Frullani, K. Fuoti, F. Garibaldi, R. Gilman, A. Glamazdin, V. Gorbenko, J. M. Grames, J. Hansknecht, D. W. Higinbotham, R. Holmes, T. Holmstrom, T. B. Humensky, H. Ibrahim, C. W. de Jager, X. Jiang, L. J. Kaufman, A. Kelleher, A. Kolarkar, S. Kowalski, K. S. Kumar, D. Lambert, P. LaViolette, J. LeRose, D. Lhuillier, N. Liyanage, D. J. Margaziotis, M. Mazouz, K. McCormick, D. G. Meekins, Z.-E. Meziani, R. Michaels, B. Moffit, P. Monaghan, C. Munoz-Camacho, S. Nanda, V. Nelyubin, D. Neyret, K. D. Paschke, M. Poelker, R. Pomatsalyuk, Y. Qiang, B. Reitz, J. Roche, A. Saha, J. Singh, R. Snyder, P. A. Souder, R. Subedi, R. Suleiman, V. Sulkosky, W. A. Tobias, G. M. Urciuoli, A. Vacheret, E. Voutier, K. Wang, R. Wilson, B. Wojtsekhowski, and X. Zheng. Parity-violating electron scattering from ^{4}He

and the strange electric form factor of the nucleon. *Phys. Rev. Lett.*, 96:022003, Jan 2006. (Cited on page 19.)

[64] C. W. Leemann, D. R. Douglas, and G. A. Krafft. "The Continuous Electron Beam Accelerator Facility: CEBAF at the Jefferson Laboratory". Annual review of nuclear and particle science, vol. 51, no. 1, pp. 413-450, 2001. (Cited on pages 22 and 25.)

[65] 12 GeV Upgrade: Future Science at Jefferson Lab. http://www.jlab.org/12GeV/index.html. (Cited on page 23.)

[66] B. Poelker. Q-weak e-Source Issues. Q-weak Collaboration Meeting, Q-weak-DocDB1436: https://qweak.jlab.org/doc-private/ShowDocument?docid=1436, June 2011. (Cited on page 24.)

[67] C. Hernandez-Garcia, P. G. O'Shea, and M. L. Stutzman. *Electron sources for accelerators.* Physics Today, February 2008. (Cited on page 24.)

[68] J. Grames, P. Adderley, J. Benesch, J. Clark, J. Hansknecht, R. Kazimi, D. Machie, M. Poelker, M. Stutzman, R. Suleiman, and Y. Zhang. Two wien filter spin flipper. *Particle Accelerator Conference Proceedings*, page 862, 2011. (Cited on page 24.)

[69] Nuruzzaman and *et. all.* List of Beam Components & Critical BPMs. Technical Report Qweak-DocDB-1203, Feb 2010. (Cited on page 25.)

[70] Sarah Phillips. *Measurement of the Strange Quark Contribution to the Vector Structure of the Proton.* PhD thesis, College of William and Mary, Virginia, Nov 2007. (Cited on page 26.)

[71] G. Krafft and A. Hofler. How the Linac Beam Position Monitors Work. CEBAF Technical Note CEBAF-TN-93-004, 1993. (Cited on page 26.)

[72] Andrew James Ruehe Puckett. *Recoil Polarization Measurements of the Proton Electromagnetic Form Factor Ratio to High Momentum Transfer.* PhD thesis, Massachusetts Institute of Technology, MA, Feb 2010. (Cited on page 27.)

[73] M. Hauger, A. Honegger, J. Jourdan, G. Kubon, T. Petitjean, D. Rohe, I. Sick, G. Warren, H. Whrle, J. Zhao, R. Ent, J. Mitchell, D. Crabb, A. Tobias, M. Zeier, and B. Zihlmann. A high-precision polarimeter. *Nuclear Instruments and Methods in Physics Research Section A: Accelerators,Spectrometers,Detectors and Associated Equipment*, 462(3):382 – 392, 2001. (Cited on page 27.)

[74] Paul Gueye. Status of the actual beam position monitors in the Hall C beamline. CEBAF Technical Note Unpublished internal document, December 1995. (Cited on page 27.)

[75] Nuruzzaman and *et. all.* Position and Angle Determination at the Q^p_{weak} Target for Beam Modulation. Technical Report Qweak-DocDB-1208, March 2010. Used as a reference for how the position and angle determination at the target for beam modulation in the Q^p_{weak} experiment. (Cited on pages 27, 53, and 91.)

[76] William R. Leo. *Techniques for Nuclear and Particle Physics Experiments: A How-to Approach*. Springer, Berlin, second revised edition, February 1994. (Cited on page 27.)

[77] Benjamin Micheal Patrick Clasie. *Measurement of Nuclear Transparency from $A(e, e'\pi^+)$ Reactions*. PhD thesis, Massachusetts Institute of Technology, MA, Aug 2006. (Cited on page 28.)

[78] Nuruzzaman. Effective Kaon-Nucleon Cross Section from Nuclear Transparency Measured in the $A(ee'K^+)$ Reaction. Master's thesis, Mississippi State University, MS, Aug 2010. (Cited on page 28.)

[79] Ramesh Subedi. Summary report on the BCMs for QWEAK. Technical Report Qweak-DocDB-1777, January 2013. (Cited on page 28.)

[80] C. Yan, R. Carlini, and D. Neuffer. Beam energy measurement using the Hall C beamline. *Conf.Proc.*, C930517:2136–2138, 1993. (Cited on page 28.)

[81] C. Yan, P. Adderley, D. Barker, J. Beaufait, K. Capek, R. Carlini, J. Dahlberg, E. Feldl, K. Jordan, B. Kross, W. Oren, R. Wojcik, and J. VanDyke. Superharp - a wire scanner with absolute position readout for beam energy measurement at {CEBAF}. *Nuclear Instruments and Methods in Physics Research Section A: Accelerators, Spectrometers, Detectors and Associated Equipment*, 365(2-3):261 – 267, 1995. (Cited on page 28.)

[82] Valery Lebedev. OPTIM: Computer code for linear and non-linear optics calculations. http://www-bdnew.fnal.gov/pbar/organizationalchart/lebedev/OptiM/optim.htm, June 2007. (Cited on pages 29, 48, 90, 130, and 131.)

[83] Nuruzzaman and *et. all.* Beam Modulation in the 3C Line for the Q^p_{weak} Experiment. Hall-C Technical Note Qweak-DocDB-2126, Jun 2009. Beam Modulation write up for Q^p_{weak} experiment. (Cited on page 30.)

[84] V. Lebedev R. Dickson. Fast Feedback System for Energy and Beam Stabilization. Technical Report JLAB-ACE-99-10, Jefferson Lab, Newport News, VA, 1999. (Cited on pages 30 and 50.)

[85] B. Bevins. A Distributed Feedback System for Rapid Stabilazation of Arbitrary Process Variables. Technical Report JLAB-ACE-01-09, Jefferson Lab, Newport News, VA. (Cited on pages 30 and 50.)

[86] M. Hauger, A. Honegger, J. Jourdan, G. Kubon, T. Petitjean, D. Rohe, I. Sick, G. Warren, H. Whrle, J. Zhao, R. Ent, J. Mitchell, D. Crabb, A. Tobias, M. Zeier, and B. Zihlmann. A high-precision polarimeter. *Nuclear Instruments and Methods in Physics Research Section A: Accelerators, Spectrometers, Detectors and Associated Equipment*, 462(3):382 – 392, 2001. (Cited on page 31.)

[87] Matthias Loppacher. *Moller polarimeter for CEBAF Hall-C.* PhD thesis, University of Basel, Basel, April 1996. (Cited on page 31.)

[88] Rakitha Beminiwattha. *A Measurement of the Weak Charge of the Proton through Parity Violating Electron Scattering using the Qweak Apparatus: A 21% Result.* PhD thesis, Ohio University, Athens OH 45701, USA, August 2013. (Cited on pages 31, 42, 44, and 110.)

[89] A. Narayan. Precision Compton Polarimetry During the Qweak Experiment. DNP 2012 Conference, Q-weak-DocDB1732: https://qweak.jlab.org/doc-private/ShowDocument?docid=1732, October 2012. (Cited on page 32.)

[90] Amrendra Narayan. *Electron Detector in Compton polarimeter for CEBAF Hall-C.* PhD thesis, Mississippi State University, Mississippi State, MS, December 2014. (Cited on page 32.)

[91] Juan Carlos Cornejo. *Photon Detector in Compton polarimeter for CEBAF Hall-C.* PhD thesis, College of William and Mary, Williamsburg, VA, USA, April 2015. (Cited on page 32.)

[92] Gregory Smith, Silviu Covrig, and Jim Dunne. "Qweak Liquid Hydrogen Target: Preliminary Design & Safety Document". Technical Report Qweak-DocDB-1041, August 2009. (Cited on page 33.)

[93] ANSYS: A fluid dynamics simulation code. http://www.ansys.com/. (Cited on page 34.)

[94] Gregory Smith. "Optics Target". Technical Report Qweak-DocDB-1144, December 2009. (Cited on page 35.)

[95] Peiqing Wang. Magnetic Field Simulation and Mapping for the Q^{p}_{Weak} Experiment. Master's thesis, University of Manitoba, Winnipeg, Manitoba, Canada, 2009. (Cited on page 37.)

[96] Lake Shore Cryotronics Inc., 575 McCorkle Boulevard, Westerville, OH 43082. *Gaussmeter Hall Probes*. (Cited on page 37.)

[97] Nuruzzaman. Hall Probe Mount Design for QTOR. Technical Report Qweak-DocDB-1244, May 2010. (Cited on page 38.)

[98] Peiqing Wang. *A Measurement Of The Protons Weak Charge Using An Integration Cerenkov Detector System*. PhD thesis, University of Manitoba, Winnipeg, Manitoba, Canada, June 2011. (Cited on page 39.)

[99] TRIUMF: Canada's national laboratory for particle and nuclear physics. http://www.triumf.ca/. (Cited on pages 39 and 60.)

[100] B. Roberts and H. Hui. *VME QWEAK 8 Channel 18-bit ADC*. TRIUMF, rev 1 edition, November 2007. (Cited on pages 39 and 60.)

[101] John Lackey. *The First Direct Measurement of the Weak Charge of the Proton*. PhD thesis, College of William and Mary, Williamsburg, VA, USA, October 2011. (Cited on page 42.)

[102] Jlab DAQ Group. CEBAF Online Data Acquisition. https://coda.jlab.org/wiki/index.php/Main_Page. (Cited on page 42.)

[103] P. Banta, J. Chen, W.G. Heyes, E. Jastrzembski, C. Timmer, et al. The Front end readout control software for the CODA data acquisition toolkit. 1997. (Cited on page 42.)

[104] Brad Sawatzky. Private communication, 2009-2014. (Cited on page 43.)

[105] Nuruzzaman and Greg Smith. Hall-C Target Status Page. https://hallcweb.jlab.org/poltar/. (Cited on page 43.)

[106] Nuruzzaman. Beam Modulation Website: Hall-C Beamline Optics. https://hallcweb.jlab.org/qweak/bmod/. (Cited on page 43.)

[107] Josh Hoskins. *Region III rotator, beam modulation sensitivities*. PhD thesis, College of William and Mary, Williamsburg, VA, December 2014. (Cited on pages 45 and 75.)

[108] Donald Jones. *Compton polarimeter*. PhD thesis, University of Virginia, Charlottesville, VA, December 2014. (Cited on pages 45, 75, and 83.)

[109] Dave Mack. Private communication, 2009-2014. (Cited on pages 45 and 46.)

[110] A. Acha, K. A. Aniol, D. S. Armstrong, J. Arrington, T. Averett, S. L. Bailey, J. Barber, A. Beck, H. Benaoum, J. Benesch, P. Y. Bertin, P. Bosted, F. Butaru, E. Burtin, G. D. Cates, Y.-C. Chao, J.-P. Chen, E. Chudakov, E. Cisbani, B. Craver, F. Cusanno, R. De Leo, P. Decowski, A. Deur, R. J. Feuerbach, J. M. Finn, S. Frullani, S. A. Fuchs, K. Fuoti, R. Gilman, L. E. Glesener, K. Grimm, J. M. Grames, J. O. Hansen, J. Hansknecht, D. W. Higinbotham, R. Holmes, T. Holmstrom, H. Ibrahim, C. W. de Jager, X. Jiang, J. Katich, L. J. Kaufman, A. Kelleher, P. M. King, A. Kolarkar, S. Kowalski, E. Kuchina, K. S. Kumar, L. Lagamba, P. LaViolette, J. LeRose, R. A. Lindgren, D. Lhuillier, N. Liyanage, D. J. Margaziotis, P. Markowitz, D. G. Meekins, Z.-E. Meziani, R. Michaels, B. Moffit, S. Nanda, V. Nelyubin, K. Otis, K. D. Paschke, S. K. Phillips, M. Poelker, R. Pomatsalyuk, M. Potokar, Y. Prok, A. Puckett, X. Qian, Y. Qiang, B. Reitz, J. Roche, A. Saha, B. Sawatzky, J. Singh, K. Slifer, S. Sirca, R. Snyder, P. Solvignon, P. A. Souder, M. L. Stutzman, R. Subedi, R. Suleiman, V. Sulkosky, W. A. Tobias, P. E. Ulmer, G. M. Urciuoli, K. Wang, A. Whitbeck, R. Wilson, B. Wojtsekhowski, H. Yao, Y. Ye, X. Zhan, X. Zheng, S. Zhou, and V. Ziskin. Precision measurements of the nucleon strange form factors at $Q^2 \sim$ (gev)^2. *Phys. Rev. Lett.*, 98:032301, Jan 2007. (Cited on pages 45 and 47.)

[111] James Birchall. Updated Requirements on Beam Properties for Qweak, August 2008. Technical Report Qweak-DocDB-818, August 2008. (Cited on page 47.)

[112] Jay Benesch. Private communication, 2009-2014. (Cited on pages 48 and 84.)

[113] Jay Benesch and Nuruzzaman. OptiM Deck for Beam Modulation in Hall-C beamline. Q-weak-DocDB1367: https://qweak.jlab.org/doc-private/ShowDocument?docid=1367, May 2011. (Cited on pages 49, 51, and 53.)

[114] Michael Tiefenback. Private communication, 2009. (Cited on page 50.)

[115] Nuruzzaman and *et. all.* How Beam Energy will be Identified in Q^p_{weak}. Technical Report Qweak-DocDB-1149, January 2010. Used as a reference for how the beam enegy will be identified in the Q^p_{weak} experiment. (Cited on page 53.)

[116] Sarin Philip. JLab MAT (or HF) coil characteristics. DocDB-979: http://qweak.jlab.org/doc-public/ShowDocument?docid=979, June 2009. (Cited on page 55.)

[117] Martin R. Kraimer. Experimental Physics and Industrial Control System (EPICS): Input / Output Controller (IOC) Application Developer's Guide. Technical Report APS Release 3.11.6, May 1994. (Cited on page 56.)

[118] GE Fanuc. *VME-4145 4-Channel 16-bit Arbitrary Waveform Generator Board with Autocalibration*, first edition edition, June 2008. (Cited on pages 56 and 57.)

[119] KWord is an intuitive word processor and desktop publisher application. With it, you can create informative and attractive documents with pleasure and ease. http://www.kde.org/applications/office/kword/. (Cited on page 56.)

[120] Chad Seaton. VME 16-Channel Relay Output Register. Technical Report Qweak-DocDB-2122, May 2009. (Cited on page 57.)

[121] Nuruzzaman. An Update on Beam Modulation for the Q-weak Experiment. Q-weak Collaboration Meeting, Q-weak-DocDB1312: https://qweak.jlab.org/doc-private/ShowDocument?docid=1312, September 2010. (Cited on page 57.)

[122] T. Allison, S. Higgins, E. Martin, W. Merz, and S. Philip. Jefferson lab's trim card ii. In *Particle Accelerator Conference, 2005. PAC 2005. Proceedings of the*, pages 3670–3672, May 2005. (Cited on page 57.)

[123] LEM, West Lancashire Investment Centre, Skelmersdale, WN8 9TG, England. *Current Transducer CT 5..25-T*, 2006-2014. (Cited on page 58.)

[124] Sarin Philip. Private communication, 2009-2010. (Cited on page 58.)

[125] LEM, West Lancashire Investment Centre, Skelmersdale, WN8 9TG, England. *Current Transducer LA 55-P/SP1*, 2006-2014. (Cited on page 59.)

[126] Nuruzzaman. LEM Current Transducer for the Beam Modulation System. Technical Report Qweak-DocDB-2120, September 2011. (Cited on page 59.)

[127] Chad Seaton. VME 32-Channel ADC Module. Technical Report Qweak-DocDB-2121, May 2010. (Cited on page 60.)

[128] Donald Jones. Ramp fill procedure documentation. ELOG-Analysis-948: https://qweak.jlab.org/elog/Analysis+&+Simulation/948, July 2013. (Cited on page 62.)

[129] Nuruzzaman, Scott Higgins, Dave Mack, and Josh Hoskins. Beam Modulation Controls and Software Sketch for the Q-weak Experiment. Technical Report Qweak-DocDB-2119, May 2010. (Cited on pages 64 and 65.)

[130] Scott Higgins. Private communication, 2009-2010. (Cited on page 64.)

[131] Nuruzzaman and *et. all.* Beam Modulation GUI proposal. Technical Report Qweak-DocDB-1140, December 2009. Submitted to accelerator division of JLab and was used as a reference for control system of Beam Modulation in the Q^p_{weak} experiment. (Cited on pages 64 and 65.)

[132] Nuruzzaman and *et. all.* Machine Protection Analysis of the Beam Modulation System for the Q^p_{weak} Experiment. Technical Report Qweak-DocDB-1207, March 2010. This analysis shows the worst case possibilities we can have during the experiment for Beam Modulation in Q^p_{weak} experiment. (Cited on page 67.)

[133] K. Kumar *et al.* The MOLLER Experiment: Measurement Of Lepton Lepton Elastic Reactions. http://hallaweb.jlab.org/collab/PAC/PAC37/C12-09-005-Moller.pdf, December 2010. (Cited on pages 70 and 130.)

[134] Nuruzzaman. Hall-A Beamline elements using Pass1 beam. MSU-ELOG-296: http://urvashi.ph.msstate.edu:8080/mepgroup/296, November 2012. (Cited on page 71.)

[135] Josh Hoskins. Effects of fitting BPM response with fixed phase. ELOG-Analysis-690: https://qweak.jlab.org/elog/Analysis+&+Simulation/690, August 2012. (Cited on page 81.)

[136] Kent Paschke. Beam Modulation response with FFB interference. ELOG-Analysis-695: https://qweak.jlab.org/elog/Analysis+&+Simulation/695, August 2012. (Cited on page 82.)

[137] Rob Mahurin. QTor misalignment estimate due to beam steering. ELOG-QTor-2: https://qweak.jlab.org/elog/QTOR/2, April 2011. (Cited on page 84.)

[138] Nuruzzaman. Estimation of beam steering due to QTOR fringe field using OPTIM. ELOG-QTor-3: https://qweak.jlab.org/elog/QTOR/3, April 2011. (Cited on page 84.)

[139] Nuruzzaman. Low Energy Electron Deflectng Due to QTOR fringe field using OPTIM. ELOG-QTor-4: https://qweak.jlab.org/elog/QTOR/4, April 2011. (Cited on page 85.)

[140] Nuruzzaman. Effect of corrector magnet in front of QTOR on beam steering due to fringe field. ELOG-QTor-5: https://qweak.jlab.org/elog/QTOR/5, April 2011. (Cited on page 85.)

[141] Nuruzzaman. Effect of different fields in the corrector magnet in front of QTOR. ELOG-QTor-6: https://qweak.jlab.org/elog/QTOR/6, April 2011. (Cited on page 86.)

[142] Nuruzzaman. Preliminary QTOR corrector magnet design and field map using TOSCA. ELOG-QTor-7: https://qweak.jlab.org/elog/QTOR/7, April 2011. (Cited on page 86.)

[143] Nuruzzaman. Realistic QTOR corrector magnet design, field map and basics using TOSCA. ELOG-QTor-8: https://qweak.jlab.org/elog/QTOR/8, April 2011. (Cited on page 86.)

[144] Nuruzzaman. Power calculation for QTOR corrector magnet. ELOG-QTor-9: https://qweak.jlab.org/elog/QTOR/9, April 2011. (Cited on page 86.)

[145] Nuruzzaman. QTOR corrector magnet sensitivity to position and angle. ELOG-QTor-10: https://qweak.jlab.org/elog/QTOR/10, April 2011. (Cited on page 86.)

[146] Nuruzzaman. QTOR corrector magnet field along different octant. ELOG-QTor-11: https://qweak.jlab.org/elog/QTOR/11, April 2011. (Cited on page 86.)

[147] Nuruzzaman. QTOR corrector magnet project summary. ELOG-QTor-12: https://qweak.jlab.org/elog/QTOR/12, April 2011. (Cited on page 87.)

[148] Buddhini Waidyawansa. Beam Position and Angle Determination in Qweak. Technical Report Qweak-DocDB-1772, December 2012. (Cited on pages 88 and 90.)

[149] Nuruzzaman. Target BPM Angle Resolution from OPTIM. Q-weak Physics Meeting, Q-weak-DocDB1779: https://qweak.jlab.org/doc-private/ShowDocument?docid=1779, January 2013. (Cited on page 91.)

[150] Nuruzzaman. Scheme Dependence of Rescaled Wien0 Main Detector Sensitivities. Q-weak Physics Meeting, Q-weak-DocDB1776: https://qweak.jlab.org/doc-private/ShowDocument?docid=1776, February 2013. (Cited on page 91.)

[151] John Leacock. Helicity Correlated Pedestal Differences for April 2011 from Qweak Run I. Technical report, VT, VA, Nov 2011. (Cited on page 93.)

[152] P. Pébay. Formulas for robust, One-Pass Parallel Computation of Covariances and Arbitrary-Order Statistical Moments. Sandia Report SAND2008-6212, Sandia National Laboratories, 2008. (Cited on page 103.)

[153] R. Suleiman, M. Poelker, and J. Grames. Mott Measurements For Hall C. HCLOG-1567146: https://cebaf.jlab.org/elog/entry/1567146, February 2011. (Cited on page 107.)

[154] Shelley Page. Beam: Polarization studies at injector. HCLOG-219054: https://hallcweb.jlab.org/hclog/1102_archive/110208121825.html, February 2011. (Cited on page 107.)

[155] Dave Mack. BCM Normalization Issues Part II: Calibrations and Linearity. Q-weak-DocDB1369: https://qweak.jlab.org/doc-private/ShowDocument?docid=1369, March 2011. (Cited on page 111.)

[156] Dave Mack. Non-linearity Specification for the Qweak Detector Chain. Technical Report Qweak-DocDB-172, November 2004. (Cited on page 111.)

[157] Joshua Magee. Private communication, 2014. (Cited on page 116.)

[158] Nuruzzaman. Beam Polarization from Moller Polarimeter for Transverse Run-II Dataset. ELOG-Ancillary-91: https://qweak.jlab.org/elog/Ancillary/91, April 2014. (Cited on page 116.)

[159] Nuruzzaman. Transverse Asymmetries for N-to-Delta in Nuclear Targets. ELOG-Ancillary-43: https://qweak.jlab.org/elog/Ancillary/43, July 2013. (Cited on page 117.)

[160] E. D. Cooper and C. J. Horowitz. Vector analyzing power in elastic electron-nucleus scattering. *Phys. Rev. C*, 72:034602, Sep 2005. (Cited on pages 118 and 120.)

[161] M. Gorchtein and C. J. Horowitz. Analyzing power in elastic scattering of electrons off a spin-0 target. *Phys. Rev. C*, 77:044606, Apr 2008. (Cited on pages 118 and 120.)

[162] Josh Magee. Aluminum Status Qweak Collaboration Meeting. Hall C collaboration meeting, Q-weak-DocDB1891: https://qweak.jlab.org/doc-private/ShowDocument?docid=1819, April 2013. (Cited on page 118.)

[163] Dave Mack. Formalism for Qweak Background Corrections and Error Propagation. Technical Report Qweak-DocDB-965, June 2014. (Cited on page 118.)

[164] Dave Mack. Wien0 Beamline Background Dilution Central Value and Uncertainty. ELOG-Analysis-784: https://qweak.jlab.org/elog/Analysis+&+Simulation/784, October 2012. (Cited on page 118.)

[165] Dave Mack. Input file for Wien 0 elastic e+p asymmetry corrections (v11 frozen modulo unblinding). ELOG-Analysis-714: https://qweak.jlab.org/elog/Analysis+&+Simulation/714, September 2012. (Cited on page 119.)

[166] Martin McHugh. Neutral Background Analysis. https://qweak.jlab.org/doc-private/ShowDocument?docid=2072, September 2014. (Cited on page 119.)

[167] Rakitha S Beminiwattha. Main Detector Neutral Background Contribution. Technical Report Qweak-DocDB-1549, July 2012. (Cited on page 119.)

[168] Buddhini Waidyawansa. Qweak Transverse Asymmetry Measurements. Hall C collaboration meeting, Q-weak-DocDB1961: https://qweak.jlab.org/doc-private/ShowDocument?docid=1961, February 2014. (Cited on page 120.)

[169] D. Androic, D. S. Armstrong, A. Asaturyan, T. Averett, J. Balewski, J. Beaufait, R. S. Beminiwattha, J. Benesch, F. Benmokhtar, J. Birchall, R. D. Carlini, G. D. Cates, J. C. Cornejo, S. Covrig, M. M. Dalton, C. A. Davis, W. Deconinck, J. Diefenbach, J. F. Dowd, J. A. Dunne, D. Dutta, W. S. Duvall, M. Elaasar, W. R. Falk, J. M. Finn, T. Forest, D. Gaskell, M. T. W. Gericke, J. Grames, V. M. Gray, K. Grimm, F. Guo, J. R. Hoskins, K. Johnston, D. Jones, M. Jones, R. Jones, M. Kargiantoulakis, P. M. King, E. Korkmaz, S. Kowalski, J. Leacock, J. Leckey, A. R. Lee, J. H. Lee, L. Lee, S. MacEwan, D. Mack, J. A. Magee, R. Mahurin, J. Mammei, J. W. Martin, M. J. McHugh, D. Meekins, J. Mei, R. Michaels, A. Micherdzinska, A. Mkrtchyan, H. Mkrtchyan, N. Morgan, K. E. Myers, A. Narayan, L. Z. Ndukum, V. Nelyubin, Nuruzzaman, W. T. H. van Oers, A. K. Opper, S. A. Page, J. Pan, K. D. Paschke, S. K. Phillips, M. L. Pitt, M. Poelker, J. F. Rajotte, W. D. Ramsay, J. Roche, B. Sawatzky, T. Seva, M. H. Shabestari, R. Silwal, N. Simicevic, G. R. Smith, P. Solvignon, D. T. Spayde, A. Subedi, R. Subedi, R. Suleiman, V. Tadevosyan, W. A. Tobias, V. Tvaskis, B. Waidyawansa, P. Wang, S. P. Wells, S. A. Wood, S. Yang, R. D. Young, and S. Zhamkochyan. First determination of the weak charge of the proton. *Phys. Rev. Lett.*, 111:141803, Oct 2013. (Cited on page 120.)

[170] Nuruzzaman. Comparison of H2 Dilutions from Geant-III, IV, and Data at the Inelastic Peak. ELOG-Ancillary-59: https://qweak.jlab.org/elog/Ancillary/59, December 2013. (Cited on page 120.)

[171] Haakon Olsen and L. C. Maximon. Photon and electron polarization in high-energy bremsstrahlung and pair production with screening. *Phys. Rev.*, 114:887–904, May 1959. (Cited on page 120.)

[172] K. A. Aniol, D. S. Armstrong, M. Baylac, E. Burtin, J. Calarco, G. D. Cates, C. Cavata, J.-P. Chen, E. Chudakov, D. Dale, C. W. de Jager, A. Deur, P. Djawotho, M. B. Epstein, S. Escoffier, L. Ewell, N. Falletto, J. M. Finn, K. Fissum, A. Fleck, B. Frois, J. Gao, F. Garibaldi, A. Gasparian, G. M. Gerstner, R. Gilman, A. Glamazdin, J. Gomez, V. Gorbenko, O. Hansen, F. Hersman, R. Holmes, M. Holtrop, B. Humensky, S. Incerti, J. Jardillier, M. K. Jones, J. Jorda, C. Jutier, W. Kahl, D. H. Kim, M. S. Kim, K. Kramer, K. S. Kumar, M. Kuss, J. LeRose, M. Leuschner, D. Lhuillier, N. Liyanage, R. Lourie, R. Madey, D. J. Margaziotis, F. Marie, J. Martino, P. Mastromarino, K. McCormick, J. McIntyre, Z.-E. Meziani, R. Michaels, G. W. Miller, D. Neyret, C. Perdrisat, G. G. Petratos, R. Pomatsalyuk, J. S. Price, D. Prout, V. Punjabi, T. Pussieux, G. Quéméner, G. Rutledge, P. M. Rutt, A. Saha, P. A. Souder, M. Spradlin, R. Suleiman, J. Thompson, L. Todor, P. E. Ulmer, B. Vlahovic, K. Wijesooriya, R. Wilson, and B. Wojtsekhowski. Measurement of the neutral weak form factors of the proton. *Phys. Rev. Lett.*, 82:1096–1100, Feb 1999. (Cited on page 121.)

[173] K. A. Aniol, D. S. Armstrong, T. Averett, M. Baylac, E. Burtin, J. Calarco, G. D. Cates, C. Cavata, Z. Chai, C. C. Chang, J.-P. Chen, E. Chudakov, E. Cisbani, M. Coman, D. Dale, A. Deur, P. Djawotho, M. B. Epstein, S. Escoffier, L. Ewell, N. Falletto, J. M. Finn, K. Fissum, A. Fleck, B. Frois, S. Frullani, J. Gao, F. Garibaldi, A. Gasparian, G. M. Gerstner, R. Gilman, A. Glamazdin, J. Gomez, V. Gorbenko, O. Hansen, F. Hersman, D. W. Higinbotham, R. Holmes, M. Holtrop, T. B. Humensky, S. Incerti, M. Iodice, C. W. de Jager, J. Jardillier, X. Jiang, M. K. Jones, J. Jorda, C. Jutier, W. Kahl, J. J. Kelly, D. H. Kim, M.-J. Kim, M. S. Kim, I. Kominis, E. Kooijman, K. Kramer, K. S. Kumar, M. Kuss, J. LeRose, R. De Leo, M. Leuschner, D. Lhuillier, M. Liang, N. Liyanage, R. Lourie, R. Madey, S. Malov, D. J. Margaziotis, F. Marie, P. Markowitz, J. Martino, P. Mastromarino, K. McCormick, J. McIntyre, Z.-E. Meziani, R. Michaels, B. Milbrath, G. W. Miller, J. Mitchell, L. Morand, D. Neyret, C. Pedrisat, G. G. Petratos, R. Pomatsalyuk, J. S. Price, D. Prout, V. Punjabi, T. Pussieux, G. Quéméner, R. D. Ransome, D. Relyea, Y. Roblin, J. Roche, G. A. Rutledge, P. M. Rutt, M. Rvachev, F. Sabatie, A. Saha, P. A. Souder, M. Spradlin, S. Strauch, R. Suleiman, J. Templon, T. Teresawa, J. Thompson, R. Tieulent, L. Todor, B. T. Tonguc, P. E. Ulmer, G. M. Urciuoli, B. Vlahovic, K. Wijesooriya, R. Wilson, B. Wojtsekhowski, R. Woo, W. Xu, I. Younus, and C. Zhang. Parity-violating electroweak asymmetry in $\vec{e}p$ scattering. *Phys. Rev. C*, 69:065501, Jun 2004. (Cited on page 121.)

[174] Peiqing Wang. Simulated octant-by-octant event rate, scattering angle and momentum

transfer. ELOG-Analysis-589: https://qweak.jlab.org/elog/Analysis+&+Simulation/589, May 2012. (Cited on page 122.)

[175] Andrei V. Afanasev and N.P. Merenkov. Collinear photon exchange in the beam normal polarization asymmetry of elastic electron-proton scattering. *Physics Letters B*, 599(1-2):48 – 54, 2004. (Cited on page 123.)

[176] Jim Birchall. Effect of averaging over azimuthal angle. ELOG-Analysis-373: https://qweak.jlab.org/elog/Analysis+&+Simulation/373, June 2011. (Cited on page 124.)

[177] Nuruzzaman and Qweak Collaboration. Beam modulation system for the q-weak experiment at jefferson lab. *AIP Conference Proceedings*, 1560(1):240–242, 2013. (Cited on page 131.)

[178] Constantia Alexandrou, Tomasz Korzec, Giannis Koutsou, Cedric Lorce, John W. Negele, et al. Quark transverse charge densities in the *Delta*(1232) from lattice QCD. *Nucl.Phys.*, A825:115–144, 2009. (Cited on page 132.)

[179] Nuruzzaman. Q-weak Physics Meeting: Helicity Correlated Pedestal Differences for Wien 0 - 9. Q-weak Physics Meeting, Q-weak-DocDB1608: https://qweak.jlab.org/doc-private/ShowDocument?docid=1608, March 2012. (Cited on page 158.)

[180] Nuruzzaman. Q-weak Physics Meeting: Pedestal Survey for the Q-weak Experiment. Q-weak Physics Meeting, Q-weak-DocDB1608: https://qweak.jlab.org/doc-private/ShowDocument?docid=1678, June 2012. (Cited on page 158.)

[181] Private communication with Paul King. pking@jlab.org. (Cited on page 158.)

[182] Nuruzzaman. Survey of Helicity Correlated Pedestal Differences for the Full Q-weak Data Set. Technical Report Qweak-DocDB-2016, July 2014. (Cited on page 162.)

[183] Buddhini Waidyawansa. New PMT weights for transverse run1 and run2 (to be used with pass5 onwards). ELOG-Analysis-800: https://qweak.jlab.org/elog/Analysis+%26+Simulation/800, October 2012. (Cited on page 168.)

[184] Q^p_{weak}: A Search for New Physics. http://www.jlab.org/qweak/. (Cited on page 200.)

Curriculum Vita

Nuruzzaman

12000 Jefferson Ave, Suite 16, Newport News, VA 23606. (757) 952-6686. nur@jlab.org. userweb.jlab.org/∼nur

Education

Ph. D.	Hampton University, Hampton, VA, USA.	December, 2014
M. S.	Mississippi State University, Mississippi State, MS, USA.	August, 2010
M. Sc.	Indian Institute of Technology Roorkee, Uttarakhand, India.	May, 2007
B. Sc.	University of Kalyani, West Bengal, India.	May, 2005

Professional Experience

Participated in the Q^p_{weak}(E02-020), PVDIS(E08-011), HKS(E05-115), HAPPEX-III(E05-109), d2n(E06-014), SANE(E07-003) and GEp-III(E04-108) experiments at Jefferson Lab, Newport News, VA

Honors and Awards

- Received Junior Scientist Travel Award from Jefferson Science Associates (JSA) for the following conferences: International Conference on New Frontiers in Physics (ICNFP) 2013 at Kolymbari, Crete, Greece; Eleventh Conference on the Intersections of Particle and Nuclear Physics (CIPANP) 2012 at St. Petersburg, Florida, USA; 4th Canada-America-Mexico Graduate Students Physics Conference (CAM) 2009 at Acapulco, Guerrero, Mexico.
- Served as the Chairman for the Particle Physics I session in the 4th Canada- America- Mexico Graduate Students Physics Conference on October 22-24, 2009 at Acapulco, Guerrero, Mexico
- Received Merit-cum-means Scholarship from IIT Roorkee during M.Sc in 2005.
- Cleared entrance exam for IIT (JAM) in 2005 with all India rank 154.
- Selected for integrated Ph.D. at Indian School of Mines (ISM) in 2005 with all India rank 1.

Selected Publications and Presentations

1. I. Korover *et al.* Approaching the nucleon-nucleon short-range repulsive core via the 4He(e,e$'$pN) triple coincidence reaction. *arXiv*:1401.6138 / To be published.
2. D. Wang *et al.* New Measurement of Parity Violation in Electron-Quark Scattering. *Nature* **506** (2014) 7486, 67-70.
3. D. Androic *et al.* First Determination of the Weak Charge of the Proton. *Phys. Rev. Lett.* **111**, 141803 (2013).
4. D. Wang *et al.* Measurement of the Parity-Violating Asymmetry in Electron-Deuteron Scattering in the Nucleon Resonance Region. *Phys.Rev.Lett.* **111** (2013) 082501.
5. X. Qiu *et al.* Direct Measurements of the Lifetime of Heavy Hypernuclei. *arXiv*:1212.1133 / To be published.
6. S. Abrahamyan *et al.* New Measurements of the Transverse Beam Asymmetry for Elastic Electron Scattering from Selected Nuclei. *Phys.Rev.Lett.* **109** (2012) 192501.
7. S. Abrahamyan *et al.* Measurement of the Neutron Radius of 208Pb Through Parity-Violation in Electron Scattering. *Phys.Rev.Lett.* **108** (2012) 112502.
8. W. Luo *et al.* Polarization components in π^0 photoproduction at photon energies up to 5.6 GeV. *Phys.Rev.Lett.* **108** (2012) 222004.
9. Z. Ahmed *et al.* New Precision Limit on the Strange Vector Form Factors of the Proton. *Phys.Rev.Lett.* **108** (2012) 102001.
10. Nuruzzaman *et al.* Nuclear transparency and effective kaon-nucleon cross section from the $A(e, e'K^+)$ reaction. *Phys. Rev. C* **84**, 015210(2011).
11. M. Meziane *et al.* Search for effects beyond the Born approximation in polarization transfer observables in ep elastic scattering. *Phys. Rev. Lett.* **106**, 132501(2011).
12. A. J. R. Puckett *et al.* Recoil Polarization Measurements of the Proton Electromagnetic Form Factor Ratio to $Q^2 = 8.5$ GeV^2. *Phys. Rev. Lett.* **104**, 242301(2010).

INDEX